$NdBaInO_4$ Based Triple (Electronic, Ionic and Protonic) Conductor for Solid Oxide Fuel Cell Applications

A thesis submitted in part fulfilment of the requirements for the degree of Doctor of
Philosophy in Materials Science and Engineering at Imperial College London

Yu Zhou

March 2021

Department of Materials

Imperial College London

2021

I hereby declare that this thesis and the work presented within is my original work. All the work included which is not my own work has been acknowledged and referenced appropriately.

Yu Zhou

2021

Acknowledgements

I hereby would like to address the utmost thanks of gratitude to Professor. Stephen John Skinner for his supervision, who offered me an opportunity to experience such a challenging and enjoyable Ph.D journey in Imperial College London. Without his guidance, this project could have ended up in nowhere. I am grateful of joining his group, sharing the research interests with the group members and more importantly having those opportunities to collaborate with researchers from Japan, Argentina etc. All those collaborations and experience are precious treasure in my memory.

I would like to acknowledge Professor. John Kilner for his useful advices. I could always feel the passion towards research of him, which encouraged me and inspired me when unexpected issues occurred during this project.

I wish to acknowledge Chen-Yu, Zijie, Zonghao, Jingyi and Jia for their helps and company during my Ph.D. Particularly, I want to thank Dr. Andrea Cavallaro, Dr. Ozden Celikbilek and Dr. Mathew Niania for their wealth of experimental experience and kindness, who helped me out a couple of times in the labs. Many thanks to all the fuel cell group members, who have been such a great bunch of interesting people to work along with.

Special thanks to Mr. Richard Sweeney for his help in XRD measurements, and also, as a fan of Arsenal FC, whom I would always love to have a conversation with when I walked pass the basement lab. I would like to express my gratitude to Dr. Sarah Fearn, who helped me a lot indeed with regard to the SIMS measurements. Conversations with them were truly relaxing.

I need to express my appreciation towards all the collaborators that I have been worked with in Tokyo Institute of Technology and in Centro Atomico Bariloche. Thanks Professor. Masatomo Yashima, Professor. Liliana Mogni, Masahiro, Yuta, Dr. Fujii, Laura and Juan for their kindness and helps during my visits.

For financial support of the Ph.D, I would like to acknowledge China Scholarship Council (CSC), who made this journey possible.

Finally, I would like to thank my family and friends both domestic and abroad, who always stand by me and share my confusions and anxiety relieving them with words of encouragement. A big thank you to Miss You, without whose companion, the pandemic lockdown period in the last year of my Ph.D would be much more difficult.

Abstract

Oxide-ion conducting materials have never failed to attract intensive attention due to their potential to be used for the applications of solid oxide fuel cell (SOFC) devices. With the aim of reducing the operating temperatures of SOFC devices to the intermediate high temperature range (500°C-800 °C), the design and synthesis of a new structure family to be used as the electrolyte material could be crucial.

In this thesis, the potential of calcium-doped layered perovskite compounds, $BaNd_{1-x}Ca_xInO_{4-x/2}$ (where x is the Ca content), as protonic conductors was experimentally investigated. The single phase of monoclinic crystal structure with the $P2_1/c$ symmetry was confirmed in the as-synthesized $BaNd_{1-x}Ca_xInO_{4-x/2}$ solid solutions by XRD characterisations. The acceptor-doped ceramics exhibited improved total conductivities that were 1-2 orders of magnitude higher than those of the parent material, $BaNdInO_4$. The highest total conductivity of 2.6 x 10^{-3} Scm^{-1} was obtained for the $BaNd_{0.8}Ca_{0.2}InO_{3.90}$ sample at a temperature of 750 °C in air. Electrochemical impedance spectroscopy measurements of the x = 0.1 and x = 0.2 substituted samples showed higher total conductivity under humid environments than those measured in a dry environment over a large temperature range (250 °C-750 °C). At 500 °C, the total conductivity of the 20% substituted sample in humid air (~3% H_2O) was 1.3 x 10^{-4} Scm^{-1}. The incorporation of water vapour decreased the activation energies of the bulk conductivity of the $BaNd_{0.8}Ca_{0.2}InO_{3.90}$ sample from 0.755(2) eV to 0.678(2) eV in air. The saturated $BaNd_{0.8}Ca_{0.2}InO_{3.90}$ sample contained 2.2 mol% protonic defects, which caused an expansion in the lattice according to the *in-situ* X-ray diffraction data. Combining studies of the impedance behaviour with 4-probe DC conductivity measurements obtained in humid air which showed a decrease in the resistance of the x=0.2 sample, it could be concluded that experimental evidence indicates that $BaNd_{1-x}Ca_xInO_{4-x/2}$ exhibits triple (oxygen-ion, proton and hole) conduction in wet atmospheres.

The oxygen and deuterium isotope exchange depth profiling measurements on the $BaNd_{0.8}Ca_{0.2}InO_{3.90}$ sample were successfully performed where valid diffusion kinetics for oxygen diffusion in this unique layered perovskite were firstly obtained. The obtained surface exchange coefficients for oxygen of the $BaNd_{0.8}Ca_{0.2}InO_{3.90}$ sample measured under wet atmospheres were significantly higher than those measured in dry $^{18}O_2$, while the diffusion coefficients in bulk material were decreased in wet atmosphere and a higher the activation energy for oxygen diffusion was achieved according to the Arrhenius plot. The activation energy for oxygen diffusion was increased from 1.08(8) eV to 1.86(11) eV after water incorporation, which implied a hindering effect of protonic defects on the oxygen diffusion process in the bulk material. Besides, fast grain boundary diffusion 'tail' was confirmed in the 500 ℃ and 550 ℃ ($H_2{}^{18}O+O_2$) wet exchange depth profiles and the grain boundary diffusion products, $D_{\mathrm{gb}} \cdot \delta$, of 6.64 x 10^{-14} and 5.31 x 10^{-13} cm^3/s at 500 ℃ and 550 ℃ respectively were calculated.

The chemical stability of the obtained phase in the $BaNd_{0.8}Ca_{0.2}InO_{3.90}$ sample was examined after long duration wet annealing by XRD and STEM-EDS materials characterization methods, where A-site cation exsolution of calcium and barium to the sample surface was confirmed forming corresponding $CaCO_3$ and $BaCO_3$ secondary phases on the surface.

In this work, processing high density Calcium substituted $BaNdInO_4$ as an electrolyte was investigated. By means of electrochemical performance characterization methods together with the isotope exchange depth profile measurement, the contribution of different charge carriers in this layered-perovskite structural material was probed. It was shown that $BaNd_{1-x}Ca_xInO_{4-x/2}$ exhibits triple (oxygen-ion, proton and hole) conduction in wet atmospheres and the migration of protons are much faster than that of oxide-ions. All these results implied a promising potential of this ceramic, with a unique layered perovskite structure, to be used as the electrolyte material for the intermediate high temperature SOFC devices.

Contents

List of Figures

List of Tables

List of Acronyms

SOFC	Solid Oxide Fuel Cell
GHG	Greenhouse Gas
MCFC	Molten Carbonate Fuel Cell
AFC	Alkaline Fuel Cells
PEFC	Polymer Electrolyte Fuel Cell
PAFC	Phosphoric Acid Fuel Cell
PC-SOFC	Proton Conducting Solid Oxide Fuel Cell
CTE	Thermal Expansion Coefficient
YSZ	Yttrium Stabilized Zirconia
TPB	Three Phase Boundary
LSCrF	$(La,Sr)(Co,Fe)O_{3-\delta}$
MIEC	Mixed Ion and Electronic Conduting
LSC	Strontium doped lanthanum cobaltate
SCO	Strontium Cobaltate
LSM	$(La,Sr)MnO_{3-\delta}$
IEDP	Isotope Exchange Depth Profiling
DC	Direct Current
AC	Alternating Current
GB	Grain Boundary
PLD	Pulsed Laser Deposition
STO	Strontium Titanate
FCC	Face-centered Cubic
EELS	Electron Energy Loss Spectroscopy

SAED	Selected Area Electron Diffraction
TGA	Thermogravimetry Analysis
NPD	Neutron Powder Diffraction
MD	Molecular Dynamics
SIMS	Secondary Ion Mass Spectrometry
LEIS	Low-energy Ion Scattering
SEM	Scanning Electron Microscopy
BNCxx	$BaNd_{1-x}Ca_xInO_{4-x/2}$
BVE	Bond Valence Energy
MSD	Mean Square Displacement
BSE	Backscattered Electron
TEM	Transmission Electron Microscopy
STEM	Scanning Transmission Electron Microscopy
EDS	Energy Dispersive X-ray Spectroscopy
FIB	Focused Ion Beam
CPE	Constant Phase Element
TMF	Thermomolecular Flow Effect
LMIS	Liquid Metal Ion Source
TOF	Time of Flight
ICP-AES	Inductively Coupled Plasma Atomic Emission Spectroscopy
EIS	Electrochemical Impedance Spectroscopy
OCV	Open Circuit Voltage
ROI	Region of Interest
RGA	Residual Gas Analyzer

Chapter 1

Introduction

1.1 What is a fuel cell and why fuel cells?

A fuel cell is an energy conversion device, which transforms the chemical energy stored in a gaseous fuel directly into electrical energy through electrochemical combination of the fuel with an oxidant. Figure 1.1(a) below shows the schematic diagram of fuel cell operation. In a fuel cell device based one oxide-ion conducting electrolyte, the combustion of the fuel, most commonly H_2, is split into two electrochemical semi reactions:

$$\mathrm{H_{2(g)}} + \mathrm{O^{2-}} \leftrightarrow \mathrm{H_2O_{(g)}} + 2\mathrm{e^-}(\mathrm{Anode})$$

$$\frac{1}{2}\mathrm{O_{2(g)}} + 2e^- \leftrightarrow \mathrm{O^{2-}}(\mathrm{Cathode})$$

$$\text{Overall reaction: } \mathrm{H_2} + \frac{1}{2}\mathrm{O_2} \rightarrow \mathrm{H_2O}$$

By using an ionic conducting and electronically isolated electrolyte material between the anode and the cathode, two half reactions are spatially separated and the electrons extracted from the oxidation of the fuel are forced to flow through an external circuit, thus generating an electric current. At the anode, fuel (H_2) reacts with oxygen ions forming water and electrons. The consumption of oxygen ions results in oxygen vacancies in the anode material, which then diffuse into the bulk and propagate through the electrolyte layer arriving at the cathode. At the same time, the electrons generated flow through a different path to the cathode and combine there with oxygen molecules forming oxygen ions, which then fill in the oxygen vacancies at the cathode and finishing the circuit. The whole process is driven by the difference in electrochemical potential between the electrodes. The charge carrier and half reactions may vary due to the different electrolytes employed. The chemical equations above describes the mechanism of a SOFC device based on an oxide-ion conducting electrolyte.

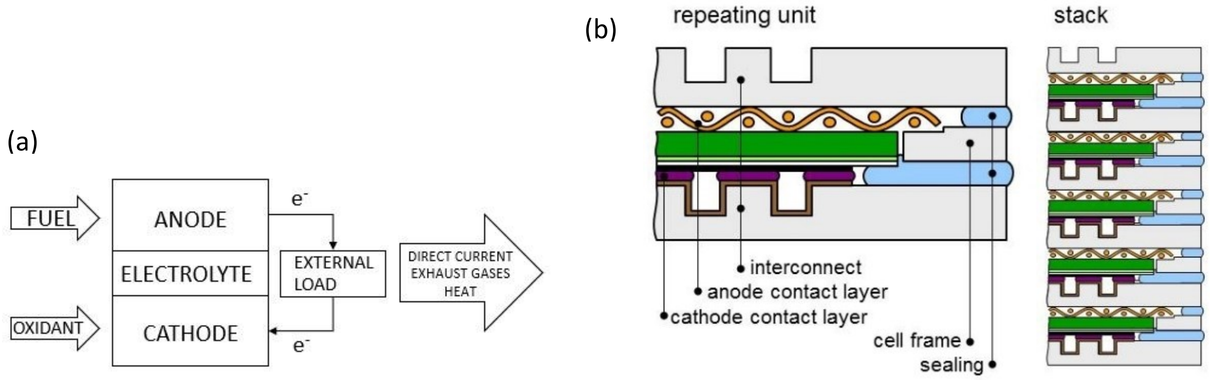

Figure 1.1 (a) The schematic diagram of fuel cell operation (b) A 6-cell Jülich® SOFC stack with the detailed cell structure together with the cell frame and sealing illustrated. Reproduced from (1) with kind permission from Martin Bram (Forschungszentrum Jülich GmbH, IEK-1).

Overall, the electrochemical device consumes fuel (H_2) and oxidant (O_2) by electrochemical reaction producing water and releasing energy at the same time. Since no intermediate form of energy is generated in the operation of a fuel cell, the energy conversion efficiency can reach up to 65%(2), which is much higher than that of a traditional combustion engine(~30%). The majority of released energy is converted into electrical power while the rest of it turns into heat dissipating within the cells as a by-product. Due to the high operating temperature of the SOFC devices, the heat by-product produced is of high temperature which can be utilized in a coupled system to further increase the overall efficiency(3). Figure 1.1(b) illustrates a state-of-art all-solid-based fuel cell stack integrated with a steel frame proposed and fabricated by Jülich®(1). Except for the three main components mentioned above, an interconnect component was deposited in between the stacks, which is meant to ensure sealing and improve electrochemical contacting in the fuel atmosphere. The electrochemical device and its structure in detail regarding the materials for each components will be discussed in the following chapters.

Climate change, greenhouse gas emission, consumption of limited fossil fuels, these eye-catching words along with a great number of reports have raised people's awareness of how our planet has been suffering from the misuse of resources over the last 200 years. The International Panel on Climate Change (IPCC) fourth assessment report in 2014(4) pointed out that 'most of the observed increase in global average temperature since the mid-20th century is mostly likely due to the observed anthropogenic greenhouse gas (GHG) concentrations'. On the other hand, the emission of GHG is highly related to the burning of fossil fuels. According to the accessible online source of U. S. Energy Information Administration (2019)(5), in 2019, the majority (more than 80%) of greenhouse gas (GHG) emissions in the United States still comes from burning fossil fuels. Even though many governments have launched programs and invested a huge amount of money and efforts on developing renewable energy generation systems, the direct burning of fossil fuel for energy still dominates the energy supply in most of the societies. Globally, PBL Netherlands Environmental Assessment Agency(6) summarized the trends in global CO_2 and total GHG emission of the G20 in the last two decades. The data showed a slowdown in growth of the GHG emissions of the most recent 5 years, however the increase in the green house emission and global climate change still seems unstoppable, which will for sure strongly affect human welfare and threatens hundreds of thousands of beings' life on Earth. Therefore, a stable environmentally friendly energy generation technique is desperately required for the continuous development of human beings.

Table 1.1 Summary of the similarities and differences between fuel cells, lithium-ion batteries, combustion engines and solar cells. (Adapted from (7))

	Fuel Cell	**Li-ion Battery**	**Combustion engine**	**Solar Cell**
Function	Energy conversion	Energy storage & conversion	Energy conversion	Energy conversion
Fundamental	Electrochemical reactions	Electrochemical reactions	Combustion	Photovoltaic effect
Typical fuel	Usually pure H_2	Stored chemicals	Gasoline, diesel	Light
Main output	DC electricity	DC electricity	Mechanical power	DC electricity
Main advantages	High efficiency Reduced emissions	High efficiency High maturity	High maturity Low cost	Eco-friendly High durability
Main disadvantages	High cost Low durability	Safety issue Low durability	Significant emissions Low efficiency	Low efficiency Low power level

In comparison with the main energy generation techniques today, table 1.1 summarized the similarities and differences between fuel cells, lithium ion batteries, traditional combustion engine and the solar cells. The applications of traditional combustion engines in stationary power plant and transportation propulsion are steadily being replaced by new energy generation technologies with high energy conversion efficiency and reduced emission of GHGs. As the alternatives, fuel cells, batteries and solar cells all function as energy conversion devices which convert either chemical energy (fuel cells, batteries) or solar energy (solar cells) into a direct current (DC) flow. However fuel cells and solar cells are systems that operated at a thermodynamic steady state with a constant voltage output as long as it is continually supplied with fuel or light from an external source. On the contrary, most batteries are closed thermodynamic systems contain an exhaustible internal supply of reactants. As these reactants (Li^+ in lithium batteries) deplete, the voltage of the battery decreases over time. The main disadvantages of the lithium-ion batteries which is also the major challenge of the field is the safety issue which stems from the flammable liquid electrolytes typically employed in Li-ion cells. Some lithium battery devices also suffer from ageing issue, the performance of which is dependent upon the number of charge-discharge cycles undergone. Solid oxide fuel cell device also suffers from low material durability because of its high operating temperature which triggered the research interest of finding an electrolyte material in replacement of the yttrium stabilized zirconia (YSZ) based cells. Being compared with solar cells as an energy generation device, fuel cell system has the merit of high power output and stability as the supply of fuel doesn't rely on season and weather. From the perspective of applications in the automotive, fuel cell units showed disadvantages of high capital cost and low maturity in commercialization compared with lithium batteries. The application of fuel cell in transportation propulsion is also limited by the fuel (H_2) supply. The production and storage of pure hydrogen will add extra cost to the employment of the fuel cell technique in the automotive applications.

Winning the merits of high energy conversion efficiency directly from fuels with reduced GHG emissions, solid oxide fuel cell technology is still a promising candidate for the future power generation system, which can effectively mitigate the reliance upon the resource of fossil fuels by using it more wisely. However, the high operating temperature of the existing SOFC devices limited its applications due to the high demanding for the materials used and the low durability. It is crucial to find an alternative conductor used as the electrolyte material and lower the operating temperature of the SOFC into intermediate temperature range(500^{o}C-800 ^{o}C).

1.2 A brief history of fuel cells

The principle of the fuel cell was discovered in 1839 by Sir William Grove(8). In his letter published in the February issue of Volume XIV of *The London and Edinburgh Philosophical Magazine* and *Journal of Science*, he described his discovery of the combination of gases by platinum on voltaic series. According to his observation, 'little electric action was manifest' at room temperature on his first attempt when employing the dilute sulfuric acid as the electrolyte between two troughs, one of plates of iron and the other of plates of copper, containing hydrogen and air respectively. This 'electric manifesting' device was reported as one type of battery at that moment, which was then known as fuel cells. After that, Grove carried out a series of related experiments and gave a presentation at Royal Society in 1842, in which he reported the invention of an apparatus named 'gaseous voltaic battery'(9). As can be seen in Figure 1.2(a), two platinized electrodes were used in the apparatus in order to increase the exposed surface area of the electrodes in the gas environment. A series of fifty such pairs semi-immersed in dilute sulfuric acid was found to 'whirl round' the needle of a galvanometer, to give a painful shock to 5 people joining hands(9). He also investigated the minimum number of such cells connected in series required to decompose water which was found to be 26.

After Grove presented his experiments to the Royal Society of London, several attempts were made by Lord Rayleigh(10), Ludwig Mond, *et al*(11) in order to improve the performance of this 'gas battery'. The prototype for the practical fuel cell was constructed in 1889 by Mond and Langer which exhibited an efficiency of nearly 50%(11). They also realized that the wasted energy was converted into heat within the battery.

Although, the concept of fuel cells emerged almost two centuries ago, the first practical application of a fuel cell system was in the 1960s, when the Gemini space flights chose the solid polymer electrolyte fuel cell system as an auxiliary power supply due to its high power and energy densities with respect to volume and weight(12). During the same period of time, all 18 Apollo missions used alkaline fuel cells (AFCs) as the continuous power supply(13). Due to their exemplary in-flight performance, International Fuel Cells (a division of United Technologies Corporation) produced an improved cell in 1970s. The improved system provided all of the electric power required for the shuttle, which was eight times more power than the Apollo ones(14). Moreover, it provided drinking water at the same time when the Space shuttle was in flight.

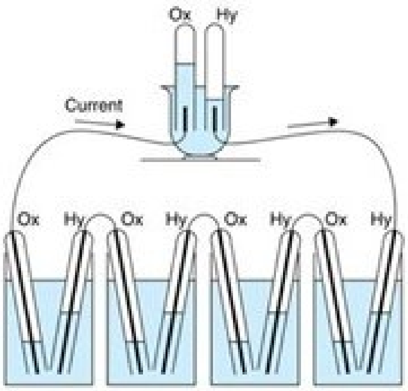

Figure 1.2 The schematic sketch of four 'gaseous voltaic battery'. Adapted from Sir William Robert Grove's origin letter.(9)

The successful application of fuel cells in the space programs stimulated great research interest worldwide. Intensive research activities were launched probing the development of fuel cell technology which was expected to be the future power generation technology with high energy conversion efficiency and low emission. People realized the potential application of fuel cell devices in stationary power supply fields providing an more environmentally friendly way of utilizing fuels. In the 1980s, national programs were established in Japan and Europe. Since then, several fuel cell technologies have been well developed and hundreds of fuel cell units have been installed worldwide (15-17). On the other hand, polymer electrolyte membrane fuel cells operated at low temperatures have recently attracted much attention due to their potential applications in portable power devices and in transportation applications (16, 18, 19).

As a power generation device, the key advantage of a fuel cell is its high conversion efficiency. Compared with other conventional energy generation methods, such as the combustion turbine system, the conversion efficiency of a fuel cell is not subjected to the Carnot limitation because it converts the chemical energy of a fuel directly without an intermediate of heat. As reported in the 5th FCDIC Fuel Cell Symposium in Tokyo in 1996(3), the theoretical conversion efficiency of an integrated solid oxide fuel cell combustion turbine power system was expected to reach up to 70%.

At this stage, according to the electrolyte used, the state-of-the-art fuel cells can be mainly classified into five types, namely, the polymer electrolyte fuel cell (PEFC), the alkaline fuel cell (AFC), the phosphoric acid fuel cell (PAFC), the molten carbonate fuel cell (MCFC) and the solid oxide fuel cell (SOFC)(3). Among all these fuel cells, the most industrialized and documented fuel cell system is the PAFC. By the end of 2005, more than 500 PAFC power plants had been installed and tested around the world(20). However, the high cost of constructing one unit of PAFC severely hindered its commercialization. In the 1990s, the discovery of polymer electrolyte membrane fuel cells triggers enormous investments and research activities in fuel cells for propulsion of passenger vehicles because of its high power density versus weight and low-to-zero emission (21, 22). Unfortunately these fuel cell vehicles were not commercialized at that time because they failed in competition with lithium-ion battery vehicles. The characteristics of all five types of fuel cells are listed in Table 1.2. Our research interest is mainly focused on SOFCs materials, to be more specific, the electrolyte materials used for SOFC applications. In the next section, the advantages of SOFC over other types of fuel cells will be discussed together with a brief introduction of materials used for different components of a SOFC stack.

Table 1.2 The Characteristics of the different types of fuel cells(adapted from (3)).

	PEFC	AFC	PAFC	MCFC	SOFC
Electrolyte	Nafion	NaOH/KOH	H_3PO_4	Na_2CO_3-Li_2CO_3	ZrO_2-Y_2O_3
Operating temperature (°C)	70-80	70	200	650-700	900-1000
Main charge carrier	H^+	OH^-	H^+	CO_3^{2-}	O^{2-}
Fuel	H_2	H_2	H_2	H_2, CO, CH_4	H_2, CO, CH_4
Expected efficiency (HHV) (%)	30-40	~70	35-42	45-60	45-65
Power, current status (kW)	12.5[a]	10[b]	100[c]	1000[d]	100[e], 15[f]
Efficiency (%)	40	>60[b]	40	45	43[d], 50[e]
Main applications	Vehicles	Standalone power generators	Portable power applications	High power application	Stationary power generator

[a] Allied signal.

[b] AFC energy.

[c] Fuji electric.

[d] MCFC Research Association, Japan.

[e] Siemens Westinghouse.

[f] Mitsubishi Heavy Industry and Electric Power Development.

1.3 Solid oxide fuel cells

A solid oxide fuel cell (SOFC) device consists of a dense layer of oxide-ion or proton conducting electrolyte sandwiched by two porous electrodes. The adoption of either oxide-ion conductor or protonic conductor as the dense electrolyte material changes the operation mechanism of a SOFC as well as its operating temperature and applications. As illustrated in Figure 1.3 the bias compensation within the structure is completed by the transportation of oxide-ions in the oxide-ion conductor based SOFC, whereas in the proton conducting solid oxide fuel cell (PC-SOFC), proton is the main charge carrier that is moving in the system.

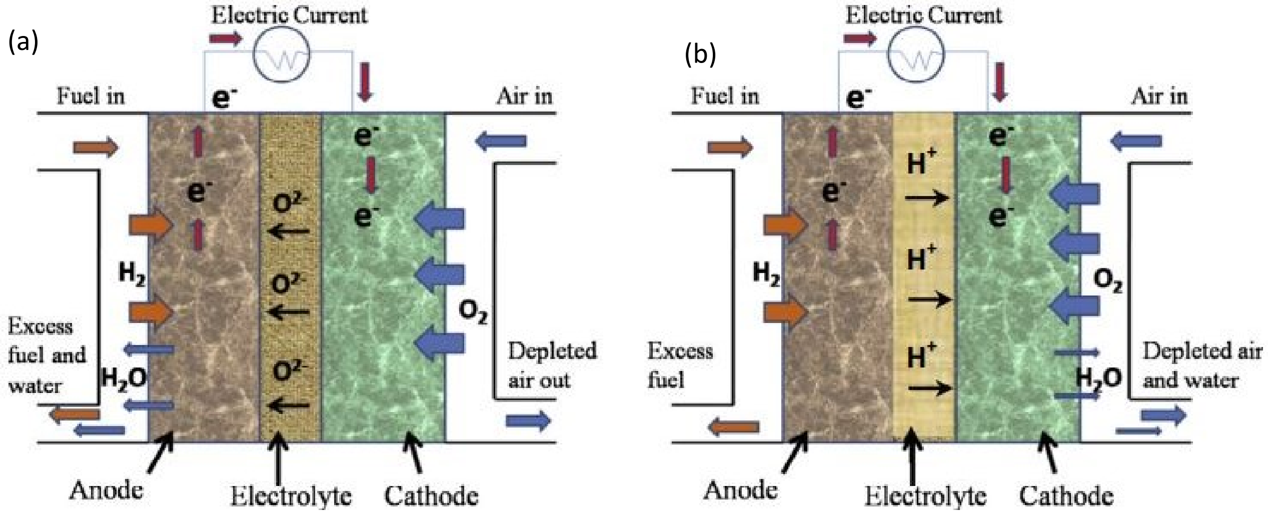

$$H_{2(g)} + O^{2-} \leftrightarrow H_2O_{(g)} + 2e^-(\text{Anode})$$
$$\frac{1}{2}O_{2(g)} + 2e^- \leftrightarrow O^{2-}(\text{Cathode})$$
$$\text{Overall reaction: } H_2 + \frac{1}{2}O_2 \rightarrow H_2O$$

$$H_{2(g)} \leftrightarrow 2H^+ + 2e^-(\text{Anode})$$
$$\frac{1}{2}O_{2(g)} + 2H^+ + 2e^- \leftrightarrow H_2O(\text{Cathode})$$
$$\text{Overall reaction: } H_2 + \frac{1}{2}O_2 \rightarrow H_2O$$

Figure 1.3 Schematic diagram of reactions in solid oxide fuel cells based on (a) an oxide-ion conducting electrolyte or (b) a proton conducting electrolyte. Reproduced from (23) with permission from Elsevier. The corresponding semi reactions and the overall reaction are illustrated below.

Due to the dehydration reaction that happens in most of the proton conducting materials at high temperatures, the operation temperature of a PC-SOFC is within the intermediate to high temperature range (500-800℃) which is slightly lower than that of a SOFC based on an oxide-ion conductor (600-1000℃). If being used in a reverse operation mode, the PC-SOFC becomes an electrolyzer which is a promising candidate for hydrogen production because it produces pure hydrogen gas at the anode side.

Among all types of fuel cell technologies discussed in the previous section, SOFCs have several distinct advantages due to their all-solid-state structure and high operating temperature. The use of nonprecious materials and no liquids involved in the system eliminates some maintenance problems regarding the materials corrosion and liquid-solid surface wetting issues. On the other hand, the high operating temperature of a SOFC system (normally over 800℃) promotes rapid reaction kinetics at the electrodes and allows the reforming of hydrocarbon fuels at the anode side within the cells which results in multi-fuel capacity of SOFC devices(24). Regarding the heat produced by the electrochemical reaction, which is inevitably generated in all types of fuel cells by ohmic losses, electrode overpotentials(25) etc, the high operation temperature of a SOFC allows possibilities for cogeneration application in coal based stationary power plants(26) which need heat for gasification. Actually, the heat is necessary to maintain the operation of cells. Other applications for the residual heat of a SOFC system such as utilization in a bottoming cycle or in production of hot water are also considered in the design of a SOFC based system. By using the heat by-product properly, the overall energy conversion efficiency of a SOFC system can be further increased(27). As reported by Buonomano et al.(28), a SOFC-gas turbine(SOFC-GT) system for combined heat and power can even achieve electrical efficiencies of as high as 70%. It is worth noting that in Buonomano's research, the margority of SOFC-GT hybrid systems are fed by methane, which is easier to manage than hydrogen(28).

Every coin has two sides. The high operating temperature of SOFCs also places stringent requirements on the choice of materials used in all cell components. The criteria of choosing materials for each component in a SOFC design varies due to the different chemical environments in different parts of a fuel cell. Since 1937 when zirconia ceramics were first used in fuel cell application(29), SOFC technologies have been through great developments in the aspect of structural design. However, the principal components in a SOFC stack are quite common in all cases, namely, an electrolyte, two porous electrodes and the interconnection.

(A) Anode Materials: The function of an anode electrode in a SOFC system dictates the complication in choosing the suitable anode materials for a particular SOFC device. It involves facilitation of fuel gas diffusion and oxidation of the fuel as well as transport of electrons and transport of the by-products of the electrochemical reaction. Regarding the high temperature and strong reducing atmosphere at the anode side during the cell operation, the anode materials need to be both chemically stable and highly resistive to degradation in order to achieve prolonged cell operation time. The basic requirements for an anode material to be used in SOFC applications is listed below:

- High electro-catalytic activity towards oxidation reaction of the fuel gases.
- Similar thermal expansion coefficient (CTE) and chemical compatibility with the adjacent components (the electrolyte and the interconnection).
- Should possess continuous porous structure to increase the effective surface area for the gas diffusion.
- Excellent carburization and sulfidation resistence to allow fuel flexibility.
- A mixed ionic and electronic conductor(MIEC).
- High wettability with respect to the electrolyte substrate, ease in fabrication and low cost.

The most well-known anodes for high temperature SOFC applications is nickel/yttria stabilised zirconia cermet(30, 31). In the cermet, Ni provides excellent catalytic activity for the electrochemical oxidation of H_2

and sufficiently high electronic conductivity ($\sim 2 \times 10^4 \mathrm{S \cdot cm^{-1}}$ at $1000°\mathrm{C}$), while YSZ constitutes a framework for the dispersion of Ni particles which stabilizes Ni from coarsening(32, 33). At the same time, YSZ provides a significantly high ionic conductivity, which allows the oxidation of H_2 to happen effectively at the nickel/YSZ/gas three phase boundary (TPB). Ni/YSZ cermet exhibits high stability in reducing atmosphere and good material capacity with the YSZ electrolyte. All these characteristics of Ni/YSZ make it a promising anode material for the high temperature SOFC applications.

Apart from Ni/YSZ, intensive research activities have been carried out in the development of alternative anode materials in the last few years. Materials such as the double perovskite $Sr_2Mg_{1-x}Mn_xMo_{6-\delta}$ (34) and Sr_2MMo_6 (M=Fe, Co, Ni)(35-37) all exhibited promising mixed ion and electronic conducting (MIEC) properties under high temperature. The stems of these MIEC materials offers an option for SOFC operation with natural gas because Ni suffers from carbon deposition during the operation of SOFC using CH_4 as a fuel(34). However, in spite of the poor carburization and sulfidation capabilities, Ni/YSZ continues to be the selected anode material for the high temperature SOFC applications(30, 31). The main disadvantage of these MIEC materials to date compared with Ni/YSZ is their poor chemical stability under long operation time of the cell. It is rather difficult to find a MIEC material that has the required catalytic activity for H_2 oxidation or methane reforming and at the same time the electronic conductivity comparable to Ni. The chemical composition and microstructure of these new anode materials need to be further optimized in order to achieve satisfactory electrochemical properties for the applications in high temperature SOFC devices.

(B) Cathode Materials: The criteria of choosing cathode materials for the high temperature SOFC application are similar to those of anode materials except for the requirements related to the oxidizing atmosphere at the cathode. Cathode materials in SOFC devices are expected to have high catalytic activity for the oxygen reduction reaction as well as sufficiently high oxide-ion conductivity to facilitate the diffusion of oxide-ions. In order to find an ideal cathode material for the high temperature SOFC applications, a wide variety of perovskite-type materials have been investigated in the last three decades. The majority of these perovskite-type oxides can be categorized into three main divisions, the strontium-doped lanthanum manganite based materials (LSM), the strontium doped lanthanum cobaltate based materials (LSC), and the strontium cobaltate based materials (SCO).

The choice of electrolyte material is of great importance when considering the cathode materials(38). According to the previous literatures, whilst LSC and SCO exhibited excellent cathodic properties in the SOFC devices using ceria-based electrolyte(38-42), LSM was utilized in the YSZ-based SOFC applications(43, 44). Initially, the $\mathrm{La_{1-x}Sr_xCoO_{3-\delta}}$ (LSC) family caught most research interests due to its considerable oxide ion conductivity(45). The intensive research activities on this material didn't last for long because of its poor performance at elevated temperatures as fabricated into a symmetric cell(39). Both A-site and B-site substitution in the LSC perovskite have been discussed which indeed improved the electrochemical properties of these materials, but further optimization is required with respect to the chemical stability of these materials. In contrast to LSC, LSM based materials are good electronic conductors rather than ionic conductors. Much of the interest in the LSM family stems from the fact that the cation deficiencies existing in the structure can effectively prohibit interfacial reactions, and thus, improve the cathode performance(45). With regard to the electrochemical properties as well as the stability and degradation, quite a few works have been done on improving the cathode performance of LSM-type perovskites(46-48). The mismatch in coefficient of thermal expansion (CTE) though, between the LSM-type perovskites and the YSZ electrolyte is the major challenge preventing it from further development. The scandium doped strontium cobaltate ($\mathrm{SrCo_{1-x}Sb_xO_{3-\delta}}$)(41, 42) or antimony doped strontium cobaltate ($\mathrm{SrCo_{1-x}Sc_xO_{3-\delta}}$)(49) represent the new perovskite-type materials that shows the as-required mixed ionic and electronic conducting properties for the cathode materials used in SOFC devices. It was noted that there was a phase transition of this material with respect to the doping levels, which change the tetragonal perovskite structure of the original $\mathrm{SrCoO_{3-\delta}}$ into a cubic *Pm-3m* perovskite(41). These materials were tested in a ceria-based SOFC system exhibiting high power densities at intermediate high temperatures (400-800°C)(41, 49).

(C) Interconnect Materials: The main purpose of the interconnect in a SOFC stack is to connect the individual cells in series and convey electrical current in between. Therefore, sufficiently high electronic conductivity under the operating atmosphere is the key requirement for the interconnect materials. However, what makes it extremely stringent to employ an appropriate interconnect material is the complicated chemical environment of an interconnect within a SOFC stack. Since an interconnect extends between the anode of one cell and the cathode of the adjacent cell, it has to be dense enough to avoid gases mixing and chemically stable in both oxidizing and reducing atmospheres at elevated temperatures. These criteria eliminate most of the candidates for this particular application. In addition, the interconnect materials should also have high thermal conductivity for heat dispersion within the cells, high creep resistance and high toughness to allow prolonged operation, and last but not least, the small mismatches in CTE with all components in the SOFC stack. Very few materials manage to fulfil all these requirements. Chromium containing alloys for the intermediate temperature application(50, 51) and $\mathrm{LaCrO_3}$-based perovskites for high temperature application(52) are two major options along with some recent research on the combination of these two types of materials(53, 54).

1.4 Electrolyte materials for SOFC application

In an oxide-ion conducting solid oxide fuel cell device as shown in Figure 1.4(a), an electrolyte material functions not only as a separator between the air and fuel gas, but also as a shuttle for the oxide-ion transportation. Therefore, it has to be of high ionic conductivity and impermeable to prevent gas permeation during cell operation. Figure 1.4(b) shows the cross-section SEM image of a planar SOFC stack design with two porous electrodes sandwiching a dense thin electrolyte layer of approximately 15 μm in thickness.

Since 1839, Faraday firstly observed ion conduction in the fluorite structure at high temperature, many materials with fluorite, perovskite and apatite related structures have been examined as the electrolytes for applications in SOFC devices. The first of all criteria is the high oxygen ion conductivity at the operating temperature of the device. Kilner et al.(55) summaried the ionic conductivities of most of the state-of-art potential ionic conductors for use of electrolyte materials in SOFC devices as shown in Figure 1.4(c).

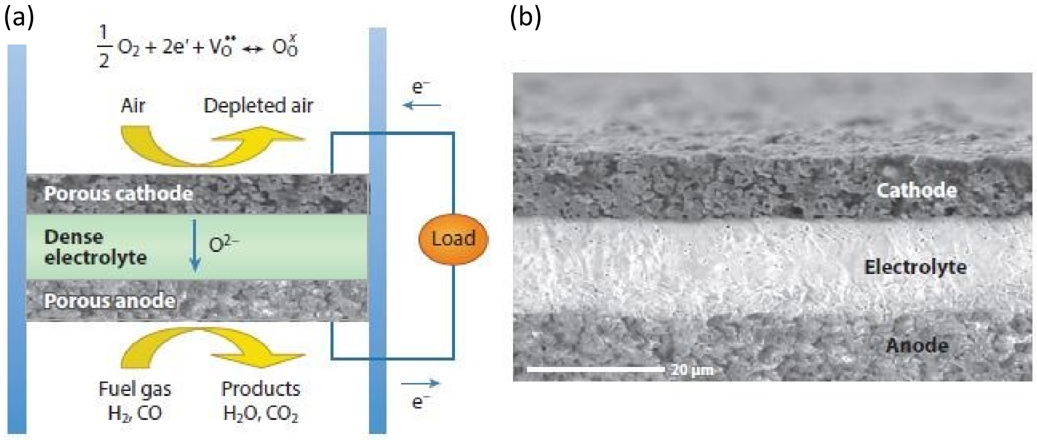

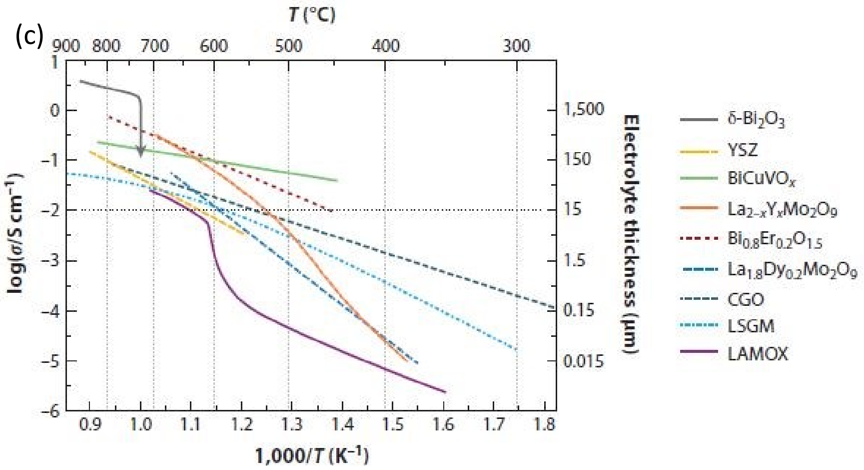

Figure 1.4 (a) Schematic of a solid-oxide fuel cell. (b) Cross section image of a first fabricated anode-support cell. Reproduced with permission from (56) (c) Arrhenius plots of the oxygen ion conductivities of the most state-of-art SOFC electrolyte materials. The horizontal dotted line represents the limit of conductivity, which is necessary to construct a device with an electrolyte thickness of 15 μm or less. Reproduced with permission from (55).

For a structure to achieve high values of ionic conductivity, a large number of interconnected equivalent sites must be present, which are partially occupied to allow high mobility of the ionic charge carriers. Partial occupation of the equivalent sites can be achieved either intrinsically or extrinsically. In a chemically stoichiometric compound, the partial occupation can be achieved through intrinsic thermal disorder. At low temperatures, the normal sites in the lattice are fully occupied by cations, while the interstitial sites are empty. As the temperature increased, once the cation at the normal site gained enough energy to overcome the energy difference between the sub-lattices, it can hop out of its regular site and fill in the interstitial site forming an interstitial-vacancy pair and resulting in partial occupation of the combined sub-lattice. A classic example of this type of material is the δ-Bi_2O_3(57). Partial occupation of equivalent sites can also be achieved extrinsically in non-stoichiometric materials. For example, the substitution of aliovalent cations into the origin system (e.g. 10mol% Gd_2O_3 stabilized CeO_2(58)) will generate extrinsic point defects, such as oxygen vacancies, causing partial occupation at the anion sites(59).

1.4.1 Oxygen transport

In this section, the ionic mobilities of the charge carriers will be discussed to investigate the important atomistic factors which govern the fast ionic conduction. As we consider a crystal with N equivalent sites per unit volume, which are partially occupied, we can define the occupied factor as c, and therefore the fraction of unoccupied sites becomes $(1 - c)$. There is always a hindrance, or in other words an energy barrier to overcome, as an ion tends to migrate through the crystal to another unoccupied equivalent site. We can define this intervening energy barrier as the Gibbs energy of migration, ΔG_{m}. The smaller the ΔG_{m}, more easily can an ion hop to an equivalent site.

In the Einstein equation, the ionic mobility is related to the ionic self-diffusion coefficient as:

$$\mu = \frac{qD}{kT} \qquad (1)$$

According to the random walk theory in a 3-D lattice, the self-diffusion coefficient, *D*, can be expanded as:

$$D = \frac{z}{6} f(1 - c) a_0^2 \upsilon_0 \exp\left\{-\frac{\Delta G_{\mathrm{m}}}{kT}\right\} \qquad (2)$$

where z is the number of adjacent equivalent sites, a_0 is the distance between equivalent sites, v_0 is a characteristic lattice frequency and ΔG_m is the Gibbs free energy of migration. The factor f is the correlation factor representing the deviation from randomness of the atomic jumps. It would have a value of ~ 0.65 in a simple cubic lattice.

Since

$$\Delta G_\mathrm{m} = \Delta H_\mathrm{m} - \Delta S_\mathrm{m} \cdot T \tag{3}$$

where ΔH_m, ΔS_m are the migration enthalpy and entropy respectively.

As we can define the term γ as,

$$\gamma = \frac{z}{6} f \exp\left\{\frac{\Delta S_\mathrm{m}}{k}\right\} \tag{4}$$

thus,

$$\mu = \frac{q}{kT} \gamma (1-c) a_0^2 v_0 \exp\left\{\frac{-\Delta H_\mathrm{m}}{kT}\right\} \tag{5}$$

Since the ionic conductivity can be derived from:

$$\sigma = nq\mu \tag{6}$$

and the volume concentration of mobile ions, n is given by the product of N and c.

Therefore,

$$\sigma = N \frac{q^2}{kT} \gamma c (1-c) a_0^2 v_0 \exp\left\{\frac{-\Delta H_\mathrm{m}}{kT}\right\} \tag{7}$$

For a material with oxygen vacancies, as is the most common situation in the oxide ion conductors, we can use an expression to replace the fraction of occupied and unoccupied sites in terms of the oxygen vacancy concentration $[V_O^{\cdot\cdot}]_\mathrm{s}$. It needs to be noted that, here the $[V_O^{\cdot\cdot}]_\mathrm{s}$ is expressed only as a site expression. Equating the $(1-c)$ with $[V_O^{\cdot\cdot}]$ gives an alternative expression for the ionic conductivity of an oxide ion conductors,

$$\sigma = N \frac{q^2}{kT} \gamma [V_O^{\cdot\cdot}]_\mathrm{s} (1 - [V_O^{\cdot\cdot}]_\mathrm{s}) a_0^2 v_0 exp\left\{\frac{-\Delta H_\mathrm{m}}{kT}\right\} \tag{8}$$

This expression can be compared with an empirical Arrhenius type equation for conductivity:

$$\sigma = \frac{\sigma_0}{T} \exp\left\{-\frac{E_\mathrm{a}}{kT}\right\} \tag{9}$$

where E_a is the activation energy for the conduction process and σ_0 is a pre-exponential constant.

It can be noted from Eq. (7) and Eq. (8) that the predicted ionic conductivity depends on two variables, the fraction of occupied sites c or oxygen vacancy concentration $[V_O^{\cdot\cdot}]_\mathrm{s}$ and the migration enthalpy ΔH_m, while the other terms are either constants (q, k) or variables that are not expected to alter substantially from oxide to oxide (N, a_0, γ, v_0). Therefore, we can derive the concentration dependence of the isothermal ionic conductivity of an oxide ionic conductor, which follows a quadratic curve with a maximum value obtained when half of the oxygen sub-lattices are occupied, a condition that is not possible for any practical oxide. In addition, according to Eq. (8) and Eq. (9), to obtain high values of ionic conductivity at a low set temperature, the activation energy E_a or enthalpy ΔH_m for the migration of oxygen ions needs to be as small as possible.

The oxygen self-diffusion coefficient D is another useful parameter in probing the oxygen transportation process in an oxide-ion conductor, which can be obtained from Eq. (5) as:

$$D = \gamma [V_O^{\cdot\cdot}]_\mathrm{s} a_0^2 v_0 exp\left\{\frac{-\Delta H_\mathrm{m}}{kT}\right\} \tag{10}$$

where $[V_O^{\cdot\cdot}]_\mathrm{s}$ is again expressed as the mobile vacancy fraction. Note that defect concentrations are normally expressed as molar fractions and are only equivalent to site fractions for simple binary oxides with stoichiometry MO. Experimentally, the oxygen self-diffusion coefficient can be derived either from isotope exchange depth profile (IEDP)(60) measurement using the ^{18}O tracer, or from measurements of the ionic conductivity, σ, using DC conductivity measurement or the AC impedance technique. Both of them are useful techniques probing the oxygen transport mechanism of an oxide-ion conductor.

1.4.2 The effect of the ambient atmosphere on the conductivity

As discussed before, the partial occupancy can be achieved extrinsically by acceptor-doping, which will cause the formation of oxygen vacancies as the charge compensating defects. Let us consider an ionic conducting oxide of the cation $\mathrm{M^{m+}}$ with the chemical composition of $\mathrm{M_2O_m}$. By introducing a lower-valent cation $\mathrm{Mf^{(m-n)+}}$ into the oxide, oxygen vacancies were introduced into the system as a charge compensator, and the process of which can be expressed as the Kröger and Vink notation below:

$$\mathrm{Mf_2O}_{m-n} + \mathrm{2M_M^x} + \mathrm{nO_O^x} \rightarrow \mathrm{2Mf_M^{n'}} + \mathrm{nV_O^{\cdot\cdot}} + \mathrm{M_2O_m}$$

In the absence of any other defect equations or electronic defects, the neutrality condition of the system will be:

$$n\left[\mathrm{Mf_M^{n'}}\right] = 2[V_O^{\cdot\cdot}] \tag{11}$$

This electroneutral condition will be modified slightly when electronic defects are involved, caused by equilibration of the lattice in the oxygen ambient environment. This equilibration can be expressed by two electronic defect equations. For high oxygen partial pressures, where oxygen is being incorporated into the lattice combining with the oxygen vacancies, the process can be written as:

$$\frac{1}{2}\mathrm{O_2(g)} + \mathrm{V_O^{\cdot\cdot}} \leftrightarrow \mathrm{O_O^x} + 2h^{\cdot} \tag{12}$$

where $\mathrm{h^{\cdot}}$ represents an electron hole. By applying the law of mass action into equation 12, we can obtain the expression for the temperature dependent constant $\mathrm{K_1(T)}$:

$$K_1(T) = \frac{[O_O^x]\cdot[h^{\cdot}]^2}{P_{\mathrm{O_2}}^{1/2}\cdot[V_O^{\cdot\cdot}]} \tag{13}$$

Rewriting the concentration of holes as *p* and noting that in most of the situations $[O_O^x]$ approximately equals 1, thus,

$$p^2 = K_1(T)\cdot P_{\mathrm{O_2}}^{1/2}\cdot[V_O^{\cdot\cdot}] \tag{14}$$

Then the condition of electroneutrality becomes:

$$n\left[\mathrm{Mf_M^{n'}}\right] = 2[V_O^{\cdot\cdot}] + p \tag{15}$$

In an aliovalent cation doped oxide-ion conductor, the concentration of oxygen vacancies is far larger than that of electron holes in most of the situations. Therefore, we can apply $p \ll [V_O^{\cdot\cdot}]$ into Eq. (15), and the electroneutral condition can be simplified as $n\left[\mathrm{Mf_M^{n'}}\right] = 2[V_O^{\cdot\cdot}]$. The substitution of this condition into Eq. (14) gives

$$p = \left[\frac{n}{2}\cdot K_1(T)\right]^{1/2}\cdot\left[\mathrm{Mf_M^{n'}}\right]^{1/2}\cdot {P_{O_2}}^{1/4} \tag{16}$$

Thus at high oxygen pressures, the concentration of electron holes is proportional to ${P_{\mathrm{O_2}}}^{\frac{1}{4}}$, whereas at reducing atmospheres or under low oxygen partial pressures, the lattice tends to further lose oxygen ions,

$$\mathrm{O_O^x} \leftrightarrow \mathrm{V_O^{\cdot\cdot}} + \frac{1}{2}\mathrm{O_{2(g)}} + 2e' \tag{17}$$

Through a similar process as above, we can obtain the expression for the electron concentration as a function of oxygen partial pressure:

$$n_e = \left[\frac{2}{n}\cdot K_2(T)\right]^{1/2} \cdot \left[\mathrm{Mf}_{\mathrm{M}}^{\mathrm{n}'}\right]^{-1/2} \cdot P_{\mathrm{O}_2}{}^{-1/4} \tag{18}$$

The P_{O_2} exponent changes from $\frac{1}{4}$ to $-\frac{1}{4}$ as the atmosphere changes from an oxygen-enriched environment to an oxygen-deficient environment. Besides, it is worth pointing out that combining Eq. (16) and Eq. (18) yields the equilibrium constant for intrinsic electron-hole pair formation, $K_{\mathrm{i}}(T)$,

$$nil \leftrightarrow h^{\cdot} + e' \tag{19}$$

$$K_{\mathrm{i}}(T) = p \cdot n_e = [K_1(T) \cdot K_2(T)]^{1/2} \tag{20}$$

Then, we can plot the concentration of defects in the system against P_{O_2}. These types of plot are described as Brouwer(61) or Kröger–Vink(62) diagrams, which are particular ways of explaining the conduction mechanism of a mixed ionic and electronic conductor at various oxygen partial pressures. By summing the products of defect concentrations with appropriate defect mobilities, we can obtain the electrical conductivity (σ_{T}) as a function of P_{O_2} (noting that the mobility of aliovalent cations on site is comparably low).

$$\sigma_{\mathrm{T}} = \sigma_e + \sigma_h + \sigma_{[\mathrm{V}_{\mathrm{O}}^{\cdot\cdot}]} = e \cdot n_e \cdot \mu_e + e \cdot p \cdot \mu_p + 2e \cdot [V_O^{\cdot\cdot}] \cdot \mu_{[\mathrm{V}_{\mathrm{O}}^{\cdot\cdot}]}$$

where μ_e, μ_p and $\mu_{\mathrm{V}_{\mathrm{O}}^{\cdot\cdot}}$ represent the mobilities of electrons, holes and oxygen vacancies respectively. Figure 1.5 shows the results of adding three contributions together. Due to the higher mobilities of electrons and holes over that of oxygen ions, the conductivity plot is divided into three distinct ranges. In region (I) where the hole conduction dominates, the total conductivity σ_{T} varies as $P_{\mathrm{O}_2}{}^{\frac{1}{4}}$, while in region (III) the exponent of P_{O_2} is $-\frac{1}{4}$. Region (II) represents the oxygen partial pressure range where oxide-ions are the main charge carriers in the system. This central range is often called the ionic domain in the literatures, and its extent is dependent upon temperature and doping amount.

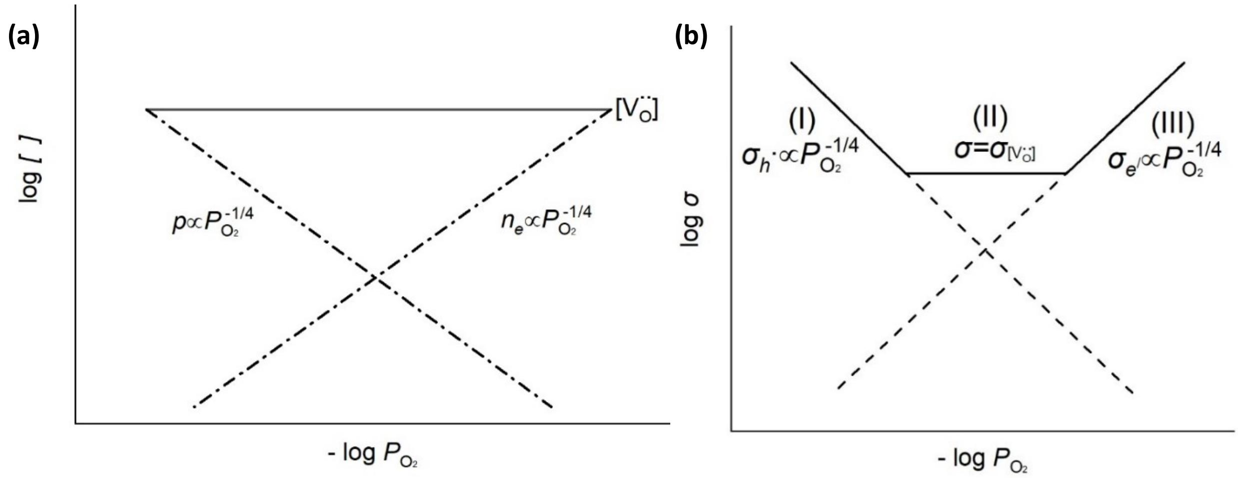

Figure 1.5 (a) Brouwer diagram for defects in an acceptor-doped oxide featuring extrinsic disorder. (b) The variation in the electrical conductivity of the oxide, σ, with oxygen partial pressure.

1.4.3 The effect of dopants on the conductivity

In order to further expand the activation energy term E_a in Eq. (9) and relate that with the migration enthalpy ΔH_m in Eq. (8), we shall go deeper exploring the dopants effect or the defect associates in the material. The term associate refers to the combination of the vacancies with the dopant cations in the lattice. This combination is mainly due to the coulombic attraction between the defects as the oxygen vacancies and dopant cations are effectively positively and negatively charge in the system. Apart from that, the relaxation of the lattice around these defects also plays an important role in the formation of these defect associates. Again, considering an ionic conductor $\mathrm{M_2O_m}$ doped with the lower-valent cation $\mathrm{Mf^{(m-n)+}}$, this time we shall be more specific about the dopant assuming that n=1 or 2.

For the case n=2 (***case 1***), there is only one possibility for the defect associate which is called the neutral associate:

$$\{\mathrm{Mf_M''}\ \mathrm{V_O^{\cdot\cdot}}\}^{x} \rightarrow \mathrm{Mf_M''} + \mathrm{V_O^{\cdot\cdot}} \tag{21}$$

which means that if no disassociation occurs, every dopant cation in the system is bound with an oxygen vacancy. This assumption was evidenced by the dielectric relaxation analysis of the oxide $\mathrm{Ce(Ca)O_{2-x}}$ done by Nowick and Park(63).

Whereas for the case n=1 (***case 2***), two defect associates are possible, a charged associate

$$\{\mathrm{Mf_M'}\ \mathrm{V_O^{\cdot\cdot}}\}^{\cdot} \rightarrow \mathrm{Mf_M'} + \mathrm{V_O^{\cdot\cdot}} \tag{22}$$

or a neutral associate:

$$\{\mathrm{Mf_M'}\ \mathrm{V_O^{\cdot\cdot}}\ \mathrm{Mf_M'}\}^{\mathrm{x}} \rightarrow 2\mathrm{Mf_M'} + \mathrm{V_O^{\cdot\cdot}} \tag{23}$$

Of these two forms of associates, the charged associate seemed to be the more favourable one because that during the fabrication process of these oxide ion conductors, the extremely high sintering temperature (normally over 1200K) leads to random distribution of the doped cations. As the sample was cooled down to room temperature, it also froze the mobility of these heavy cations leaving them randomly distributed in the system. Therefore, it was almost impossible to find two dopant cations being adjacent to each other forming the neutral associate. Evidence supporting this assumption can be found in the electron spin resonance (ESR) measurements of the trivalent dopants in fluorite oxides (Abraham *et al.*)(64). The literature showed that a large fraction of dopant cations had cubic environments with no oxygen vacancy in the first-nearest adjacent sites.

For ***case 1***, we can apply the law of mass action to Eq. (21) which gives

$$\frac{[V_O^{\cdot\cdot}]\cdot[\mathrm{Mf_M''}]}{[\{\mathrm{Mf}_M''\ V_O^{\cdot\cdot}\}^{x}]} = K_{A1}(T) \tag{24}$$

where $K_3(T)$ is the equilibrium constant of the disassociation of the associates, which can also be expanded as

$$K_{\mathrm{A1}}(T) = \frac{\exp\left(-\frac{\Delta H_{\mathrm{A1}}}{kT}\right)}{W} \tag{25}$$

W is the number of orientations of the associate and ΔH_{A1} is the association enthalpy(65). Since the electroneutrality of the system dictates that $[V_O^{\cdot\cdot}] = [\mathrm{Mf}_{\mathrm{M}}'']$, and we can substitute Eq. (25) into Eq. (24) which gives

$$[V_O^{\cdot\cdot}] = \left(\frac{[\{\mathrm{Mf}_M'' \ V_O^{\cdot\cdot}\}^x]}{W}\right)^{\frac{1}{2}} \exp\left(-\frac{\Delta H_{\mathrm{A1}}}{2kT}\right) \tag{26}$$

Since the majority of defects remains as associates, $[\{\mathrm{Mf}_M'' \ V_O^{\cdot\cdot}\}^x]$ can be approximately replaced by the total dopant concentration, C_{M}. It should be noted that C_{M} is a site fraction of the cation lattice. So the equation becomes:

$$[V_O^{\cdot\cdot}] = \left(\frac{C_{\mathrm{M}}}{W}\right)^{\frac{1}{2}} \exp\left(-\frac{\Delta H_{\mathrm{A1}}}{2kT}\right) \tag{27}$$

We can then substitute this into equation (8), assuming that $[V_O^{\cdot\cdot}]_{\mathrm{s}} \approx 0$,

$$\sigma = N\frac{q^2}{kT}\gamma\left(\frac{C_{\mathrm{M}}}{W}\right)^{\frac{1}{2}} a_0^2 v_0 \exp\left\{\frac{-\left(\Delta H_{\mathrm{m}} + \frac{\Delta H_{\mathrm{A1}}}{2}\right)}{kT}\right\} \tag{28}$$

Compare the result with equation (9), which gives a relation of $E_{\mathrm{a}}, \Delta H_{\mathrm{m}}$ and ΔH_{A1} as:

$$E_{\mathrm{a}} = \Delta H_{\mathrm{m}} + \frac{\Delta H_{\mathrm{A1}}}{2} \tag{29}$$

In ***case 2***, we can obtain a similar relationship by repeating the process above based on the reaction of the charge associates,

$$\{\mathrm{Mf}_{\mathrm{M}}' \ \mathrm{V}_{\mathrm{O}}^{\cdot\cdot}\}^{\cdot} \rightarrow \mathrm{Mf}_{\mathrm{M}}' + \mathrm{V}_{\mathrm{O}}^{\cdot\cdot}$$

This time the electroneutrality condition gives

$$[\{\mathrm{Mf}_M' \ V_O^{\cdot\cdot}\}^{\cdot}] + 2[V_O^{\cdot\cdot}] = [\mathrm{Mf}_M']$$

Assuming that the majority of defects remains as associates, thus $[\{\mathrm{Mf}_M' \ V_O^{\cdot\cdot}\}^{\cdot}] \gg [V_O^{\cdot\cdot}]$, and

$$[\{\mathrm{Mf}_M' \ V_O^{\cdot\cdot}\}^{\cdot}] = [\mathrm{Mf}_M'] \tag{30}$$

Substituting Eq. (29) into the equilibrium equation of the disassociation reaction of case 2:

$$\frac{[V_O^{\cdot\cdot}] \cdot [\mathrm{Mf}_{\mathrm{M}}']}{[\{\mathrm{Mf}_M' \ V_O^{\cdot\cdot}\}^{\cdot}]} = K_{\mathrm{A2}}(T) = \frac{\exp\left(-\frac{\Delta H_{\mathrm{A2}}}{kT}\right)}{W} \tag{31}$$

gives

$$[V_O^{\cdot\cdot}] = \left(\frac{1}{W}\right) \exp\left(-\frac{\Delta H_{\mathrm{A2}}}{kT}\right) \tag{32}$$

Therefore, the relationship between activation energy and enthalpies this time can be expressed as:

$$E_{\mathrm{a}} = \Delta H_{\mathrm{m}} + \Delta H_{\mathrm{A2}} \tag{33}$$

where ΔH_{A2} represents the enthalpy of the disassociation of the charged associates.

Both Eq. (28) and Eq. (29) show the effects of dopants on the conduction mechanism of an oxide ion conductor. We should also include another case regarding that all the oxygen vacancies are free in the system, a situation that occurs most likely at very high temperature. In that case, the activation energy $E_\mathrm{a} = \Delta H_\mathrm{m}$ since there is no associate between oxygen vacancies and doping cations. Overall, the tendency of oxygen vacancies to be associated with the heavy doping cations increases the activation energy of conduction by adding an association enthalpy into E_a. This type of drawback in the ionic conduction is mainly due to the aforementioned coulombic attraction between various defects in that material. The enthalpies of the associates, ΔH_A1 & ΔH_A2, can be approximately estimated based on the coulombic forces between the associated defects, which is proportional to $Q_1 Q_2/(\varepsilon \cdot r)$, where Q_1 and Q_2 represent the quantity of electricity of the associated defects, ε is the electric constant and r is the distance between the defects. Further empirical investigation on the association enthalpies can be found in the previous literature reported by Nowick and Park(63), which leads to a more comprehensive understanding of how dopants and defect type affect the lattice conductivity.

1.4.4 The effect of microstructures on the conductivity

In the last section, some major factors that governs the conductivity of an oxygen ion conductor in the lattice were discussed. However, in most of the literatures, polycrystalline samples were extensively synthesized and analysed where the grain boundaries, porosities and other microstructures also play an important role in determining the total conductivity of the electroceramics. Apart from these homointerfaces, extensive research interests have been attracted to the investigation on the heterointerfaces formed between two layers of different materials, for example, deposition of YSZ thin films on LSM substrates. The chemical and physical nature of these interfaces together with their location and shape will significantly influence the ionic conduction. The development of the AC impedance spectroscopy technique has widened the scope of our investigation into the microstructure influence on the total conductivity of various materials which can effectively probe different conducting processes happened across the sample.

It is widely accepted in the field of ionic conducting materials that grain boundary (GB) diffusion is faster than that of the bulk. In some cases such as NiO(66), the improved oxygen diffusivity along the grain boundaries was reported to be of six orders of magnitude larger than that in lattice. Presumably, this improvement in the grain boundary diffusion is attributed to the higher percentage of displaced atoms with corresponding strained bonds and the excess free volume for fast oxygen diffusion between the adjacent misaligned grains. Grain boundaries thus, normally being referred to as homo-interfaces in the system(67), exhibit two key features for the enhanced oxygen diffusivity: one is high defect concentration, the other is high mobility for oxygen ions due to the interconnected free volumes. However, high ionic diffusivities are not enough by themselves to insure high ionic conductivities. The fraction of cross-sectional area of the GB which lie parallel to the direction of conduction pathways is rather small compared with that of the bulk. In fact, for oxygen ion conductors, GBs that are transverse to the ion flux display blocking behaviour to the oxide ion conduction. Consider the idealized 'brick model' as schematically illustrated in Figure 1.6, in which the cubic grains have a length of L which are separated from each other by GBs of a constant width $2b$.

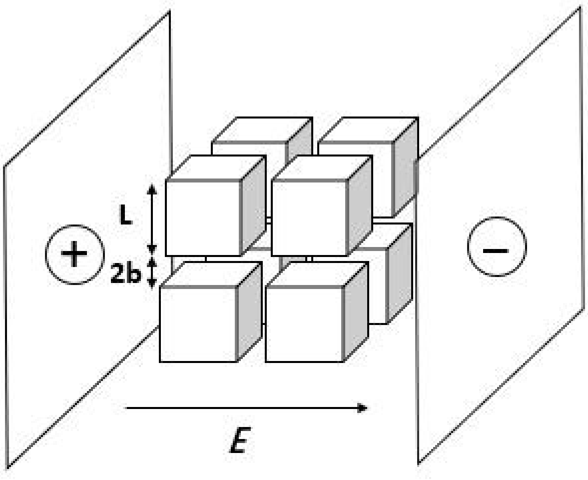

Figure 1.6 The brick layer model of an idealized polycrystalline structure between two plate electrodes. The horizontal arrow shows the direction of electric field.

If we ignore the aforementioned blocking effects of GBs perpendicular to the ion flux, the relative ratio of cross-sectional areas is

$$\frac{A_{\mathrm{Bulk}}}{A_{\mathrm{GB}}} = \frac{L}{4b} \tag{34}$$

To achieve equal conductance with the bulk, the GB conductivity σ_{GB} must be larger than the bulk conductivity σ_{Bulk},

$$\sigma_{\mathrm{GB}} = \frac{L}{4b}\sigma_{\mathrm{Bulk}} \tag{35}$$

For typical polycrystalline samples with an average grain size of $\sim 1\ \mu\mathrm{m}$ and the relatively narrow grain boundary with a width of $\sim$ 2-8 nm(68), the GB conductivity σ_{GB} is required to be 200 times larger than that of bulk in order to achieve equal conductance. Therefore, although GB possesses fast ionic diffusion due to the high local defect concentration and excess free volume, the ionic conductivity in GB is somehow lower than that of bulk in oxide ion conductors. But this fast oxygen diffusion phenomenon in GBs also launched a new research topic in nano-crystalline materials, in which the dimension of GBs is comparable to the grains. In the last few years, a number of known ionic conductors, such as zirconia and ceria, have been prepared as the average grain size of which was decreased down to the nanometer domain(69-71), which showed an significant enhancement in the total conductivity (caused by more GBs). However, contradiction was found in the previous literatures about the GB effects on the total conductivity in these nanomaterials, as shown in Tuller's(70) review in 2000. Recent isotope diffusion measurements in nano-scaled YSZ carried out by De Souza *et al.* (72) showed no evidence for enhancement in GB diffusion. These variations in the behaviour observed in the nano-scaled materials are probably due to the metastable state of these phases, which would undergo significant changes if treated in different procedures.

Another widely accepted explanation for the enhanced ionic conductivities at GBs corresponds to the formation of space charged layers or regions in the grains near the GBs. Charge species, segregation of the secondary phases, additives and other impurities all tend to accumulate at the GBs in order to lower the strain and decrease the electrostatic energy of the system. These boundary charges are then compensated by the formation of space charged layers in the adjacent grains. If the bulk defects of high mobility are gathered together in the space charged region, the overall conductivity of the system should increase as a result because it provides a fast pathway for the major charge carriers along the GBs.

On the other hand, the enhancement of ionic conductivity at heterointerfaces triggered the research interest in the fabrication of multilayer thin film structures. Significant decreases in the ionic conductivities were observed as some ionic conducting materials were fabricated into nano-scaled or micron-scaled thin films, which may be due to formation of a defect concentrated layers in the space charged regions at interfaces or through the reduction of ΔH_{m} by tensile interfacial lattice strain. Kosacki *et al.* (73) managed to grow a YSZ thin film of $< 60\mathrm{nm}$ thickness on a MgO substrate through pulsed laser deposition (PLD) technique, the electrical conductivity of which was enhanced by approximately 3 to 4 orders of magnitude due to the significant contribution from the 1.6-nm-thick interface layers. The activation of conduction of the deposited YSZ film was reported to decrease from 1.04 eV to 0.45 eV. To date, the PLD technique has been systematically used to fabricate the stabilized zirconia-insulator heterostructures(74-76). Based on the these results, Korte *et al.* (77) calculated the lattice strain within the zirconia layer and related it to the changes in both E_a and conductivity which confirmed that tensile strain lowers, whereas compressive strain increases, E_a. Another report from Garcia-Barriocanal *et al.* (78) presented an epitaxial trilayer of 10-nm strontium titanate (STO)/1-nm YSZ/10-nm STO deposited on an STO substrate, which showed up to eight orders of magnitude enhancement of the lateral ionic conductivity near room temperature. They proposed an atomic reconstruction mechanism at the interface between highly dissimilar structures, which leads to a large number of charge carriers and a high-mobility plane. The attribution of colossal values of the ionic conductivity in this trilayer structure needs more experimental and simulation results to confirm. However, this research did open up an approach extending the applications of these ionic conducting materials in the low-temperature devices.

The effect of porosity on the total conductivity was first studied by Inozemtsev *et al.*(1974)(79). In the research, the effect of porosity on the GB resistance for the fine-grained $\mathrm{Zr(Sc)O_{2-x}}$ samples was investigated through impedance dispersion analysis, and the porosity made a remarkable difference in the GB resistance of the samples. The GB resistance was increased by two orders of magnitude as the porosity amount increased, which became larger than that of bulk and dominated the total resistance of the sample.

The conduction mechanism of ions through those microstructures remains unknown, which makes the interpretation of the conductivity measurements on the GB and other microstructures in the system rather uncertain. However, by controlling the fabrication process, we can somehow manipulate the grain sizes, the concentration of the porosity and the heterostructures to the required status, and therefore, optimize the electrochemical properties of these materials. But it needs to be pointed out that the aging phenomena tends to happen inevitably at these chemically metastable sites, which will then contribute greatly to the total resistance and even block the oxide-ion conduction in the end. Among those, GB is of most research interests due to its existence in almost every sample made. The GB resistance is a complex function of many microstructural parameters, and consequently it is extremely hard to assess its contribution to the total resistance. We should always take GB into consideration when discussing the conducting property of a material.

In summary, the main parameters affecting the conductivity of an oxide-ion conducting electrolyte have been discussed in previous sections. In the following sections, we shall look through some examples of the state-of-art electrolyte materials for the SOFC applications starting with the fluorite oxides.

1.5 Fluorite structured oxides

Many ceramic materials with fluorite, perovskite, apatite, and related crystal structures have been investigated to be used as the electrolyte materials for SOFC applications. Figure 1.4(c) plots the ionic conductivities of the most important state-of-art electrolyte materials over temperature, with a horizontal dotted line showing the limit of conductivity required to construct a device with an electrolyte thickness of 15 μm. Of these candidates, the aliovalent cation doped fluorites are perhaps the most well-understood and also the most instructive fast oxygen ion conductors. In a basic fluorite-structured material like ZrO_2 and CeO_2, the cations adopt a face-centred cubic (FCC) arrangement whereas oxygen ions occupy all eight tetrahedral interstitial sites of the system leaving the octahedral ones completely free. The original fluorite oxides don't have fast ionic conductivity until some of the host cation sites are replaced by low-valence cations such as Y^{3+}, Ca^{2+}. The missing charge from the substitution is balanced by the formation of oxygen vacancies in the sub-lattice which gives rise to the ionic conductivity. Let us take the formation of the solid solution $\mathrm{Ce_{1-x}M_xO_{2-x/2}}$ (M=Y, Nd, Gd et. al) as an example. The substitution of the trivalent cation on the cerium cation site can either be illustrated schematically as Figure 1.7(a), or using an aforementioned defect equation, the Kröger-Vink notation, as shown below:

$$\mathrm{M_2O_3 + O_O^x + 2Ce_{Ce}^x \rightarrow 2M'_{Ce} + V_O^{\cdot\cdot} + 2CeO_2}$$

The neutrality condition gives $[M'_{Ce}]=2[V_O^{\cdot\cdot}]$, which implies that the concentration of oxygen vacancies is directly proportional to the degree of substitution. If all the oxygen vacancies generated are mobile, then the ionic conductivity in the lattice will depend quadratically on the degree of substitution according to Eq. (8). However at low temperatures the defects interact with each other, and the two concentrations can differ. This could be referred to the ***case 2*** in Section 1.4.3, where the resulting defects, $\mathrm{M'_{Ce}}$ and $\mathrm{V_O^{\cdot\cdot}}$, have the opposite effective charges in the lattice and tend to attract each other resulting in the formation of the defect associate $\{\mathrm{M'_{Ce}\ \ V_O^{\cdot\cdot}}\}^{\cdot}$, the process of which can be expressed in the disassociation equation below, with a dimer binding enthalpy, ΔH_a:

$$\{\mathrm{M'_{Ce}\ \ V_O^{\cdot\cdot}}\}^{\cdot} \rightarrow \mathrm{M'_{Ce} + V_O^{\cdot\cdot}}$$

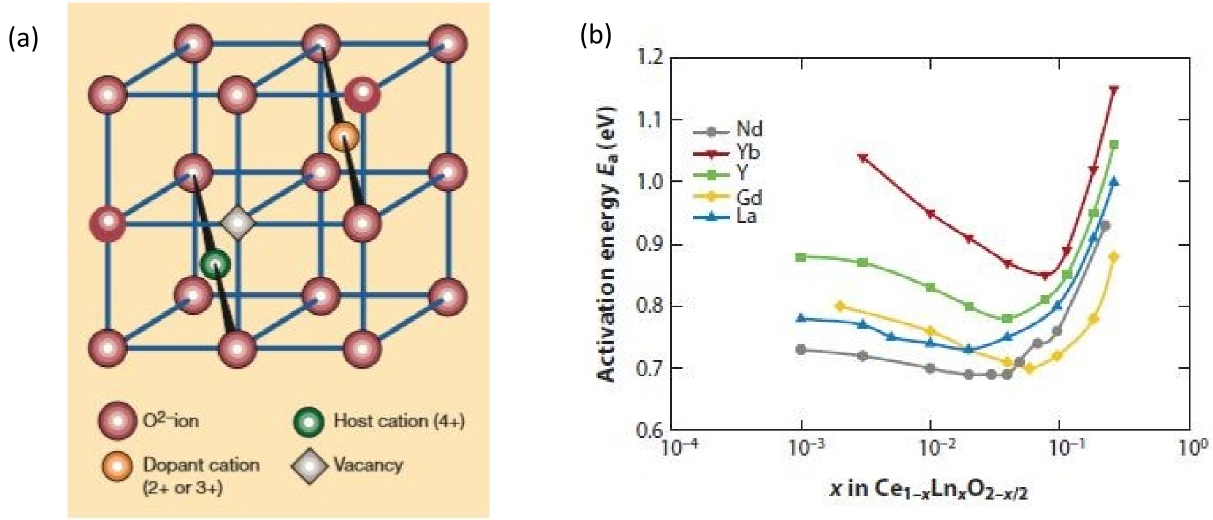

1.7 (a) A half unit cell of the acceptor-doped fluorite structure showing the position of a dopant cation-oxygen vacancy associate with a first-nearest-neighbour configuration. Adapted with permission from (80). (b) Activation energies of ceria solid solutions versus doping amount. Reproduced from (81) with kind permission form Annual Reviews.

As discussed in section 1.4.3, the dimer binding enthalpy ΔH_a determines the concentration of the free oxygen vacancies at equilibrium at a set temperature (Eq. 32). At low temperatures when oxygen vacancies are fully associated with the cation defects, the measured activation energy E_a is the sum of ΔH_m and ΔH_a. Experimentally, a considerable curvature is expected as we plot the Arrhenius plots over a large range of temperature which is because of the change in the mobile vacancy population. Kilner and Waters(82) pointed out that in the previous literatures, when comparing the activation energies of the fluorite-type electrolyte materials, some data taken under different temperature ranges were incorrectly put together to make a comparison.

Therefore, when comparing the experimentally obtained activation energies of the same structured samples, extra care should be taken with regard to the temperature range at which the data was collected. As known from the derivation of some of the expressions in the previous sections, the maximum of the lattice conductivity of a system could be achieved when the activation energy for conduction is decreased to its minimum. Experimentally, this phenomenon was observed in all fluorite systems, as the maximum in conductivity was obtained when the minimal activation energy for the conductivity of the system was reached by increasing the additive concentration. Figure 1.7(b) shows these minima for the $\mathrm{CeO_2}$-$\mathrm{LnO_2}$(Ln here refers to lanthanides, $\mathrm{Ln=Nd, Yb, Y, Gd, La}$) solid solutions, the data of which were all taken under the same temperature range at low temperatures (300-600 K)(81). The amount of dopant, x, required for minimizing the activation energy and the lowest activation energy of the system both depend on the identity of the Ln^{3+} cation. We can make an assumption that ΔH_m is a constant in $\mathrm{CeO_2}$-based systems. The variation in E_a then is results from the changes in the association enthalpy, ΔH_a. As mentioned before, the association enthalpy is composed of two major terms: a Coulomb term which is almost constant since we are considering only the trivalent substitutions, and an elastic strain term from the relaxations originated from the size mismatch between the solute and the host cation. In order to understand better the relationship between the minimum activation energies and the solutes, an extra axis regarding the ionic radius of the solute is included as shown in Figure 1.8. Assume that the Coulombic force between the defects stays the same, and therefore, the minimum in the 3-D plot reflects the minimal energy associated with the lattice relaxation around the solute cation. The as-presented approach is very useful for determining the global minimum of activation energy for the ceria systems, and thus, finding the conductivity maximum. However, it is worth pointing out that, at high additive concentrations, the preexponential factor is no longer concentration independent(83). Burbano *et al.* suggested that the vacancy-vacancy interactions become the dominant factor for the determination of conductivity at high values of x in the $\mathrm{Ce_{1-x}Y_xO_{2-x/2}}$ solid solution, with preferential ordering of oxygen vacancy pairs along the $\langle 111 \rangle$ direction in the lattice driven by the strong repulsion between these vacancies at short distance(84). This effect explains the presence of the maximum in lattice ionic conductivity in each of the specific solid solution, which didn't take ionic radius of the solute cations into consideration.

Theoretically, some recent studies have proposed an explanation to the presence of this global maximum ionic conductivity in the $\mathrm{CeO_2}$-$\mathrm{LnO_2}$ systems. Atomistic simulations calculations based on energy minimisation techniques has been used to study the relationships between the minimal activation energy and the defect configurations, which showed that an alternation in the configuration of the associate from a first nearest-neighbour (nn) configuration for $r_\mathrm{ion} \leq r_{\mathrm{Gd}^{3+}}$ to a second nearest-neighbour (nn) configuration for $r_\mathrm{ion} \geq r_{\mathrm{Gd}^{3+}}$ is crucial in determination of the global minimal activation energy(85). The crossover occurs at approximately the ionic radius of Gd^{3+} that exhibits the smallest binding energy of the associate. The calculated association enthalpies are within the range of 0.4-0.6 eV for lanthanide solutes which could make a great difference when comparing activation energies E_a of these systems. Density functional theory (DFT) calculations for the $\mathrm{CeO_2}$-$\mathrm{LnO_2}$ systems have also been carried out recently on probing the correspondence between vacancy-dopant interactions and the macroscopic ionic conductivity(86). The vacancy-dopant interaction can be divided into the repulsive elastic part and the attractive Coulombic part. The quantum mechanical first-principles study of the $\mathrm{CeO_2}$-$\mathrm{LnO_2}$ systems presented in this article revealed that, in the optimal electrolyte, these two forces should balance(86). The optimized effective atomic number to achieve this balance was found to between 61(Pm) and 62(Sm), and therefore, the combinations of Nd/Sm and Pr/Gd were proposed which should show enhanced ionic conductivity.

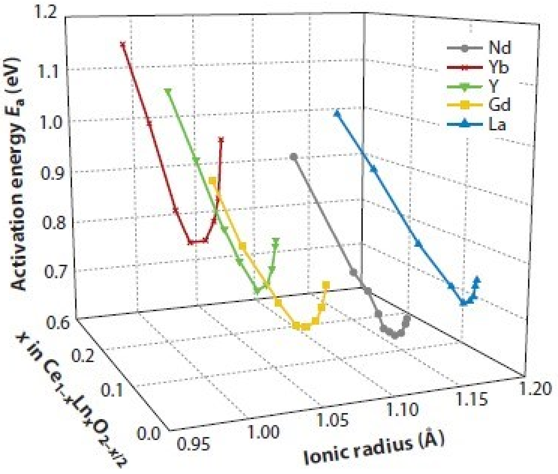

Figure 1.8 Activation energies of ceria solid solutions versus doping amount with regard to the solute ionic radius. Reproduced from (56) with kind permission from Annual Reviews.

Experimentally, the dependence of the configurations of the defect associates in some CeO_2-LnO_2 solid solutions on the ionic radius were examined using calorimetric methods as reported by Navrotsky *et al*(87), which indicated that the oxygen vacancy adopts a first nn site to the solute ion for CeO_2-Y_2O_3, CeO_2-Gd_2O_3 and unexpectedly for CeO_2-La_2O_3 system. The latter one is more of a surprise since the ionic radius of La^{3+} is larger than the theoretical radius at which a shift to the second nn configuration is expected to take place as predicted by the atomistic simulations. However, this study was carried out in concentrated solid solutions where $x \approx 0.2$. As mentioned before, at high solute concentrations, some complex defect interactions may result in an abnormal alignment of the oxygen vacancies from the association configurations and lay a profound influence on the conducting properties of the materials.

The discussion above examines the influence of ionic size on the defect associate configuration mostly for the dilute solid solution of CeO_2-LnO_2 at low temperatures. As for solute concentrations x much greater than 0.05, rather than isolated dimers, larger clusters, e.g., trimers, are more likely to form. To investigate these defect structures, techniques such as extended X-ray absorption fine structure (EXAFS) and X-ray absorption near edge structure (XANES) were employed, which gives information on the local chemical environment of the solute cation(88, 89). Yamazaki *et al.* reported the finding of large defect clusters with two or four lanthanoid cations together with one or several oxygen vacancies combined in a nn configuration in the CeO_2-Y_2O_3 and CeO_2-Gd_2O_3 systems, while this large cluster structure is more likely to form for Y^{3+}(88). Even larger cluster structure was found in the CeO_2-Y_2O_3 system by Deguchi *et al.*(89) that the original structure of the dopant oxide is even kept in the ceria lattice without separating as a secondary phase. More widely Ou *et al.* studied the CeO_2-Sm_2O_3, CeO_2-Gd_2O_3, CeO_2-Dy_2O_3, CeO_2-Yb_2O_3 systems using the electron energy loss spectroscopy (EELS) and the selected area electron diffraction (SAED) techniques, which drew a conclusion on the tendency of forming cluster structure in the lattice following the order $(\mathrm{Gd}, \mathrm{Sm}) > \mathrm{Dy} > \mathrm{Yb}$. Some discrepancies were found in these literatures with regard to the trends for the ionic radius to form large cluster structures. Kilner(56) suggested that these discrepancies might arise from the difficulties in achieving the equilibrium defect distribution in these systems due to the sluggish nature of the cation lattice in the fluorite type materials.

In conclusion, the optimization of the lattice oxygen-ion conductivity of the ceria-based systems can be achieved by choosing a trivalent substitution cation that minimizes the lattice strain generated from the association of defects. The discussion should then be extended to the interfacial transport of oxygen ions along homo- or hetero-interfaces in the system, searching for further optimizations in the ionic conductivity. One of the most attractive topics within this field lies in the investigation of the correlation between grain size and ionic conductivity. As mentioned before, though the grain boundaries are commonly believed to be the fast oxygen diffusion sites in the oxide-ion conductors, the contribution of GB conductivity to the total electrical conductivity is a complex function of several factors. By decreasing the grain size down to the nanometer regime, factors that govern the GB conductivity could be investigated with more details. A study by Aoki *et al*. (69) illustrated this correlation between grain size and GB conductivity in the CaO-stabilized zirconia, as plotted in Figure 1.9(a). A combination of high resolution STEM and complex impedance spectroscopy was used to probe the dependence of GB conductivity on the amount of Si segregation at the GBs. Aoki related the dramatic drop in the specific GB conductivity initiated with increasing grain size to the silicate ($\mathrm{Si_2Ca_3O_7}$) coverage of the grain boundaries(69). Note that in the regime of these studies, the solute coverage averages below a monolayer without saturating on the grain boundaries, otherwise the specific GB conductivity would not change with the grain size.

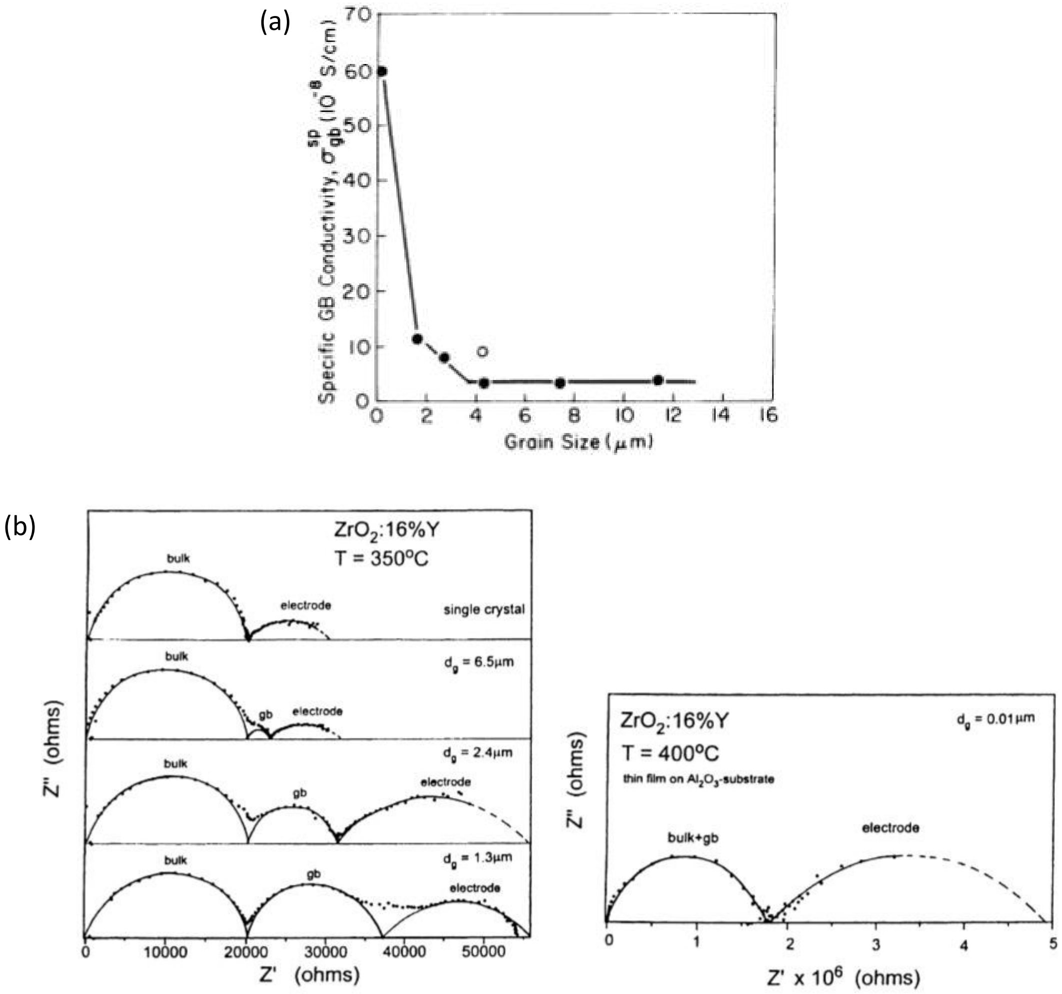

(c)

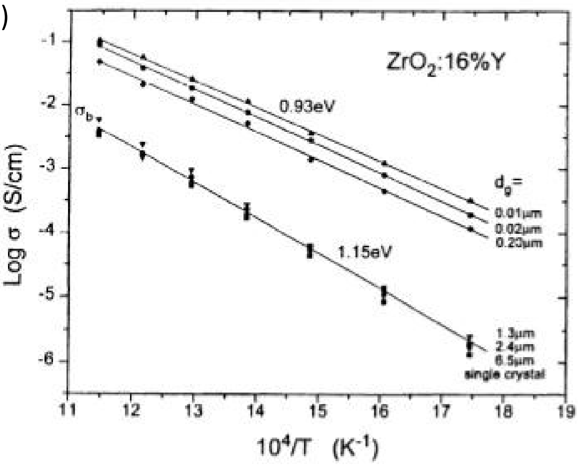

Figure 1.9 (a) Specific grain boundary conductivity in calcia stabilized zirconia at 500°C against grain size. Adapted from (69) with permission from John Wiley and Sons. (b) Complex impedance spectra obtained for (left) single crystal and microcrystalline YSZ bulk specimens and (right) for nanocrystalline YSZ films. Adapted with permission from (90) (c) Comparison of electrical conductivities of single crystal, bulk microcrystalline specimens and nanocrystalline thin films of YSZ. Adapted with permission from (90).

In the relatively pure nanocrystalline conductors, there was a contradiction in the grain boundary conductivity among the previous literatures. Mondal and Hahn(91) reported the success in preparing nanocrystalline YSZ (2-3mol% yttria) specimens by the inert-gas condensation technique. The resultant specimens were of 82% to 93% relative density with a grain size range between 35 and 50nm. An increased activation energy for GB conductivity (1.0±0.1 eV) over that of the bulk (0.85±0.05 eV) was observed, which is in agreement with values for materials with micron-scaled grains. Likewise, Jiang *et al.* (92) prepared ultra-fine grained YSZ samples through combustion method using metal nitrates as precursors, which showed activation energies of 0.95 and 1.2 eV for bulk and GB respectively. However, Kosacki *et al.*(90) found a contradictory result in the activation energies for the bulk and GB conductivities during the investigation of YSZ (16mol% yttria) thin films prepared through a polymer-precursor process on alumina substrates. As shown in Figure 1.9 (c), the electrical conductivities of the nanocrystalline thin films of YSZ were approximately two orders of magnitude larger than those of the bulk microcrystalline specimens. Through the complex impedance spectra of the polycrystalline YSZ samples with grain sizes over 1μm, a clear GB contribution at intermediate frequencies was observed, while in the spectrum of the nanocrystalline film only one semi-circle representing the superposition of the bulk and GB responses was found. It is believed that this enhancement in conductivity as the grain sizes of YSZ were decreased from micron scale down to the sub-micron scale is associated with the reduction of the activation energies for conduction from 1.15 to 0.93eV(90). The reason why these studies showed a large discrepancy can only be speculated through some evidence from the reports, which could be due to the different preparation processes or the humidity effect on the thin film samples. However complicated the fabrication of a chemically stable fine structured thin film of YSZ would be, the success in increasing the electrical conductivity of this well-established electrolyte material by several orders of magnitude did propose a solution to extend its application into the intermediate temperature range.

1.6 Perovskite electrolytes

One of the alternatives to the fluorite-structured oxides for the electrolyte materials used in SOFC application is the ABO_3 perovskite family. The intensive research interest of the perovskite family ceramics was triggered by the purpose of finding an ionic conductor possessing considerably high ionic conductivity at intermediate temperature (600 °C-800°C) so that the operating temperature of SOFC could be reduced, and therefore, increasing the flexibility in the choice of materials and the durability of these high temperature devices. The perovskite electrolyte $La_{0.8}Sr_{0.2}Ga_{0.83}Mg_{0.17}O_{2.815}$(LSGM)(93, 94), in particular, has demonstrated superior oxide-ion conduction. According to the previous reports, an encouraging cell performance was achieved in the single ceramic fuel cell tests using a thick-film (>500 μm) LSGM as the electrolyte at an operating temperature $T<800$ °C(95, 96). The main advantages of the LSGM-based electrolyte over its competitor yttria-stabilised ZrO_2 (YSZ), are the lower operating temperature of the LSGM-based fuel cells and the chemical compatibility with perovskite cathode materials that are identified as mixed ionic and electronic conductors (MIEC)(97).

The investigation of the electrochemical properties of perovskite electrolytes can be traced back to 1980 when Takahashi and Iwahara(98) substituted some valence-stable cations on both the A and B sites forming perovskite structures showing both ionic and protonic conductions. Subsequent studies have been focused on the as-discovered protonic conduction in these perovskite-related structures, especially in the doped strontium and barium cerates(99-104). Using a protonic conductor as the electrolyte of a SOFC device, as shown in Figure 1.3(b), not only lowers the operating temperature of a SOFC device into the intermediate temperature range, but also avoids the mixing of H_2 and steam at the anode site when using an ionic conductor, which will result in a loss of the total EMF.

The crystal structure of perovskites is composed of corner sharing metal oxygen octahedra, BO_6, and larger cations, A, occupying the interstices between the octahedral units, as shown in Figure 1.10(a). Some perovskite materials, such as $SrTiO_3$, adopt a cubic perovskite structure where the octahedra are aligned along the a, b, c axes, however in the majority of cases, the alignment of the octahedra are tilted to an extent in one or more directions, resulting in lower symmetries and larger unit cells. For example, in the previous literature(105) the crystal structure of yttrium doped barium cerate, $\mathrm{BaCe_{0.9}Y_{0.1}O_{2.95}}$, was studied by high resolution neutron diffraction data, the crystal structure of which varies in the elevating temperature, changing from the low temperature orthorhombic phase with the space group of $Pmcn$, to a higher symmetry cubic phase with the space group of $Pm\bar{3}m$, at $\sim750°\mathrm{C}$(105). The pristine barium cerate shows a similar phase transition but adopts a rhombohedral structure at room temperature(106). The orthorhombic structure of $\mathrm{BaCe_{0.9}Y_{0.1}O_{2.95}}$ at room temperature is illustrated in figure 1.10(b), which consists of two non-equivalent oxygen sites labelled as O1 and O2. According to the time of flight neutron diffraction data, the oxygen vacancies created by acceptor doping are not distributed evenly among these sites, but are located exclusively on the O2 sites instead(105). On the contrary, all oxygen sites in the cubic perovskite at high temperatures, and also in the rhombohedral phase, are equivalent and consequently the oxygen vacancies are equally distributed in the structures(107). The $\mathrm{BaCe_{1-x}Nd_xO_{3-x/2}}$ system for $x = 0$ to 0.20 was also confirmed to have the same symmetry as the Y-doped compound with oxygen vacancies located on the O2 sites(108), while $\mathrm{BaCe_{0.9}Gd_{0.1}O_{2.95}}$ was found to have an almost identical structure but the oxygen vacancies of which could not be refined due to the high neutron absorption of gadolinium and the consequent low quality diffraction data(105).

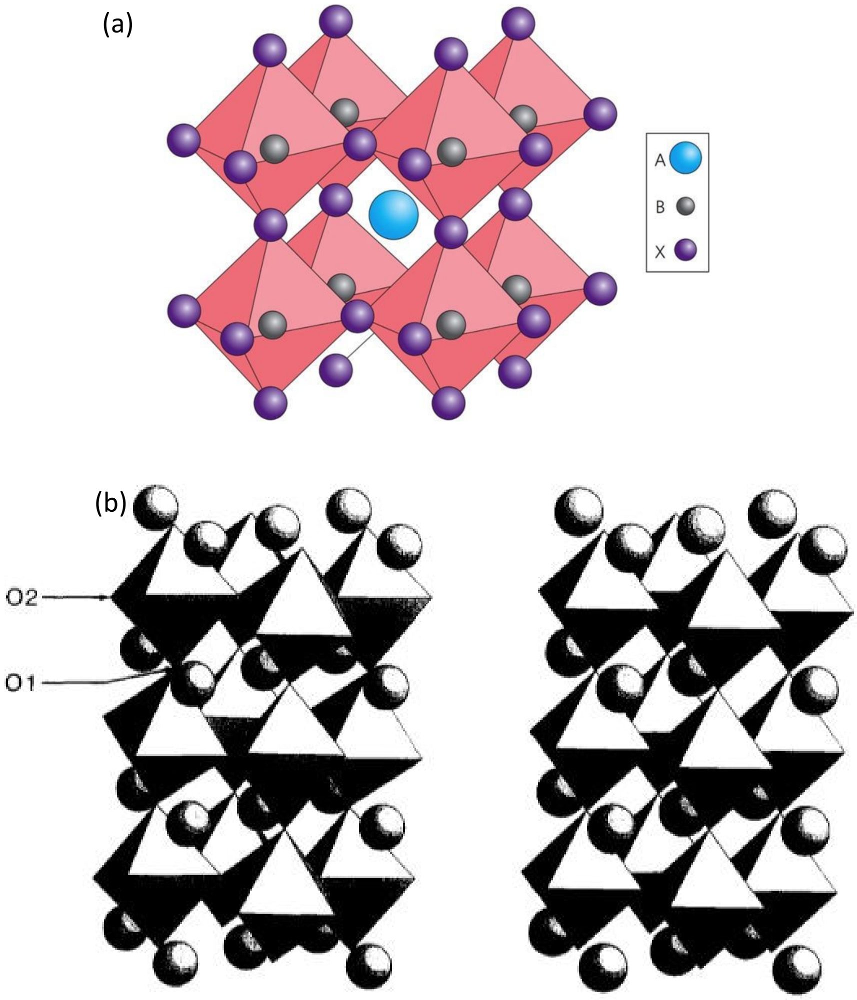

Figure 1.10 (a) The structure of an ABX_3 perovskite with A-site cation(blue) at the centre of a interstice surrounded by eight corner sharing BX_6(blue/purple) octahedra. & Crystal structure of $\mathrm{BaCe_{0.9}Y_{0.1}O_{2.95}}$. (b) The unit cell of the low temperature orthorhombic phase, space group $Pmcn$, and the high temperature cubic phase, space group $Pm\overline{3}m$, shown using the same number of atoms. Adapted from (109) with permission from Elsevier.

1.7 Other structures

Other than the aforementioned fluorite and perovskite based structures, some other classes of solid electrolytes such as materials based on $La_2Mo_2O_9$(110)and materials based on $Ba_2In_2O_5$(111) were also investigated in the previous literatures. These two families share the similarity that they could be both regarded as a derivative from the fluorite and perovskite structure. While the former one adopts the pyrochlore structure which can be thought of as a heavily doped fluorite structure with one oxygen missing per unit cell, the latter one was shown to be isostructural with brownmillerite, which could be also regarded as an oxygen-deficient perovskite structure. A number of pyrochlore structures have been investigated. These materials are intrinsic oxygen ion conductors, the oxygen vacancies among which are generated intrinsically through Frenkel disorder. Kramer and Tuller(112) (113) have made an extensive investigation on materials with this structure, $Gd_2Ti_2O_7$ in particular suggesting that pyrochlores can also be acceptor doped to introduce oxygen vacancies. Both A and B-sites doping were tried in their research. It is worth noting that there is a clear minimum in the activation energy for ionic conductivity of these doped materials as they varied the acceptor substitution amount. The result of that was consistent with the research on fluorite type oxides as shown in Section 1.5. Kramer and Tuller also related the conducting behaviour of these materials with the effects of dopant ion size with a conclusion drawn, namely that defect association happens in the pyrochlore materials, and the degree of that association was affected by the mismatch between the host and the dopant cations.

Oxide-ion conductivity in the oxygen-deficient perovskite material, $Ba_2In_2O_5$, is temperature dependent due to a first-order transition of this material into a fast oxide-ion conductor at a temperature above 930℃. At room temperature and temperatures below 650℃, $Ba_2In_2O_5$ exhibits a low extrinsic oxide-ion conductivity. As the temperature increases, the conducting mechanism of this material changes from extrinsic to intrinsic oxide-ion conductivity in the interval 650-930℃(111). Goodenough et al. also prepared some doped single-phase compounds, $Ba_3In_2MO_8$ (M=Ce, Hf or Zr), via solid state reactions, which were shown to be oxygen-deficient perovskites with an ordering of two oxygen layers of corner-shared octahedra and one layer of corner-shared tetrahedra. The M^{4+} cations were believed to distribute randomly over these two type of layers introducing oxygen-vacancy disorder into the layers, and thus significantly enhanced extrinsic conductivity in the temperature range 100-450℃. As reported by Zhang et al.(114) $Ba_2In_2O_5$ also showed protonic conduction at the temperature region $T<925$℃ according to the electrical conductivity and electromagnetic fields (EMF) measurements as a function of temperature and $P(O_2)$. The brownmillerite oxides are extreme case of the acceptor-doped perovskites. The discovery of protonic conductivity in the brownmillerite oxides prompts the investigation on the protonic conductivity in other perovskite-related structures.

1.8 Summary and the aim of this research

In conclusion of the above sections, solid oxide fuel cells (SOFC) can effectively convert the chemical energy in a variety of fuels into electrical power with reduced CO_2 emissions, which are the promising candidates for the future energy generation system. In order to meet the requirements regarding the fabrication and operation conditions of the devices, finding an appropriate material used for a specific part in a SOFC device is the major challenge in this field. For the solid electrolyte, the key requirement is high ionic conduction to minimize cell impedance, and low electronic conduction at the same time to avoid huge leakage current during operation. Among all the candidate materials, the fluorite type and perovskite type oxides are the most well characterised ones. Several simulation models have been used to explain the oxygen transport mechanism within these structures. In most cases, high ionic conductivity in these ceramics were achieved by acceptor doping which introduces oxygen defects. It is believed that the defect association effects have an important effect on the ionic transport in the acceptor doped oxide-ion conductors. Size effects and the tolerance factor with respect to the cation radii ratio are the key parameter in reducing the activation enthalpy for oxygen transport in the lattice. Theoretically, to probe the conducting mechanism of the solid electrolyte materials, the isotope exchange depth profile (IEDP) technique coupled with secondary ion mass spectrometry (SIMS)(60) could be introduced to obtain direct experimental evidence for the transportation of the charge carriers. The development of low-energy ion scattering (LEIS) technique provides an opportunity of correlating exchange kinetics with the chemical processes on the sample surface. With the help of these powerful surface characterisation techniques, we could get a deep understanding of the conducting mechanism knowing which charge carrier is the major one and how fast does it transport in the materials. The theory and experimentation of IEDP and SIMS techniques will be introduced in the experimental chapter 3.

The aim of this work is to investigate the electrochemical properties of a new layered perovskite structural family, improving the oxide-ion conductivity by acceptor-doping and probing the potential of proton conduction within the system under wet gaseous atmospheres. By means of combining the electrochemical characterization techniques (Chapter 5) with isotope exchange depth profile measurements (Chapter 6), the conduction mechanism regarding different charge carriers in the system is discussed. With a comprehensive understanding of the electrochemical properties and conduction mechanism of this unique layered perovskite structure in different environments, the potential of this structural family to be fabricated as the electrolyte membrane used in an intermediate temperature range SOFC device can be analysed in the future. The fact that this layered perovskite structural material exhibits triple (oxide-ion, electronic and protonic) conduction under wet atmospheres highlights a new research field suggesting that discovery of a new crystal structure family, which is similar to the known structures, could be a breakthrough in finding good oxide-ion conductors.

Chapter 2

Literature Review

2.1 Crystal structure of $BaNdInO_4$

The target ceramic oxide-ion conductor of this research, $BaNdInO_4$ related oxides, was first designed and synthesized through solid-state reactions by Yashima et al. in 2014(115). The crystal structure of the oxides was determined using synchrotron X-ray diffraction (PXRD) and powder neutron diffraction (PND) techniques and the Rietveld refinement (the patterns of which are shown in Figure 2.2), which confirmed that the synthesized $BaNdInO_4$ adopted a monoclinic crystal structure with the $P2_1/c$ symmetry. As illustrated in Figure 2.1 (a), the lattice of $BaNdInO_4$ is composed of alternating slabs of Nd-O units and $Ba_{6/8}Nd_{2/8}InO_4$ units. There are seven independent sites in the lattice of $BaNdInO_4$, Ba, Nd, In, O1, O2, O3 and O4. Ba, Nd and In are fully ordered at the Ba, Nd, In sites as confirmed by refinement of the occupancy factors in the Rietveld refinement. In the perovskite $Ba_{6/8}Nd_{2/8}InO_4$ units, each InO_6 octahedron is surrounded by 8 cations (two Nd^{3+} and six Ba^{2+}). As illustrated in Figure 2.3, the InO_6 octahedra in the $BaNdInO_4$ also exhibit out-of-phase tilting along the [-0.33564 0.5 -0.0868], [0.33564 0.5 0.0868] and [0 0 1] axes with approximately 5.5°, 5.5° and 4.2°, respectively(116). Unlike other perovskite-related structures, such as Ruddlesden-Popper (117, 118), Dion-Jacobson (119) and Aurivillius-type (120) structures, in the crystal structure of this unique layered perovskite, the InO_6 octahedra tilts 45° from the apical oxygen facing mode showing an edge facing mode between the two slabs, as shown in Fig 2.1(b).

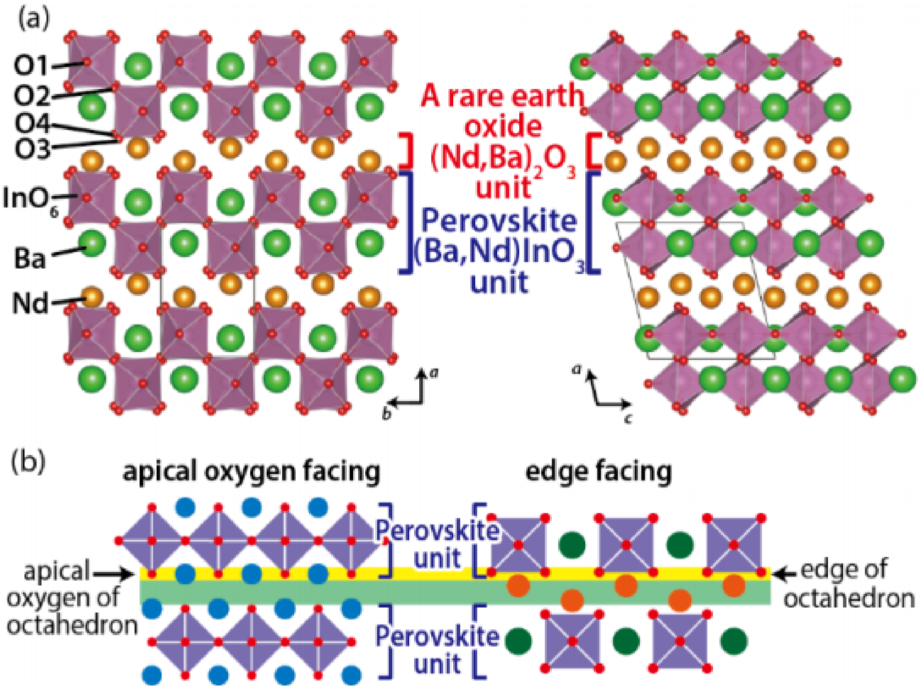

Figure 2.1 (a) Crystal structure of $BaNdInO_4$ viewed along the *c*-axis (left) and *b*-axis (right). The quadrilaterals represent the unit cell in each view. Reproduced with permission from (116) (b) Schematic figures of apical oxygen facing (left) and edge facing (right) between the two slabs in the lattice structure. Reproduced from (116) with kind permission from American Chemical Society.

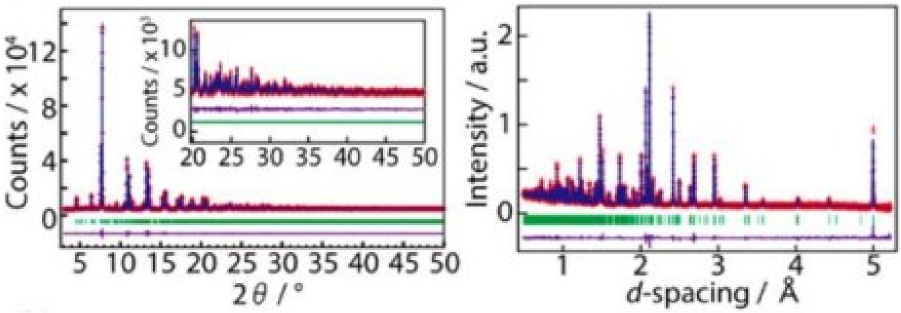

Figure 2.2 Refined patterns of synchrotron X-ray powder diffraction (left) and powder neutron diffraction (right) data of $BaNdInO_4$ taken at 27℃ and 24℃ respectively, showing the experimental (red + marks), fitted (blue solid line) and difference (purple line) data. Reproduced from (115) with kind permission from American Chemical Society.

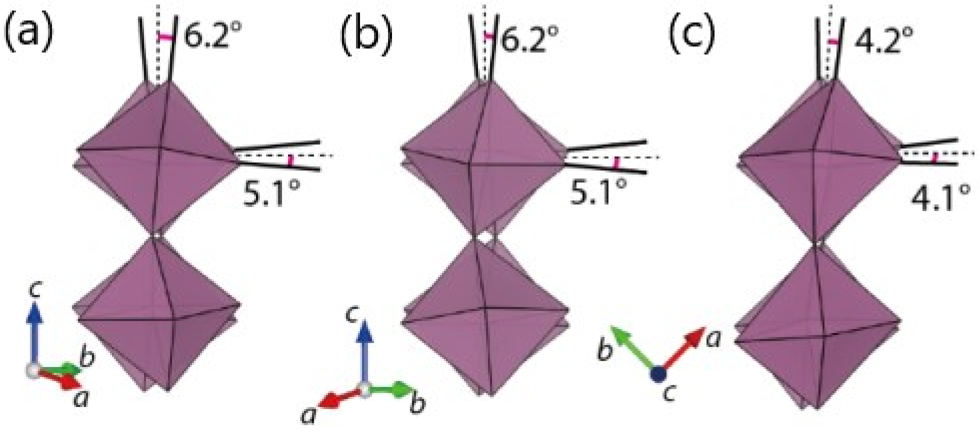

Figure 2.3 Projection of the crystal structure of $BaNdInO_4$ along the (a) [-0.33564 0.5 -0.0868], (b) [0.33564 0.5 0.0868] and (c) [0 0 1] axes showing the tilting of the InO_6 octahedra in the structure. The tilt system is $a^- \, b^- \, c^-$. The tilt angles along the [-0.33564 0.5 -0.0868], [0.33564 0.5 0.0868] and [0 0 1] axes are 5.5°, 5.5° and 4.2°, respectively, which are the average of the two angles shown in the figures. Adapted from (116) with kind permission from Dr. Fujii.

Structure analysis using the in situ PND data in the previous literature(115) revealed that the primitive monoclinic phase with the $P2_1/c$ symmetry of $BaNdInO_4$ is stable and retained up to 1000℃ under vacuum of around 10^{-4} Pa. Some other related oxides, such as $BaSmInO_4$, $BaYInO_4$, $BaHoInO_4$, $BaErInO_4$ and $BaYbInO_4$ were also synthesized by the solid-state reaction method at 1400℃. The crystal structures of all the resulting compounds were confirmed to be primitive monoclinic structure, and the variation of the refined lattice parameters of which was concluded in a review on the $BaNdInO_4$-family.(116) Thus, a new $BaNdInO_4$-type family with a perovskite-related layered crystal structure was successfully discovered. The electrical conductivities of $BaRInO_4$ (R= Nd, Sm, Y, Er) were measured in air by the dc 4-probe method.(121) The total conductivity of $BaNdInO_4$ was the highest among the $BaRInO_4$ (R= Nd, Sm, Y, Er) oxides as illustrated in Fig 2.4 (a). Recently, $BaNdInO_4$-based materials became an interesting research topic which were investigated by several research groups(121-124). Figure 2.4 (b) shows the comparison of the total conductivities of $BaNdInO_4$ (115) and $BaNdCaInO_{3.9}$ (122) obtained from the previous literatures with those of the state-of-art electrolyte materials used in SOFC as concluded by Kilner et al(55). The $BaNdInO_4$-related oxides have shown reasonably high conductivities based on a unique layered perovskite crystal structure. Further investigation of this structural family is worth trying. In this research, $BaNdInO_4$ was also referred as the prototypical material.

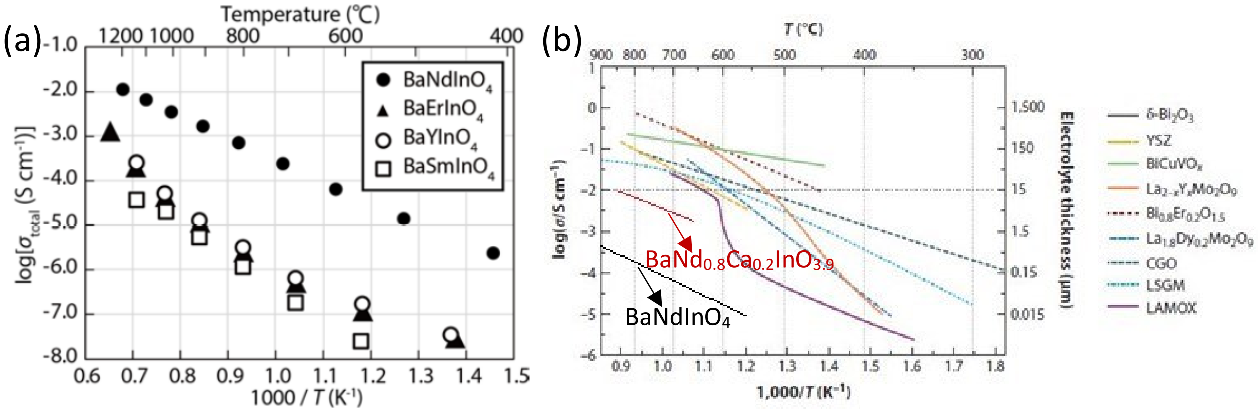

Figure 2.4 (a) Arrhenius plots of the total conductivities σ_{Total}. Adapted with permission from (116). (b) The comparison of total conductivities of $BaNdInO_4$ (Illustrated as red solid line) (115) and $BaNd_{0.8}Ca_{0.2}InO_{3.9}$ (Illustrated as dark solid line)(122) with other SOFC electrolyte materials in the previous literatures. Reproduced with kind permission from (55).

2.2 Improved oxide-ion conductivity of $BaNdInO_4$ by aliovalent cation doping

Based on the original layered-perovskite structure, many groups have reported improved electrochemical properties of the $BaNdInO_4$-based materials by aliovalent cation doping(121-124). One of the effective approaches is acceptor substitution on the Nd sites using the alkaline-earth metal cations such as Ca, Sr and Ba. As mentioned in Chapter 1, acceptor doping in the oxide-ion conducting oxides can create oxygen vacancies and thus enhance the oxide-ion conductivity of the material.

$BaNd_{1-x}Sr_xInO_{4-x/2}$ (x=0.1, 0.2, 0.3)(121) and **$Ba_{1+x}Nd_{1-x}InO_{4-x/2}$** (x=0.1, 0.2, 0.4)(124) compounds were synthesized and investigated by Fujji *et al*, the crystal structures of which were characterised by the crystal structure analyses of single-crystal X-ray diffraction and neutron powder diffraction data. The doped Sr and excess Ba cations were confirmed to exist at the Nd site in the $BaNd_{0.9}Sr_{0.1}InO_{3.95}$ and $Ba_{1.1}Nd_{0.9}InO_{3.95}$ according to the Rietveld refinements of the neutron diffraction data(121, 124). The $P2_1/c$ $BaNdInO_4$-type crystal structure was retained up to 800℃ as confirmed by Rietveld analyses of the neutron-diffraction data. As shown in Figure 2.5, the total conductivities of $BaNd_{1-x}Sr_xInO_{4-x/2}$ (x=0.1, 0.2, 0.3) and $Ba_{1+x}Nd_{1-x}InO_{4-x/2}$ (x=0.1, 0.2) compounds were higher than that of the parent materials $BaNdInO_4$. The highest total conductivities were achieved in the $BaNd_{0.9}Sr_{0.1}InO_{3.95}$ and $Ba_{1.1}Nd_{0.9}InO_{3.95}$ composition, respectively in the two doping series. The activation energy for the total conductivity was 0.685(7) eV for $BaNd_{0.9}Sr_{0.1}InO_{3.95}$ as reported in the previous literature(121), which was lower than that of $BaNdInO_4$ (0.91(4) eV). Although the activation energy for the total conductivity of the $Ba_{1.1}Nd_{0.9}InO_{3.95}$ was not given, according to the slope of the Arrhenius plots in Figure 2.5(b) the $Ba_{1.1}Nd_{0.9}InO_{3.95}$ also exhibited a lower activation energy for the total conductivity.

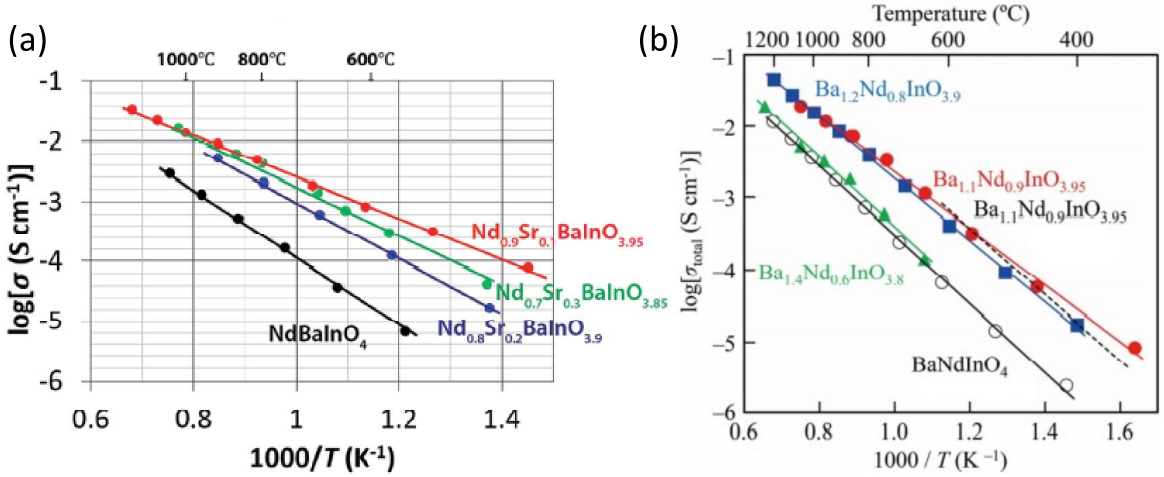

Figure 2.5 Arrhenius plots of total conductivities σ_{Total} of (a) $Ba_{1+x}Nd_{1-x}InO_{4-x/2}$ (x=0.1, 0.2, 0.4)(121) and (b) $Ba_{1+x}Nd_{1-x}InO_{4-x/2}$ (x=0.1, 0.2, 0.4) compounds measured in air. Adapted with permission from (124).

In order to probe the dominant charge carrier species under different atmospheres, the oxygen partial pressure $P(O_2)$ dependence of the electrical conductivity of $BaNdInO_4$-type compounds was investigated using a dc 4-probe method under controlled gas atmospheres. As shown in Figure 2.6 (a), in the high $P(O_2)$ range (region A and B), the total conductivities σ_{Total} of $BaNdInO_4$ and $BaNd_{0.9}Sr_{0.1}InO_{3.95}$ decreased with decreasing oxygen partial pressure. The total conductivities remained constant in the intermediate $P(O_2)$ range (region C) and increased with decreasing oxygen partial pressure in the low $P(O_2)$ range (region D). Similar experiments conducted on $Ba_{1.1}Nd_{0.9}InO_{3.95}$ showed a similar trend as shown in Figure 2.6 (b). The slope of log(σ_{Total}) versus log($P(O_2)$) in region A and region B indicated that $BaNdInO_4$-related oxides show p-type conductivity in high oxygen partial pressure and mixed oxide-ion and hole conduction in intermediate high oxygen partial pressure, respectively. The total conductivity was independent of $P(O_2)$ in region C indicated a pure oxide-ion conduction, and in region D, a mixed oxide-ion and electron conduction mechanism might explain the increase in total conductivity. The defect chemistry happened in region B and region D can be expressed as the equations below:

$$\text{In region (D):}\quad O_O^x \rightarrow {}^1/_2\, O_{2(g)} + V_O^{\cdot\cdot} + 2e' \qquad (36)$$

$$\text{In region (B):}\quad {}^1/_2\, O_{2(g)} + V_O^{\cdot\cdot} \rightarrow O_O^x + 2h^{\cdot} \qquad (37)$$

Figure 2.6 (a) and (c) show Arrhenius plots of the oxide-ion conductivity σ_{ion} of $BaNd_{0.9}Sr_{0.1}InO_{3.95}$ and $Ba_{1.1}Nd_{0.9}InO_{3.95}$ in comparison with that of the primitive $BaNdInO_4$. Both Sr-doped and Ba-doped oxides showed higher oxide-ion conductivities than parent material, and the activation energies of two compounds were 0.795(10) eV (121) and 0.86(3) eV (124) which were lower than that of $BaNdInO_4$ (0.91(4) eV)(115). Therefore, the substitution of Nd site with Ba and Sr can improve the oxide-ion conductivity of $BaNdInO_4$ and lower its activation energy.

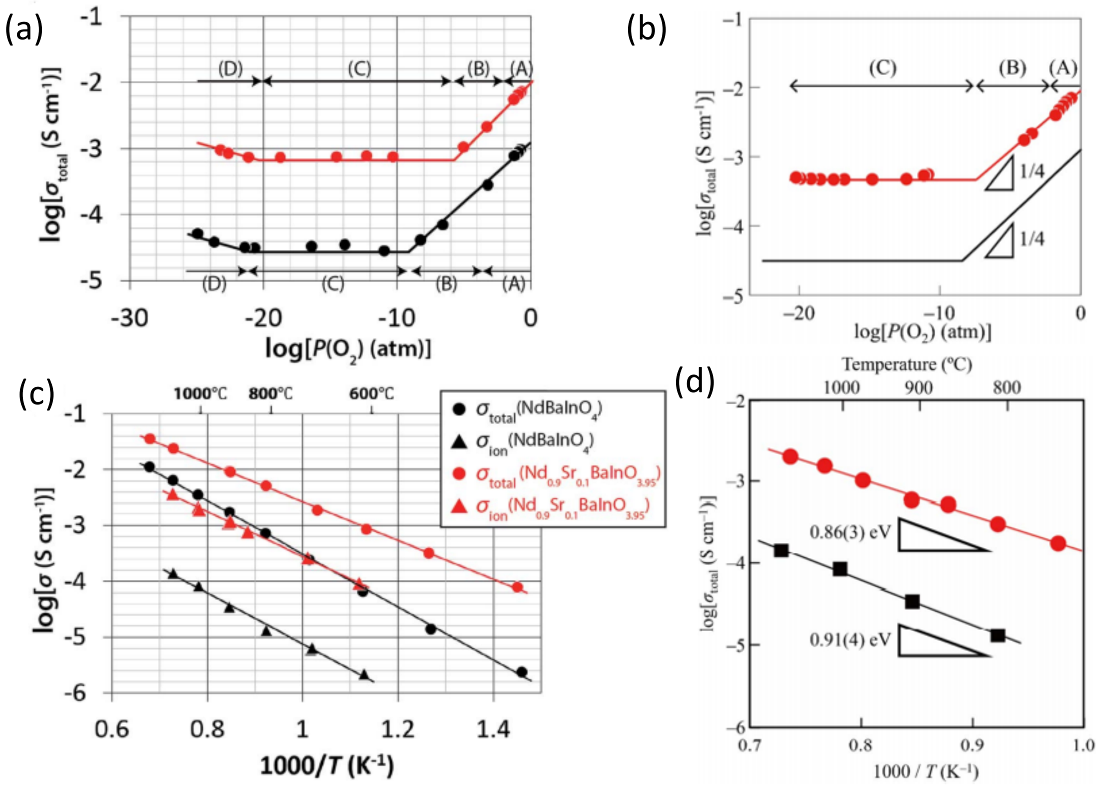

$BaNd_{0.9}Sr_{0.1}InO_{3.95}$ $Ba_{1.1}Nd_{0.9}InO_{3.95}$

Figure 2.6 (a)&(b) Oxygen partial pressure $P(O_2)$ dependence of the total conductivity σ_{Total} of $BaNdInO_4$ (black), $BaNd_{0.9}Sr_{0.1}InO_{3.95}$ (red, left) and $Ba_{1.1}Nd_{0.9}InO_{3.95}$ (red, right). Reproduced with permission from (121, 124). (c) Arrhenius plots of the total conductivity σ_{Total} (circles) and ionic conductivity σ_{ion} (triangles) of $NdBaInO_4$ (black) and $BaNd_{0.9}Sr_{0.1}InO_{3.95}$ (red). Adapted from (121) with permission from RSC. (d) Arrhenius plots of oxide-ion conductivities σ_{ion} of $NdBaInO_4$ (black squares) and $Ba_{1.1}Nd_{0.9}InO_{3.95}$ (red circles). Adapted with permission from (124).

$BaNd_{1-x}Ca_xInO_{4-x/2}$ (x=0.05, 0.1, 0.15, 0.2) compounds were successfully synthesized by Yang *et al.* in 2017(122), which also exhibited higher oxide-ion conductivities and lower activation energy for oxide-ion conduction. Comparing with the Sr and Ba substitution, Ca doped $BaNdInO_4$ compounds showed a decreasing trend in the unit cell volume. The solubility limit for calcium at the Nd site can reach up to x=0.3, which is higher than that of the Sr and Ba doped series. The higher solubility of Ca might result in higher carrier concentration in the bulk material, and thus increase the electrical conductivity further more. The activation energy for oxide-ion conduction of the $BaNd_{0.8}Ca_{0.2}InO_{3.9}$ was 0.70(2) eV according to the inserted Arrhenius plot shown in Figure 2.7 (b). The solid solution of $BaNd_{0.8}Ca_{0.2}InO_{3.9}$ also exhibited higher oxide-ion conductivities than those of Sr and Ba doped samples reported in Fujii *et al.*'s publications according to electrochemical impedance spectroscopy (EIS) data measured in air. Based on the state-to-art results on the $BaNdInO_4$-related structures, calcium seemed to be the optimal doping cation on the Nd site in terms of improving the oxide-ion conductivity of $BaNdInO_4$ by acceptor doping. With regard to the characterization methods used for determination of the oxide-ion conduction of the system, the dc 4 probe conductivity method and EIS measurements conducted in the reducing atmosphere with $P(O_2)<10^{-10}$ atm were both direct methods which measure the total conductivity of the system at certain conditions. However, the accuracy of the values may be argued due to the uncertainty of the 'pure oxide-ion conducting region'. Instead an indirect method regarding IEDP technique could be introduced to determine the oxide-ion conduction.

$BaNdIn_{1-x}Ti_xO_{4+\delta}$ solid solution were investigated by Ishihara *et al*(123). The electrical conductivities of $BaNdIn_{0.9}M_{0.1}O_{4+\delta}$ (*M*=Mg, Ce, Ga, Cr, Nb, Zr, Ta, Ti, Si and Sn) was measured by the dc 4-probe method and the $P(O_2)$ dependence was also investigated by controlling the gas atmosphere during the conductivity measurement. Overall, $BaNdIn_{0.8}Ti_{0.2}O_{4.1}$ showed the highest oxide-ion conductivity and reasonably high chemical stability. However, there could be an influence of impurity phases, such as $Ba_2In_2O_5$, since the XRD patterns of the $BaNdIn_{1-x}Ti_xO_{4+\delta}$ compounds in their publication showed some unidentified peaks.

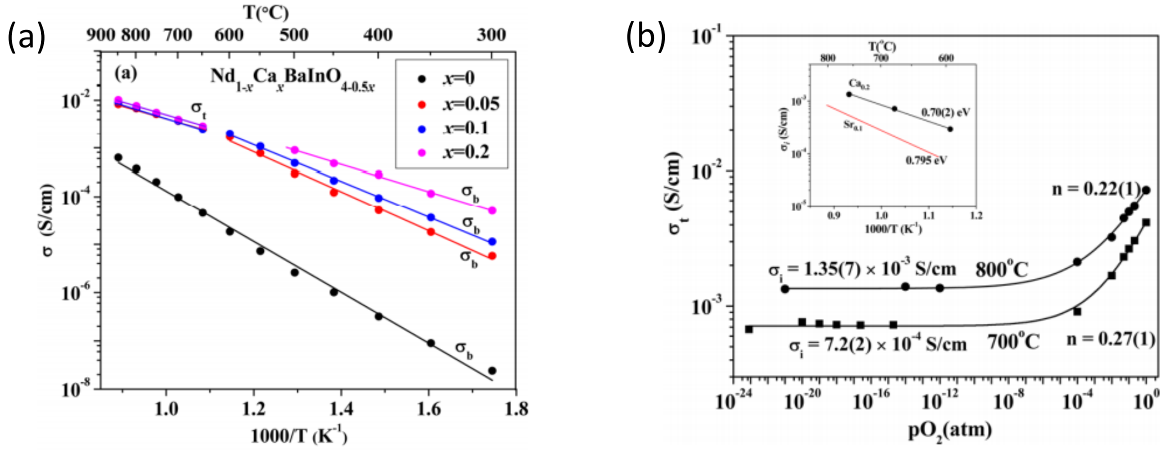

Figure 2.7 (a) Arrhenius plots of the total conductivities of $BaNd_{1-x}Ca_xInO_{4-x/2}$ (x=0.05, 0.1, 0.15, 0.2) compounds measured in air. The breaks in the data were due to the change in processing the Impedance data as bulk response disappeared at high temperatures. Reproduced from (122) with permission from ACS Publications. (b) Oxygen partial pressure $P(O_2)$ dependence of the total conductivity σ_{Total} of $BaNd_{0.8}Ca_{0.2}InO_{3.9}$ at 700℃ and 800℃. The insert shows the comparison of the Arrhenius plot of oxide-ion conductivity of $BaNd_{0.8}Ca_{0.2}InO_{3.9}$ (dark) with that of $BaNd_{0.9}Sr_{0.1}InO_{3.95}$ (red) from Fujji *et al.* Adapted with permission from (121).(122)

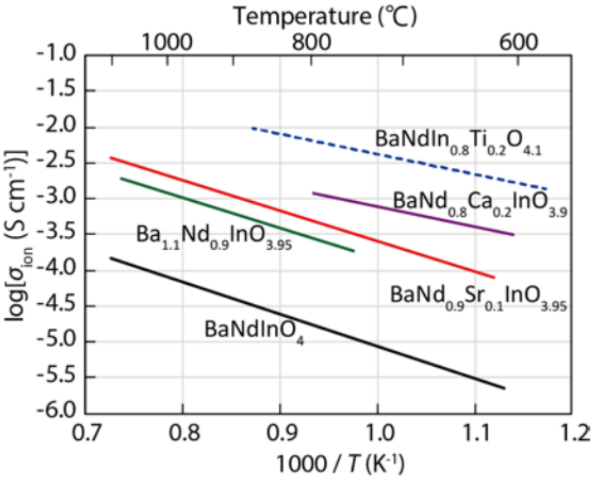

Figure 2.8 Arrhenius plots of oxide-ion conductivities σ_{ion} of $BaNdInO_4$ (115), $BaNd_{0.9}Sr_{0.1}InO_{3.95}$ (121), $Ba_{1.1}Nd_{0.9}InO_{3.95}$ (124), $BaNd_{0.8}Ca_{0.2}InO_{3.9}$ (122) and $BaNdIn_{0.8}Ti_{0.2}O_{4.1}$ (123). The σ_{ion} of the $BaNd_{0.8}Ca_{0.2}InO_{3.9}$ was calculated multiplying the oxde-ion transport number by total electrical conductivity measured in air from Ishihara *et al*(123). Reproduced with permission by Fujji(116).

To conclude the previous reports on the $BaNdInO_4$-based materials, the electrical conductivity of the parent $BaNdInO_4$ oxide can be effectively improved by acceptor doping using the alkaline-earth metal cations such as Ca, Sr and Ba. The substitution of Sr and Ba on the Nd site was confirmed by neutron diffraction data. Simultaneously, the oxide-ion conductivity of $BaNdInO_4$ was significantly decreased and the activation energy of the ionic conduction decrease by Ca, Sr and Ba doping. Among all the aliovalent doping cations, calcium seemed to be the optimal doping cation on the Nd site in terms of improving the oxide-ion conductivity of $BaNdInO_4$ and decreasing the activation energy for the ionic conduction. This can be ascribed to the smallest mismatch in the cation size between Ca^{2+} and Nd^{3+} ($|r(Ca) - r(Nd)| = 0.014 < |r(Sr) - r(Nd)| = 0.164 < |r(Ba) - r(Nd)| = 0.334$)(116). Besides, the higher solubility of calcium at the Nd site allows the formation of higher charge carrier concentration which also improve the electrochemical property of the material. Therefore, we chose calcium doped $BaNdInO_4$ as the main target in this research.

2.3 Oxide-ion migration in $BaNdInO_4$

In order to probe the oxide-ion migration paths in $BaNdInO_4$ and its solid solutions, bond-valence method and static lattice simulations along with molecular dynamics method was proposed by Yashima *et al*.(121) and Yang *et al*.(122), respectively. The investigation of oxygen migration using the statistical simulation methods gives a more profound understanding of the conduction mechanism of these oxide-ion conductors. Both bond-valence method and the static lattice simulations and molecular dynamics simulation suggested two-dimensional oxide-ion migrations in the rare earth Nd_2O_3 unit/slab on the *bc* plane in $BaNdInO_4$ and its solid solutions.

Bond Valence Method: As reported by Fujii *et al*.(121), diffusion pathways of oxide ions in the lattice of $BaNd_{0.9}Sr_{0.1}InO_{3.95}$ and $BaNdInO_4$ were investigated by the bond valence based energy (BVE)(125) method using the 3DBVSMAPPER(126) program which was built based on the crystal structure of the target materials at a certain temperature. In the research, the calculations were carried out based on the crystal structure of $BaNd_{0.9}Sr_{0.1}InO_{3.95}$ and $BaNdInO_4$ determined by refinement of the powder neutron diffraction data obtained at 800℃. The refined neutron diffraction data was shown in Figure 2.9 (a)&(b). As shown in Figure 2.9(c), the blue area represented the isosurfaces where the BVE for an oxide-ion is +1.6 eV. In this landscape, the O4 site which is the most stable position in the lattice was set to 0 eV. According to the BVE isosurfaces, O1 and O2 sites are localized in the crystal structure, while the isosurfaces around O3 and O4 sites spread in the rare earth structure unit $(Nd,Sr)_2O_3$ and are connected with each other along the *bc* plane indicating a two-dimensional oxide-ion pathway since the energy barriers of the paths along the *b*- and *c*-axes have similar energy barriers of 1.42 and 1.47 eV which are much lower than that of the *a*-axis (2.72 eV). As for the parent material, $BaNdInO_4$, the BVE barriers along the *a*-, *b*- and *c*-axes calculated based on the crystal structure obtained at 24℃ were 1.72, 3.95 and 2.01 eV which are higher than those in $BaNd_{0.9}Sr_{0.1}InO_{3.95}$ (1.47, 2.88, 1.69 eV). These simulation results are consistent with the activation energy data mentioned in section 2.2 that $BaNd_{0.9}Sr_{0.1}InO_{3.95}$ exhibited a lower activation energy for oxide-ion conduction. In the same article(121), the author attributed the decrease of energy barriers in $BaNd_{0.9}Sr_{0.1}InO_{3.95}$ to the geometrical change in the crystal structure when substituting Sr at the Nd site. As observed in the BVE landscape, the highest BVE point along the possible oxide-ion diffusion pathway is surrounded by two (Nd or (Nd,Sr)) cations and one Ba cation which construct a triangle bottleneck. The substitution of Nd with Sr increases the bottleneck area according to the cation's radius, thus lowers the activation energy of oxide-ion conduction. However the calculation of the bottleneck area in the literature was not carried out within the lattice structure. The effects of oxygen vacancies and other oxygen pathways should also be included.

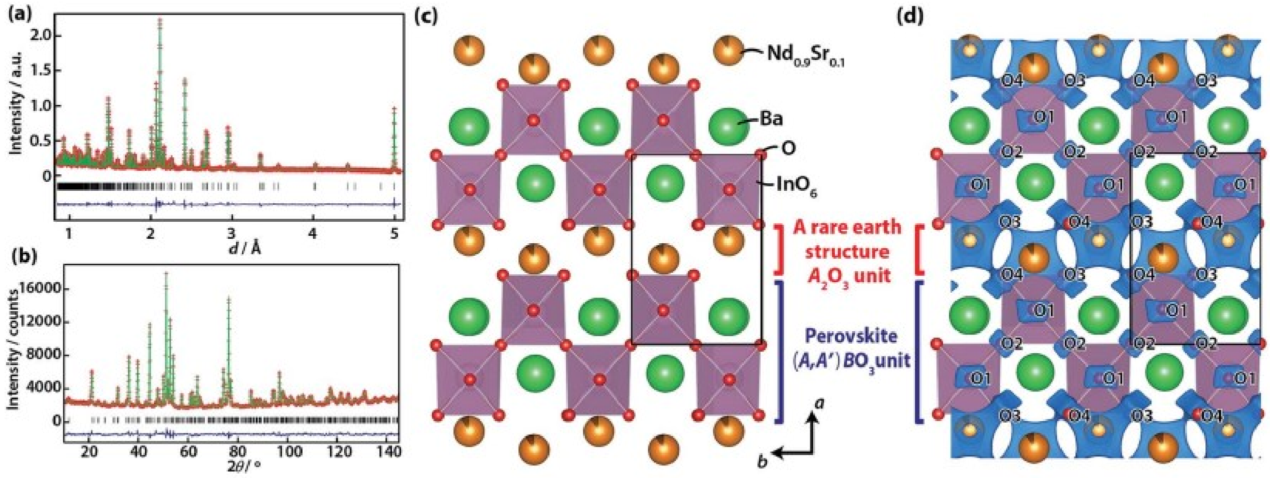

Figure 2.9 Refined NPD data of $BaNd_{0.9}Sr_{0.1}InO_{3.95}$ measured at (a) 24℃and at (b) 800℃, where the red marks, green solid line and blue lower line represented the experimental, simulated and difference plots, respectively. (c) Crystal structure of $BaNd_{0.9}Sr_{0.1}InO_{3.95}$ according to the refinements of the neutron diffraction data. The dark solid line represents the unit cell. (d) Bond valence-based energy (BVE) landscape for an oxide ion with an isovalue at 1.6 eV in $BaNd_{0.9}Sr_{0.1}InO_{3.95}$ at 800℃. As *A* and *A'* represent the relatively large cations and *B* is the smaller cation which is In in this case. Reproduced with permission from (121).

Static Lattice and Molecular Dynamic Simulations: The atomistic static lattice simulations in Yang *et al.*'s publication were carried out using the General Utility Lattice Program (GULP) on the basis of the interatomic potential(122), the detailed information of which could be found in the previous literatures. The energy barriers for both the linear and curved paths for the seven octahedral edge O-O paths together with six intra-slab and inter-slab oxygen migration pathways in $BaNdInO_4$ were calculated as illustrated in Figure 2.10 below.

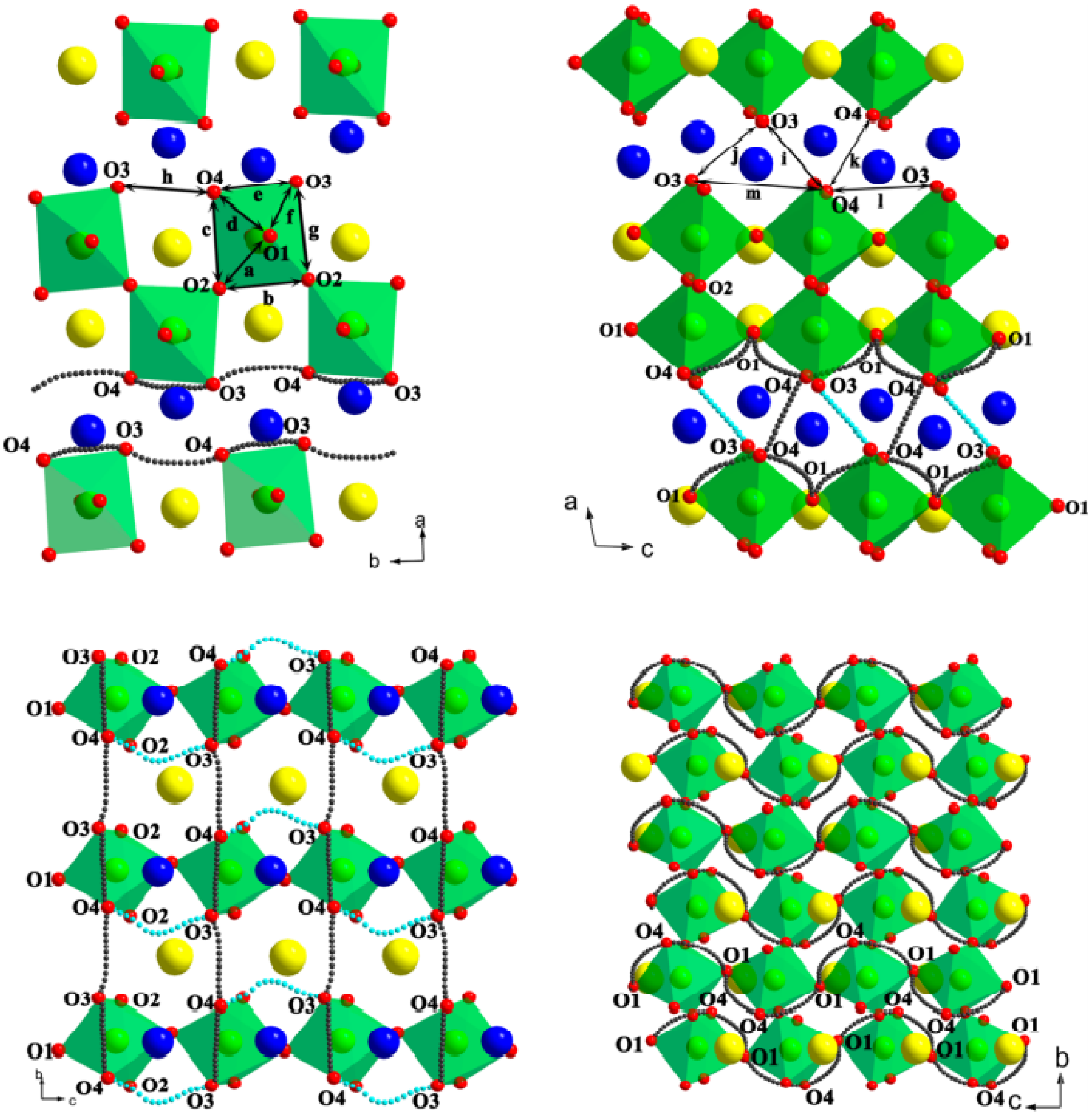

Figure 2.10 Oxygen migration paths in the BaNdInO$_4$ lattice: a(O1-O2), b(O2-O2), c(O2-O4), d(O1-O4), e(O3-O4), f(O1-O3) and g(O2-O3) denoting the migration paths within the Octahedral; h (intra-slab O3-O4), i (inter-slab O3-O4), j (inter-slab O4-O4), l (intra-slab O3-O4) and m (intra-slab O3-O4) denoting the inter-octahedral oxygen migration paths. Adapted from (122) with permission from ACS. The dark grey dotted lines represent the oxygen migration pathways with energy barriers ~0.52-0.60 eV and those in cyan represent the pathways with energy barriers ~0.82-0.85 eV.

The calculated lowest energy barriers for all 13 migration paths were listed below. And the energy-favourable oxygen migration paths are d (O1-O4) and e (O3-O4) within the InO$_6$ octahedron and h (intra-slab O3-O4) between the octahedra. The former ones are oxygen migration paths via the alternative octahedral edge along the *c*-axis and the latter one is via curved inter-octahedral O3-O4 paths parallel to the *b*-axis within the Nd$_s$O$_3$ layer.

Table 2.1 Energy barrier (ΔE) for oxygen vacancy migration along O-O sites as labelled in Figure 2.10. Adapted from (122).

Path	O-O separation (Å)	ΔE (eV)
	Octahedral Edge Path	
a (O1-O2)	2.993	1.20
b (O2-O2)	3.054	1.06
c (O2-O4)	3.209	1.19
d (O1-O4)	2.998	0.52
e (O3-O4)	2.85	0.47
f (O1-O3)	2.994	1.27
g (O2-O3)	3.310	1.66
	Interoctahedral Path	
h (intraslab O3-O4)	3.289	0.60
i (interslab O3-O4)	3.233	0.85
j (interslab O3-O3)	3.144	1.08
k (interslab O4-O4)	3.038	0.54
l (intraslab O3-O4)	3.741	0.82
m (intraslab O3-O4)	4.557	2.47

Interatomic-potential-based molecular dynamic (MD) simulations were also carried out on the $BaNd_{0.9}Ca_{0.1}InO_{3.95}$ solid solution with the DL_POLY code to probe the oxygen vacancy migration(122). The detailed information of the simulation code can be found in the previous literature(127). Figure 2.11 below shows scatter plots of ion positions from the MD simulation result of $BaNd_{0.9}Ca_{0.1}InO_{3.95}$ at 1400℃.

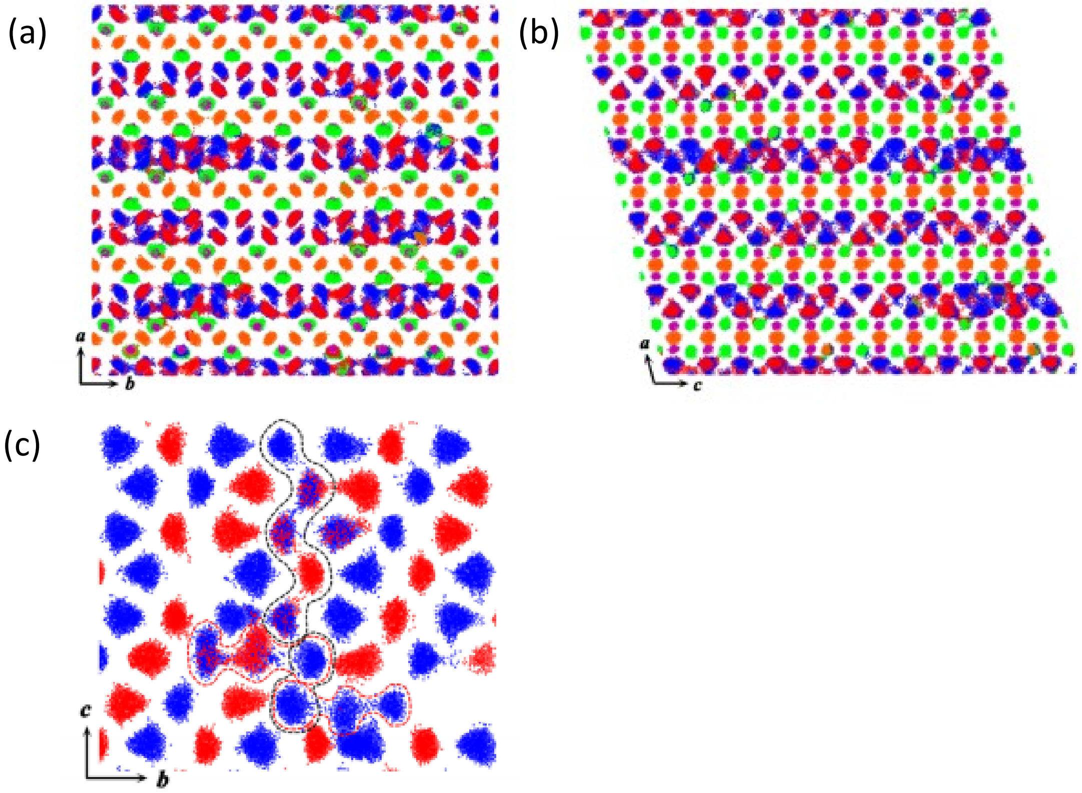

Figure 2.11 Scatter plots of ion positions from the MD simulation of $BaNd_{0.9}Ca_{0.1}InO_{3.95}$ at 1400℃ viewed along (a) *c*-axis and (b) *b*-axis. (c) An enlarged scatter plot of ion position viewed along *a*-axis to show the inter-slab and intra-slab migration as marked by black and red dashed lines, respectively. Green, orange, blue, red and purple represent ions originally on O1, O2, O3, O4 and In sites, respectively. The dashed lines with red and dark color illustrates respectively the short- and long-range sinusoidal-like path. Reproduced with permission from (122)

The overlapping of colors in Figure 2.11 indicates the vibration of ions and the possibility of the ion leaving its original site and migrating to occupy another adjacent site. Obviously, O1, O3 and O4 are most likely to be involved in the oxygen migration in the lattice as the area of green, red and blue are larger, while the isolated orange patterns implies that O2 are seldomly involved. The overlapping of red and blue are significant indicating a two dimensional oxygen migration in the Nd_2O_3 units which is consistent with the DBVS mapping results in Fujii *et al.*'s paper. The author also proposed that the long-range sinusoidal-like path along the *c*-axis, as shown in Figure 2.11 with black dashed lines, are more favoured for the inter-slab vacancy migration according to the MD simulation results than the short-range migration revealed by the static lattice simulation. The mean square displacement (MSD) values of O1, O3 and O4 were used to calculate the oxygen diffusion coefficients which were in the range of 10^{-6}-10^{-7} cm^2/s, though there are no direct experimental data then to make a comparison.

Both BVE method and MD simulations suggested a 2D oxygen migration mechanism along the *bc* plane within the rare earth layer in the lattice. Combining the fact that the undoped $BaNdInO_4$ stoichiometry also exhibited oxide-ion conduction(115) where no excess oxygen vacancies were generated by acceptor-doping, the migration of oxide-ions within the rare earth slabs may follow the oxygen interstitial diffusion mechanisms proposed in the previous literatures on the Ruddlesden-Popper oxides(128, 129). As described in the oxide-oxide interstitialcy-mediated diffusion mechanism(129), according to the density functional (DFT) theory, oxygen interstitials intercalated into a Ruddlesden-Popper material may reside in the rocksalt layer being located at the center of the A-cation tetrahedron. The oxygen migration was completed by hopping between these interstitial sites. The oxygen interstitial diffusion proposed in the Ruddlesden-Popper material can be one of the hypothesises that account for the oxide-ion conduction discovered in the parent $BaNdInO_4$ oxide.

2.4 Water incorporation and protonic defects in perovskite materials

Since the discovery of proton conduction in the strontium and barium cerate perovskites in the 1980s, the incorporation of water into the perovskite-type structure and the electrochemical properties of the resulting hydrated material has been widely studied. Apart from the aforementioned oxygen annihilation (Equation 12), water can also dissociate into the system and occupy the oxygen vacancies forming hydroxide ions. The incorporation of water can be expressed by Kröger-Vink notation as

$$\mathrm{H_2O + V_O^{\cdot\cdot} + O_O^x \leftrightarrow 2OH_O^{\cdot}} \tag{38}$$

The equilibrium condition of the equation is written:

$$K_\mathrm{w} = \frac{[OH_O^{\cdot}]^2}{\left([V_O^{\cdot\cdot}]\cdot[O_O^x]\cdot p_{\mathrm{H_2O}}\right)} \tag{39}$$

As shown by the reaction, oxygen vacancies play an important role in formation of protonic defects, which can be generated extrinsically by acceptor doping in the perovskites. The migration of the consequent protonic defects is faster than that of the original oxygen vacancies in most of the cases due to the lower effective charge and smaller ionic radius of the protons. Although there are still debates going on with the conduction mechanism of the protonic defects in the barium cerate perovskite system, the conductivity of those systems was found to be improved by the water incorporation(130-132). By using high resolution neutron powder diffraction and the isotope techniques, the location of protons in the lattice could be located. The concentration of protonic defects can be determined by thermogravimetric analysis (TGA), where the change in mass of the sample is precisely observed in an elevating temperature program for a given water partial pressure ($p_{\mathrm{H_2O}}$), or with a variation in $p_{\mathrm{H_2O}}$ for a given temperature. Recording the weight at a constant water vapour pressure as a function of temperatures gives the hydration isobar, which yields the thermodynamic parameters including the hydration enthalpies and entropies. Kreuer(99) managed to conclude hydration isobars of various perovskite-type oxides and compare the experimental data with the theoretical expression. The expression of the concentration of protonic defects as a function of $p_{\mathrm{H_2O}}$ and K_{w} is derived from the combination of Eq. (39) with the site restriction (because of high defect concentration),

$$[O_O^x] + [V_O^{\cdot\cdot}] + [OH_O^{\cdot}] = 3 \tag{40}$$

together with the electroneutrality condition (taking yttrium doped barium cerate system as an example),

$$2[V_O^{\cdot\cdot}] + [OH_O^{\cdot}] + [Y_{Ba}^{\cdot}] = [Y_{Ce}'] \tag{41}$$

The equilibrium constant can be then written as

$$K_{\mathrm{w}} = \frac{4[OH_O^{\cdot}]^2}{p_{\mathrm{H_2O}}(S - [OH_O^{\cdot}])(6 - S - [OH_O^{\cdot}])} \tag{42}$$

where S is the effective dopant concentration and also the water solubility limit. Then the concentration of protonic defects can be expressed as:

$$[OH_O^{\cdot}] = \frac{3K_{\mathrm{w}}p_{\mathrm{H_2O}} - \sqrt{K_{\mathrm{w}}p_{\mathrm{H_2O}}\left(9K_{\mathrm{w}}p_{\mathrm{H_2O}} - 6K_{\mathrm{w}}p_{\mathrm{H_2O}}S + K_{\mathrm{w}}p_{\mathrm{H_2O}}S^2 + 24S - 4S^2\right)}}{K_{\mathrm{w}}p_{\mathrm{H_2O}} - 4} \tag{43}$$

Equation (42) then is used to simulate the hydration isobars of the perovskites, which can be seen in Figure 2.12 as the smooth curves.

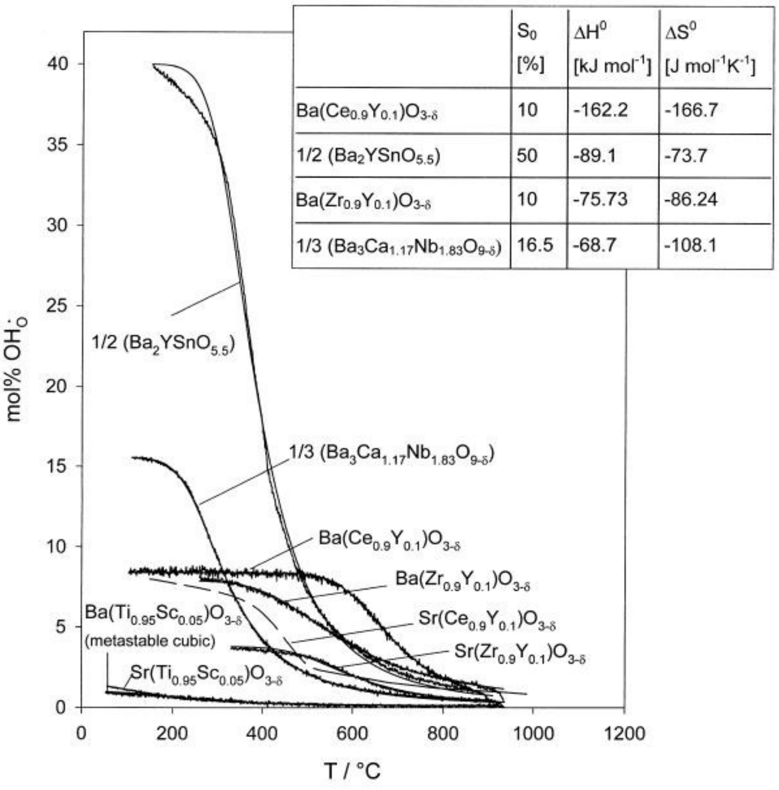

	S_0 [%]	ΔH^0 [kJ mol^{-1}]	ΔS^0 [J mol^{-1}K^{-1}]
$Ba(Ce_{0.9}Y_{0.1})O_{3-\delta}$	10	-162.2	-166.7
1/2 ($Ba_2YSnO_{5.5}$)	50	-89.1	-73.7
$Ba(Zr_{0.9}Y_{0.1})O_{3-\delta}$	10	-75.73	-86.24
1/3 ($Ba_3Ca_{1.17}Nb_{1.83}O_{9-\delta}$)	16.5	-68.7	-108.1

Figure 2.12 Hydration Isobars for different perovskite-type ceramics (at $p_{\mathrm{H_2O}}$=23 hPa) where the experimental data shown as the rough curves are fit with the smooth curves derived from equation. Adapted from (99) with kind permission from Elsevier. The dashed line in the plot represents the decomposition of $\mathrm{Sr(Ce_{0.9}Y_{0.1})O_{3-\delta}}$ below ~ 500°C.

For cubic perovskites, such as $\mathrm{BaCe_{0.9}Y_{0.1}O_{2.95}}$ at high temperature range, which has only one type of oxygen site in the lattice, the expression fit quite well with the hydration isobar obtained from TGA measurement. Despite the lattice distortion of $\mathrm{Y{:}\,BaCeO_3}$ system at room temperatures into orthorhombic phase which results in two oxygen sites with different chemical environments, the fit with only one standard chemical potential differences is still surprisingly good(99). Since $kT\ln(K_{\mathrm{w}}) = T\Delta S^0 - \Delta H^0$, for a given water partial pressure, the hydration enthalpies and entropies can be achieved from simulation of these hydration isobars. Figure 2.12 also shows the fitted thermodynamic parameters of the hydration reaction for the cubic perovskites except for the titanates because they didn't take up sufficient water under experimental conditions to give a fit of high significance(133). For $\mathrm{Y{:}\,SrZrO_3}$ and $\mathrm{Y{:}\,SrCeO_3}$ systems, the lattice structure of which are significantly deviated from an ideal cubic perovskite(134), the hydration isobars cannot be fitted simply with Eq. (42). In addition, the existence of different oxygen sites within the structure seemed to prohibit the water uptake(134) due to their different affinities towards hydration.

2.5 Protonic conductivity in perovskite-related materials

The protonic conductivity of the acceptor-doped perovskite system can be determined by impedance measurement carried out in a water-saturated atmosphere. The Nyquist plots obtained from impedance spectroscopy allows one to extract the bulk resistance from all other responses from other components in the system. In a complex impedance data, the bulk response normally shows up in the high frequency range as a semi-arc corresponding to a specific capacitance of about 10^{-12}-10^{-11} F, while the presence of a grain boundary response often appears at slightly lower frequency corresponding to a capacitance of 10^{-11}-10^{-8} F(135).

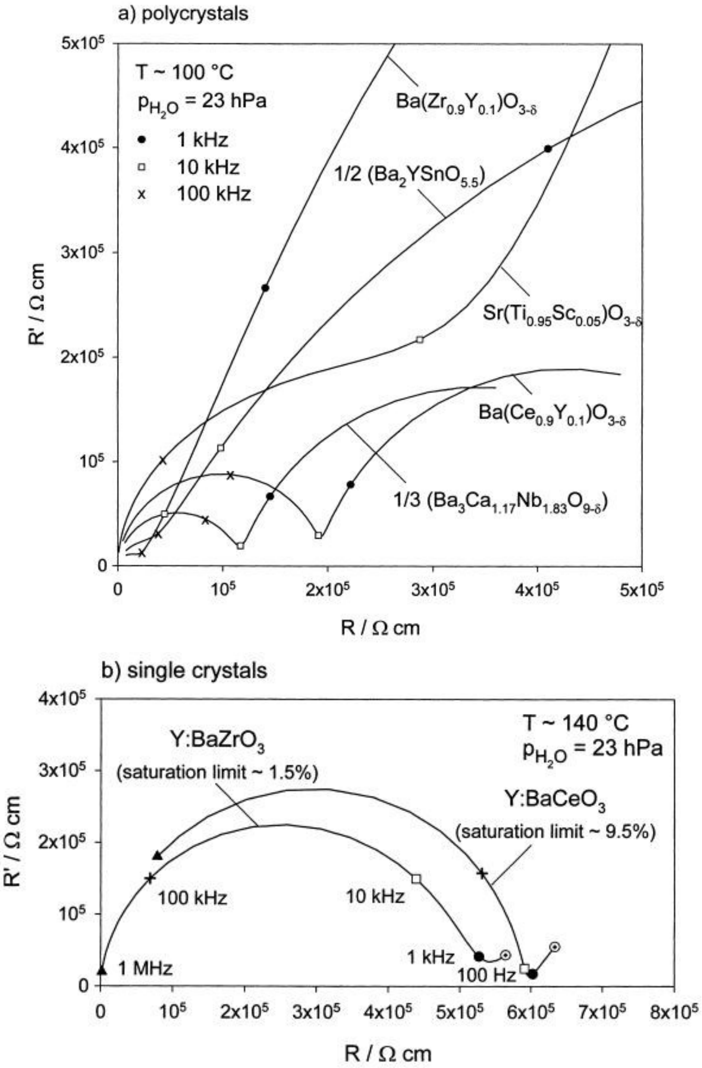

Figure 2.13 Impedance spectra of representative (a) polycrystalline samples and (b) single crystal samples. Adapted with permission from (99)

As shown in Figure 2.13(a), for polycrystalline samples, the bulk semi-arc may be resolved with the other responses at lower temperatures. The availability of single crystal samples, as shown in Figure 2.13(b), confirms the attribution of the high frequency arc to the bulk proton conductivity(99). Figure 2.14(a) shows the bulk proton conductivities of perovskite-type oxides in the temperature ranges where impedance spectroscopy allows a reliable separation of the bulk response. With the concentration values of the protonic defects taken from the previous hydration isobars (shown in Figure 2.12), the diffusivities of protonic defects in these perovskites, illustrated in Figure 2.14(b), can be calculated via the Nernst-Einstein relationship. The activation enthalpies of the proton mobility in these oxides are within 0.42-0.58 eV which are much lower than the activation enthalpies for the mobility of oxygen vacancies obtained in the previous literature (0.67-1.13 eV)(136).

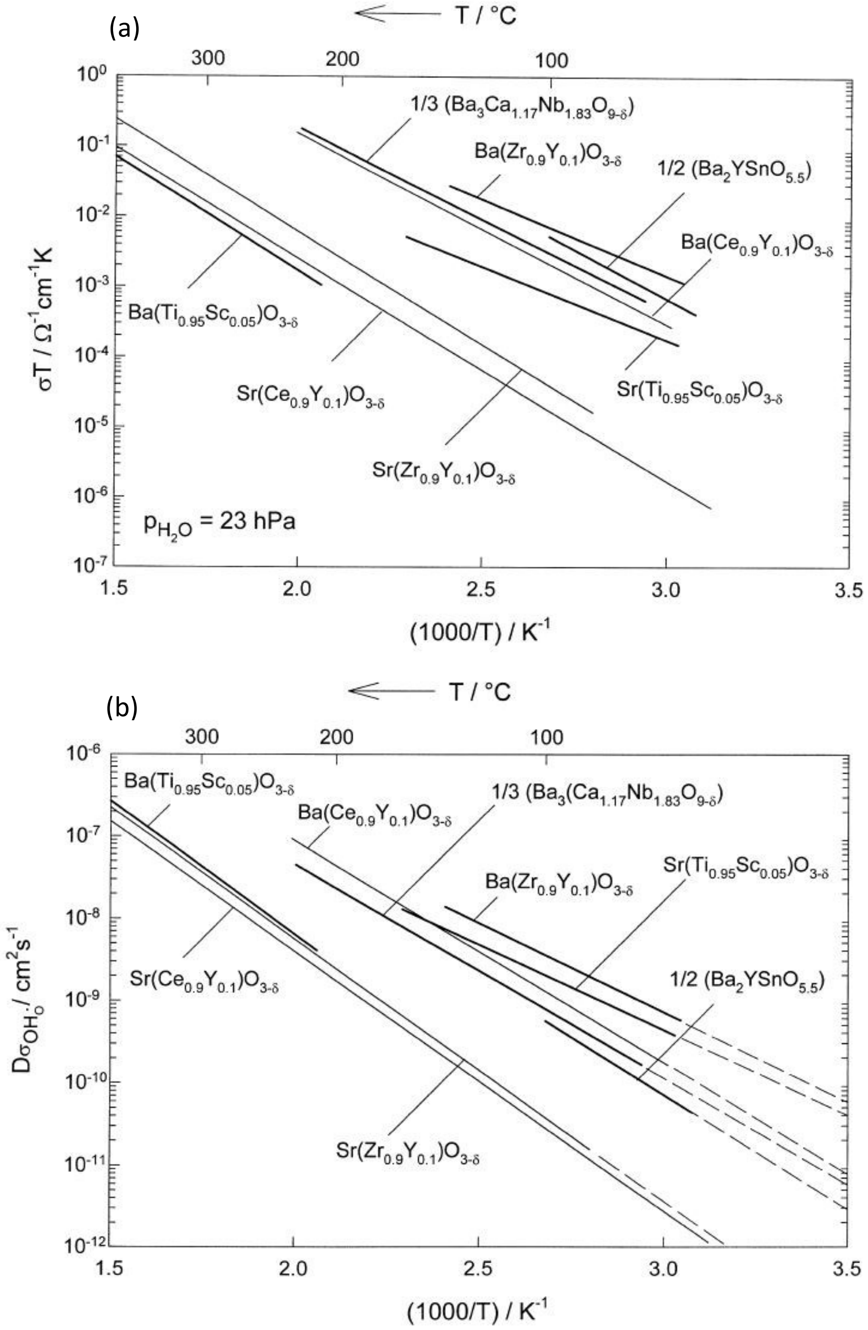

Figure 2.14 Proton conductivities (a) and diffusivities of protonic defects (b) of different perovskite oxides. Adapted with permission from (99). The data of the cubic perovskites are illustrated as bold lines.

Kreuer(137) also summarized the proton conductivities calculated from the available data on protonic concentrations and mobilities (from Reference (138)) according to Equation (42), not only for the perovskite-type oxides, but also for binary rare earth oxides with fluorite-related crystal structures and ternary metal oxides with the pyrochlore structure.

$$\sigma_{\mathrm{OH}_\mathrm{O}^{\cdot}} = e \cdot [OH_O^{\cdot}] \cdot \mu_{\mathrm{OH}_\mathrm{O}^{\cdot}} = \left(\frac{e^2[OH_O^{\cdot}]}{kT}\right) D_{\mathrm{OH}_\mathrm{O}^{\cdot}} = \left(\frac{e^2[OH_O^{\cdot}]}{kT}\right) D^0_{\mathrm{OH}_\mathrm{O}^{\cdot}} \exp\left(-\frac{\Delta H_\mathrm{m}}{kT}\right) \tag{44}$$

where $D_{\mathrm{OH}_\mathrm{O}^{\cdot}}$ and $D^0_{\mathrm{OH}_\mathrm{O}^{\cdot}}$ are respectively the diffusivity and standard diffusivity of the protonic defects, ΔH_m is the migration enthalpy of the protonic defects in the lattice. It is worth pointing out that the latter part of Equation (44) treats the concentration and proton transport separately, which can only be applied to an ideal system where the proton migration is independent of the concentration. According to the previous literatures(137, 138), the proton conductivities of these systems were examined over an extended temperature range, for which the protonic defects are not always accessible experimentally. Among all these protonic conductors, barium cerates and barium zirconates demonstrates the highest proton conductivities, and the conductivities of which are much higher than that of strontium cerates and strontium zirconates. These observations are consistent with the aforementioned empirical results and the data from other literature(139-141).

2.6 Proton transport mechanism

Since 1980, Takahashi and Iwahara(98) first reported the discovery of protonic conduction in perovskite-type ceramics, tremendous efforts have been dedicated into probing the transport mechanism of protonic defects not only empirically through material characterization techniques such as the infrared (IR) spectra and high-resolution neutron powder diffraction (NPD), but also theoretically by numerical simulations. The most commonly accepted proton conduction mechanism so far is the Grotthuss-type mechanism where the proton is the only mobile species while the oxygen resides in the vicinity of its original position in the lattice. The principal features of this proton transport mechanism consist of two processes, namely the rotational diffusion of the proton defect and the transfer of the proton toward a neighbouring oxygen as schematically presented in Figure 2.15. Experimental results(142, 143) by quasielastic neutron scattering as well as the quantum molecular dynamics (MD) simulation results(144, 145) have suggested that the rotational diffusion is a comparably fast step with low-activation barriers, thus indicating that the proton transfer reaction is the rate-limiting step in the considered perovskites. However the IR spectra(146) showed strong red-shifted OH-stretching absorption suggesting the existence of strong hydrogen-bond interactions, which favour the proton transfer reactions rather than the bond-breaking proton rotational diffusion process. The contradiction of these results could be explained from the structural perspective.

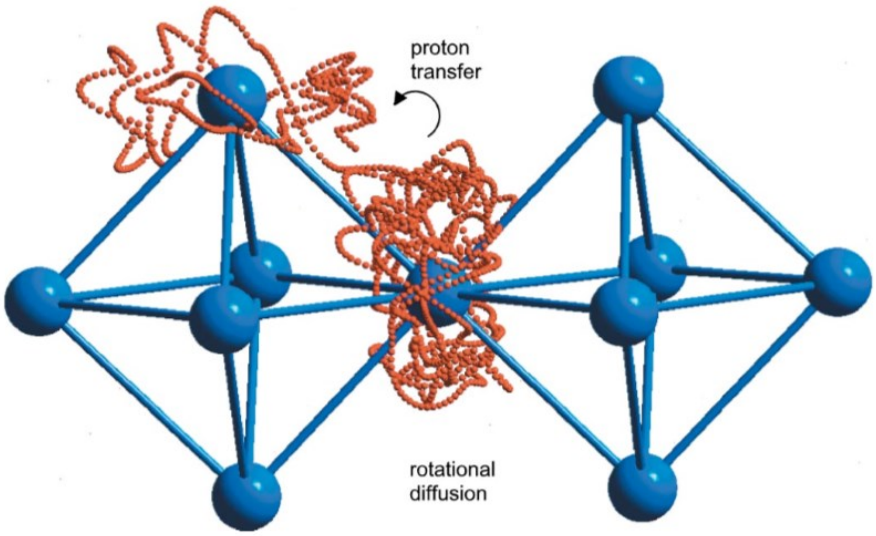

Figure 2.15 The schematic diagram of the Grotthuss-type proton migration mechanism in the perovskite type oxides. Adapted with permission from (145).

Basically, the structural oxygen separation in most perovskite-type oxides is larger than 290 pm which is significantly higher than the required distance for the formation of strong hydrogen bonds. Thus, in order to form hydrogen bonds, the lattice is distorted to an extent so that the free energy gained by the system from the formation of hydrogen bonds is competing with the free energy required for the lattice distortion. A quantum-Molecular Dynamics(MD) simulation result of a protonic defect in cubic $\mathrm{BaCeO_3}$(147) showed that these two contributions to the free-energy of the system are almost balanced for a wide range of oxygen separations which is approximately 250-300 pm. Therefore, short oxygen separations preferring the proton transfer reaction and large oxygen separations, which allow rapid bond breaking and proton rotational diffusion, have almost the same probabilities of happening. More interestingly, the simulation suggested that one protonic defect is attached with all eight nearest oxygen neighbours in the form of short but transient hydrogen bonds(148). In the time-averaged view according to the diffraction experiments, the overall structural OH/O separation is reduced by such dynamical hydrogen bonding configuration, but in the instant configurations obtained during a MD simulation, only one of the eight OH/O separations is reduced down to about 280 pm as a result of hydrogen bonding. Although the formation of hydrogen bonding in this configuration has a stabilizing effect of about 0.5 eV, the bond is soft, high-energy hydrogen bond with extended bond length variations(148). Due to the formation of such dynamical hydrogen bonds, theoretically one may expect an activation enthalpy of long-range proton diffusion to be no more than 0.15 eV assuming that the configuration of OH/O is linear. However, the mobility activation enthalpies of protonic defects in cubic perovskites is as large as 0.4-0.6 eV(133), which is mainly due to the fact that for most configurations with short OH/O separations, the proton is found being repulsed out of the edge of the octahedron leading to a strongly bent hydrogen bond as shown in Figure 2.16(a). This distortion from a linear hydrogen bond probably arises from the strong repulsive interaction between the proton and the highly charged B-site cation. Besides, a deformation of the $\mathrm{CeO_6}$-octahedron was captured in the instant configuration resulting from the hydrogen bonding, the energy required for which compensates the energy gained by the strong hydrogen bonding. As a result, the protons need to overcome an extra energy barrier when transportation, and thus the mobility activation enthalpy of protonic defects is increased.

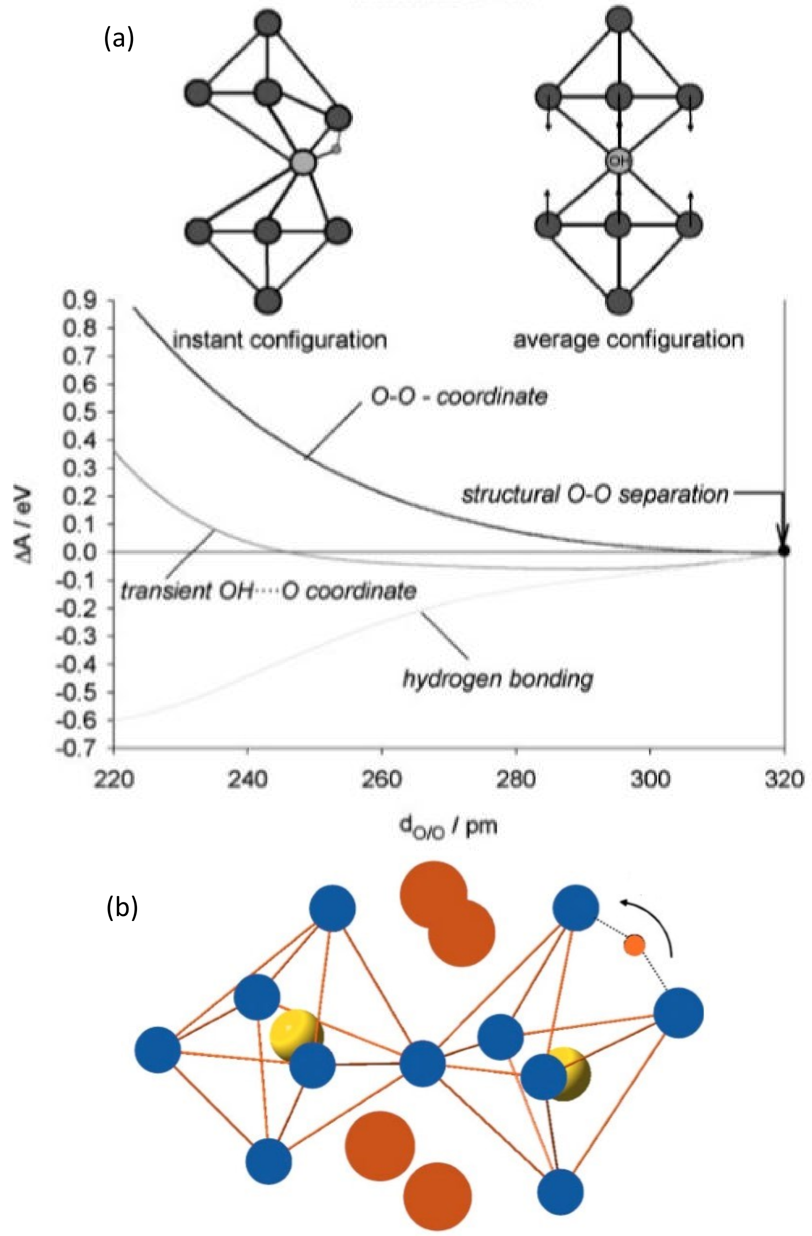

Figure 2.16 (a) Schematic diagrams of the instant and average configurations for the dynamical hydrogen bonding in $BaCeO_3$(Top panel) and the Helmholtz energy difference of the system as a function of the O/O and OH/O separation(Second panel). (b)An instant configuration obtained during a MD simulation as one of the transition state configurations of proton transfer. Large orange circles-Ba^{2+}, blue circles-O^{2-}, yellow circles-Ce^{4+}, small orange circles-H^{+}. Adapted with permission from (150).

A more detailed inspection of the MD simulation data on the transition state configurations of the proton transfer showed that the B-O bonds are elongated as observed in the instant configurations obtained during the MD simulations which displaced the transferring proton to the edge of the distorted octahedron. The elongation of the B-O bond will lead to a lower energy barrier for the proton transfer because the H/B repulsion is reduced in this specific configuration and the hydrogen bond formed is almost linear. However, the B-O bond elongation has its contribution to the activation enthalpy of the proton transfer, together with the new proton transfer barrier. Nevertheless, the H/B repulsive interaction can be used to estimate the upper limit for these two contributions to the activation enthalpy. Experimental evidence which supports these simulation inspections could be found in the previous literature(147), where the cubic perovskites with pentavalent B-site cations (I-V perovskites) have significantly higher activation enthalpies of proton mobility than the cubic perovskites with tetravalent B-site cations (II-IV perovskites).

Besides, the aforementioned structural deviations from the ideal cubic perovskite structure may lead to an increase in the activation enthalpy. This structural factor has been investigated by comparing the dynamical features of proton defects in Y:$BaCeO_3$ and Y:$SrCeO_3$ systems. As shown in Figure 2.17, due to the large orthorhombic distortion of Y:$SrCeO_3$, the oxygen sites in the lattice degenerate into two sites with probabilities of 1/3(O1 site) and 2/3(O2 site) with different chemical environments, while in Y:$BaCeO_3$ there is only one oxygen site (O2 site). Owing to the different chemical interactions between the A-site cations and the oxygen, the electron densities (basicities) of the oxygen ions in these two systems are quite different from each other resulting in different binding energies for the proton. In the Y:$SrCeO_3$ system, the proton tends to bind with O1 which is the most basic oxygen, whereas in Y:$BaCeO_3$ it is O2. Assuming that at the beginning of the proton transfer process, protons are associated with these sites within their own system, then the long-range proton transport in $BaCeO_3$ involves the transfer from the O2 site to the adjacent O2 site while in Y:$SrCeO_3$ a chemical difference from O1 site to O2 site must be overcome. The extra barrier of the latter finding is believed to be the reason why Y:$SrCeO_3$ showed higher activation enthalpy and lower conductivity compared with the Y:$BaCeO_3$ system.

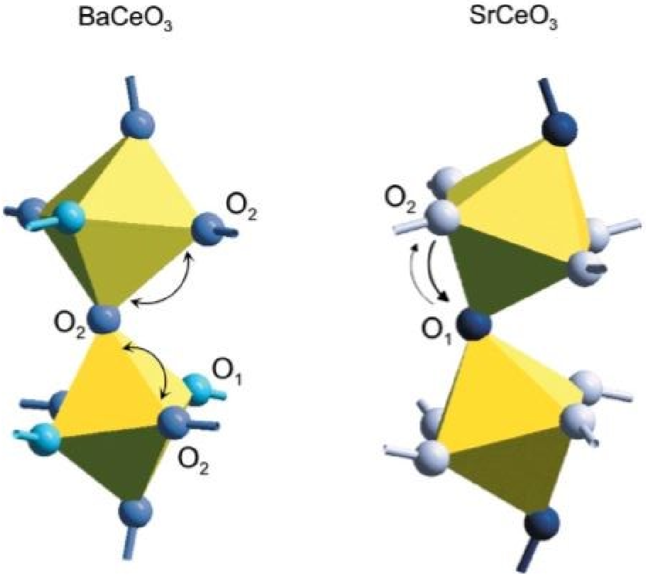

Figure 2.17 Effect of the orthorhombic distortion of $BaCeO_3$ and $SrCeO_3$ on the basicity of O1 and O2 (basicity indicated by the darkness of oxygen ions). The predominant routes for proton transfer are indicated by arrows. Reproduced with permission from (147).

Other than the reduction of crystallographic symmetry, the local structural and chemical perturbation introduced by acceptor doping or mixed occupancy on the B-site also plays a part in determining the mobility of proton defects. The oxide ion and proton conductivities of the M:$BaZrO_3$ (M=Sc^{3+}, In^{3+}, Y^{3+}) oxides show different trends as a function of the ionic radius of the chosen aliovalent cation. For oxide ion conductors, aliovalent cations with matching ionic radii are chosen to generate higher ionic conductivities as Sc^{3+} doped zirconia exhibited higher conducting properties than that of Y^{3+} doped zirconia(150). However, when adapted into a humid atmosphere, this approach fails. The Y^{3+} doped zirconia showed highest proton conductivity, although Sc^{3+} and In^{3+} match Zr^{4+} better regarding their ionic radii. Another interesting observation is, only for Y doped zirconia, the proton mobility and activation enthalpy of which are independent of the dopant concentration(134, 151). The explanation for that is probably because of the chemical match of the dopant.

Although the Y^{3+} doping at the Zr^{4+} site leads to a tetragonal distortion from the cubic phase at concentrations about 5 mol%, the acid/base properties of the coordinating oxygen remain almost unchanged, which makes it 'invisible' to the proton diffusion process(150). Another investigation of the proton conductivity in the $\mathrm{SrTiO_3}$- $\mathrm{BaTiO_3}$- $\mathrm{SrZrO_3}$- $\mathrm{BaZrO_3}$ system(150) showed that Zr/Ti mixing on the B-site led to a significant suppression of the proton conduction, which is consistent with the results investigating the $\mathrm{Ba_3Ca_{1+x}Nd_{2-x}O_{3-\delta}}$ system(152) showing that Ca/Nd ordering will reduce the proton conductivity significantly.

In summary, the protonic conductivity and its transport mechanism within the perovskite lattice were discussed. A strong, dynamical hydrogen bonding of the protonic defect with its eight nearest neighbor oxygen sites in the perovskite lattice was found which are strongly affected by the crystallographic symmetry as well as the local structural and chemical perturbation introduced by the doping(133). Empirically, however, it was extremely difficult to synthesize ceramics with both high thermodynamic stability and high proton conductivity. The incorporation of water content not only changes the conducting mechanism within the grain, but also leads to severe decomposition on the grain boundaries and on the sample surfaces.

2.7 Chemical stability of perovskite-based structural systems

As mentioned above, a high basicity of a perovskite structure is advantageous for the formation of proton defects, and therefore achieving high protonic conductivities. However, the chemical stability of the basic oxide with respect to the operating atmospheres for many applications such as SOFCs needs to be considered. Because basic oxides exhibited high proton conductivity, such as cerates, can easily react with acidic conditions or even with air at intermediate temperatures to form sulfates, carbonates or hydroxides. The rather stable zirconates, on the other hand, are reported to dissolve less water and show much higher activation enthalpies for proton conduction(132, 134). Empirically, it seems to be difficult to achieve both high thermodynamic stability and high proton conductivity at the same time in perovskite structured materials. Since this conflicting situation is highly relevant for many applications such as proton conducting SOFCs, the chemical stability of the perovskite related ceramics will be discussed a little more in detail in this section.

The most commonly investigated decomposition reaction of the perovskite materials is the reaction with H_2O or CO_2 which could decompose the perovskite into the binary oxides and then forming related hydroxide or carbonates. The hydroxides generated from reaction (45) will then easily react with CO_2 from the environment forming relevant carbonates. Considering a simple (II-IV) perovskite, ABO_3 where cation A is bivalent and cation B is tetravalent, the reaction with CO_2 could be written as:

$$\mathrm{ABO_3 + H_2O \rightarrow A(OH)^2 + BO_2} \tag{45}$$

$$\mathrm{A(OH)^2 + CO_2 \rightarrow ACO_3} \tag{46}$$

$$\mathrm{ABO_3 + CO_2 \rightarrow ACO_3 + BO_2} \tag{47}$$

According to the equation above, the thermodynamic stability of the perovskite is decided by the addition of the formation enthalpy of the perovskite from the binary oxides, which mainly corresponds to the compatibility of the cations, and the decomposition enthalpy of the carbonate with respect to AO. Therefore, the tolerance factor regarding the ionic radii r_A / r_B is crucial to determining the thermodynamic data of the perovskites. The perovskites with low tolerance factors tend to have low thermodynamic stabilisation. The chemical stability of these ceramics with respect to the decomposition reactions can be illustrated through the phase equilibrium graphs below.

For Sr and Ba cerates, the thermodynamic data for the reactions with CO_2 are almost the same, whereas because of the less basicity of SrO, the formation of $BaCO_3$ from BaO is more advantageous. As a result, the chemical stability of $BaCeO_3$ is higher than that of $SrCeO_3$. Previous literatures(153-155), showed the association of the stability of the carbonate, ACO_3, with the chemical stability of the perovskite type oxides in the phase equilibria plots whilst the lattice energy and the hydration enthalpy are also related. The phase equilibria plots showed that the equilibrium constant *K(T)* for $SrZrO_3$ decomposition into the hydroxide is higher than that of the thermodynamically less stable $SrCeO_3$. That is to say, although the oxide basicity favours the formation of protonic defects and the decomposition in acidic gases at the same time, the stability of the oxides will increase the formation of protonic charge carriers but suppress the decomposition reactions. Another interesting observation of the phase equilibria above is that the formation of protonic defects as well as the decomposition reaction of the perovskite into hydroxides in the cerates appear at lower water partial pressures than the zirconates. In accordance with increasing tolerance factors, for the perovskite type oxides with alkaline earth metal cations on the A-site, an increasing stability in these materials with respect to the decomposition reaction above can be observed in the following order: cerates→zirconates→titanates(146).

For perovskites with large B cations and low tolerance factors, the thermodynamic stability of the oxides may significantly affect the mechanical stability of the microstructures of the corresponding ceramics. As observed in the $BaCeO_3$-based ceramics(156), Ba^{2+} shows a tendency to occupy the B-site in some region of the $BeCeO_3$ crystal, particularly in the grain boundary region which will weaken the microstructure and therefore lower the mechanical stability of the ceramics. The phase equilibria from the same literature also suggested that the decomposition partial pressures for the $SrCeO_3$ and $BaCeO_3$ are slightly higher than those for the corresponding alkaline earth oxides due to the small Gibbs free energies of the formation reaction from the binary oxides. Therefore, as the metastable sites, the grain boundary regions as well as the surface layer of these perovskite materials are preferred by the decomposition reaction, and then form the secondary phases. However, even for relatively stable perovskites, (e.g. $BaTiO_3$, $SrTiO_3$ and $KNbO_3$) the structural instabilities still have an impact on the mechanical stability of the grain boundary regions which will lead to the formation of an intergrowth of Magnéli and Ruddlesden-Popper phases at the surfaces(157).

2.8 Summary

In summary of the previous literatures, the unique layered-perovskite type oxide, $BaNdInO_4$, and its solid solutions have exhibited considerably high oxide-ion conductivities. The oxide-ion conductivity of the parent $BaNdInO_4$ can be significantly increased by acceptor doping of the Nd site with alkaline-earth metal cations such as Ca, Sr and Ba, while the activation energy for the ionic conduction in these materials can be decreased. Ca^{2+}, the ionic radii of which is the closest to that of Nd^{3+}, is the optimal doping cation at the Nd site as the composition of $BaNd_{0.8}Ca_{0.2}InO_{3.9}$ exhibited highest oxide-ion conductivity and lowest activation energy for the oxide-ion conduction. The investigation of oxygen migration in the $BaNdInO_4$ related structure using the bond valence (BVE) method and the molecular dynamics (MD) simulation gave a profound insight of how an oxygen vacancy migrates in the lattice. Both BVE and MD simulation results suggested a two-dimensional oxide-ion migration mechanism in the A rare earth oxide unit on the *bc* plane in the $BaNdInO_4$ related structure. The oxygen diffusion coefficients were estimated by the mean square displacement (MSD) values of O1, O3 and O4 obtained in the MD simulation, which is in the range of 10^{-6}-10^{-7} cm^2/s. However, there is no direct empirical data of the oxygen diffusion coefficients of these materials, which remains a research gap in this field.

The sections 2.4-2.7 included literature reviews on protonic conductivity observed in the perovskite-related structural systems and the underlying protonic conduction mechanism proposed. The most commonly accepted theory regarding the proton conducting mechanism is the Grotthuss-type mechanism which suggests that the protons are the mobile species. However, all the discussions about the charge carriers and how they move around in a particular system are based on simulation results. Very little direct experimental evidence could be found in the previous literatures that could prove these theories. On the other hand, finding a proper solid solution for the intermediate temperature SOFC applications is still challenging. Protonic conductors are one of the candidates to be used as the electrolyte materials, which could lower the operating temperature of the existing high temperature SOFC products. But empirically high thermodynamic stability and high proton conductivity seem to exclude one another. Therefore, it is worth trying to design and synthesize a new structure family for further innovative development of the SOFC industry.

There has been no literature published so far regarding the protonic conduction in the acceptor-doped $BaNdInO_4$ system, which could be an interesting point as the acceptor doping could create oxygen vacancies and a variety of perovskites have been proved to be good protonic conductors(132, 158, 159). Those gaps elicit the main motivation of this project. The main purpose of this research is further developing the $BaNdInO_4$-based solid solutions and investigating the potential of the calcium-doped $BaNdInO_4$ being used as a proton conductor. The isotope exchange depth profiling (IEDP) method will be introduced to measure the oxygen diffusion coefficients and surface exchange coefficients of those materials and give direct experimental data to be compared with the results from the former statistical simulations.

Chapter 3

Experimental methods

3.1 Solid state reaction

In a traditional solid state reaction process, stoichiometric amounts of the precursors (in most of the cases metal oxides or carbonates) are mixed using pestle and mortar with volatile organic solvent, such as ethanol and acetone, to improve the mixing of powders. Then the dried mixture is calcined at a certain temperature and atmospheric condition depending on the decomposition conditions for the carbonates or other substance in the precursors. In order to achieve a pure single-phased product, the resulting ashes from the calcination step are then pressed into pellets and sintered at a higher temperature to let the precursors react with each other. The pressing and sintering steps are usually repeated twice to let the oxides react with each other completely. There are advantages and disadvantages of applying the solid state reaction methods. The main advantage of this approach is because of its straight forward and relatively simple processes with a short synthesis period. The drawbacks of this approach include the difficulties in the weighing steps to mix precursors with exactly stoichiometric ratio, which might lead to secondary phases caused by the excess precursors or non-stoichiometric products. Secondly, this approach can be only applied to synthesis using metal oxides and carbonates, while some metals, such as Pr, don’t have stable carbonate precursors. Therefore, solid state reaction method is not applicable to the synthesis of materials containing those cations. Last but not least, the mixing with pestle and mortar in a solid state reaction can only achieve mixture at the particle level. To achieve atomic level mixing, a sol-gel synthesis approach should be applied.

3.2 Pressing and the densification process

In order to achieve dense pellet samples with relative density over 95%, before the sintering processes, the powders were firstly pressed in a 13 mm circular die under a load of 2-3 tons holding for 5 mins using a uniaxial press. The resulting pellets were then placed in one finger of the nitrile glove sealed by a portable vacuum pump followed by a 5-mins isostatic press process at ~ 300 MPa to achieve high density. Then the densified pellet samples were removed from the glove and placed in an alumina crucible for a sintering process. The sample was covered by the residual powders on both surfaces to avoid the over-reacting of the sample on the top surface and prevent the reaction with alumina crucible on the bottom. The pellet was finally sintered in a set temperature program with the heating and cooling rate of 5 ℃/min in lab air in a furnace. The temperature program involved a heating step to 1400℃ with a holding step of 1 hour and the first cooling step down to 1300℃ followed by a 24 hours holding step, then another cooling step down to room temperature. The one hour holding step at 1400℃ allows a fast densification of the pellet and the following long period sintering procedure at 1300℃ enables the growth of grains and the full densification of the pellet as the pores between the grains were eliminated. Besides, the relatively lower sintering at 1300 ℃ could effectively avoid overheating the sample surface which might introduce secondary phases into the material.

3.3 Dilatometry test

The determination of the sintering temperature for $BaNdInO_4$ and its solid solution in this research was done by dilatometry, which is a straight forward material characterisation method for measuring the changes in the dimensions of a solid specimen as a function of temperature. As shown in the schematic (Figure 3.1), the specimen is placed in the sample carrier clamped by the alumina pushrod. As the temperature in the furnace rises, the changes in the length of the specimen are detected by a displacement transducer (LVDT). The gas atmosphere can be controlled by the vacuum flange and purge gas inlet and outlet. The displacement along with the temperature regime is recorded by the connecting computer. Compared with other thermal analysis techniques, dilatometry is the most straight forward method to achieve the thermal expansion coefficient of a solid sample. The coefficient of thermal expansion, α, can be derived from the equation below:

$$\alpha(T) = -\frac{\partial L}{\partial T} \tag{48}$$

where L is the length of the specimen and T is the temperature.

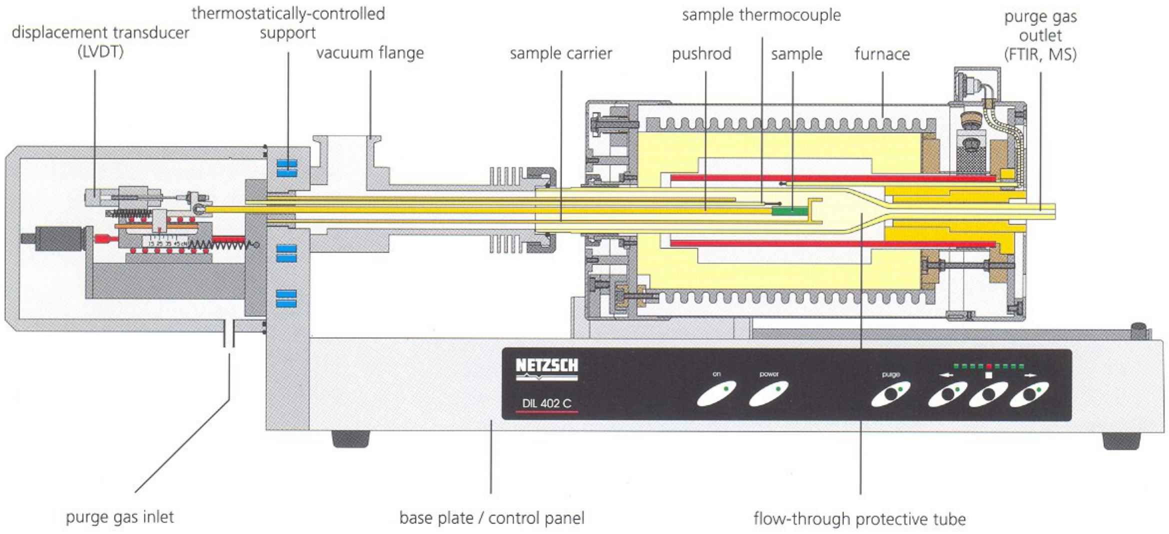

Figure 3.1 A Schematic diagram of a NETZSCH® dilatometry equipment. Adapted with permission from (160).

In order to achieve the best sintering temperature for $BaNdInO_4$ and its solid solutions, a strip-shaped specimen was prepared which had not been sintered. The temperature regime of the dilatometry measurement was set as two segments. In the first segment, the furnace was heated up from room temperature to 1370℃ at a heating rate of 10 ℃/min. Then the temperature was held at 1370℃ for two hours to monitor the sintering behaviour of the specimen.

3.4 Density measurement

The density of the pellets was measured by the Archimedes method with water using a water balance. The theoretical density ρ_{theory} of the material can be calculated according to Equation 47, where the parameter of a unit cell could be substituted. Then n is the number of formula units per unit cell, M_w is the molecular mass of all the atoms in a unit cell, V is the unit cell volume obtained from XRD data refinements and N_A is the Avogadro number.

$$\rho_{\text{theory}} = \frac{nM_{\text{w}}}{N_{\text{A}}V} \tag{49}$$

The Archimedes method is basically a solution linking the buoyancy of a solid immersed in a liquid with the density of the liquid ρ(fl). By measuring the weight of sample in air W(a) and the weight in liquid W(fl) using the electrical water balance below, the buoyancy is given by W(a)-W(fl) and, to allow for buoyancy of sample in the air, corrections are made regarding the density of air ρ(a)=0.0012 g·cm^{-3} under standard conditions. The density of the sample then can be derived by the equation (50), where the density of the water ρ(fl) can be obtained from the standard tables(161) according to the temperature of the water during the measurement:

$$\rho = \frac{W(\text{a})[\rho(\text{fl}) - \rho(\text{a})]}{\rho(\text{fl})[W(\text{a}) - W(\text{fl})]} + \rho(\text{a}) \tag{50}$$

In this research, sintered samples were polished by SiC grinding paper first, then measured in air and in water step by step. To avoid air bubbles inside the pellet which might contribute to an increased buoyancy in the following measurement, the sample after polishing was immersed in boiling water for 10 mins to eliminate the air bubbles attached on the pellet sample when being immersed into the water balance.

3.5 X-ray diffraction and the crystal structure analysis

The crystal structure and phase purity of the synthesized pellet samples were analysed by X-ray diffraction (XRD) and *in-situ* XRD methods. Le Bail refinement of the diffraction data was carried out using the FullProf program(162) for determination of the space groups, lattice parameters and unit cell volumes of the materials.

3.5.1 X-ray diffraction and Le Bail refinement

X-ray diffraction is a commonly used non-destructive material characterisation method for the determination of the crystal structure of crystalline materials. By applying X-rays from an angle onto the sample surface, the X-rays with a wavelength which is close to the spacing between layers or rows of atoms within the crystalline materials can be scattered, which is then collected by a radiation detector providing information on the unit cell dimensions. Constructive interference is governed by wavelength and separation of the points, and in X-ray diffraction, the arrangement of the atoms near the sample surface can be treated as diffraction grating. Bragg's Rule(163) as expressed as Equation (51), is used to determine the conditions under which X-ray diffraction could occur, where d represents the interplanar spacing, θ is the angle of incidence with respect to the scattering planes and λ is the wavelength.

$$2d\sin\theta = n\lambda \tag{51}$$

The X-rays are generated by bombarding a metal target, Cu in most cases, with high energy electrons. The bombardment results in the ejection of the inner shell electron of the metal atoms leaving the atom in an energetically excited state. The characteristic X-rays are then released as an electron of higher energy drops into the vacancy emitting the excess energy in the form of an X-ray photon. K_α radiation is one of the X-ray sources which is created by an electron transition from a 2p orbital of the second outermost L shell to the innermost K shell (1s orbital), and occurs as a doublet owing to spin-orbital interactions. At the same time, the incident electrons decelerate as they plunge into the metal, generating radiation with a continuous range of wavelengths, which is called the Bremsstrahlung radiation.

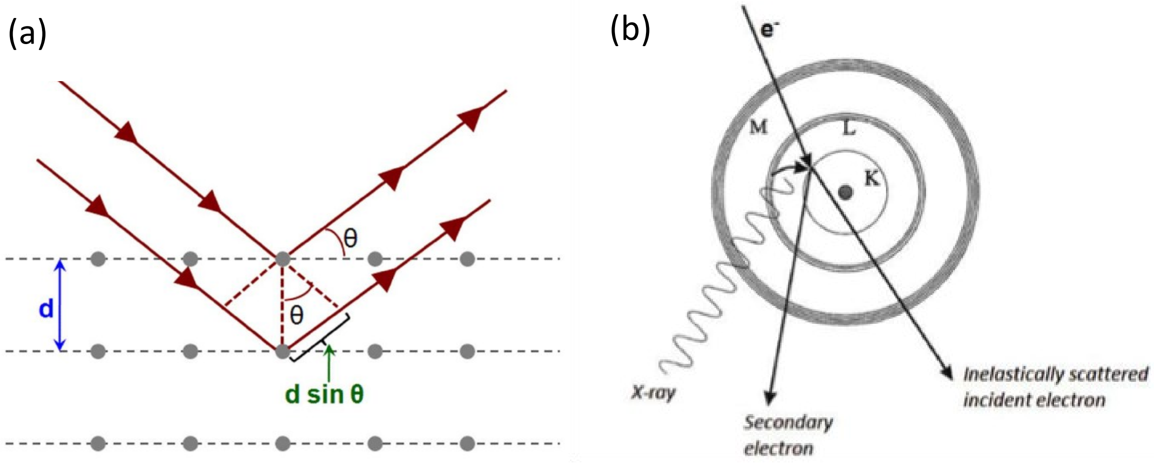

Figure 3.2 (a) Schematic illustration of Bragg’s Law. The blue arrow labels the d-spacing between two planes. The red arrows shows the direction of X-rays. θ labels the incident angle. $d\sin\theta$ in green mark labels the path difference of the diffracted X-rays (b) Schematic diagram of the generation of characteristic X-rays. Adapt with kind permission from (164).

The characteristic X-rays are directed to the sample through the slits set and diffracted by the crystalline materials in the sample according to Bragg’s Law. As the diffracted X-rays go through the slits and are collected by the detector, the constructive interference when $n\lambda = 2d\sin\theta$ is recorded as peaks in the XRD pattern. The angle at which reflections can occur is determined by the lattice symmetry and unit cell parameters, where the interplanar spacing d_{hkl} is related to the unit cell parameters, as illustrated in Equation (52), where *h, k, l* are Miller indices describing a set of parallel planes in the lattice.

$$\frac{1}{d_{\mathrm{hkl}}^2} = \frac{h^2 + k^2 + l^2}{a^2} \text{(for the case of a cubic structure)} \tag{52}$$

$$a^2 = \frac{\lambda^2}{4\sin^2\theta}(h^2 + k^2 + l^2) \tag{53}$$

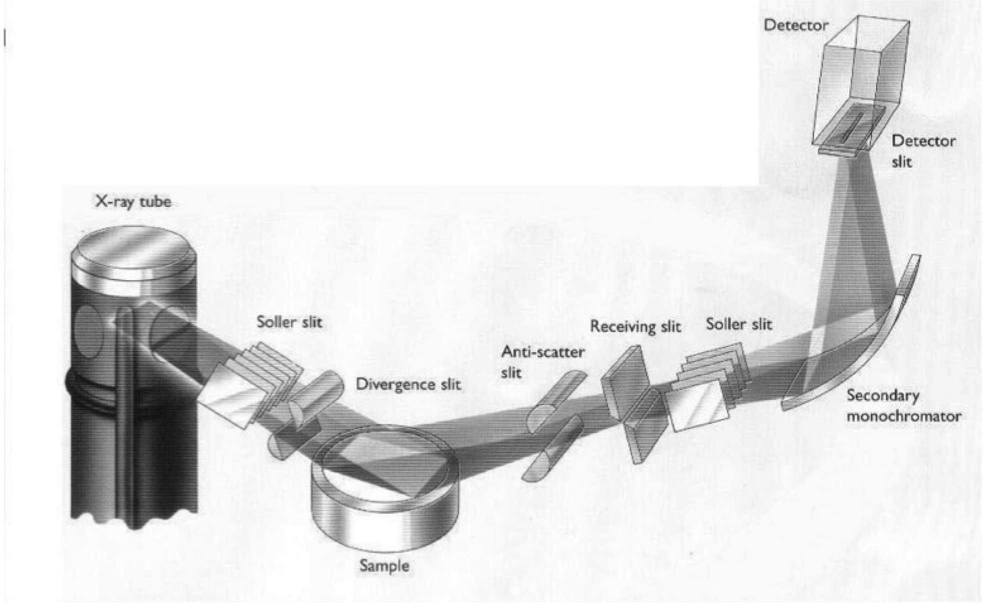

Figure 3.3 Schematic representation of a powder diffractometer. Adapted with permission from (164)

The peak position as discussed above is determined by the lattice symmetry and unit cell parameters according to Bragg's Law. The observed peak intensity of the reflection, however, is a function of several factors which depend on a set of parameters regarding the experimental set-up and the elemental properties concerning the chemical composition of the materials being analysed. For an ideal powder diffraction sample, the intensity of a particular peak is determined by several factors:

$$I(hkl) = cL(2\theta)P(2\theta)A(2\theta)j_{\mathrm{hkl}}|F(hkl)|^2 \tag{54}$$

where $I(hkl)$ is the intensity of the $\{hkl\}$ reflections. *c* is the scale factor. $L(2\theta)$ is the Lorentz factor which control X-ray intensity with respect to diffraction angle. $P(2\theta)$ is the polarisation factor which allows for the partial polarisation of the reflected beam and the geometry of the measuremnt, $A(2\theta)$ represents the X-ray mass absorption factor and j_{hkl} is the multiplicity factor which describes the relative proportion of planes contributing to the same reflection. The structure factor, $F(hkl)$, represents the summation of the scattering from *hkl* planes in the direction θ from all the atoms in unit cell. Assuming that the unit cell contains *N* atoms and the j^{th} atom with the fractional unit cell coordinates (x_j, y_j, z_j) has a scattering factor $f_j(hkl)$, then the structure factor can be derived as:

$$F_{hkl} = \sum_{j=1}^{N} f_j(hkl)\,\exp 2\pi i(hx_j + ky_j + lz_j)\,\exp\,(-W_j) \tag{55}$$

where the scattering factor $f_j(hkl)$ of an atom is the total amount of scattering in direction θ from that atom, W_j is Debye-Waller factor depending of the temperature, which describes the atomic displacement of the j^{th} atom.

As illustrated in Fig 3.3, in practice, a normal powder diffraction experiment is carried out by varying the position of the X-ray source relative to the detector, and the diffraction patterns are produced by measuring the intensity detected as a function of 2θ. The characteristic X-rays generated from a Cu target in the X-ray tube contain three main wavelengths, Cu-$K_{\alpha1}$ (λ=1.5405 Å), Cu-$K_{\alpha2}$ (λ=1.5444 Å) and Cu-K_{β} (λ=1.3922 Å), hence a monochromator was used to filter the Cu-K_{β} component.

X-ray diffraction characterisation method was carried out on pellet samples in this work. The crystal structure of the formed phase in the $BaNd_{1-x}Ca_xInO_{4-x/2}$ solid solution series was determined in static air by X-ray diffraction (XRD) using a PANalytical X'Pert PRO diffractometer (Cu K_{α} radiation). XRD patterns were typically obtained between 10 to 100 °2θ with a step size of 0.0167 °2θ.

3.5.2 *In-situ* X-ray diffraction

An Anton Paar HTK1200N oven with z axis adjustment was used to control the sample temperature to obtain *in-situ* XRD (HT-XRD) patterns. The addition of an oven allows diffractograms to be collected under various conditions regarding the temperature and gas atmospheres, which is useful in identifying the chemical/structural changes of a material upon heating. During the measurement, the X-ray window, being made of Kapton, Graphite, PEEK or Beryllium in most cases, of the heating attachment allows the X-ray beam to pass the instrument. The in-situ XRD used in this research is equipped with a Beryllium X-ray window. In the centre of the instrument the alumina (or silicon single crystal) sample holder is located and the temperature sensor is mounted inside the sample holder. The sample holder height during the measurement is automatically adjusted at different temperatures to compensate the thermal expansion of the holder itself.

The main disadvantage of utilizing this characterisation method on the pellet samples is the influence of sample thickness on the temperature deviation, where a thin pellet sample preparation is recommended.

In an *in-situ* X-ray diffraction measurement, the effect of material expansion upon heating has to be accounted as otherwise the sample location is not always at the centre of the goniometer resulting in severe peak shifts. As shown in Figure 3.4(b), to keep the sample at the prealigned position at elevated temperatures, the height of the instrument is adjusted either manually on the adapter of the instrument or by using the Z-stage for automatic adjustment of the instrument.

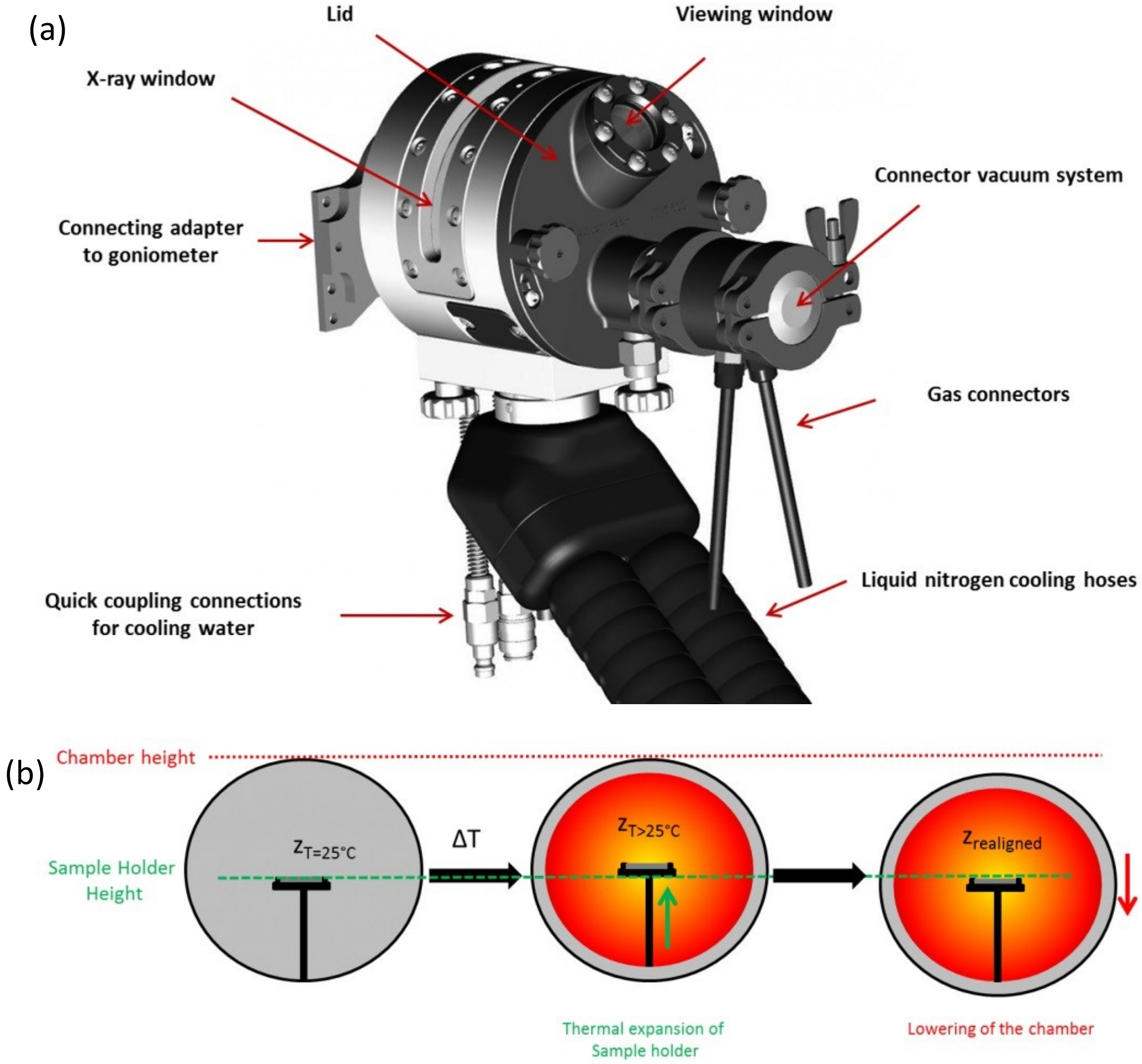

Figure 3.4 (a) Principal components of a non-ambient heating attachment used in *in-situ* X-ray diffraction method. (b) Schematic diagram of thermal height expansion correction with Z-stage. The red dotted line shows the chamber height and the green dashed line shows the sample holder heright. Adapted with permission from (165).

3.5.3 Le Bail refinement

Le bail refinement is a quantitative analysing approach for the X-ray diffraction data. In this type of analysis, the structure factor as expressed in Equation (55) and associated structural parameters is not necessary since they are not considered and the unit cell and the approximate space group of the sample must be predetermined. Linear interpolation of the selected background points was applied to exclude the background intensity. A Pseudo-Voigt peak shape function was used to fit the diffraction peaks' shape. A least squares analysis was carried out to minimise the difference between the observed intensities, Y_{obs}, and the calculated intensities, Y_{calc}, by modifying the lattice parameters. The calculation and fitting was performed using the FullProf(166) software suite. The goodness of fit is defined as χ^2 or as the profile residual, R_{p}, and weighted profile residual, R_{wp}, which can be calculated from the equations below,

$$\chi^2 = \frac{\sum_{i=1}^{n} \omega_i (Y_{\mathrm{obs}} - Y_{\mathrm{calc}})^2}{n - p} \tag{56}$$

$$R_{\mathrm{p}} = \frac{\sum_{i=1}^{n} |Y_{\mathrm{obs}} - Y_{\mathrm{calc}}|}{\sum_{i=1}^{n} Y_{\mathrm{obs}}} \times 100\% \tag{57}$$

$$R_{\mathrm{wp}} = \sqrt{\frac{\sum_{i=1}^{n} \omega_i (Y_{\mathrm{obs}} - Y_{\mathrm{calc}})^2}{\sum_{i=1}^{n} \omega_i Y_{\mathrm{obs}}^2}} \times 100\% \tag{58}$$

where ω_i is the weighted factor for the i^{th} intensity, n is the total number of points from the experiment and p is the total number of variables refined. It is worth mentioning that the somewhat arbitrary choice of starting values will produce a bias in the calculated values of Le Bail refinements. Therefore, in this research, the input starting lattice parameters were selected based on the refined results from the neutron diffraction data reported by Fujii *et al(115)*.

3.6 Electron microscopy

Electron microscopy (EM) is a technique using a focused electron beam to probe the surface topography of a specimen sample. The electrons in the beam interact with the sample producing various signals, as shown in Figure 3.5, that can be used to obtain information about the surface topography and chemical composition. According to the Rayleigh criterion, the minimum resolvable detail in the imaging process is limited by diffraction and proportional to the wavelength, λ, of the source(167). Therefore, high resolutions can be achieved in the electron microscopy as it directs a beam of high energy accelerated electrons to the surface, for example an electron with energy around 20 keV has a wavelength of around 0.012 nm which is significantly lower than that of visible light (400-700 nm).

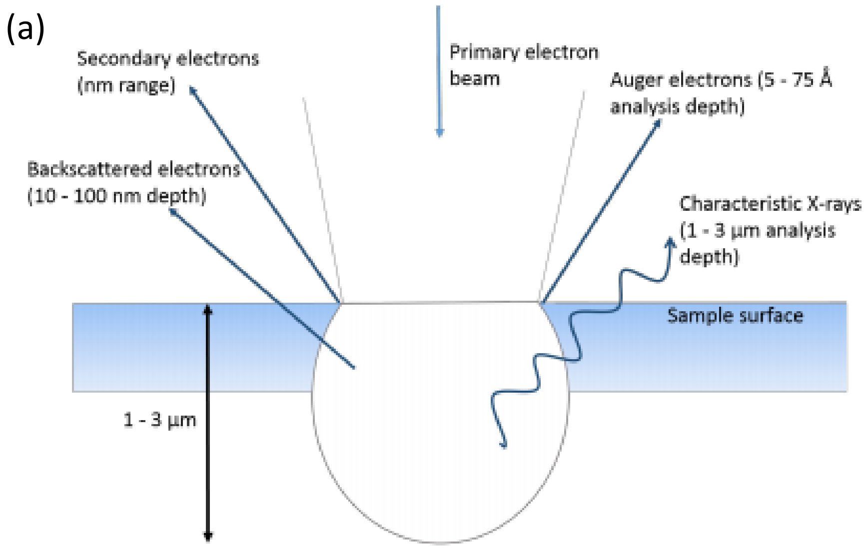

Figure 3.5 Representation of the main electron interactions occurring when a primary electron beam interacts with a sample under analysis in an electron microscopy equipment. Adapted with permission from (168).

3.6.1 Scanning electron microscopy

Scanning electron microscopy (SEM) is the most commonly used electron microscopy technique in which the data are collected over a selected area of the sample surface to generate a 2-dimensional image of the sample. The signals detected in an SEM measurement result from interactions of the primary electrons contained in the electron beam with atoms at various depths within the sample surface. Different types of signals are produced during the electron beam bombardment, such as secondary electrons (SE), the reflected or back-scattered electrons (BSE), characteristic X-rays, light produced by cathodoluminescence and Auger electrons.

Secondary electrons (SE) have very low energies on the order of 50 eV, which are produced when electrons from the conduction band of the sample interact with the incident electrons, when the interaction provides enough energy for their ejection. SEs are emitted only from the very surface of the sample, typically 5 to 50 nm. As the angle of incidence increases, the incident electrons travel deeper into the surface region of the sample, which results in a higher apparent ejection of SEs in these areas. Therefore, the edges and ridges of the sample usually seem brighter in SEM images due to the ejection of more SEs. By collecting the ejected second electrons, one can obtain topographical information of the sample surface.

Backscattered electrons (BSE) are electrons that are reflected from the sample surface by elastic scattering. BSEs have much higher energy than SEs which can be emitted from depth of 10-100 nm. With a much larger interaction volume, the resolution of a BSE image is lower than that of an SE image. However, BSEs are often used in the determination of elemental distribution of the sample because the intensity of the BSE signal is strongly related to the atomic number (Z). Characteristic X-rays are emitted when a higher-energy electron fills the inner shell vacancy caused by primary electron bombardment, the process of which releases energies depending on the orbital energy of the atoms. The energy or wavelength of these characteristic X-rays can be measured by Energy-dispersive X-ray spectroscopy or Wavelength-dispersive X-ray spectroscopy giving information on the elemental abundance in the sample. The generation of Auger electrons is similar to that of characteristic X-rays, when an inner-shell vacancy of an atom is filled by a higher energy electron from the same atom. Most of the energy of this process was released in the form of photons, while the energy can also be transferred to another electron which is ejected from the atom and is called an Auger electron((169)).

During this work, a JSM-6010 LA SEM (JEOL Ltd.) and a Zeiss Crossbeam 340 (Zeiss Ltd.) were the main analytical SEM instruments applied in probing the material topographic information and compositional analysis. The beam conditions and other parameters of the measurement will be illustrated specifically in the SEM images.

3.6.2 (Scanning) Transmission electron microscopy

Transmission electron microscopy (TEM) is a microscopy technique in which a beam of highly accelerated electrons (200 to 300 keV) is transmitted through a specimen to form an image(170). Therefore, the sample with a thickness less than 50 nm needs to be specifically prepared to allow the electrons to pass through it without a significant energy loss. The principal of the TEM technique in detail can be reached in the textbook written by Goodhew *et al*.(171) which will not be discussed in this thesis.

The TEM can be operated in two modes: normal TEM and scanning-TEM modes. The main difference between TEM and STEM is that instead of a parallel incident electron beam incident on the sample in TEM mode, a converged beam focused at a spot is directed on the specimen surface. To create a map of the sample surface, the incident beam is rastering across the sample surface and the signal from each point is recorded on an annular detector. Therefore, in the equipment set-up of the STEM measurement, no objective lens is needed for imaging the sample, and the achievable magnification is theoretically unlimited(172). In this research, the scanning TEM mode was used to probe the chemical compositional information with a high resolution, where STEM-EDS, in particular, was used.

The energy dispersive X-ray spectroscopy (EDS) is a chemical microanalysis technique which can be used in conjunction with scanning transmission electron microscopy (STEM). When the sample is bombarded by the STEM electron beam, electrons are ejected from the atoms comprising the sample surface. The resulting electron vacancies are filled by higher energy electrons form outer orbitals, and an X-ray is emitted to compensate the energy difference between two different electron orbitals. The released X-ray is characteristic of the element from which it was emitted. By detecting the X-rays emitted from the sample during the bombardment of the incident electron beam, the EDS technique is useful in the characterisation of the elemental composition of the analysed volume in the specimen.

Sample preparation in TEM is the crucial step since the target sample must be electron-transparent for TEM measurement. That is to say, the thickness of the target sample needs to be 10-300 nm depending on the material. The preparation of thin samples were finished by focused ion beam (FIB) milling using H-bar with a direct lift-out method as shown in Figure 3.6. The sample preparation using ‘H bar’ method is comprising procedures including Platinum deposition at the site of interest for protection, milling of a thin strip using FIB, lifting out the strip by a fine glass micro-manipulator, the attachment of the strip onto a support grid by platinum paste and the final milling using FIB to achieve electron transparency. The sample preparation methods for TEM measurement is discussed in detail by Li *et al*.(173) where several other sample preparation methods were included.

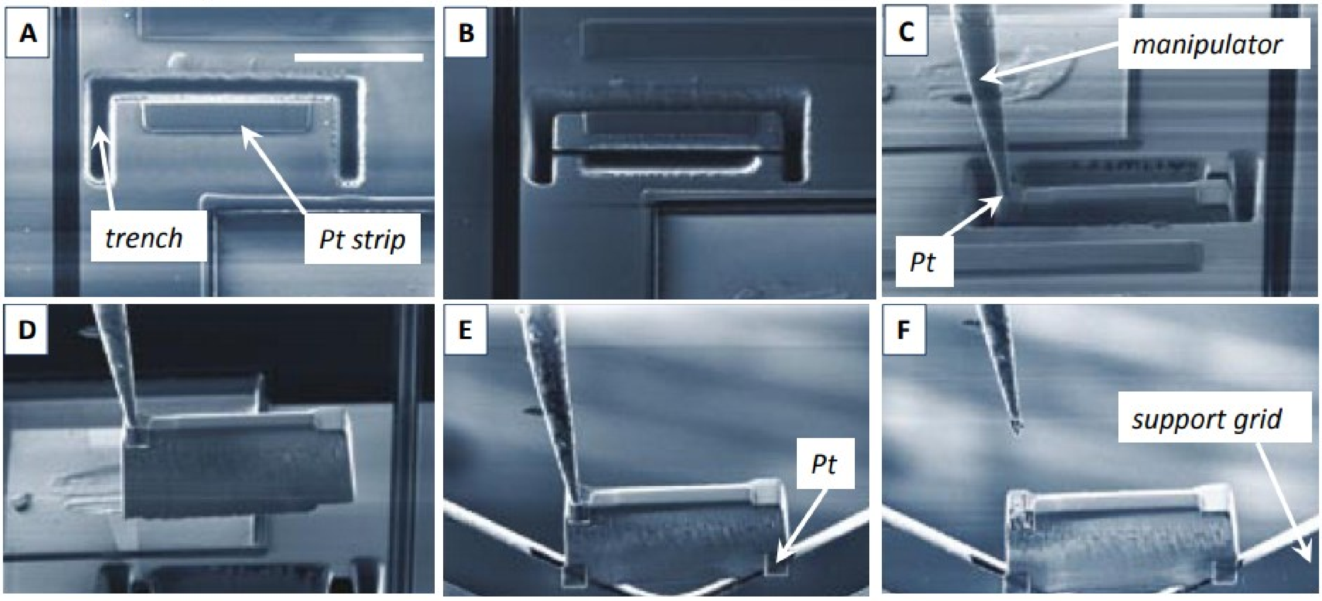

Figure 3.6 The illustration of sample preparation process in a FIB milling method using 'H bar' method. Adapted with permission from (174).

Experimental detail: In this work, STEM-EDS analyses were carried out on the exchanged specimens using a TEM 2100F operated in STEM mode under 200 keV accelerating voltage by Dr. Cati Ware. Aztec software was used in the STEM-EDS measurement to obtain the distribution of elements within the scanned area of the sample.

3.7 Electrical property analysis

4-point DC conductivity measurements and electrochemical impedance spectroscopy (EIS) are the major techniques in this work to investigate the electrical properties of the materials, while the 4-point dc conductivity measurement was specifically carried out in the lab of Centro Atomico of Bariloche using a unique system coupling with a symmetrical thermogravimetric analysis system.

3.7.1 Four-probe DC conductivity measurement

4-probe method is the most common technique used for measuring sheet resistance. The technique involves using four equally-placed, co-linear probes, normally made of platinum, to make electrical contacts with the material. In this research, the platinum wires were used as the probe, which were stuck onto the sample by applying platinum paste followed by a high temperature annealing treatment. The 4-probe dc measurement is implemented to mitigate the electrode effects. As a current is applied from the two outer electrodes, a voltage drop will be measured. The resistance of the inner strip sample is then calculated using Ohm's law and the conductivity can be obtained by Equation (59).

$$\sigma = \frac{L}{RA} \tag{59}$$

where L and A is the length between the two inner electrodes and the cross-section area of the bar sample, respectively.

The conductivity measurement of samples was performed under various gas atmospheres in a sealed system. The unique coupling system will be introduced in detail in the following section.

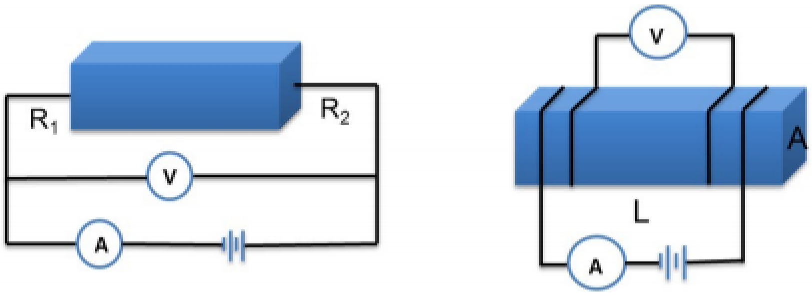

Figure 3.7 Schematics of the (left) two-point and (right) four-probe DC measurement.

3.7.2 Electrochemical Impedance Spectroscopy (EIS)

Electrochemical impedance spectroscopy is a powerful *in-situ* characterisation technique whereby the individual contributions from different responses within the material can be distinguished. Compared with the dc conductivity methods, a small sinusoidal perturbation of AC voltage with constant magnitude (V_0) and various frequencies (ω) is introduced and the resulting current with magnitude (I_0) and phase shift (φ) is recorded(175). The impedance of a specific process measured can be derived by Equation. 60(175). It is worth noting that if the magnitude of impedance $|Z|$ equals to the ratio of V_0 and I_0, the expression of impedance Z can be written as Equation (61), where *Z'* and *Z''* represent the real and imaginary parts of the impedance.

$$Z(\omega) = \frac{V(\omega)}{I(\omega)} = \frac{V_0 e^{i\omega t}}{I_0 e^{i(\omega t+\varphi)}} = \frac{V_0}{I_0}(\cos\varphi - i\sin\varphi) \tag{60}$$

$$Z(\omega) = Z' + iZ'' \tag{61}$$

The different processes occurring in the material can be characterized according to their specific electrical relaxation times in response to the AC voltage supply. The time constant, τ, which also can be referred to as relaxation time, is given by Equation (62), where $\omega_{\max}$ is the angular frequency at which the tested system experiences the maximum loss and *R, C* represent the resistance and capacitance of the testing process, respectively.

$$\tau = \frac{1}{\omega_{\max}} = RC \tag{62}$$

In general, the result of an EIS measurement can be either presented in a complex plot called Nyquist plot, where the real impedance *Z'* is plotted against the imaginary part *Z''*, or in a Bode plot where the magnitude of impedance $|Z|$ or phase shift (φ) is plotted against frequency. A typical Nyquist plot and two different Bode plots are illustrated below. The representing Nyquist plot is composed of two semi-circles corresponding to two different processes occurring in the sample. The impedance data in this work was analysed using ZView® software where an equivalent circuit is used to simulate the process and the data were fitted by the complex non-linear least squares approach. A normal semi-circle as the first semi-circle appears at higher frequency in the representitive Nyquist plot (Figure 3.8 (a)) can be simulated by a resistor and a capacitor connected in parallel, while during fitting of the depressed semi-circle, a constant phase element (CPE) is introduced. The physical meaning of the constant phase elements (CPE) is still under debate(176-178). However, in determining the resistances of the bulk and grain boundary responses only without discussion of the complicated processes, such as gas diffusion and interlayer response, simulating with CPE is a convenient approach when analysing impedance data. The capacitance, *C*, of a process analysed using R-CPE circuits can be derived from Equation (63), where *CPE(T)* and *CPE(P)* are the two main parameters fitted.

$$C = \frac{[R \times CPE(T)]^{\frac{1}{CPE(P)}}}{R} \tag{63}$$

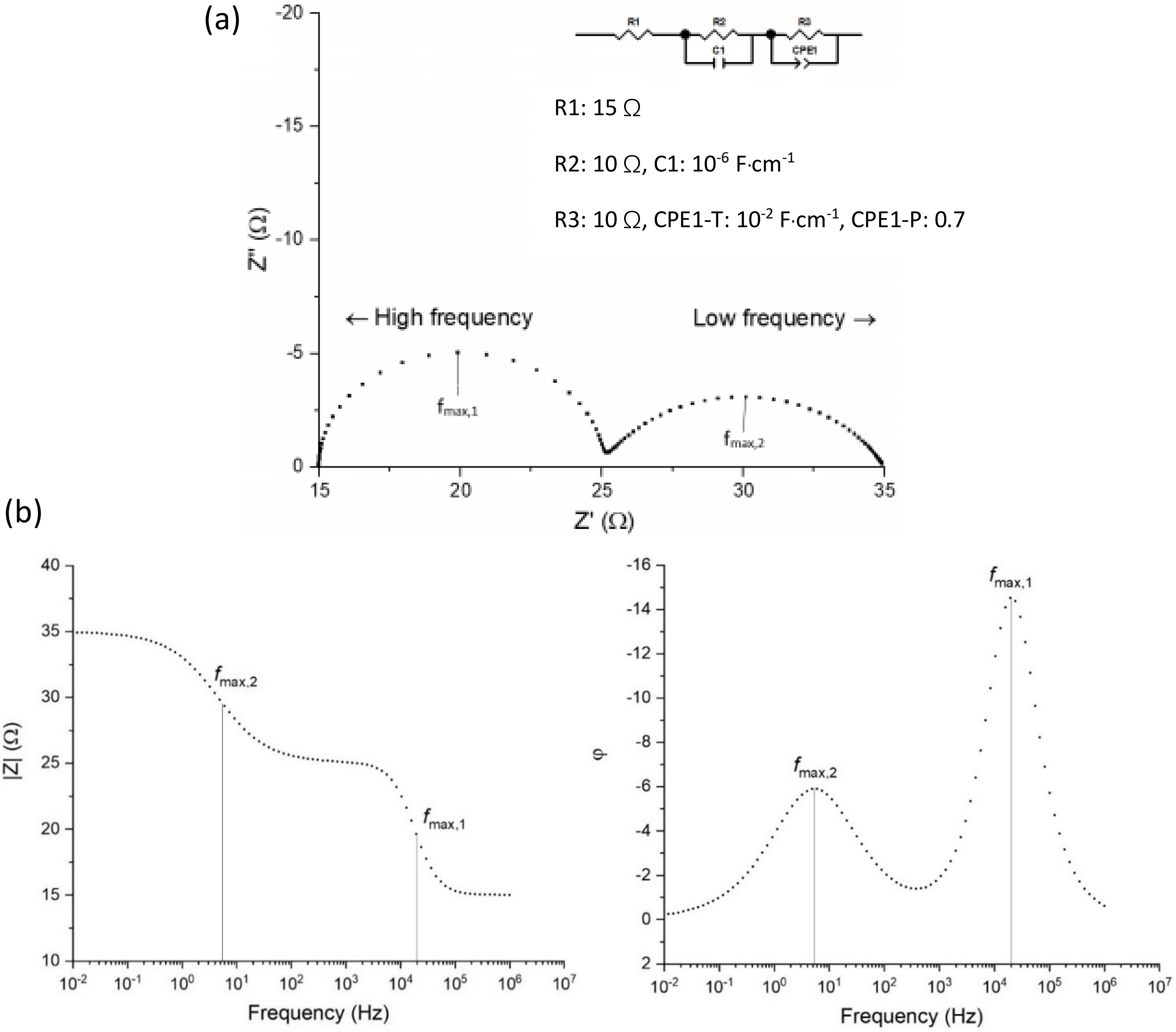

Figure 3.8 Illustration of (a) a typical Nyquist plot with one high frequency semi-circle and one depressed semi-circle, and (b) two corresponding Bode plots. Reproduced from (175) with permission from Electrochemical Society.

The orders of magnitude of the capacitances and their possible corresponding interpretations are listed in Table 3.1 below.

Table 3.1 Capacitance values and their possible interpretation for a material with unit cell constant (i.e. l/A=1 cm^{-1}) and a typical permittivity, e_0, of ~10. (C=ε' e_0 l/A, where ε' is the permittivity of the medium). Adapted with permission from(179).

Capacitance/F·cm^{-1}	Phenomenon Responsible
$\mathbf{10^{-12}}$	Bulk
$\mathbf{10^{-11}}$	Minor, second phase
$\mathbf{10^{-11} - 10^{-8}}$	Grain boundary
$\mathbf{10^{-10} - 10^{-9}}$	Bulk ferroelectric
$\mathbf{10^{-9} - 10^{-7}}$	Surface layer
$\mathbf{10^{-7} - 10^{-5}}$	Sample-electrode interface
$\mathbf{10^{-4}}$	Electrochemical reactions

Instrumentation and experimental set-up: The impedance set up used in this research is a home-made apparatus which is composed of a movable outer alumina tube, a fixed inner pole, thermocouple and platinum wires for connection, as shown in Figure 3.9. During the impedance measurement, the pellet sample was coated on both surface with platinum paste constructing a symmetrical cell, which is sandwiched by two platinum meshes placed in the alumina tubes. The thermocouple is located close to the sample. A computer-controlled furnace was used for *in-situ* measurements. Electrochemical impedance spectroscopy (EIS) measurements in this research were carried out with a Solartron Analytical 1260 frequency response analyser (Solartron, UK) over a frequency range from 10^7 to 10^{-1} Hz. The pellet samples were coated with platinum paste on the opposite faces, and then annealed at 800 °C for 2 hrs in order to dry the platinum paste and ensure good adhesion between the sample surface and the platinum electrodes. Each sample was tested in a thermal cycle comprising a heating program with a heating rate of 5 °C/min to each temperature, starting from 250 °C, followed by 60 mins thermal equilibration, with step sizes of 25 °C until a maximum temperature of 750 °C was reached. This was followed with a cooling programme with the same steps and ramp rates to probe if there was any hysteresis in the material. The whole apparatus was sealed during the measurements while the flow of compressed air or nitrogen was introduced through a drying tube containing $CaSO_4$ before entering the impedance rig to create dry atmospheres. A water bubbler was connected into the system between the gas cylinder and the impedance rig to examine the influence of water vapour on the electrochemical properties of the materials. With this set-up it was possible to measure the same sample, first in the dry atmosphere and then in the wet atmosphere. Before the impedance spectroscopy measurement in the humid atmosphere, the sample was annealed in humid gas at 500 °C overnight to ensure that the equilibrium of the water incorporation was achieved. The impedance data were analysed using the ZView (180) software package.

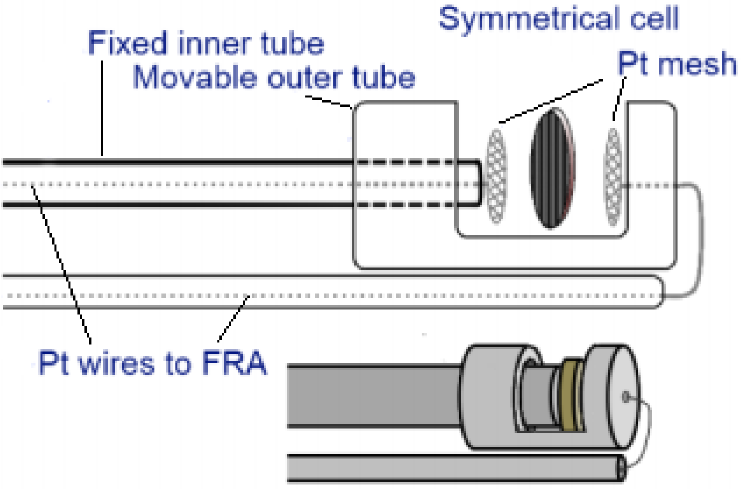

Figure 3.9 Schematic diagram of the AC impedance apparatus. Image adapted with permission from (181).

3.7.3 Symmetrical thermogravimetric analysis and DC conductivity measurement

Thermogravimetric analysis (TGA) on the water uptake of the BNC20 sample under a humid atmosphere was conducted using the unique equipment developed by Caneiro *et al.*(182). This equipment couples a symmetrical thermogravimetric analysis system based on a Cahn 1000 electrobalance to an electrochemical system for $P(O_2)$ regulation. The internal environment of the apparatus was precisely controlled so that the TGA measurement had a sensitivity of 0.5 µg and noise of 5 µg peak to peak(182).

Thermogravimetric system: The measurement of weight changes in the scale of micrograms is carried out with a symmetric design as shown in Figure 3.10, the design was conceived to considerably reduce the influences of buoyancy, radiometric effects, thermomolecular flow effect (TMF) and gas flow effects when recording the weight of the test sample(182). A Cahn 1000 electrobalance with a sensitivity of 0.5 µg was used to record the weight changes of the sample. The sample was located in an alumina crucible which hangs from one of the arms of the balance with a Pt-30% Rh wire, while the other arm of the balance is connected to a reference alumina crucible containing some inert materials of roughly equal volume with the testing sample. Two separated identical quartz tubes, one for each arm, were placed in the middle of a furnace, which was designed to reduce the effect of aerodynamic forces on the crucible with a blocking tube fixed right after the alumina crucible. By using that blocking tube, the linear velocity of the oxygen controlled atmosphere in the zone of the furnace where higher gradients of temperature exists is increased. The outer surface of the quartz tubes are painted with platinum paste in a length of 10 cm and then electrically grounded in order to eliminate electrostatic forces(182). In order to stabilize the temperature during measurements, a bell jar made of stainless-steel was used which is connected to a flowing water bath. The weighing unit, thus, can be thermalized at 25±0.1℃ at room temperature.

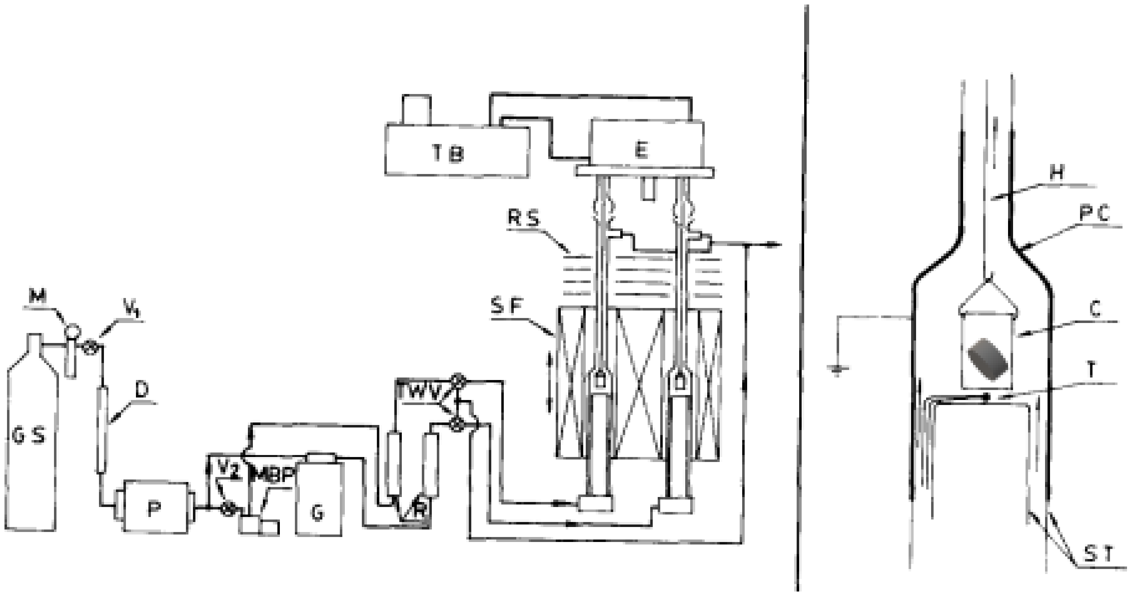

Figure 3.10 Schematic diagram of experimental set-up of the symmetrical thermogravimetric analysis and DC conductivity measurement. G.S., gas source; M, manometer; V_1, V_2, needle valves; D, drying colume; P, electrochemical pump; G, oxygen sensor; MBP, metal bellow pump; TWV, three-way valve; SF, symmetrical furnace; RS, radiation shields; TB, thermostatic bath; E, electrobalance; ST, quartz tubes; T, Pt-Pt 10% Rh thermocouple; C, alumina crucible; H, hanging wires; PC, platinum coating. Adapted with permission from (182).

Coupling between the electrochemical system for measurement and regulation of *P*(O_2) with TGA system: As illustrated in Figure 3.10, the gaseous circuit consists of the gaseous source (GS), the electrochemical pump (P), the zirconia gauge (G), the rotameters (R) and the TGA system. The needle valve (V_2) functions as the controller for the gaseous flux pumped by the metal bellow pump (MBP), by means of which the flux relation between the two arms can be adjusted so that the gas flow effects could be minimized. The three-way valve allows isolation of the TGA system from the rest of the gaseous system(182). The system is sealed with Swagelock tube fittings and viton O rings.

Electrochemical system for measurement and regulation of *P*(O_2): The electrochemical pump comprising a tube of stabilized zirconia provided with a metal coating (electrode) in both the inner and outer surfaces. The oxygen partial pressure of the gas flow before entering the TGA system can be controlled by varying a continuous electrical current applied to the electrodes. The electrical current can vary from a few microamperes to several amperes, depending on the flow rate of the gas and the required oxygen partial pressure. The working temperature of the pump was 750℃(182). A closed-end tube of stabilized zirconia was used as the oxygen gauge in the system. The external reference electrode was prepared with platinum paste and it was in direct contact with air. The gauge allows the measurement of *P*(O_2) based on Nernst's law,

$$E = 4.958 \times 10^{-5} T \log_{10}\left[\frac{P(O_2)}{0.209 \cdot P_{\text{atm}}}\right] \tag{64}$$

where *E* is the voltage in volts, P_{atm} is the ambient atmospheric pressure in atm and T is the temperature in K. The control of oxygen partial pressure in the gas atmosphere also depends on the gaseous source, which was discussed in detail in the literature(182).

Coupling dc conductivity measurement: The TGA system was adapted from the original design adding two platinum wires along the blocking tube, which are connected to a conductivity measurement circuit. Another pellet sample from the same batch as the sample for TGA measurement was coated on both surfaces with platinum electrodes and mounted on the blocking tube right beneath the alumina crucible, so that the two samples are placed in the same atmosphere. The platinum wires were then attached with the platinum electrodes on the sample surface to measure the resistance of the sample. Therefore, the mass change and the conductivity change of the material can be recorded simultaneously.

3.8 Diffusion and Isotope exchange depth profiling technique

3.8.1 Diffusion theory

In order to measure the oxygen tracer diffusion coefficient, *D*, and the surface exchange coefficient, *k*, directly and then probe the mass transport in the electroceramics, a technique known as Isotope Exchange Depth Profiling(IEDP) was proposed and developed in the previous literature(60, 183). The main process of the IEDP technique includes two parts; introducing tracer atoms, the so called exchange part, coupled with compositional analysis performed by secondary ion mass spectrometry(SIMS). The establishment of the Isotope Exchange Depth Profiling technique was based on Fick's first and second laws of diffusion, which describe the diffusion of substances under steady and non-steady state diffusion conditions respectively. Fick's first law postulates that the diffusive flux from regions of high concentration to regions of low concentration is proportional to the concentration gradient, which can be written as equation (65):

$$J = -D\frac{\partial C}{\partial x} \tag{65}$$

where *J* is the flux of a diffusing substance with the unit of mol·cm^{-2}·s^{-1}, $\frac{\partial C}{\partial x}$ is the concentration gradient along the x direction and *D* is the diffusion coefficient or diffusivity with the dimension of area per unit time, usually in cm^{2}·s^{-1}.

Fick's first law can be used to derive the second law which predicts the change of concentration over time as a result of diffusion. If we suppose $\varphi = \varphi(x, t)$ is the concentration that depends on location *x* and time *t*, then the differential of φ against *t* equals to the change of diffusive flux at position *x* according to the mass conservation law:

$$\frac{\partial \varphi}{\partial t} = -\frac{\partial J}{\partial x} = \frac{\partial}{\partial x}\left(D\frac{\partial \varphi}{\partial x}\right) = D\frac{\partial^2 \varphi}{\partial x^2} \tag{66}$$

In order to solve this partial differential equation, appropriate boundary conditions are required to be defined. In most of our cases, the specimen samples in this research can be treated as semi-infinite sample, so that the boundary condition of $\varphi(x = \infty, t > 0) = C_{\mathrm{bg}}$ is always valid, where C_{bg} is the original background concentration, in other words, the natural abundance of the chosen isotope. Apart from the diffusivity in the bulk material, the exchange coefficient which correlates the isotope fraction on the sample surface with the isotope fraction in the atmospheric gas is another crucial parameter that can be obtained through IEDP method. If we include the surface coefficient *k*, then another boundary condition could be derived as: $-D\left(\frac{\partial \varphi}{\partial x}\right)_{x=0} = k[C_{\mathrm{gas}} - \varphi(x = 0, t)]$, where C_{gas} is the isotope enrichment of the gas, *t* represents the exchange time. The solution for a semi-infinite medium with this boundary condition has been given by Crank(184).

$$C'(x,t) = \frac{C(x,t) - C_{\mathrm{bg}}}{C_{\mathrm{gas}} - C_{\mathrm{bg}}} = \operatorname{erfc}\left(\frac{x}{2\sqrt{Dt}}\right) - \left[\exp\left(\frac{kx}{D} + \frac{k^2 t}{D}\right) \times \operatorname{erfc}\left(\frac{x}{2\sqrt{Dt}} + k\sqrt{\frac{t}{D}}\right)\right] \tag{67}$$

In order to obtain the kinetic parameters *D* and *k*, the depth profile obtained from SIMS need to be fitted to the Crank solution above using a non-linear least square method. The Crank equation (67) can also be written into a simplified Equation (68) below as we define two dimensionless parameters *x*' and *h*' as,

$$x' = \frac{x}{2\sqrt{Dt}}, \qquad h' = \frac{k}{D}\sqrt{Dt}$$

$$C'(x,t) = \operatorname{erfc}(x') - \left[\exp\left(2x'h' + h'^2\right) \cdot \operatorname{erfc}(x' + h')\right] \tag{68}$$

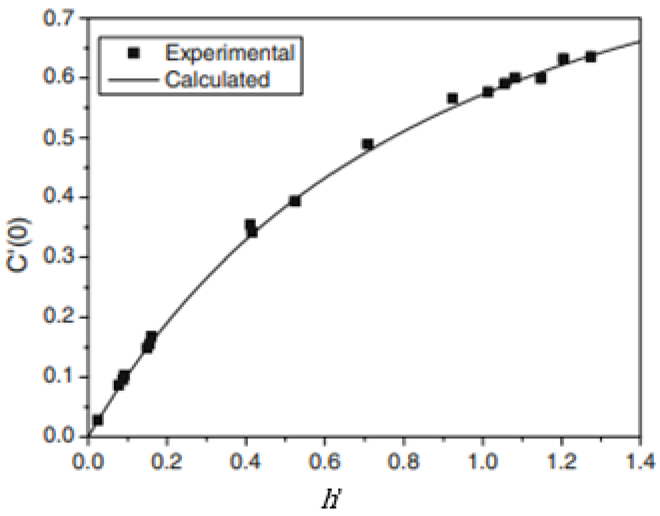

Figure 3.11 Calculated and empirically observed ^{18}O surface fraction as a function of *h*'. Reproduced with permission from (185).

Figure 3.11 shows an example of fitted data from a number of exchange experiments on $La_{0.6}Sr_{0.4}CoO_{3-\delta}$ where normalised surface concentration is plotted against *h*'(185). The non-linear least square fitting of the obtained depth profiles in this research were done using the home-written MATLAB app TraceX(186).

3.8.2 Isotope exchange depth profiling(IEDP) technique

After preparing a semi-infinite specimen with a polished mirror finish surface as the exchange starting point, the sample is annealed in an tracer enriched atmosphere in a set condition for a recorded exchange time to let the tracer diffuse into the bulk material. The tracer could be $^{18}O_2$, $H_2{}^{18}O$ or D_2O depending on the research purpose. The isotope ^{18}O instead of ^{17}O was chosen as the tracer of the IEDP technique due to the resolution of a traditional quadrupole detector is 2000 (m/Δm) which is not enough to separate the hydroxide species OH^- signal with the target ^{17}O signal. Besides, the natural abundance of ^{18}O (0.205(14)) is higher than that of ^{17}O (0.038(1)), and therefore a higher concentration $^{18}O_2$ gas can be obtained more easily. On the other hand, labelled water vapor can also be chosen as the diffusion source in the wet exchange set-up, in which the samples are annealed in a wet atmosphere with labelled water vapor of around 30 Torr with or without normal oxygen of around 150 Torr. The schematic diagrams of the dry oxygen tracer exchange apparatus together with the wet oxygen tracer set-up are shown below.

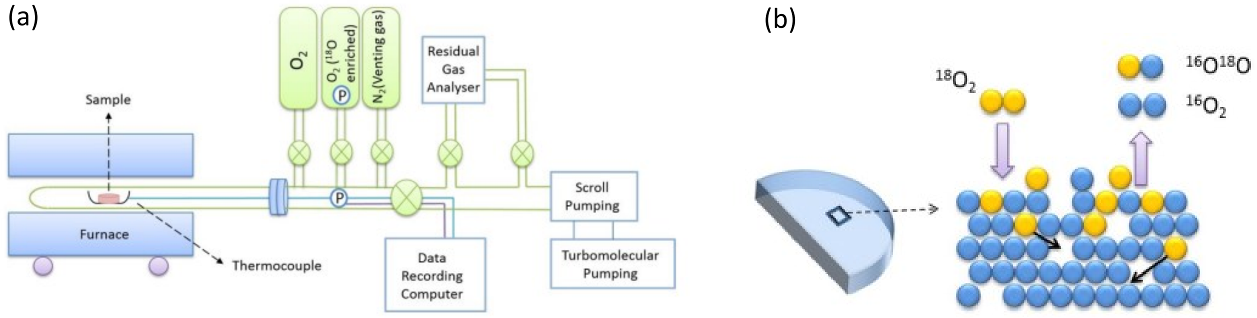

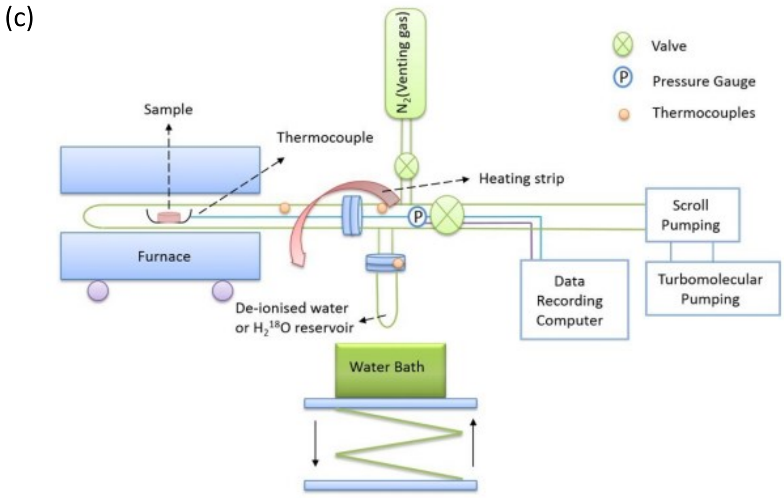

Figure 3.12 Schematic diagrams of the (a) dry $^{18}O_2$ isotope exchange set-up and (c) wet $H_2{}^{18}O$ exchange set-up. Replotted with permission from (187). (b) Schematic of the oxygen isotope exchange process on the surface and the diffusion process in bulk.

The dry $^{18}O_2$ isotope exchange system consists of a pump system which is composed of a primary scroll pump and a secondary turbomolecular pump to enable a high vacuum of 10^{-7} mbar, exchange main parts including a silica tube, several gas reservoirs for different uses and a furnace to control the exchange temperature. All the data during the experiment is recorded by the Data Recording computer. Unlike the dry exchange apparatus, the wet exchange system uses a combination of a $H_2{}^{18}O$ reservoir and a water bath to produce required tracer gas atmosphere. In particular, the main parts of the exchange system excluding the furnace need to be thermally protected in order to prevent the condensation of $H_2{}^{18}O$ water vapor at some place other than the $H_2{}^{18}O$ reservoir.

To determine the accurate exchange time, a thermocouple is placed next to the silica sample boat in the exchange tube to record the real-time exchange temperature of the experiment. After the isotope exchange anneal, a normal thermal cycle of an isotope exchange anneal is presented in Figure 3.13(a) below, where the dotted lines are fitted to the heating and cooling parts. From the intersections of those dotted lines, the anneal time is estimated.

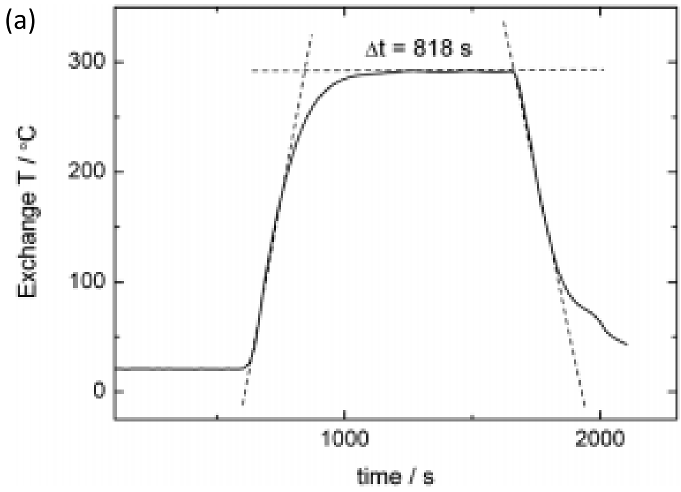

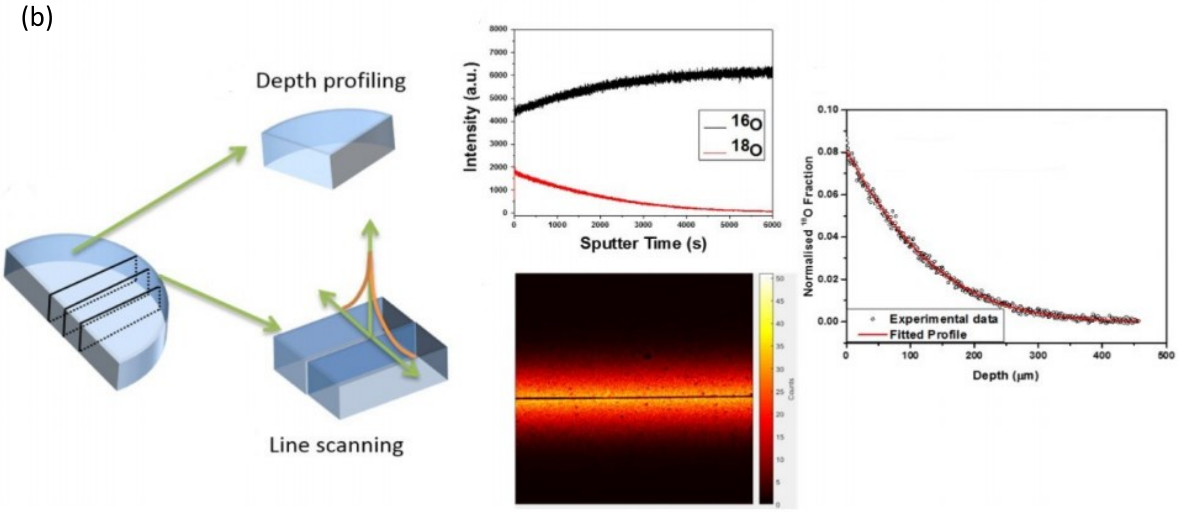

Figure 3.13 (a) Thermal treatment of a representative isotope exchange experiment. The dashed lines were used to estimate the exchange time, Δt. (b) The schematic diagrams of the whole diffusion data analysing process including two analysis modes used in IEDP technique. Adapted with permission from (187).

In order to get high quality diffusion profiles with appropriate diffusion length, the exchange time and exchanging temperature of the experiment need to be designed according to the material diffusivity. Depending on the obtained diffusion length of the exchanged sample, two processing modes, namely the **depth profile** and **line scan** methods, could be use to achieve a diffusion profile. For exchanged sample with a diffusion length less than 5 μm, the relatively straightforward depth profile method can be used in which the exchanged sample is directly loaded in the main chamber of SIMS equipment. As the surface ions are sputtered by ion bombardment, the sputtered ions are collected by a high extraction field into the mass spectrometer to produce a profile of the isotope fraction, $^{18}O/(^{16}O+^{18}O)$. For an exchange sample with a diffusion length over 100μm, when the depth profile method is no longer suitable because of the extremely long sputtering time, the line scan mode can be used instead. In line scan mode, the exchanged samples are sectioned, and then two line scan sample are sticked together with the original polished surface facing each other to avoid the edge effect when using SIMS analysis. After being polished again on the lateral surface which is vertical to the original exchanged(polished) surface, the sample is then being analysed under SIMS using the flood gun mode to generate a map regarding the isotope fraction across the sample surface(lateral). Figure 3.13(b) shows the whole diffusion data analysing process of the two modes. The detailed instrument set-up of the secondary ion mass spectrometry (SIMS) will be introduced in the next section.

3.8.4 Experimentation of isotopic exchange depth profiling (IEDP)

Sample preparation: In order to achieve reliable diffusion coefficients, *D*, and the surface exchange coefficient, *k*, of a material, the testing samples need to fulfil several requirements with respect to shape, thickness, relative density and surface roughness. To reduce dimensional influence of oxygen diffusion and simplify the data analysis process, a pellet shaped or a slab sample is preferred, and the thickness of the sample should meet the requirement of a semi-infinite boundary condition for a specific diffusion process. Depending on the diffusion coefficient of the material, the thickness of the sample should be larger than $4\sqrt{Dt}$, where *D* is the diffusion coefficient, *t* is the isotopic exchange time and $2\sqrt{Dt}$ is the permeation depth of the tracer derived from Equation (65), so that the tracers diffused from the opposite surfaces of the sample wouldn't interfere with each other. Since open porosities in the sample provide short-cuts for the oxygen diffusion, which will lead to a high error in diffusion coefficient, especially for materials with small diffusivity, the relative density of the sample needs to be over 95% to avoid open porosities according to the previous literature(188). Last but not least, the roughness of the sample surface needs to be small enough to provide a flat beginning edge for the tracer diffusion. A high surface roughness has a significant influence not only on the reliability and validity of the obtained diffusion kinetics, but also in the SIMS analysis as it introduces uncertainty in determination of depth. In particular, the geometric features on the sample surface will heavily affect the surface exchange process as the tracer can enter the sample through different routes. To reduce the error caused by surface roughness in practice, the sintered pellet samples are ground initially using SiC grinding papers (Struer® Co.) with grits of 600, 1200 and 2000 successively. The resulting surface is then automatically polished using a Struer-automated polishing machine (Struer® Co.) in the water-based diamond suspensions of 6 μm, 3μm, 1μm and a quarter μm successively. The corresponding polishing time and force exerted on the sample for each step was 10 min/20 N, 10 mins/20 N, 20 mins/15 N and 20 mins/10 N respectively until a mirror-finish on the sample surface was achieved.

Experimental procedures for a dry oxygen isotope exchange experiment: The oxygen isotopic exchange experiment consists of two major steps, namely the $^{16}O_2$ pre-annealing and the $^{18}O_2$ exchange annealing. The main purpose of the $^{16}O_2$ pre-annealing process is to mitigate the mechanical damage introduced in the grinding and polishing procedures and to equilibrate the oxygen composition of the sample to make sure that the diffusion process is oxygen self-diffusion without the interference from any other oxygen gradient(60). The period for $^{16}O_2$ pre-annealing is normally 10 times longer than the isotopic exchange time. The procedures with respect to time scale of a typical isotopic exchange experiment are demonstrated in Figure 3.14. The exchange time of each experiment was carefully chosen in order to obtain an appropriate permeation depth of the tracer.

After placing the sample in the sample boat stored in the silica tube, as shown in Figure 3.12 (a), the exchange tube needs to be properly sealed. Before isolating the exchange chamber, the whole system is vacuumed initially by the primary scroll pump, then by the secondary turbomolecular pump till the chamber pressure is below 4×10^{-7} mbar. Then 200 mbar of high purity oxygen $^{16}O_2$(99.9995%) is introduced into the exchange chamber and the furnace set at the required temperature is rolled on to start the pre-anneal process. It is worth noting that, the silica tube should be placed in the furnace hot zone so that the temperature around the sample boat is kept in a controllable range.

When the pre-anneal finishes, the furnace is rolled off to let the tube and the sample cool down to room temperature. The exchange tube is then evacuated again to intermediate-high vacuum before introducing $^{18}O_2$. Similarly, 200 mbar of $^{18}O_2$ with a concentration of around 93% is introduced, and the furnace is rolled on to start the exchange procedure. Before the exchange experiment, the isotope enrichment of ^{18}O was confirmed using the residual gas analyser (RGA, Hidden Analytical Ltd, UK). After the exchange annealing, a small amount of residual gas in the system is leaked out to the RGA for mass spectrometry measurement, while the majority of $^{18}O_2$ gas in the system is recovered using liquid nitrogen.

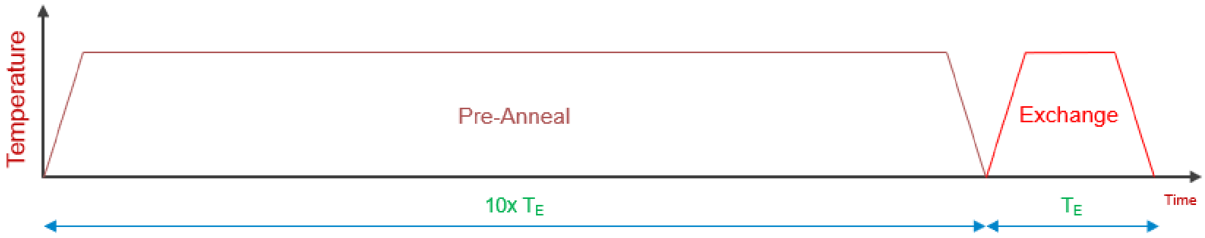

Figure 3.14 Procedures in a typical isotopic exchange experiment with respect to time scale.

Experimental procedures for a wet exchange experiment using $H_2{}^{18}O$ or D_2O: Compared with the dry $^{18}O_2$ exchange experiment, the wet isotopic exchange apparatus uses $H_2{}^{18}O$ or D_2O as the tracer source. Thus, a wet gaseous atmosphere containing $H_2{}^{18}O/D_2O$ and normal $^{16}O_2$ is introduced in the exchange annealing. An addition of a water bath component in the wet exchange apparatus is functioning as the controller for the partial pressure of $H_2{}^{18}O/D_2O$ water vapor in the system. After vacuuming the main chamber below 4×10^{-7} mbar, the valve of the $H_2{}^{18}O/D_2O$ reservoir is opened to let the water evaporates into the exchange chamber. The equilibrium of the evaporation and condensation takes about half an hour, during which the whole system was wrapped by thermal straps and aluminium foil for thermal protection in order to avoid cooling points other than the water reservoir. After the equilibrium of water vapor, 200 mbar extra $^{16}O_2$(99.9995%) is let in. The rest of the steps are similar to that of dry $^{18}O_2$ exchange experiment. It needs to be mentioned that the scrambling of gas molecules in the wet exchange is much more severe than that in dry exchange experiment resulting in a more complicated gas environment during exchange. Since the residual of exchanging gas contains lots of information about the surface exchange process, a residual gas analyser(RGA) was used to identify the gas content. The isotope enrichment is measured prior to the exchange experiment by the RGA, which can be used to make a comparison with the residual gas after the exchange experiment.

3.9 Secondary ion mass spectrometry (SIMS)

Secondary Ion Mass Spectrometry (SIMS) is a technique used to analyse the composition of solid surfaces by sputtering the ions on the surface with a high energy primary ion beam in high vacuum. The SIMS technique is particularly useful in combination with the IEDP technique to achieve the elemental information of the sample as a function of depth. In the line scan mode of IEDP technique as discussed in Section 3.8, SIMS can also be used as the analytical method to obtain the mapping of $^{16}O/^{18}O$ across the sample surface.

3.9.1 Introduction to the technique

As shown in the following schematics, in a typical SIMS measurement, a primary ion beam with high energy (typically 10 to 40 keV) is used to bombard the sample surface in high vacuum causing sputtering of atoms and molecules from the surface. As the high energy primary ions reach the surface, some of their kinetic energy is transferred to the lattice by billiard-ball type collisions, producing a collision cascade within the solid. However, if the energy of the primary ions is insufficient to overcome the binding energy of the atoms in the lattice, instead of causing a collision cascade, the primary ion will come to rest and implant into the sample. After causing a collision cascade, some of the sputtered particles are ionised, which are known as the secondary ions. These ejected secondary ions are attracted by the acceleration potential, which then are collected and analysed by a mass spectrometer, where the intensities of the species are plotted against the corresponding mass/charge ratio. The intensity or the collected secondary ion current is dependent on several factors, which can be expressed as:

$$I_S^X = I_P C_x s \gamma F \tag{69}$$

where I_S^X is the secondary ion current of X, I_P represents the current of the primary ion beam, C_x is the fractional concentration of X in the target, *s* is sputter yield (number of X atoms sputtered per incident primary ion), λ is the ionisation efficiency for X (number of X ions per sputtered X atoms) which depends on beam conditions and the surrounding matrix and *F* is an instrumental transmission factor which describes the efficiency of ion extraction and transport to the mass spectrometer from the sample surface.

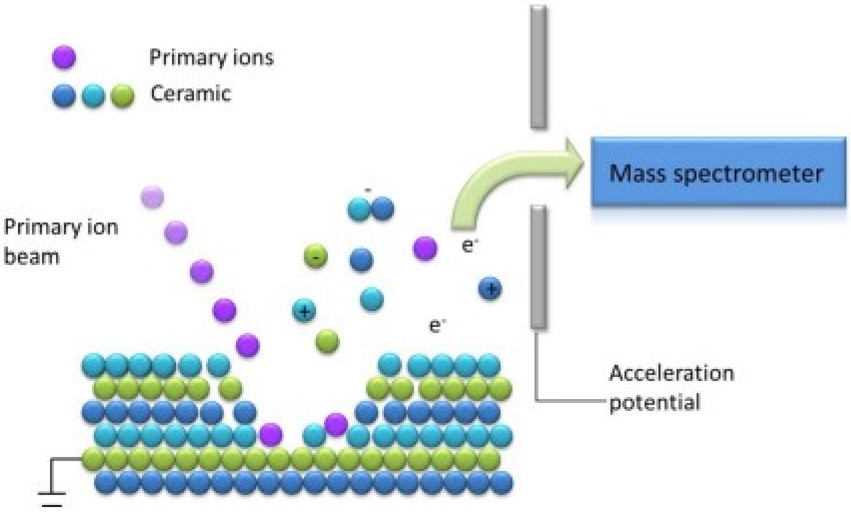

Figure 3.15 Principal of Secondary Ion Mass Spectroscopy. Adapted with permission from (189). The purple circles are the primary ions, blue, cyan and green icons represent the ions of the ceramic sample.

Since the sputter yield and ionisation efficiency of different elements vary according to many factors regarding the surrounding environment of the element, such as the chemical state of the surface (also known as matrix effect), quantification of the elemental composition of a certain layer etc, additional calibration of secondary ion intensity is required when comparing the currents from different elements. However, tremendous and complicated data analytical processes related with the matrix effect could be avoid for the isotopic study, because for isotopes the matrix effect makes no contribution to the intensities. For the oxygen diffusion study in the present work, since the ^{18}O are replacing ^{16}O sites, the chemical environments for the two species are identical(187, 190). For the wet exchange, the ^{18}OH and ^{16}OH species were considered, which also have the same chemical environments in the matrix. The situation for D_2O exchanged sample analysis may be a little bit complicated as the chemical environments for H^+ and for D^+ in the matrix are not identical. As a replacement, the OD and OH species were recorded to extract the depth profiles.

3.9.2 Instrumentation

A secondary ion mass spectrometer consists of five main parts including a primary ion gun generating the primary ion beam, a primary ion column which accelerates and focuses the beam onto the sample, an ultra-high vacuum chamber equipped with the secondary ion extraction lens, a mass analyser separating the ions according to their mass/charge ratio and a detector.

For **Primary ion source**, three types of ion gun, namely duoplasmatron, surface ionisation and liquid metal ion source (LMIS), are commonly employed. Depending on the gun design, different sensitivity and spatial resolution can be achieved. In this research, the liquid metal ion gun (LMIG) is chosen as the ion source, the focused spot size of which can reach sub-micron level. The LMIG is operated with metals or metallic alloys, which are liquid at room temperature or slightly above. It contains a tungsten needle covered with a thin layer of liquid metal, normally gallium or bismuth etc., which emits ions under influence of an intense electric field. The emitted ions are then accelerated along the **primary ion column** and focused on the sample surface. The Time-of-Flight SIMS used in this project is equipped with a bismuth source LMIG, which can produce ion pulses in two modes, namely the high current bunch mode (HCBM) with high mass resolution and low lateral resolution, and the burst alignment mode (BAM) with low mass resolution but high lateral resolution for mapping application.

To avoid collisions between the primary ions and the residual gas molecules in the chamber, the main chamber of SIMS equipment needs to be vacuumed to ultra-high vacuum. In other words, the mean free path of gas molecules within the detector must be large compared to the size of the **vacuum chamber** to avoid collision of the residual gas molecules with the sample surface or the primary ions.

There are three basic **mass analyzers** available for SIMS equipment: quadrupole, magnetic sector and Time-of-Flight (TOF), the characteristics of which are listed in Table 3.2. Each mass analyzer separates the secondary ions according to their mass/charge ratio based on different physical principals.

Table 3.2 Characteristics of three types of mass analyzers used in SIMS technique(191).

	Quadrupole	Magnetic sector	TOF
Upper mass limit (m/z)	4000	20000	1000000
Mass resolution	2000	100000	10000
Ion sampling	Continuous	Continuous	Pulsed
Transmission F	0.01-0.1	0.1-0.5	0.5-1
Relative sensitivity	1	10	10000`

A radio frequency quadrupole mass analyser comprises four parallel rods. The m/z separation is completed by the electric field caused by two sinusoidal electric fields perpendicular to each other and with 90 degrees phase shift in between four quadrupole rods(191). For a certain applied voltage, only the species with a certain m/z ratio can pass through the quadrupoles with a stable trajectory, while all other secondary ions collide with the rods in their trajectories flying through the rods. Therefore, different secondary ions are connected by switching the applied voltage of the analyzer and the detection process is thus sequential.

A magnetic sector mass spectrometer uses a combination of an electrostatic potential and a magnetic field to separate the secondary ions. Before entering a perpendicular magnetic field in a magnetic sector mass spectrometer, all ions are accelerated by an electrostatic potential with various ending velocities(190). As moving charges enter a magnetic field, the charge is deflected to a circular motion of a unique radius in a direction perpendicular to the applied magnetic fields. Therefore, as the ions travel through the magnetic sector, ions of different velocities end up with different radii of curvature. By fixing the electrostatic and magnetic field applied, only species with corresponding m/z ratio can pass through the curved sector reaching the counter. The detection process is thus sequential.

A Time-of-Flight mass analyzer separates the ions in a field-free drift path according to their velocities. Pulses of secondary ions are firstly accelerated to possess nearly the same kinetic energy, then drift freely to the detector when the ions can be simultaneously separated based on the flight time to the counter which is inversely dependent on the square root of their mass. Time-of-Flight (TOF) is by far the most frequent analyser currently used in imaging mass spectrometers(191). In this work, the ToF-SIMS instrument (ION-TOF GmbH, Münster®) is equipped with a TOF mass analyzer.

Detector: After being separated by the mass analyzer, the ions are collected by an electron multiplier, in which an impact of a single ion can start off an electron cascade resulting in a pulse of 10^8 electrons. The electron cascade is directly recorded. As a replacement for the electron multiplier, a microchannel plate detector with higher lateral resolution but lower amplification factor is used in the detector of a SIMS instrument, where the signals are recorded with a fluorescence detector or a CCD-camera.

In general, there are two possible operation mode of producing primary ion pulses of sufficiently short duration for high mass resolution, namely the high current bunched mode (HCBM, or bunched mode) and the 'pulsing-enabled burst alignment mode' (BAM, or burst mode). The first is to send a ~20 ns pulse of ions through a condenser in order to bunch the ions together and form an ion pack of only ~0.6 ns, as shown in figure 3.16(a). The other is to modulate a long pulse of ~100 ns with a MHz signal in order to cut several pulses of ~1 ns out of a larger ion pack (figure 3.16(b)). In TOF-SIMS where all masses are measured simultaneously, high count rates for major peaks are sometimes saturated in the detector while the count rates for minor isotopes or elements are not sufficient yet. Therefore, severe error would be introduced due to the dead time of the detector. Using a pulsed burst mode instead of the bunched mode is an effective way to prevent saturation of the detector whilst enabling high count rates to be maintained during the collection of minor isotopes. The error caused by counting statistics in the measurement of isotopic ratios using the TOF-SIMS technique can be minimised in this way. However, since the detector is a single-ion counting system, the dead time error (regarding the possibility of several ions arriving at roughly the same time while the former on is not yet released by the detector) has to be corrected by mean of Poisson statistics(192).

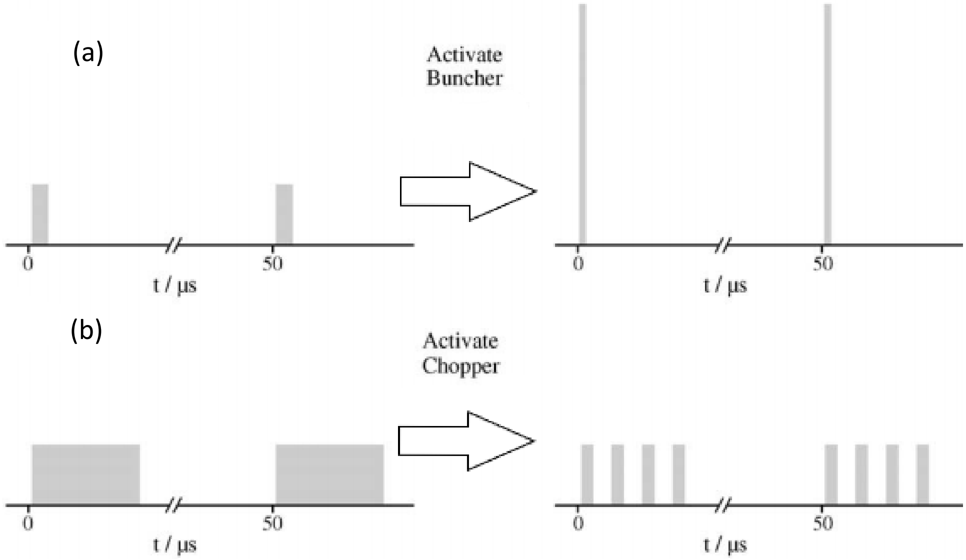

Figure 3.16 Schematic diagram showing the two operational modes of TOF-SIMS equipment, namely (a) the bunched mode and (b) the burst mode. Reproduced from (193)

There are three analytical modes of SIMS for different research purposes, namely mass spectrometry, depth profile and the elemental mapping.

In a mass spectrum, arbitrary intensity is recorded as a function of m/z ratio, which is useful in identifying the existing species in the sample. Due to the aforementioned matrix effect of different species, the peak intensity in a mass spectrum is not quantified, which needs further correction for direct quantification analysis. However, in the case of using isotopes of one element, such as ^{18}O and ^{16}O, a direct comparison of the intensities can be applied to obtain isotopic fractions.

In a depth profiling analysis, the intensities of selected secondary ions are plotted as a function of sputtering time, which is a strong method for direct observation of the diffusion process. This analysis method is usually coupled with the crater depth measurement using a Zygo instrument to achieve depth profiles.

For the elemental mapping mode, the distribution of elements in a selected area can be observed. This analytical method, thus, is capable of investigating the phase distribution, elemental segregation on grain boundaries or sample surface and the cation/labelled ions' migration on a sample surface, which is extremely useful for the line scan sample analysis.

3.9.3 Instrumental set-up of the ToF-SIMS equipment

In this project, the Time-of-Flight (ToF) SIMS (ION-TOF GmbH, Münster®, Germany) working at ultra-high vacuum with a dual ion-beam source are used for analysis of the exchange profiles. The ion-beam source is equipped with a liquid metal ion gun (LMIG) of bismuth (Bi) as the primary ion beam source, which can form high energy Bi ions beam with a good focus through a field emission process induced by a very high extraction field. This high lateral resolution mode is coupled with a high current, low energy sputter gun in dual beam mode to enable depth-profiling analysis. The sputtering gun of Tof-SIMS is fitted either with an electron impact source i.e. O_2^+ ions, Ar_n^+ clusters, or with a surface ionisation source i.e. Cs$^+$ ions depending on the analysis purpose for detection of different species. In practice, oxygen bombardment is beneficial for positive secondary ion yields, while Cs$^+$ source are used in sputtering negative secondary ions. Therefore, the analysis of the $^{18}O/^{16}O$ exchange profiles obtained in the dry oxygen diffusion experiments in this research was done using a high current Cs$^+$ thermal ionization source, while the D/H or OD/OH exchange profiles obtained in the wet exchange experiments was conducted using an O_2^+ electron impact source to enhance the deuterium and hydrogen ion yields.

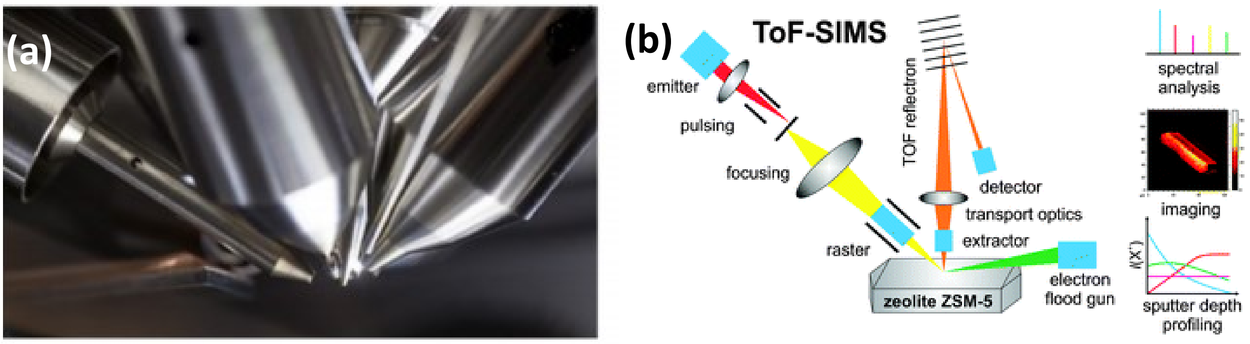

Figure 3.17 (a) A Photograph showing the insight of the main chamber of a ToF-SIMS equipment. (b) A schematic of the main components of a ToF-SIMS with a ion source, a TOF analyzer, a detector and an electron flood gun. The three plots asides are three major SIMS operation modes, namely the mass spectrum, the depth profile and the elemental mapping mode(194).

Specially, for insulating or poorly conducting materials, an electron flood gun is employed to compensate the charge build-up on the analyzed sample surface during the ion bombardment. The insight of the main chamber of a ToF-SIMS along with a schematic of the main components in a ToF-SIMS equipment are shown in Figure 3.17 (a)&(b).

3.10 Summary

This chapter gives a broad instruction on the material synthesis method and the characterisation techniques used in the current research. Most data, as discussed in the following Chapters, are obtained using the equipment in Department of Materials, Imperial College London, while some experiments were carried out in the laboratories of collaborators in Tokyo Institute of technology and in Atomic Centre of Bariloche. The principal and instrumentational information of the characterisation methods are not extended in detail in this thesis. The reader is directed to the comprehensive literatures about these technique through the reference materials.

Chapter 4

Synthesis and crystal structure characterization of $BaNd_{1-x}Ca_xInO_{4-x/2}$

In this chapter, the synthesis of $BaNd_{1-x}Ca_xInO_{4-x/2}$ (x = 0, 0.05, 0.10, 0.15, 0.20, 0.25, 0.30) compounds and the parent compound will be discussed with more experimental details. The sintering behaviour of $BaNdInO_4$ was investigated by dilatometry to find the best sintering condition for the $BaNdInO_4$-related materials. Preliminary material characterisation was carried out on the sintered pellet samples, i.e. density measurements using an Archimedes balance, X-ray diffraction for identification of phases and determination of the crystal structure, scanning electron microscopy (SEM) for observation of grain sizes and energy dispersive spectrometer (EDS) for checking chemical compositions. Samples are referred to in the following as BNCxx where xx refers to the mol% Ca substitution. In this notation the $BaNd_{0.80}Ca_{0.20}InO_{3.90}$ is defined as BNC20.

4.1 Synthesis of $BaNd_{1-x}Ca_xInO_{4-x/2}$ coumpounds

$BaNd_{1-x}Ca_xInO_{4-x/2}$ (x = 0, 0.05, 0.10, 0.15, 0.20, 0.25, 0.30) compounds were prepared by the solid state reaction method. Stoichiometric amounts of Nd_2O_3 (99.9% purity, Alfa Aesar), $BaCO_3$ (99.999& purity, Sigma-Aldrich), In_2O_3 (99.9% purity, Alfa Aesar) and $CaCO_3$ (99.99% purity, Sigma-Aldrich) were mixed for 30mins using pestle and mortar with ethanol in order to enhance the mixing of powders. In particular, the Nd_2O_3 powder was dried at 800 °C for 6 hours before weighing to remove moisture. The resulting green-coloured slurry was dried in the fume hood covered with aluminium foil to avoid cross-contamination. The powder mixture was then calcined at 1000 °C in static laboratory air for 14 hrs to decompose the carbonates and eliminate the CO_2. After the calcination process the ashes were ground again using pestle and mortar to decrease the particle size before pressing. The grey-coloured powder was then pressed into pellet shape with a 13 mm circular die under a load of 2-3 tons holding for 5 minutes. The pellets were then placed in a rubber glove sealed by a portable vacuum pump followed by a 5-mins isostatic press process at ~ 300 MPa to achieve high density. After being sintered at 1400 °C for 24 hours, the pellet samples were ground with SiC grinding paper to remove the top most layer which has different colours (partly brown, while the bulk are dark) and contains more secondary phases due to the over-heating. The colour of the pristine $BaNdCaInO_4$ material synthesized in this process exhibited a blue appearance, while the calcium doped sample were all dark in colour.

4.2 Density measurement and the modified two-sintering-step synthesis procedures

The relative densities of the sintered pellets were measured by the Archimedes method with water using a water balance. To avoid air bubbles inside the pellet which might contributed to an increased buoyancy in the following measurement, the sample after polishing was immersed in boiling water for 10 mins to eliminate the air bubbles inside the pellet. The resulting relative densities of the pellet samples, as calculated according to equation (52), are around 87 ~ 91%, which are not dense enough for the requirement of the exchange experiment. The data of the density measurement in detail is listed in Table 4.1 below.

Table 4.1 Density measurements of $Nd_{1-x}Ca_xBaInO_{4-x/2}$(x=0, 0.05, 0.10, 0.15, 0.20, 0.25, 0.30) compounds. The calculations were based on the equation: $\rho = \frac{W(a)\cdot[\rho(fl)-0.0012\ g\cdot cm^3]}{0.99983\cdot G} + 0.0012 g/cm^3$

Chemical formula	W(a)/g	G/g	Temp/°C	$\boldsymbol{\rho(fl)/g \cdot cm^3}$	Meas. $\boldsymbol{\rho}$	Calc. $\boldsymbol{\rho}$	Relative density
$NdCaBaInO_4$(x=0)	0.8402	0.1447	20.0	0.99823	6.051	6.93	87.3%
$\boldsymbol{x = 0.05}$	0.9206	0.1528	20.0	0.99823	6.009	6.87	87.5%
$\boldsymbol{x = 0.10}$	0.9659	0.1579	20.0	0.99823	6.101	6.77	90.1%
$\boldsymbol{x = 0.15}$	0.8744	0.1420	20.9	0.99804	6.141	6.69	91.8%
$\boldsymbol{x = 0.20}$	0.9655	0.1586	20.0	0.99823	6.071	6.64	91.4%
$\boldsymbol{x = 0.25}$	0.8484	0.1487	20.9	0.99804	5.690	6.51	87.4%
$BaNd_{0.80}Ca_{0.20}InO_{3.90}$*	0.8991	0.1374	19.7	0.99829	6.582	6.64	98.4%

*: Samples synthesized in a different process which will be discussed in the following section. The calculated density (theoretical density) ρ were calculated using the refined lattice parameters from the XRD patterns shown in the following Section.

Therefore, in order to improve the relative density of the sample, an optimization of the synthesis procedures regarding the sintering temperature and grinding method was carried out.

Dilatometry test: The sintering behavior of the pristine material, $BaNdInO_4$ was investigated using dilatometry. The tested sample was synthesized using the same procedures as described in the last section. However, instead of a full sintering step of 24 hours, the uniaxially-pressed sample was cut into an appropriate shape which then went through a pre-sintering process at 1300°C for 2 hours to achieve considerably high rigidity of the sectioned sample, so that it wouldn't break under the pressure applied by the pushrod in the dilatometry measurement.

In the dilatometry experiment, the heating program was set as two segments including a heating step at the rate of 10 K/min from room temperature to 1370℃ and a thermal equilibrium step when the temperature was held at 1370 ℃ for another 2 hours to let the material sinter.

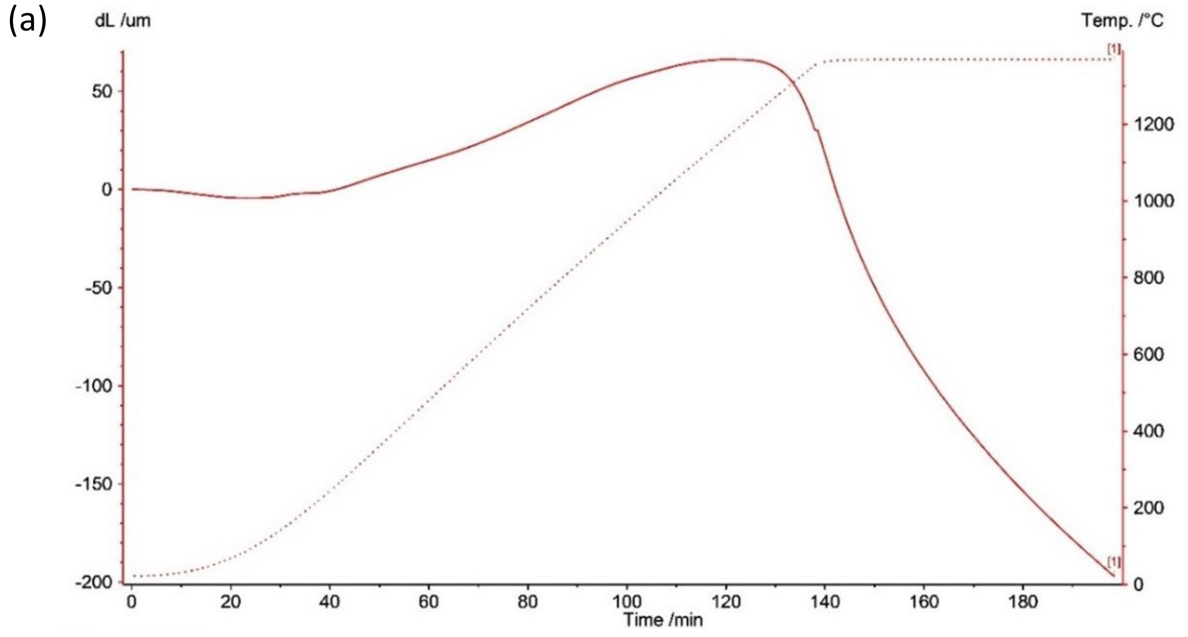

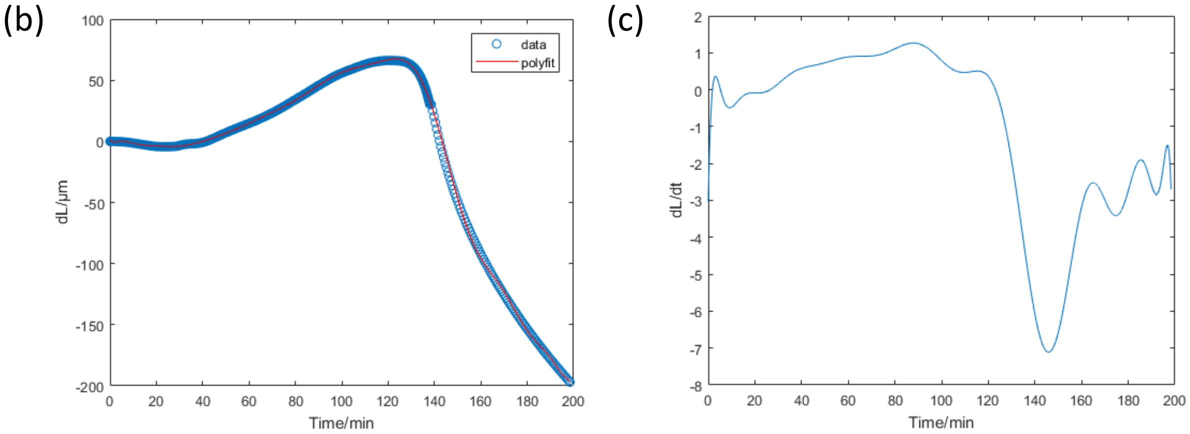

Figure 4.1 (a) Graph of Dilatometry test where the dimensional change, *dL*(μm), of the sample and temperature, *T*(℃), were plotted against time. (b) Polynomial curve fitting of the dimensional change graph. The blue circles represents the experimental data and the red solid line represents the fitted data. (c) The derivation of length [d(d(L))/dt] versus Time graph.

As can be seen in Figure 4.1 (a), the sample under test experienced a thermal expansion first in elevated temperatures from room temperature to around 1300℃. Then, as the temperature increased further, sintering of the material was triggered and the strip-shaped sample started to shrink. Due to the equipment limitation, higher sintering temperature as well as a long duration measurement at 1370℃ were not accessible. As can be seen in the plots, the sintering process was not finished after two hours annealing, which implies that the sintering process of $BaNdInO_4$ oxide at 1370 ℃ is a relatively slow process. To investigate the sintering behavior of $BaNdInO_4$ a little bit further, the dimensional change graph (Figure 4.1 (a)) was fitted using a polynomial curve of degree 19 in Matlab, which resulted in a considerably good fit, and the deviation of length over time was plotted against time in minutes based on this fit result, as shown in Figure 4.1 (c). An obvious trough can be seen starting from the 125th minutes, where the corresponding temperature was 1280℃, while the fastest sintering rate was achieved at 1370℃ as the derivation reached the minimum value at the 145th minute.

Due to the equipment limitation, higher temperature and longer sintering time are not available in the dilatometry experiment. To investigate the sintering behaviour of $BaNdInO_4$ at higher temperatures, a pellet sample was sintered in high temperature furnace at 1420 ℃ for 24 hours, which resulted in a melted brown-colored product. The dilatometry result together with the high temperature sintering test implies that instead of further increasing the sintering temperature, a long sintering process is more feasible to complete the sintering and achieve high pellet density in $BaNdInO_4$ oxides. Therefore, the sintering time of 24 hours in the original synthesis procedures are kept and the sintering temperature need to be optimized.

Sintering temperatures and the grain size: In order to investigate the influence of sintering temperature on the microstructure of the pellet samples, two $BaNd_{0.8}Ca_{0.2}InO_{3.90}$ (BNC20) pellet samples were synthesized through the process described in Section 4.1, while the sintering process of two samples were done at 1150 ℃ and 1400 ℃ for 24 hours. SEM images of the as sintered pellets were taken using the JEOL JSM-6010 LA equipment as shown in Figure 4.2.

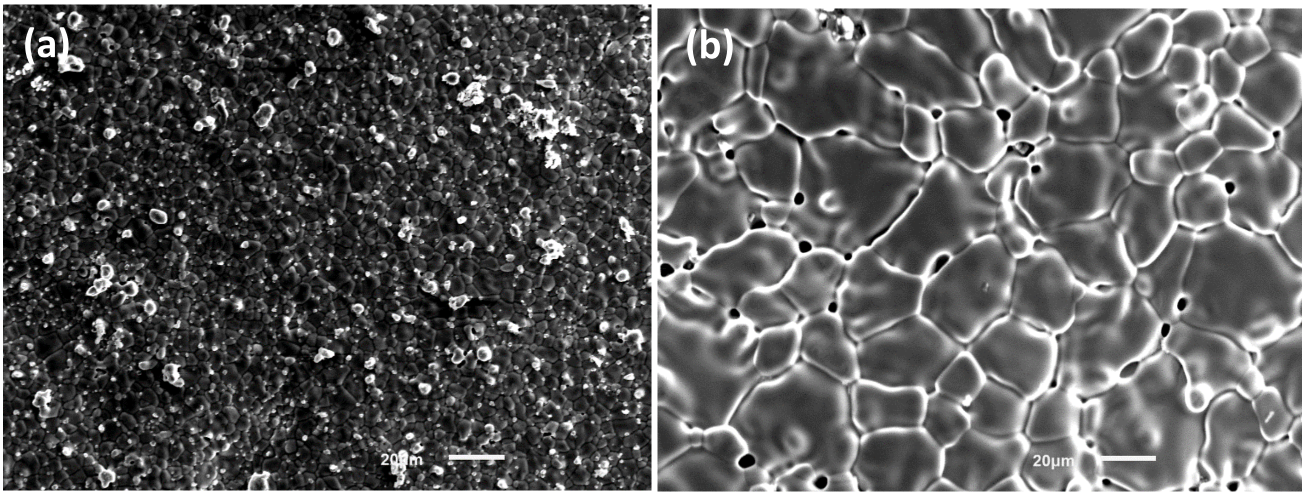

Figure 4.2 SEM images of the BNC20 samples sintered at (a) 1150℃ and (b) 1400℃

These two images showed that different sintering temperatures will significantly affect the microstructure of the resulting pellets, especially in the grain size. The grain size of pellets sintered at 1150 ℃ is approximately several microns, while the grains of pellets sintered at 1400 ℃ are much larger with an average size of about 30 μm. The relative densities of two samples were measured using the Archimedes method, which were 87% (1150℃) and 92% (1400℃) respectively. Although, the grains of the BNC20 sample sintered at higher temperature are larger than that sintered at 1150 ℃, the relative densities of the samples were not improved significantly and the open pores between the grains are still inevitable. Therefore, instead of switching the sintering temperature, a ball milling process was employed before sintering to decrease the particle size, which has been proved to be an effective approach to achieve high relative densities in ceramics in the previous literature(195-197).

Ball milling: A planetary ball milling step was adapted into the original synthesis procedures before the sintering step. The calcinated ashes were ball milled in the Planetary Micro Mill in ethanol at a spinning rate of 300 rpm for 6 hours. Then the slurry was again dried in a fume hood and the resulting powder was ground by pestle and mortar.

In the optimized process, the ball milled powder was firstly pressed only by the uniaxial press and sintered at 1300 ℃ for 24 hours to let the precursors react with each other completely to form the target $BaNd_{1-x}Ca_xInO_{4-x/2}$ compounds. The pellets were then crushed and ball milled again in ethanol at a spinning rate of 300 rpm for 6 hours to decrease the particle size. After drying the slurry, the obtained powder was uniaxially-pressed at a load of 2-3 tons for 5 mins and isostatically-pressed at ~ 300 MPa for 5 mins, successively. The final sintering step was modified from the original one, the thermal program of which was set as shown in Figure 4.3 below.

The pellets were first sintered at 1400 ℃ for 1 hour as a fast sintering process, in which the sintering of the material was triggered by the high temperature, followed by a much longer sintering period of 24 hours at 1300 ℃ which enables the growth of grains so that the porosities in the bulk can be pushed out. In order to avoid the cross contamination from the alumina crucible and the over heating on the top surface of the pellet samples, the residual powder from the former step was spread around to cover the surface of the pellet. The diameter of the resulting dark pellets were around 10.40 mm, which is much smaller than the diameter after uniaxial press (13 mm). The change in the pellet dimension implied that the pellet densification was quite successful using the modified synthesis procedures.

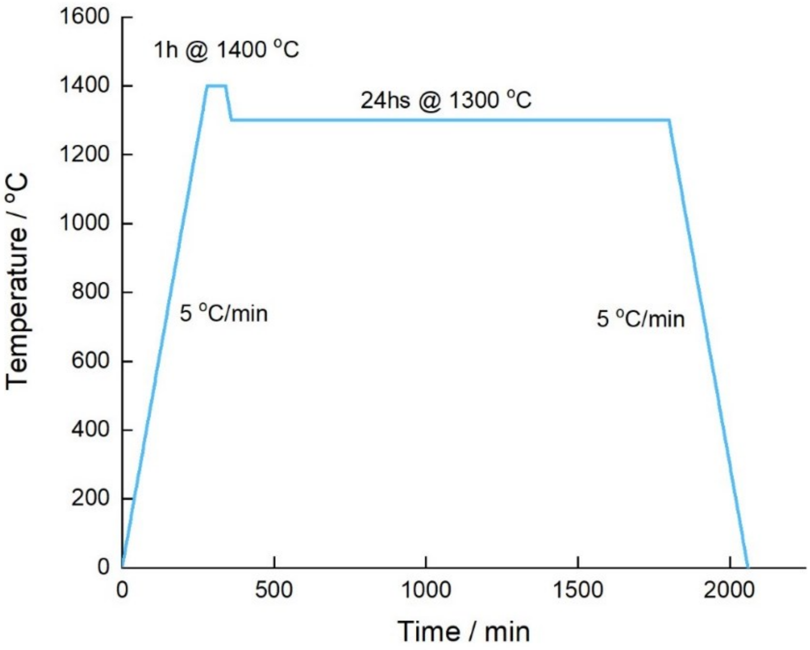

Figure 4.3 Optimized thermal program for sintering process.

The relative densities of the pellet samples synthesized using the new approach reached up to 98% measured by the Archimedes method with water using a water balance (shown in the last row in Table 4.1). An a comparison between the polished samples synthesized through the original method and the optimized solution was shown in the SEM images below (Figure 4.4). The as-sintered sample was polished using SiC grinding papers with grits of 600, 1200 and 2000 successively before being coated with gold and imaged under SEM. A clear improvement regarding the size of the porosities was achieved. In the following chapters, unless being mentioned in particular, all the measurements were conducted on the $BaNdInO_4$-related ceramics synthesized using the modified two-sintering-steps process. Although, the porosities were not completely eliminated by using the optimized synthesis process, the relative density of the pellet samples were 98% which implies that the porosities observed in the SEM images are closed porosities which won't affected the IEDP measurement severely.

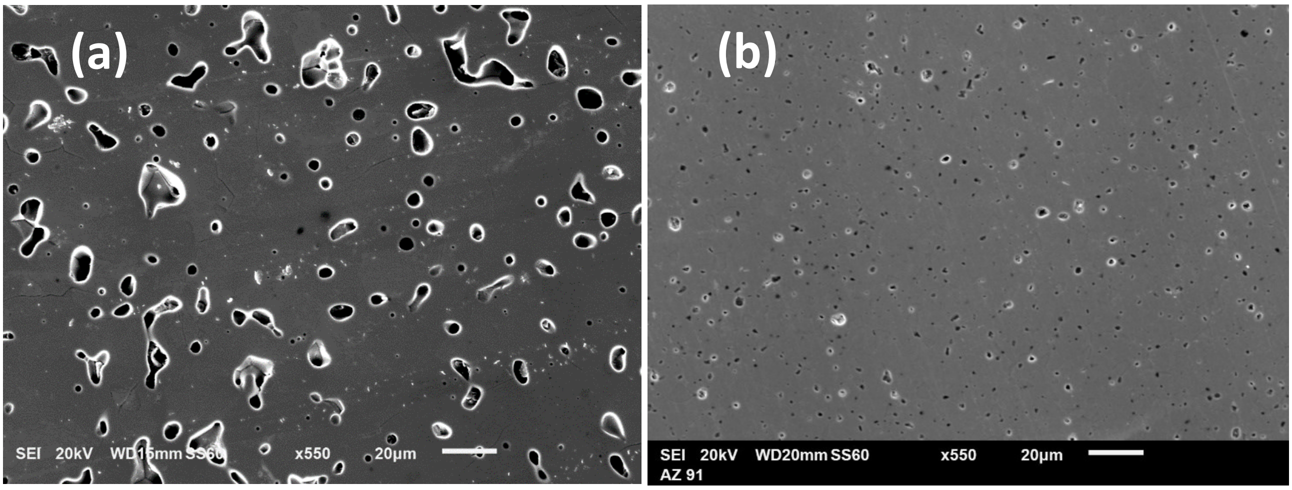

Figure 4.4 Surface secondary electron images of the $BaNdInO_4$ polished pellet samples synthesized through (a) the original method and (b) the optimized two-sintering-step process as described in this Section.

4.3 X-ray diffraction and Le Bail refinement

The crystal structure of the formed phase in the $BaNd_{1-x}Ca_xInO_{4-x/2}$ (x = 0, 0.05, 0.10, 0.15, 0.20, 0.25, 0.30) solid solution series was determined in static air by X-ray diffraction (XRD) using a PANalytical X'Pert PRO diffractometer (Cu K_α radiation). The XRD patterns are demonstrated in Figure 4.5(a) and a representative Le Bail refinement result for the BNC20 composition is shown in Figure 4.5(b). A single phase of primitive monoclinic crystal structure with the $P2_1/c$ symmetry was identified in most of the samples except for the BNC30. The lattice parameters and unit-cell volumes of the synthesized oxides were obtained by Le Bail refinement of the XRD patterns using FullProf(166) software. The starting lattice parameters' values were all set as a = 9.0954 Å, b = 6.04935 Å, c = 8.25619 Å, β = 103.4041° selected from the powder neutron diffraction data from ref(115). Crystallographic data of each composition in detail are listed in Table 4.2 below.

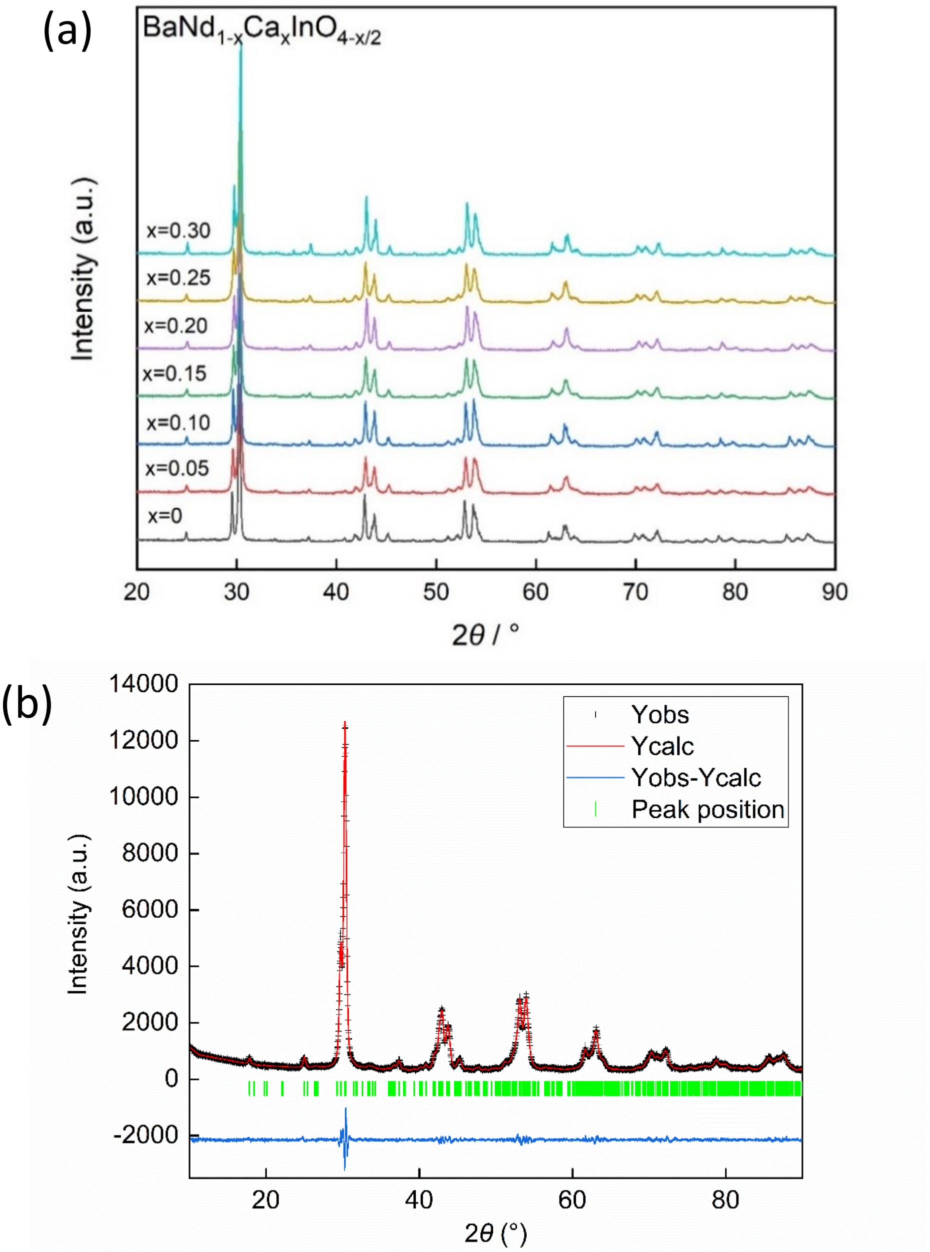

Figure 4.5 (a) Full XRD patterns of $BaNd_{1-x}Ca_xInO_{4-x/2}$ (x = 0, 0.05, 0.10, 0.15, 0.20, 0.25, 0.30) compounds. (b) Le Bail refinement result for the BNC20 composition. The dark marks are the observed experimental data; red solid line represents the calculated intensities; green vertical bars label the positions of Bragg reflection; and the blue solid line is the difference between the observed intensities and the calculated ones.

Table 4.2 Crystallographic data of $BaNd_{1-x}Ca_xInO_{4-x/2}$ obtained by Le Bail refinement.

Chemical Formula	**$BaNdInO_4$** From ref(198)	$BaNdInO_4$	$BaNd_{0.95}Ca_{0.05}InO_{3.975}$	$BaNd_{0.90}Ca_{0.10}InO_{3.95}$
Formula weight	460.38	460.38	454.78	449.17
$a/Å$	9.09538(3)	9.09311(14)	9.07978(14)	9.09297(9)
$b/Å$	6.04934(2)	6.04430(7)	6.03382(8)	6.02961(6)
$c/Å$	8.25620(2)	8.25849(12)	8.25821(14)	8.26429(9)
$\beta/°$	103.4041(3)	103.4011(14)	103.4136(13)	103.3702(9)
Unit-cell volume/$Å^3$	441.89(2)	441.540(11)	440.091(11)	440.826(8)
χ^2	/	2.61	3.00	2.56
Calculated $\rho/(g/cm^3)$	6.92	6.93	6.87	6.77

Chemical Formula	$BaNd_{0.85}Ca_{0.15}InO_{3.925}$	$BaNd_{0.80}Ca_{0.20}InO_{3.90}$	$BaNd_{0.75}Ca_{0.25}InO_{3.875}$	$BaNd_{0.70}Ca_{0.30}InO_{3.85}$
Formula weight	443.56	437.95	432.35	426.74
$a/Å$	9.08713(22)	9.06445(16)	9.10445(29)	9.09412(18)
$b/Å$	6.02438(12)	6.01195(7)	6.02169(13)	6.02482(9)
$c/Å$	8.26731(17)	8.26269(12)	8.27123(20)	8.25938(13)
$\beta/°$	103.2906(21)	103.2966(14)	103.2937(28)	103.3319(15)
Unit-cell volume/$Å^3$	440.467(16)	438.205(11)	441.312(20)	440.339(13)
χ^2	2.87	2.35	2.75	6.42
Calculated ρ/cm^3	6.69	6.64	6.51	6.44

The theoretical/calculated densities of each composition were determined using Equation (49), which were then used to obtain the relative densities of the compounds as shown in Table 4.2. As can be noticed in Table 4.3, according to the goodness of fitness, all the XRD patterns except for the BNC30 composition were refined relatively well by Le Bail refinement with a monoclinic crystal structure and the $P2_1/c$ symmetry, which agreed well with the previous literature(115, 122). In the selected region (15-35°) XRD patterns, where all the reflections were indexed with solid circles according to a primitive monoclinic unit cell as shown in Figure 4.6, the unidentified peak at 30.20° (2θ) was labelled with a hollow circle. According to previous literature(122, 199), this unidentified peak may suggest a secondary phase of barium indium oxide, $Ba_2In_2O_5$, had formed in this nominal composition sample.

Table 4.3 Refined lattice parameters of the $BaNd_{1-x}Ca_xInO_{4-x/2}$ (x = 0, 0.05, 0.10, 0.15, 0.20, 0.25, 0.30) compounds

Composition	*a*(Å)	*b*(Å)	*c*(Å)	β(°)	*V*(Å^3)
$BaNdInO_4$	9.0931(1)	6.0443(1)	8.2585(1)	103.401(1)	441.54(1)
[a]$BaNdInO_4$	9.0954(3)	6.04935(2)	8.25619(2)	103.4041(3)	441.89(1)
$BaNd_{0.95}Ca_{0.05}InO_{3.975}$	9.0798(1)	6.0338(1)	8.2582(1)	103.414(1)	440.09(1)
$BaNd_{0.9}Ca_{0.1}InO_{3.95}$	9.0930(1)	6.0296(1)	8.2643(1)	103.370(1)	440.83(1)
$BaNd_{0.85}Ca_{0.15}InO_{3.925}$	9.0871(2)	6.0244(1)	8.2673(2)	103.291(2)	440.47(2)
$BaNd_{0.8}Ca_{0.2}InO_{3.9}$	9.0644(2)	6.0120(1)	8.2627(2)	103.297(1)	438.21(1)
$BaNd_{0.75}Ca_{0.25}InO_{3.875}$	9.1045(3)	6.0217(1)	8.2712(2)	103.294(3)	441.31(2)
$BaNd_{0.7}Ca_{0.3}InO_{3.85}$	9.0941(2)	6.0248(1)	8.2594(1)	103.332(2)	440.34(1)

[a] The time-of-flight (TOF) neutron powder diffraction data at 24 °C from reference(200).

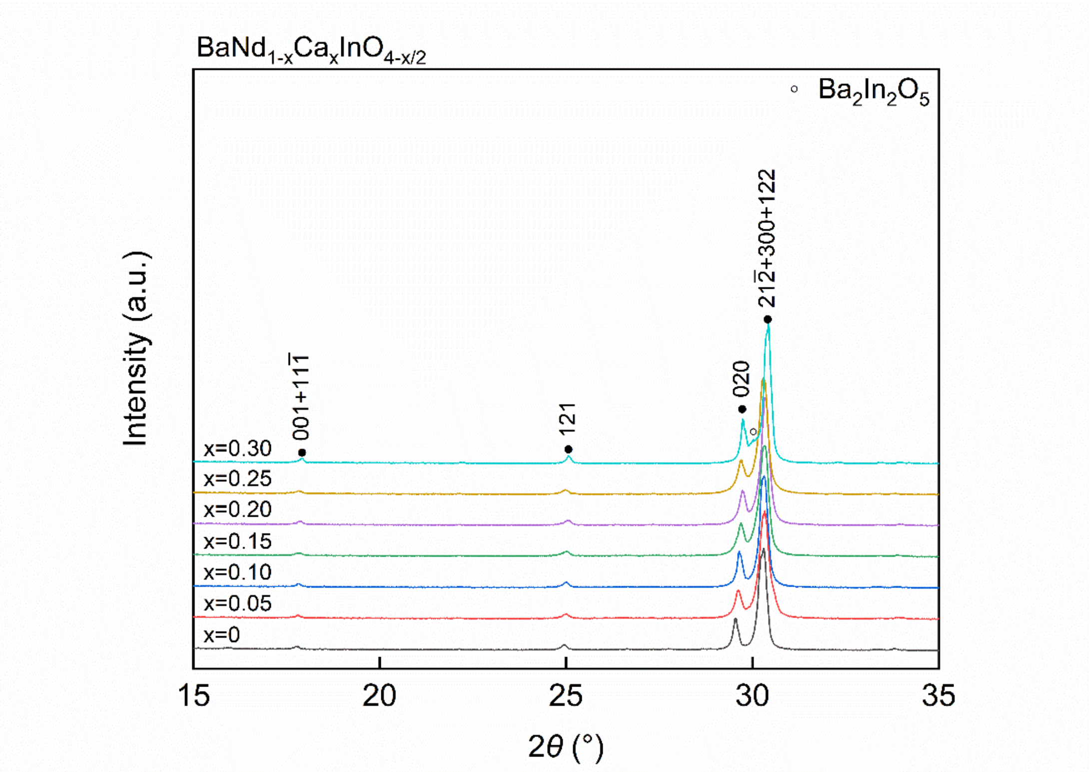

Figure 4.6 Selected region (15-35°) of the measured XRD patterns of $BaNd_{1-x}Ca_xInO_{4-x/2}$ compounds. All the reflections were indexed with solid circles according to a primitive monoclinic unit cell and the unidentified peak at 30.2° (2θ) was labelled with a hollow circle.

The substitution of calcium at the Nd sites in $BaNd_{1-x}Ca_xInO_{4-x/2}$ caused a contraction in the unit cell volume as the calcium content x increased from 0 to 0.2 (Figure 4.7 (a)), which was consistent with previous study(122). The refined lattice parameters of the BNC05 composition are off trend, and the unit cell volume of which showed a great decrease. One possible explanation for this abnormal observation in the lattice parameters of the BNC05 composition is that the calcium content was too little to form uniform $BaNd_{0.95}Ca_{0.05}InO_{3.975}$ chemical composition in the whole pellet material. As a relatively volatile element, calcium cations in the pellet sample tend to saturate in the near surface area which caused non-uniformity of the sample. During the pellet sample XRD measurement, the X-ray only interact with the material near the sample surface. Thus, the refined lattice parameters of the BNC05 composition showed off-trend values. Further experimental evidence is required to confirm the exact reason that caused this observation. Besides, a great lattice contraction in the BNC20 composition was observed, which was consistent with the previous literature(122).

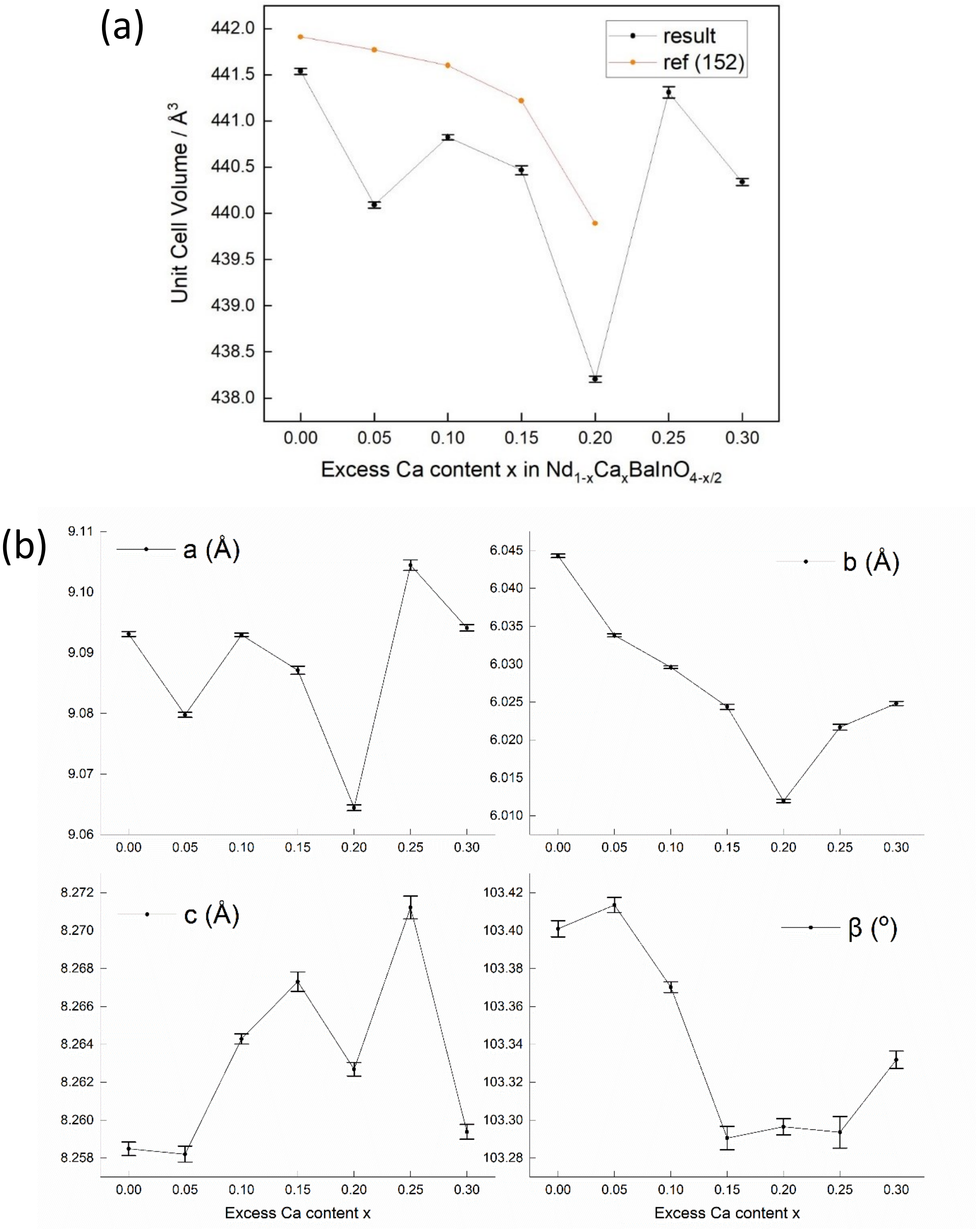

Figure 4.7 Le Bail refinement results of the (a) unit cell volume and (b) lattice parameters with error bars (3σ) of $BaNd_{1-x}Ca_xInO_{4-x/2}$ compounds versus excess calcium content x. The data points labelled as orange circles was from Yang *et al.*(122)

As illustrated in Figure 4.7 (b), the b lattice parameter showed a decreasing trend when the calcium content increased from 0 to 0.2 as well. However, the changes in the a, c and β lattice parameters are not conclusive. The non-linear fluctuation of the refined lattice parameters (unit cell volume and parameter b) as the Ca content x exceeded 0.2 implied that the solubility limit of Ca in the system was approximately 25% (i.e x =0.25). Theoretically, for the chemical compositions with Ca content exceed the solubility limit, the lattice parameters from XRD data should remain the same. Instead, remarkable fluctuations were observed in the refined lattice parameters for BNC25 and BNC30 compositions, which might due to a complex structural rearrangement as the Ca content further increase. The explanations for the aforementioned abnormal observations in the refined lattice parameters need more crystallographic information which could be obtained through other diffraction methods, i.e. neutron powder diffraction.

In comparison with the previous literatures(121, 124), the substitution of Sr^{2+} and Ba^{2+} at the Nd^{3+} site both resulted in a lattice expansion due to the larger ionic radii of the doping cations(121, 122, 124). The cation radius of the relative elements are listed in Table 4.4 below. Although the ionic radius of Ca^{2+} with a coordination number 8 is 1.120 Å which is slightly higher than that of Nd^{3+}, instead of an expanded unit cell, the substitution of Ca^{2+} at Nd^{3+} sites caused a lattice contraction. This contraction in the unit cell volume can be ascribed to the small size mismatch of the calcium and neodymium cations, which may also lead to the inequality of the solubility limits $x_{Ca} > x_{Sr} > x_{Ba}$ as described in this research and the previous literatures. The higher solubility limit of calcium doping in the $BaNdInO_4$ system allows a higher concentration of oxygen vacancies to be introduced by acceptor doping, and thus, a higher electrical conductivity could be achieved in the $BaNd_{1-x}Ca_xInO_{4-x/2}$ compounds.

Table 4.4 The ionic radii of the doping cations and the unit cell volume data from the previous literatures.

M	Cation radius*/ Å	Chemical composition	Unit cell volume** / Å^3
Nd^{3+}	1.109 (CN=8)	$BaNdInO_4$	441.89(2)$^{(115)}$
Sr^{2+}	1.260 (CN=8)	$BaNd_{0.9}Sr_{0.1}InO_{3.95}$	442.716(8)$^{(121)}$
Ba^{2+}	1.420 (CN=8)	$Ba_{1.1}Nd_{0.9}InO_{3.95}$	443.132(7)$^{(124)}$
Ca^{2+}	1.120 (CN=8)	$BaNd_{0.8}Ca_{0.2}InO_{3.90}$	439.89(9)$^{(122)}$

*The cation radius values are quoted from the online Database of Ionic Radii(201).

**The unit cell volume of the $NdBaInO_4$, $Nd_{0.9}Sr_{0.1}BaInO_{3.95}$ and $Nd_{0.9}Ba_{1.1}InO_{3.95}$ composition quoted from reference(115, 121, 124) were measured by synchrotron powder X-ray diffraction, while the data of the $Nd_{0.8}Ca_{0.2}BaInO_{3.90}$ composition was measured by X-ray powder diffraction according to reference(122).

4.4 Chemical composition characterisation

The chemical composition of the synthesized $BaNd_{1-x}Ca_xInO_{4-x/2}$ (x = 0.10, 0.15, 0.20, 0.25) compounds of the first batch, which were synthesized using the original synthesis method, were confirmed by Energy Dispersive X-ray Spectroscopy (EDS) using the JSM-6400 scanning electron microscope (JEOL Ltd.) equipped with a Noran energy dispersive X-ray analyzer. The as-sintered samples were polished manually using SiC grinding papers with grits of 600 and 1200, then coated with gold on the top surface before being imaged by SEM. Compared with a full grinding process introduced in Section 3.8.4, the manual polishing process here was rough, which could cause surface damage and introduce topographic features.

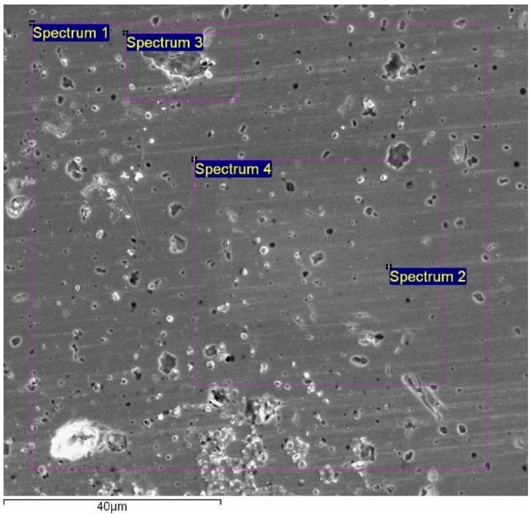

Figure 4.8 The SEM image of the 1st batch BNC20 sample. The purple squares with the spot signs labelled the chosen regions or spots tested under EDS, the spectra of which could be found in the next page.

Figure 4.8 above was achieved using SEM in the secondary electron imaging mode illustrating the surface of the polished BNC20 sample, in which a lot of topographic features can be observed. The purple squares along with the spots labelled the chosen regions or spots being tested with EDS, the corresponding EDS spectra of which can be found in Figure 4.9 in the next page. In order to check the elemental composition near the pores, region 3 was chosen particularly to be tested under EDS. As can be seen in the EDS spectra of region 3, there are slight changes in the peak intensities of the major cations which could be confirmed in detail with the atomic ratio data. An extra peak with relatively high intensity which belongs to Au was recorded as well in spectrum 3. In practice, the detector window of the EDS equipment is made of Be or a radiation-resistant polymer to stop X-ray-absorbing impurities condensing onto the cold detector. However, the windows also absorb low-energy X-rays, which results in a very poor accuracy in detecting light elements(174). Therefore, the accuracy of the quantitative analysis on the calcium and oxygen atomic ratio obtained by the EDS spectrum needs to be pay more attention. Here, it is worth using the EDS technique to get an approximation of the chemical composition for the synthesized compounds.

Table 4.5 Atomic fractions of the BNC20 1st batch sample obtained by EDS spectra and the calculated atomic ratio where Ba content is set as 1.

BNC20 1st batch	Ba	Nd	Ca	In
Spectrum 1				
Atomic fraction (%)	13.15	10.04	2.36	12.85
Atomic ratio	1	0.76	0.18	0.98
Spectrum 2				
Atomic fraction (%)	13.30	10.67	2.37	13.21
Atomic ratio	1	0.80	0.18	0.99
Spectrum 3				
Atomic fraction (%)	14.60	7.58	2.13	9.83
Atomic ratio	1	0.52	0.15	0.67
Spectrum 4				
Atomic fraction (%)	13.37	10.54	2.36	13.59
Atomic ratio	1	0.79	0.18	1.01

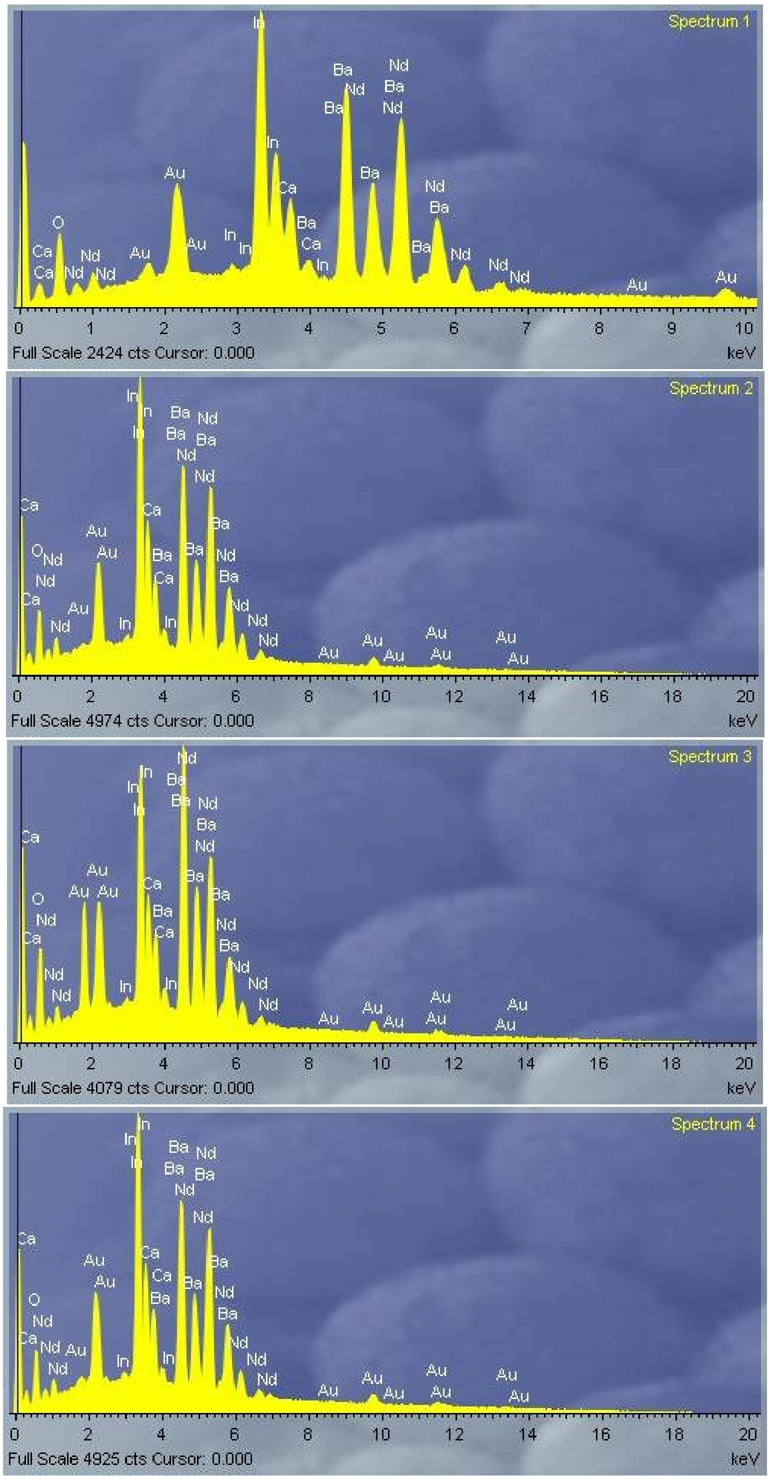

Figure 4.9 EDS spectra of the 1st batch BNC20 sample corresponding to regions 1, 2, 3 and 4 as labelled in figure 4.4.1.

In Table 4.5, the atomic ratios of each element were derived comparing the atomic fraction of the corresponding element with the barium content, as the barium contents were set as 1. The 3rd spectrum correlated to the porosity region on the sample surface showed an enrichment of barium and oxygen content according to the obtained atomic fractions which implied a possible secondary phase of barium oxide near the pores. The SEM image along with the EDS results raised a concern about the incomplete reaction of the precursors in the pellets synthesized in the original one sintering-step process. Therefore, in the modified synthesis method, the pellet samples were sintered twice, as the first sintering process was mainly aiming at completing the chemical reaction of the precursors. A ball milling step was also included in order to decrease the particle size down to micron scale, and hence improve the reaction efficiency. Apart from the abnormal data set of the 3rd spectrum, the rest of the spectra of regions 1, 2 and 4 are almost the same, where the calcium contents were slightly lower than the nominal stoichiometric amount and the Nd contents showed some fluctuation around 0.8. The small fluctuation of Nd contents could be due to the poor resolution of the technique in separating the Nd and Ba signals, the peaks of which overlapped severely in the EDS spectra. The slightly lower atomic ratio of the calcium content may be due to the exsolution of calcium cations out of the system during the high temperature sintering process. Therefore, in order to avoid the possible loss of calcium, a modified sintering process was completed at 1300℃ instead as described in Section 4.2. Another possible explanation for the low atomic ratio of calcium is because of the absorption of characteristic X-rays generated from the light element by the gold coating on the sample surface. In order to mitigate the error resulted from the absorption by gold coating, carbon coating can be processed in preparing the EDS samples as an alternative.

In order to investigate the chemical stability of the phase in the as-sintered pellets, the BNC20 synthesized using the aforementioned two-sintering-steps process was polished using SiC grinding papers with grits of 600, 1200 and 2000 successively. The polished pellet was annealed at 800℃ for 6 hours, then coated with gold and imaged under SEM backscattered electron (BSE) imaging mode to identify any segregation or secondary phases. The secondary electron (SE) and backscattered electron (BSE) images of the sample before and after annealing are shown in Figure 4.10. Unlike the secondary electron imaging mode of SEM, where the difference in brightness of the image is due to the topographic features of the sample surface, in the backscattered electron imaging mode, the brightness change is ascribed to the elemental difference in a specific region. According to the two following BSE images, there was no segregation or secondary phase emerging on the sample surface during the high temperature sintering process or the subsequent annealing process. Some scratches resulted from the polishing step can be observed in the SE images of the sample before annealling, which were more obvious after being annealed at 800℃ for 6 hours. It is worth noting that with the same contrast and brightness, the SE image of the sample after annealing showed some patterns with a different colour which could be ascribed to different grains. According to Figure 4.10(c), the size of the grains were 10 ~ 20 μm (sintered at 1400℃ for an hour first, then sintered at 1300℃ for 24 hours) which were slightly smaller than the grain size of the 1400℃-sintered sample (15 ~ 30 μm) showed in Figure 4.2(b).

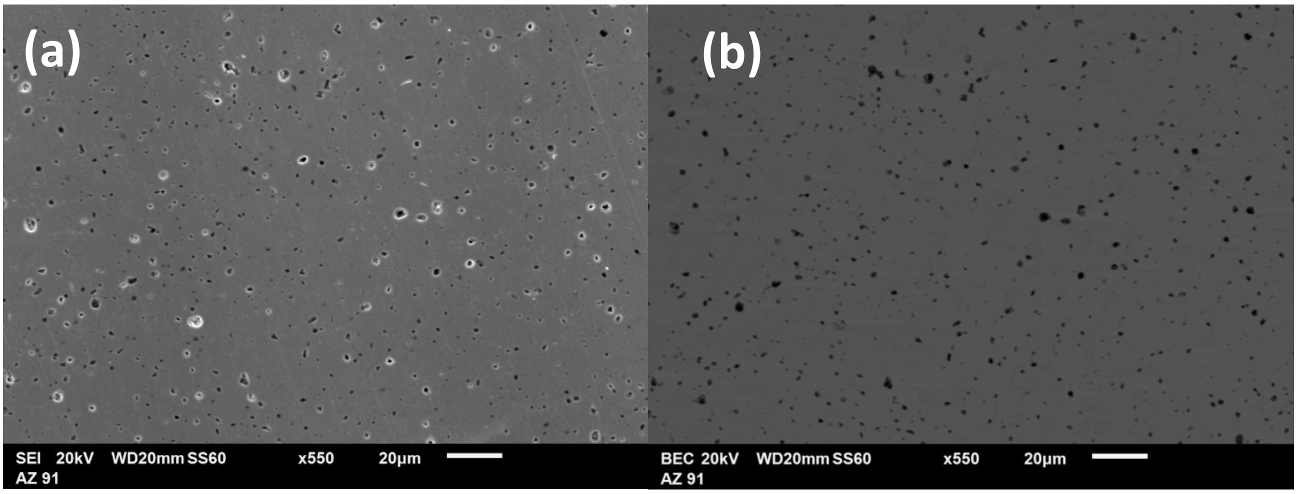

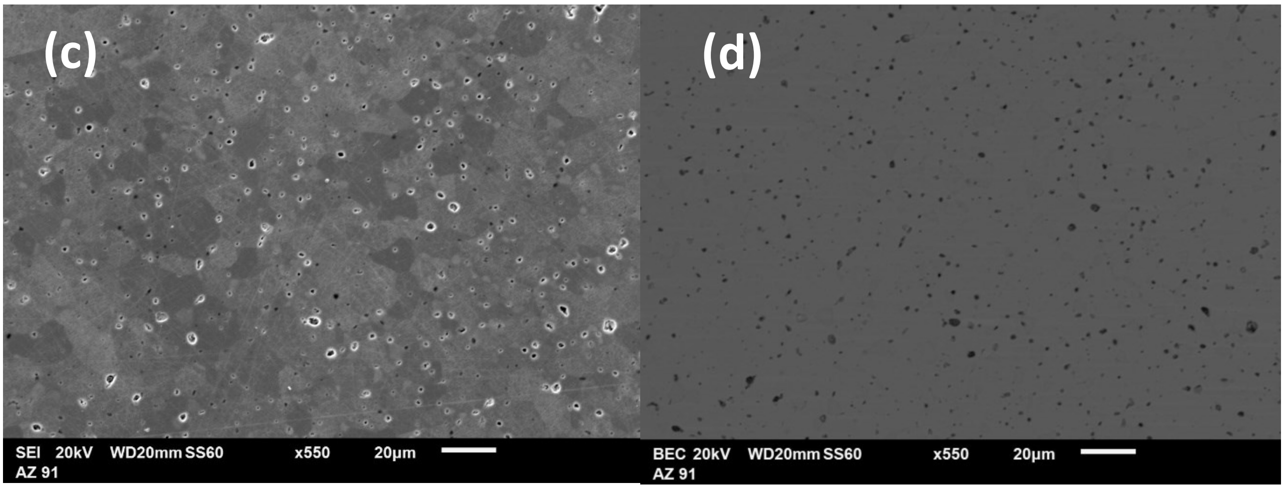

Figure 4.10 The (a) SE and (b) BSE images of the same area on the surface of the 2nd batch polished BNC20 pellet sample before annealing process. The (c) SE and (d) BSE images of the same area on the 2nd batch polished BNC20 pellet sample after 800 ℃ annealing for 6 hours.

The chemical composition of the 2nd batch BNC20 sample was also confirmed by Energy Dispersive X-ray Spectroscopy (EDS) this time using the JSM-6100 SEM (JEOL Ltd.) equipped with an energy dispersive X-ray detector (Zeiss Leo Gemini 1525, with an extra high tension of 20 kV, and an aperture size of 60 μm). The EDS spectrum of the selected region was recorded in the BSE mode of the SEM equipment as shown in Fig 4.11 & Fig 4.12.

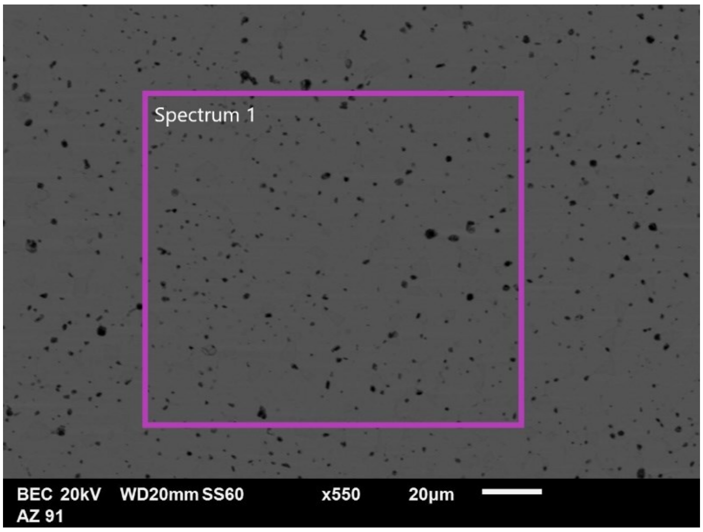

Figure 4.11 BSE image of the 2nd batch BNC20 sample surface. The purple square presents the interesting area tested under EDS.

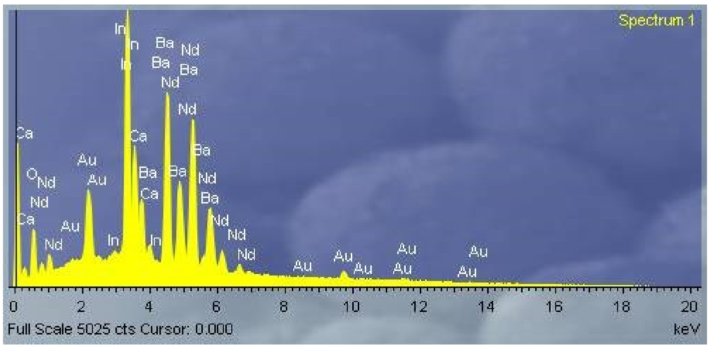

Figure 4.12 EDS spectrum of the 2nd BNC20 sample corresponding to region 1 as labelled in Figure 4.4.4.

Table 4.6 Atomic fractions of the BNC20 2nd batch sample obtained by EDS spectra and the calculated atomic ratio where Ba content is set as 1.

BNC20 2nd batch	Ba	Nd	Ca	In
Spectrum 1				
Atomic fraction (%)	13.01	10.24	2.24	13.08
Atomic ratio	1	0.79	0.17	1.01

The atomic ratio of calcium and neodymium were again slightly lower than the designed stoichiometric amount, which may be due to the detection limits of the equipment. However, the surface of the sample looked uniform under the BSE imaging mode, which implied a single-phase product was successfully synthesized using the modified process. Furthermore, the material chemical stability was tested through an annealing process at 800 ℃ in static lab air for 6 hours. No secondary phase or segregation was observed in the backscattered electron images.

The chemical compositions of other synthesised compounds were also checked using the EDS characterisation method, the concluded results are listed in Table 4.7 below where the atomic fraction of each element was calculated by averaging the atomic fraction data of at least 3 different EDS spectra on the same sample. As can be seen in Table 4.7, the atomic ratio of the BNC10 and BNC15 sample agreed well with the designed stoichiometry, both of which showed a slightly lower calcium concentration, while the BNC25 sample showed a relatively large deficiency of the Nd and Ca content in the EDS measurement. The standard deviation values of the atomic fraction data for the BNC25 sample are quite large compared with those of the other samples. Although quantitative analysis using the EDS technique is affected by various factors, which may have an impact on the accuracy of the derived atomic fractions, the results of these EDS measurements, especially the significant elemental deficiency and higher deviation in the data of the BNC25 sample, implied that the solubility limitation of calcium substitution at the Nd site in $BaNdInO_4$ is approximately around 25%. This observation was consistent with the XRD results.

Table 4.7 Atomic fractions of the $BaNd_{1-x}Ca_xInO_{4-x/2}$ (x = 0.10, 0.15, 0.25) compounds obtained by EDS technique and the calculated atomic ratio where Ba content is set as 1.

	Ba	Nd	Ca	In
BNC10	1	0.9	0.1	1
Atomic fraction (%)	14.05(2)	12.51(1)	1.33(1)	15.18(1)
Atomic ratio	1	0.89	0.095	1.08
BNC15	1	0.85	0.15	1
Atomic fraction (%)	14.67(1)	11.72(1)	1.93(1)	15.00(1)
Atomic ratio	1	0.83	0.14	1.00
BNC25	1	0.75	0.25	1
Atomic fraction (%)	15.5(3)	10.12(5)	3.2(5)	14.91(5)
Atomic ratio	1	0.65	0.20	0.96

4.5 Summary

In summary, based on some preliminary material characterisation methods including dilatometry, scanning electron microscopy (SEM) and energy dispersive X-ray spectroscopy (EDS), the original solid state reaction synthesis method as described in Section 4.1 was modified into a two-sintering-steps process. By using the new synthesis approach, single-phase dense pellet samples with relative densities around 98% were successfully prepared.

The crystal structure of the formed phase in the $BaNd_{1-x}Ca_xInO_{4-x/2}$ (x = 0, 0.05, 0.10, 0.15, 0.20, 0.25, 0.30) solid solution series was determined in static air by XRD, by which a single phase of primitive monoclinic crystal structure with the $P2_1/c$ symmetry was confirmed in most of the samples except for the BNC30 sample. According to the refined lattice parameters obtained by Le Bail refinement of the XRD patterns, the substitution of calcium at the Nd sites in $BaNd_{1-x}Ca_xInO_{4-x/2}$ caused a contraction in the unit cell volume as the calcium content x increased from 0 to 0.2. This decrease in the lattice size can be ascribed to the small size mismatch of the calcium and neodymium cations. An additional peak corresponding to the emerged secondary phase of $Ba_2In_2O_5$ was identified in the XRD pattern of the BNC30 sample, which can be used in combination with the out-of-trend changes in the lattice parameters as the calcium content x exceeded 20% to estimate the solubility limit of calcium doping in the $BaNdInO_4$ system (~ 25%).

The chemical compositions of the solid solutions were confirmed by the EDS characterisation method, where a lower atomic fraction of calcium was observed in all compositions which could be due to the exsolution of calcium cations out of the system during the high temperature sintering process. Gold coating on the sample surface may also account for the relatively low atomic ratio of calcium which absorbs the characteristic X-rays generated from the light elements underneath. The EDS results also suggested that the solubility limit of calcium doping in the $BaNdInO_4$ system is approximately around 25% as the atomic fraction data for the BNC25 sample fluctuated significantly when changing the analysed regions. Besides, severe deficiency of Nd and Ca content was observed in the EDS data of the BNC25 sample.

By using the modified synthesis method, dense samples with high relative density and high quality were successfully prepared. Therefore, in the following chapters, all the measurements and discussion are based on samples synthesized using this optimized method.

4.6 Possible future work

Other characterisation methods, such as inductively coupled plasma atomic emission spectroscopy (ICP-AES), for the determination of chemical compositions of the synthesised $BaNd_{1-x}Ca_xInO_{4-x/2}$ (x = 0, 0.05, 0.10, 0.15, 0.20, 0.25, 0.30) solid solutions could be carried out to make a comparison with the EDS data. So that a more comprehensive understanding on the chemical composition information of the synthesised ceramics could be achieved. The STEM-EDS technique can also be applied to probe the distribution of all elements in the system and to detect any local deficiency of a particular element near grain boundaries or some inhomogeneous features in the bulk material.

Apart from that, to probe the more detailed crystallographic information of the synthesized $BaNd_{1-x}Ca_xInO_{4-x/2}$ solid solutions, synchrotron or neutron powder diffraction techniques can be applied, which are powerful technologies in probing the precise lattice structures and coordinates of all atoms within the lattice. In particular, it is worth conducting some further crystallography study on these calcium doped $BaNd_{1-x}Ca_xInO_{4-x/2}$ solutions to confirm the exact substituting sites of calcium cations. The Rietveld refinement of high quality diffraction data can give more detailed information about the phase quantities, atomic coordinates and bond lengths, micro strain and oxygen vacancies, which are crucial in understanding the oxygen diffusion mechanism in the system.

Chapter 5

Electrochemical performance and triple (electron, oxide-ion and proton) conduction in $BaNd_{1-x}Ca_xInO_{4-x/2}$

The electrochemical properties of the $BaNd_{1-x}Ca_xInO_{4-x/2}$ solid solutions synthesized using the two-sintering-steps process described in Chapter 4, was measured by several electrochemical characterization methods, the results of which will be discussed in this Chapter. According to the electrochemical impedance spectroscopy (EIS) results on the pristine $BaNdInO_4$, the BNC10 and BNC20 samples, a significant enhancement in the electrical conductivity caused by calcium doping was observed. The EIS measurements of the BNC10 and BNC20 samples under various gaseous atmospheres showed evidence of triple (electronic, ionic and protonic) conduction in the system. The protonic conduction of the BNC20 sample was then confirmed using a coupled thermogravimetric analysis and DC conductivity measurement system. On the other hand, clear evidence showed that the chemical stability of the material was affected by the wet gaseous environments. The surface topography of the BNC20 sample before and after being annealed in a wet atmosphere was analyzed by SEM.

5.1 Electrochemical impedance spectroscopy (EIS) measurements

5.1.1 Sample preparation and detailed experimental procedures

Samples of $BaNd_{1-x}Ca_xInO_{4-x/2}$(x=0, 0.1. 0.2) solid solutions for AC impedance measurements were synthesized through the modified solid state route, which were polished manually using SiC grinding papers with grit sizes of 800 and 1200 successively after sintering. Further finer polishing process was not carried out on these samples since a relatively rough surface could improve the adhesion between the electrodes and the pellet surfaces in the following step. Then, platinum conducting paste (for brush application, 71% Pt, Glentham Life Science Ltd.) was applied on both sides of the pellets using a brush. The pellet with Pt paste was preliminarily dried on a hot plate, then put into a furnace to be annealed at 800 ℃ for 2 hours in order to let the ink dry completely and improve the electrodes' adhesion at the same time. Special attention needs to be paid to the condition of the platinum paste since a thin platinum suspension will result in cracks in the electrodes. The nonuniformity of the electrodes on the pellet surfaces will lead to significant error in the following AC impedance measurements. A multimeter was used to test the surface resistivity of the applied electrodes and platinum meshes were used during the EIS measurements to avoid the artifacts caused by the electrodes surface non-uniformity.

As discussed in Chapter 3, the as-prepared symmetrical cells were put into the home-made apparatus where two platinum meshes and a movable outer tube were used to support the cell. The impedance signals were produced and introduced by a Solartron 1260a Impedance Analyser under the open circuit voltage (OCV) condition with a frequency range from 10 MHz to 0.01 Hz measuring 40 points per decade, and the amplitude was set as 100 mV. The impedance measurements of the pristine, BNC10 and BNC20 samples were conducted in a thermal cycle comprising a heating program with a heating rate of 5 °C/min to each temperature, starting from 250 °C, followed by 60 mins thermal equilibration, with step sizes of 25 °C until a maximum temperature of 750 °C was reached. This was followed with a cooling programme with the same steps and ramp rates to probe if there was any hysteresis in the material. The whole apparatus was sealed during the measurements while the flow of compressed air or nitrogen was introduced through a drying tube containing $CaSO_4$ before entering the impedance rig to create dry atmospheres. A water bubbler was connected into the system between the gas cylinder and the impedance rig to examine the influence of water vapour on the electrochemical properties of the materials. With this set-up it was possible to measure the same sample, first in the dry atmosphere and then in the wet atmosphere. It needs to be mentioned that before the impedance spectroscopy measurement in the humid atmosphere, the sample was annealed in humid gas at 500 ^oC for 8 hours to ensure that the equilibrium of the water incorporation was achieved. The impedance data were analysed using ZView (180) software package.

5.1.2 Various atmospheric EIS measurements and protonic conductivities

The electrical conductivity of the pristine $BaNdInO_4$ together with the 10% and 20% calcium substituted samples was measured by electrochemical impedance spectroscopy in dry air. As described in the last section, AC impedance measurements of each symmetrical cell sample were conducted first in a heating cycle, then in a cooling cycle with the same temperature steps. No significant difference was observed between the data points obtained at the same temperatures in dried air from the heating and cooling cycles for all three samples. The consistency of the data sets for each sample implied that there was not any hysteresis in the materials. Representative fitted impedance spectra along with the equivalent circuits created in ZView to simulate the Nyquist plots are shown in Figure 5.1(a)&(b). As can be noticed, at low temperatures (523-573 K) the Nyquist plots contain two semicircles representing the bulk and grain boundary contributions, respectively, that can be simulated with two R-CPE (constant phase element) components connected in series. The associated capacitances, C_1 and C_2, can be estimated using the relation $2\pi f_{max}RC=1$ and were $\sim 1.1 \times 10^{-11}$ Fcm^{-1} and $\sim 1 \times 10^{-8}$ Fcm^{-1}, indicative of the bulk and grain boundary responses respectively, where f_{max} is the frequency at the arc maximum. However, at high temperatures the bulk resistance can only be obtained as the left intercept of the plots with the real part of the impedance (Z'), and the complex impedance plots can be simulated with one inductor and two R-CPE components connected in series.

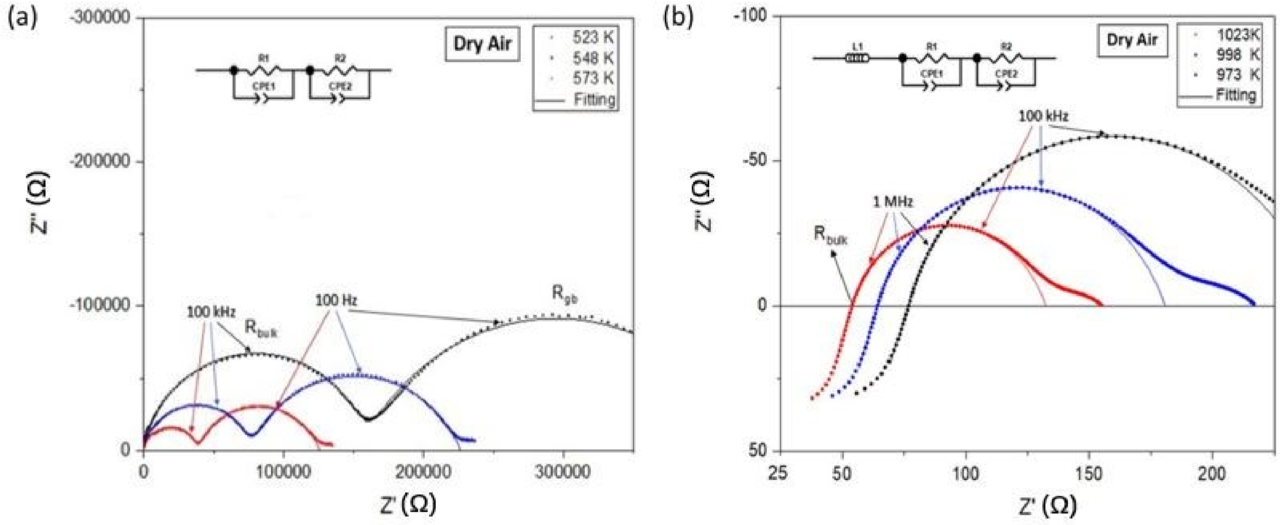

Figure 5.1 Impedance spectra of BNC20 measured in dry air at (a) low (523-573 K) and (b) high (973-1023 K) temperatures. Solid lines show the fit to the equivalent circuit models. Low frequency electrode response is omitted from the fit.(202).

The detailed AC impedance data fitting results of the BNC20 sample measured in the cooling cycle in dry air is included in the Appendices as Table A.1. The goodness of fit, χ^2, were all around $10^{-4}\sim10^{-5}$ which means that the proposed equivalent circuits fit quite well with the analysed system. The constant phase element was introduced in the fitting of the two semi-circles in Nyquist plots, where the as-derived corresponding parameters *CPE-P* and *CPE-T* can be used to calculate the capacitance of the process (according to Equation 65). The capacitances, C_1 and C_2, derived through this method were also within the capacitance range of the bulk and grain boundary responses. The low frequency electrode-related responses are omitted from the fit since we mainly focused on the electrolyte materials. When the temperature reached 550 ℃ or higher temperatures, the values of *CPE-P* were fixed as 1 during simulation and the CPE component can be replaced by a pure capacitor. It is worth noting that *CPE-P* is a value of between 0 and 1. A value larger than 1 in the *CPE-P* parameter is not acceptable, and therefore, the value of *CPE-P* parameter was fixed as 1 in the corresponding simulations in which case the Nyquist plot was fitted to a R-capacitor component.

By doing the analysis above, the total conductivities of three samples were calculated using the addition of bulk and grain boundary resistance and the geometrical parameters of the pellets. All three Arrhenius plots of the total conductivities are presented in Figure 5.2, which indicates a significant improvement of the total electrical conductivity on calcium substitution at the Nd^{3+} site. Among those samples, the BNC20 sample showed the highest total conductivity of 2.6 x 10^{-3} Scm^{-1} at 750 °C, while the total conductivity of the BNC10 sample was 1.8 x 10^{-3} Scm^{-1} at the same temperature. According to the EIS results, the electrical conductivity of the $BaNdInO_4$ pristine material could be enhanced by 1-2 orders of magnitude over a large temperature range through calcium substitution. This enhancement can be ascribed to the formation of oxygen vacancies in the system by acceptor doping:

$$2\mathrm{CaO} + 2\mathrm{Nd}_{\mathrm{Nd}}^{\mathrm{x}} + \mathrm{O}_{\mathrm{O}}^{\mathrm{x}} \rightarrow 2\mathrm{Ca}_{\mathrm{Nd}}' + \mathrm{V}_{\mathrm{O}}^{\cdot\cdot} + \mathrm{Nd}_2\mathrm{O}_3 \tag{70}$$

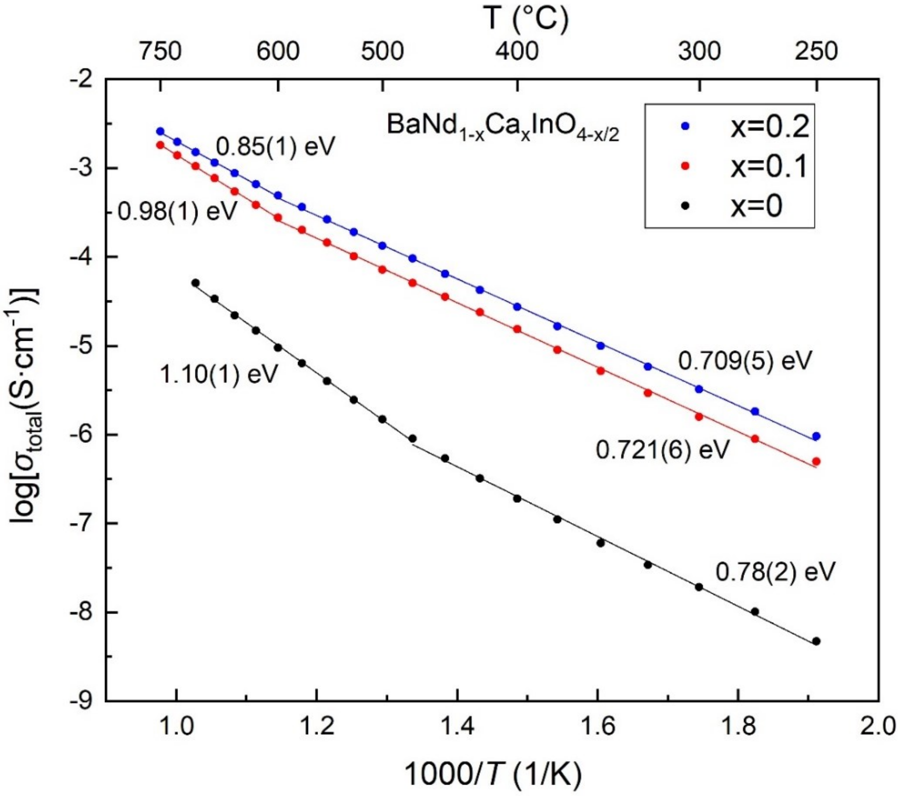

Figure 5.2 Arrhenius plots of the total conductivity of the $BaNdInO_4$ (black), BNC10 (red) and BNC20 (blue) samples measured in dry air with the calculated activation energies displayed in both low and high temperature regimes(202).

A change in the slope of the Arrhenius plots is observed in all three chemical compositions which is not due to any irreversible chemical change during the impedance measurements as the data obtained on a cooling cycle for all samples showed no significant difference compared to those obtained on the heating cycle. One hypothesis is that the change in the activation energies is due to the change of the dominant charge carriers in the system. In the low temperature range (250-500 °C for the parent material and 250-600 °C for the Ca substituted samples), the materials exhibit mixed conduction (electronic and ionic) which allows a mixture of charge carriers to flow through the system including oxide-ion and hole conduction(121, 122). However, when the temperature was increased (>500 °C for the parent material and >600 °C for the substituted samples), oxide ions became the dominant charge carriers as the number of hole defects was reduced due to the loss of oxygen in the system according to the defect equation below:

$$\mathrm{O_O^x} + 2\mathrm{h^{\cdot}} \leftrightarrow \mathrm{V_O^{\cdot\cdot}} + \frac{1}{2}\mathrm{O_2} \uparrow \tag{71}$$

As a result of this reduction in p-type transport, the activation energy of the pristine material increased from 0.78(2) eV (mixed p-type and oxide-ion conduction) to 1.10(1) eV (predominant oxide-ion conduction) as the temperature increased. As for the calcium doped samples, the slope changing temperature is higher because of the higher concentration of oxygen vacancies in the system due to the acceptor-doping, which inhibits the loss of oxygen to some extent, according to the equation above. Therefore, the activation energies of the BNC10 and BNC20 samples changed from 0.72(1) eV and 0.71(1) eV respectively to 0.98(1) eV and 0.85(1) eV when the temperature increased beyond 600 °C. The Arrhenius plots also indicate that the activation energy for the total conductivity of the pristine material can be reduced by calcium doping in both the lower and higher temperature ranges, which could be ascribed to the increase of oxygen vacancies in the system.

To probe the potential for protonic conductivity, water vapour was introduced into the sealed tube in the EIS system by placing a water bubbler in line between the supply gas cylinder and measurement apparatus. The flowing gas carried ~3% H_2O (25 °C) vapour into the system which was then incorporated into the BNC20 and BNC10 samples forming protonic defects as shown in the equation below:

$$\mathrm{H_2O} + \mathrm{V_O^{\cdot\cdot}} + \mathrm{O_O^x} \leftrightarrow 2\mathrm{OH_O^{\cdot}} \tag{72}$$

In practice, each sample was annealed in the humid environment at 500 °C for at least 8 hours to ensure that the equilibrium of the water incorporation was achieved before the ‘wet’ impedance spectroscopy measurement was performed. Special care was taken upon analysing these wet atmospheric impedance data with respect to the influence of water vapor on the phase stability. The consistency of the data sets of the BNC20 sample measured in the heating and cooling cycles in wet air is illustrated in Figure 5.3. A small difference was noticed in the low temperature range of the two Arrhenius plots, which may be due to the incomplete hydration of the pellet samples in the pre-annealing step. The detailed AC impedance data fitting of the BNC20 sample measured in the cooling cycle in wet air is listed in the Appendices as Table A.2, where the two R-CPE model still gave good fitting results as the goodness of the fits, χ^2, were all below 1 x10^{-3}.

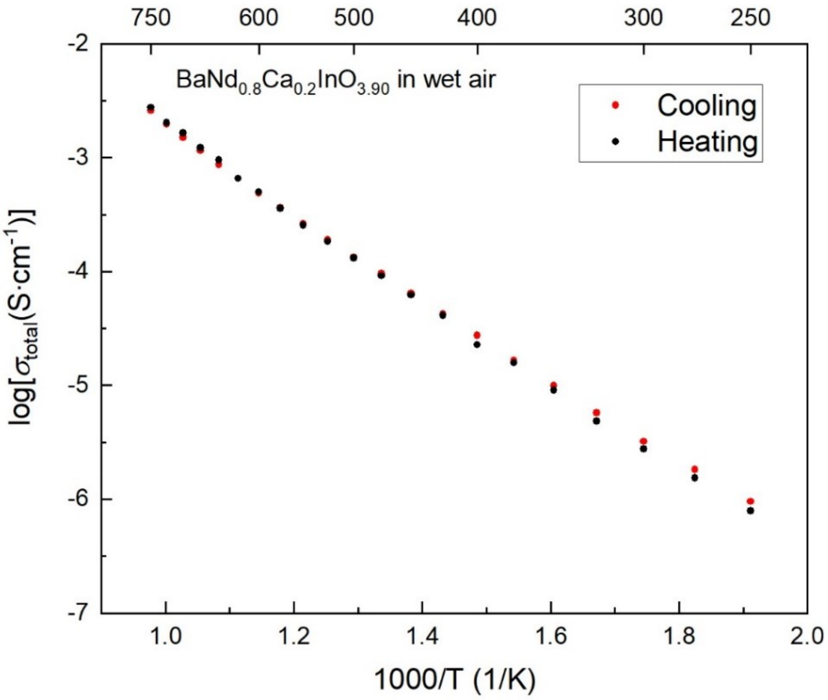

Figure 5.3 Arrhenius plots of the total conductivity of the BNC20 sample measured in heating (dark circles) and cooling (red circles) in wet air.

As can be seen in Figure 5.4 (a) & (b), both BNC10 and BNC20 samples exhibited higher total conductivity under humid air than those obtained in dry air over a large temperature range (250-750 °C) which could be ascribed to the formation of protonic defects in the material. The total conductivity of BNC20 in wet air at 500 °C was 1.3 x10^{-4} Scm^{-1} which was higher than the total conductivity of most of the state-of-the-art proton conducting materials measured under the same conditions (203). EIS measurements on the BNC20 sample were also carried out in dry and wet N_2 resulting in a similar trend as observed in dry air. The total conductivity of the BNC20 sample measured in N_2 atmosphere was lower than when measured in air, which implies that this material exhibits p-type conduction in O_2 rich atmospheres. This result is consistent with previous reports (115, 122).

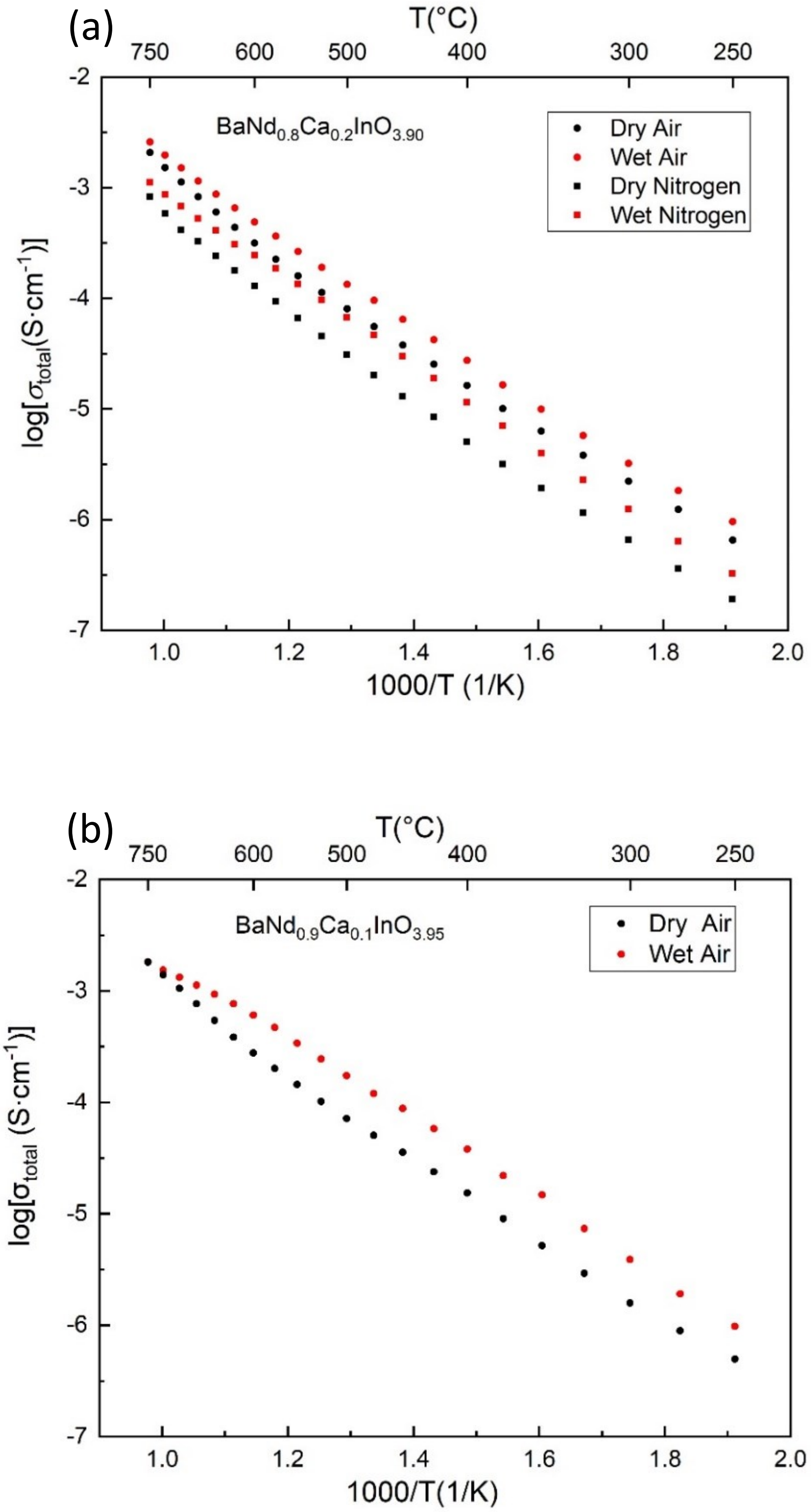

Fig 5.4 Arrhenius plots of the total conductivity of the (a) BNC20 and (b) BNC10 samples measured in dry and wet atmospheres

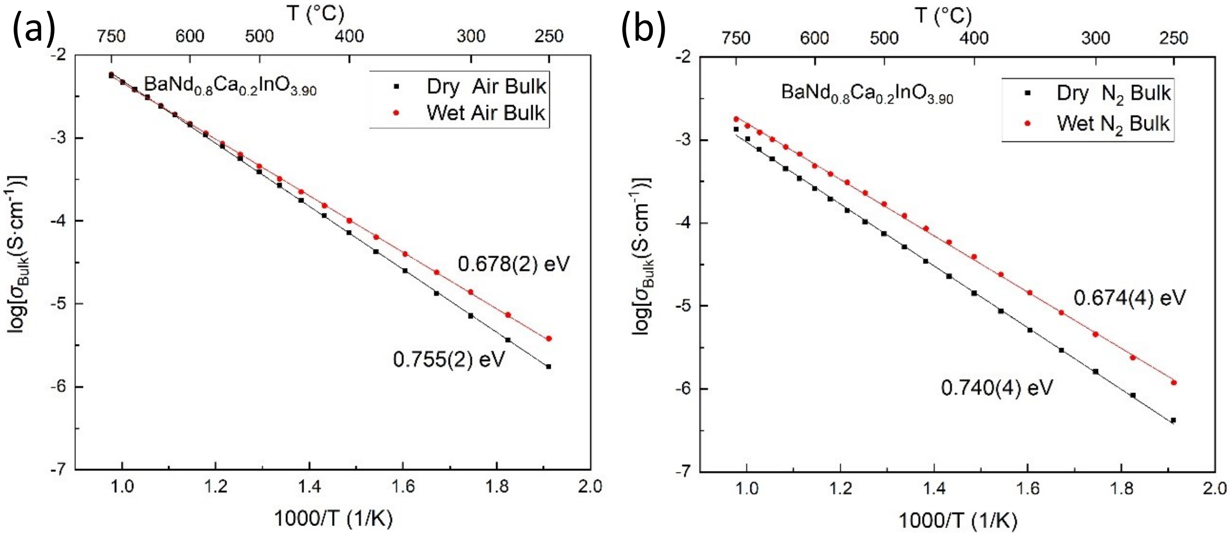

Fig 5.5 Arrhenius plots of bulk conductivity of a BNC20 sample under (a) dry and wet air and (b) dry and wet N_2 respectively

In order to investigate the influence of humidity on the electrochemical properties of BNC20 samples more deeply, the bulk conductivity was deduced by extracting the bulk resistance and calculating according to the brick layer model (204) assuming the area of the bulk in the material equals the whole area of the sample. As shown in Figure 5.5 (a) & (b), four Arrhenius plots of the bulk conductivity of BNC20 samples under different atmospheres fit well to a straight line which gives the activation energies for bulk conductivity as 0.755(2) eV in dry air, 0.678(2) eV in wet air, 0.740(4) eV in dry N_2 and 0.674(4) eV in wet N_2. There was an increase in the bulk conductivities of the samples both in air and in N_2 when water vapour was introduced to the system. The influence of the humidity on bulk conductivities were more significant in a N_2 atmosphere than in air, which can be ascribed to the excessive amount of oxygen vacancies in an O_2 deficient environment according to the equation below:

$$\frac{1}{2}\mathrm{O}_2 + \mathrm{V}_\mathrm{O}^{\cdot\cdot} \leftrightarrow \mathrm{O}_\mathrm{O}^\mathrm{x} + 2h^{\cdot} \qquad \text{for high } p(\mathrm{O}_2)$$

In addition, the activation energies for the bulk conduction decreased on introducing water vapour to the system, which implies a change in the conduction mechanism in the bulk material. Since the proton mobility is higher than that of oxygen ions (138, 205), the decrease in the activation energies could be evidence of proton conduction in the bulk material. Comparing the data in Figure 5.5(a)&(b), the activation energy of the bulk conductivity in both dry and wet atmospheres is independent of $p(O_2)$ within the O_2-N_2 $p(O_2)$ range, suggesting limited impact of electronic charge carriers on the activation energies. In conclusion, the BNC20 sample exhibits p-type and oxide-ion mixed conduction under dry atmospheres within the O_2-N_2 $p(O_2)$ range, while the incorporation of humidity can significantly increase the conductivity in the bulk and decrease the activation energies of the bulk conductivity which implies that this material may exhibit triple (oxygen-ions, protons and holes) conduction under wet atmospheres. The transport number of protons is the fraction of the total electrical current carried by protons, t_p , which can be estimated using the equation:

$$t_\mathrm{p} = \frac{\sigma_p}{\sigma_{tot}} = \frac{\sigma_{wet\ N2} - \sigma_{dry\ N2}}{\sigma_{wet\ N2}} \qquad (73)$$

assuming that in dry N_2 the total electrical conductivity is attributed to oxide-ions alone, and thus the proton conductivity could be estimated by the subtraction of total conductivity in wet N_2 and the total conductivity in dry N_2. In the temperature range from 250 °C to 475 °C the transport number of protons t_p increased from 0.41 to 0.57. Then it shows a decreasing trend as the temperature further increases which is likely due to the dehydration of the sample at high temperatures. The transport number t_p as a function of temperature is illustrated in Figure 5.6. Further direct measurements would be required to verify the assumption and the transport number of protons in this material.

It is interesting to note that there was no change within error in the activation energy for bulk conductivity of the BNC20 sample as the atmosphere changed from wet air (0.678(2) eV) to wet N_2 (0.674(4) eV). However, the bulk conductivity was still higher in wet air than in wet N_2 which, as discussed above, is due to the filling of oxygen vacancies by O_2 introducing extra holes. This could be evidence suggesting that mobility of protons is much faster than that of oxide-ions in the system, and therefore, the change in the oxygen partial pressure barely influences the conducting mechanism of the system.

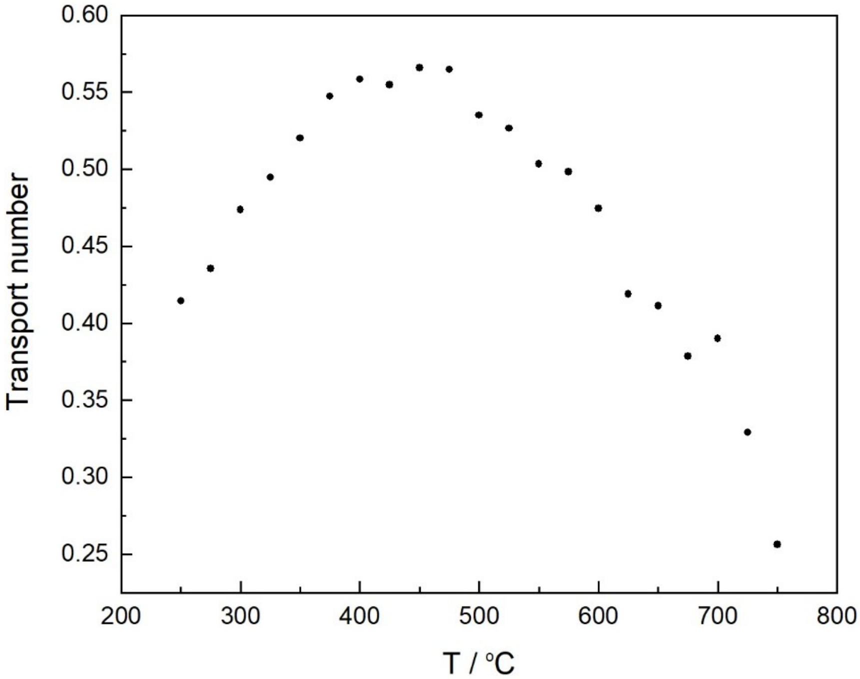

Figure 5.6 The transport number t_p as a function of temperature derived from the wet conductivity data of the BNC20 sample measured in wet N_2.

By assuming that in dry N_2 the total electrical conductivity is attributed to oxide-ions alone, we could also derive the activation energy for the oxide-ion conduction in the grains of the BNC20 sample to be 0.740(4) eV, which is a little higher than the value (0.70 (2)) obtained in Yang *et al.*'s work, but still lower than the activation energies for oxide-ion conduction obtained in the $Ba_{1.1}Nd_{0.9}InO_{3.95}$ (0.86(3) eV)(124) and $BaNd_{0.9}Sr_{0.1}InO_{3.95}$ (0.795(10) eV)(121) compositions and as reported by Shiraiwa, Fujii *et al*. The lower energy barriers in $Ba_{1.1}Nd_{0.9}InO_{3.95}$ and $BaNd_{0.9}Sr_{0.1}InO_{3.95}$ for oxide-ion migration compared to that of the pristine $BaNdInO_4$ (0.91(4) eV(115)) were confirmed in the BVE landscapes in the literature, which were attributable to the larger bottleneck sizes after substitution of the barium and strontium cations at the Nd sites, according to the author(116). Similar conclusion was drawn in Shiraiwa's paper on the solid solution of $Ba_{1.1}Nd_{0.9}InO_{3.95}$(124). However, there seems to be a contradiction in calculation of the bottleneck areas using the BVE method, as the areas of the diffusion triangles for $BaNdInO_4$ in two papers were different, 6.768(2) $Å^2$ in reference (124) and 6.911(3) $Å^2$ in reference (121). Apart from that, assuming that the activation energy change does result from the larger bottleneck sizes for Sr and Ba doped sample, then the triangle area in the Ba doped lattice should be larger leading to a lower energy barrier for oxygen diffusion. But the experimental results for Ba and Sr doped samples exhibited a reverse trend. The 'bottleneck theory' can neither explain why $BaNd_{0.8}Ca_{0.2}InO_{3.90}$ solid solution showed the lowest activation energies for oxide-ion conduction in the system among all the acceptor dopants, as the calcium substitution caused a lattice contraction as mentioned in Section 4.3.

Table 5.1 The activation energies for oxide-ion conduction in $BaNdInO_4$-type solid solutions obtained in this research (labelled with *) and in previous literatures.

M	Cation radius **(201)**	Chemical composition	Activation energy $E_{\text{oxide-ion}}$ / eV
(Nd)	1.109(CN=8)	$BaNdInO_4$	0.91(4)
Sr	1.26(CN=8)	$BaNd_{0.9}Sr_{0.1}InO_{3.95}$	0.795(10)
Ba	1.38(CN=8)	$Ba_{1.1}Nd_{0.9}InO_{3.95}$	0.86(3)
Ca	1.12(CN=8)	$BaNd_{0.8}Ca_{0.2}InO_{3.90}$	0.71(1)
Ca*		**$BaNd_{0.8}Ca_{0.2}InO_{3.90}$**	**0.740(4)**

The activation energies for oxide-ion conduction of the acceptor doped $BaNdInO_4$ solid solutions according to the doping cations are in the sequence of $(\mathrm{Nd}) > \mathrm{Ba} > \mathrm{Sr} > \mathrm{Ca}$, which could be ascribed to the defect association in the system as discussed in the Introduction part (Section 2.4.3). Based on the defect associations in the system, the tendency of oxygen vacancies to be associated with the heavy dopant cations would increase the activation energy of conduction by adding an association enthalpy ΔH_{A}(63). However, further investigations with empirical or simulation methods are required to verify for this hypothesis.

Table 5.2 Comparison of total conductivities of the state-of-art proton conducting electrolytes at 500℃ in conditions when proton conducitivity dominates.

Chemical Composition	$\boldsymbol{\sigma_{\mathrm{Total}}/\mathrm{S\cdot cm^{-1}}}$ **@500℃**	**Reference**
$BaCe_{0.7}Zr_{0.1}Y_{0.2}O_{3-\delta}$	8×10^{-3}	(206)
$BaCe_{0.4}Zr_{0.4}Y_{0.2}O_{3-\delta}$	4×10^{-3}	(206)
La_6WO_{12}	1×10^{-3}	(207)
$BaNd_{0.8}Ca_{0.2}InO_{3.90}$	1×10^{-4}	From this work
$Ca_{0.01}La_{0.99}NbO_{4-\delta}$	1×10^{-4}	(208)
$La_2(Nb_{0.3}Y_{0.7})_2O_7$	4×10^{-5}	(209)
$Ca_{0.03}La_{0.97}NbO_7$	2×10^{-5}	(210)
$Sr_{0.01}La_{0.99}PO_4$	4×10^{-6}	(211)
Y_3NbO_7	1×10^{-6}	(212)

The total conductivity of the BNC20 composition measured at 500 ℃ in wet air is compared with other protonic conductor as reported in the literatures in table 5.2. The protonic conductivity of BNC20 sample is comparable with that of lanthanum tungstate and higher than other recently discovered protonic conductors.

5.2 Symmetrical thermogravimetric analysis and DC conductivity measurement

5.2.1 Sample preparation and experimental set-up

The simultaneous thermogravimetric analysis (TGA) and 4-probe DC conductivity measurement were conducted on the BNC20 sample synthesized using the optimized solid reaction method using a coupled apparatus. The working principal of the coupled system was introduced in the Chapter 3. In order to keep the consistency of the result with the impedance measurements, a pellet sample of BNC20 was used in the DC conductivity measurement as shown in Figure 5.7, while another BNC20 sample made in the same batch with the same shape and similar weight was placed in the alumina crucible suspended just above the DC conductivity measurement sample.

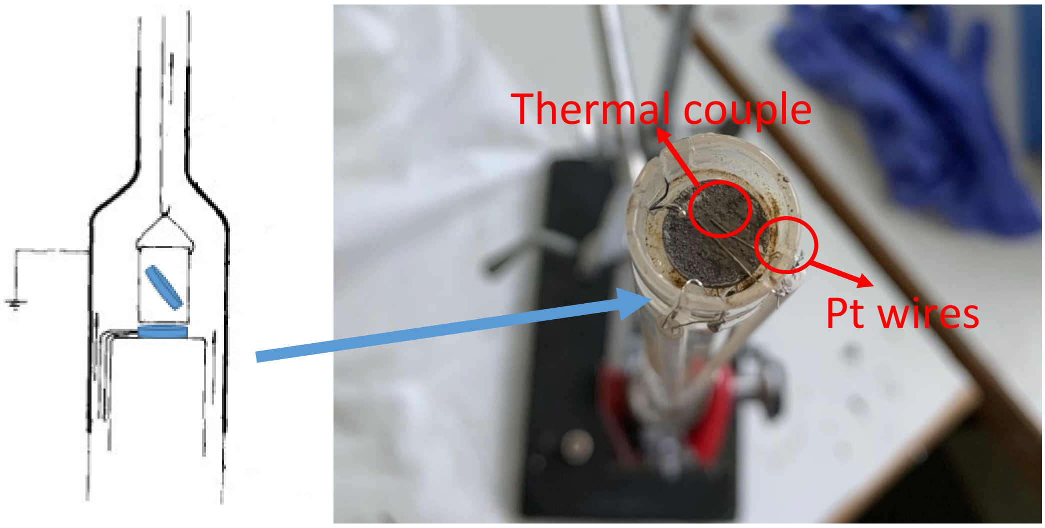

Figure 5.7 Schematic diagram of the TGA apparatus in the quartz tube(182) and the picture taken after the experiment of the sample for DC conductivity measurement. The pellet sample was 10.31 mm in diameter and 1.69 mm in thickness.

The BNC20 pellet sample for conductivity measurement was coated with platinum paste one both sides and each surface was attached with two platinum wires for connection with the outer wires on the quartz tube in the following step. Then the sample with platinum paste was annealed at 900 ℃ for 2 hours to dry the solvent and improve the adhesion. The resulting symmetrical cell with 4 platinum wires was mounted on the platform of the inner quartz tube and the Pt wires were connected with the wires outside the blocking quartz tube to be in contact with the measuring circuit. The adhesion between inner and outer Pt wires was improved by applying Pt paste and a fast annealing process using a small butane torch. The goodness of contact was confirmed with a digital multimeter from the bottom side of the platinum wires. The gaseous atmosphere during the measurement was controlled by different gas supply coupled with an oxygen pump. A water bubbler was connected in the gas flow with a switch for alternation of dry or wet atmospheres.

5.2.2 Water incorporation and protonic conduction

Two BNC20 samples were placed in exactly the same chemical environment in an airtight quartz-tube which was heated to 500 °C. One sample was placed in an alumina crucible hanging from one of the arms of the symmetrical electrobalance, whilst the other sample was coated on both faces with platinum paste and located just below the crucible on a blocking tube for the conductivity measurement. Figure 5.8 below shows the mass and resistance change of the BNC20 sample as the atmosphere changed from dry to wet and from wet to dry after reaching a plateau in both resistance and mass, which can be considered as a sign of full hydration in these two samples.

As depicted in Figure 5.8, a few minutes after the introduction of water vapour, a dramatic decrease in resistance was observed, while the process of water uptake in mass was much slower taking over 3 hours to reach a plateau. However, the increase in mass started immediately after the change of atmosphere, while the decrease in sample resistance seemed to have a ‘delay’ of 240 seconds. The difference in the behaviour of mass and resistance change of the sample (the ‘delay’) could either be ascribed to the enhancement of water uptake in the BNC20 sample by platinum coating on the surface or applying a voltage upon the sample, or result from the sudden change in conducting mechanism as the sample for conductivity measurement absorbed water to some extent. The exact relationship between the changes in mass and in resistance are still unknown, since the measurements were carried out on two different samples placed in the same environment. After the full hydration, the chemical composition of the sample was calculated to be $BaNd_{0.8}Ca_{0.2}InO_{3.90}\cdot 0.011H_2O$. The maximum concentration of protonic defects $\mathbf{OH}_{\mathbf{O}}^{\cdot}$ in the BNC20 sample at 500 °C was calculated to be 2.2 mol%. In comparison, the recovery process both in mass and resistance after switching to a dry atmosphere was much slower. The blue solid circles in Figure 5.8 labelled the deflections in the measured resistance of the sample after changing the atmosphere which could be ascribed to the surface exchange process of water molecules on the sample surface. In the dc conductivity measurement, all the conducting processes happened between two platinum electrodes were recorded. Therefore, the surface exchange process of water molecules on the sample surface triggered by the change of atmosphere may play an role in determining the overall resistance of the sample in this experiment which resulted in the labelled deflections in the resistance plot. The obvious spike occurred after the second switch was due to the power cut during the measurement.

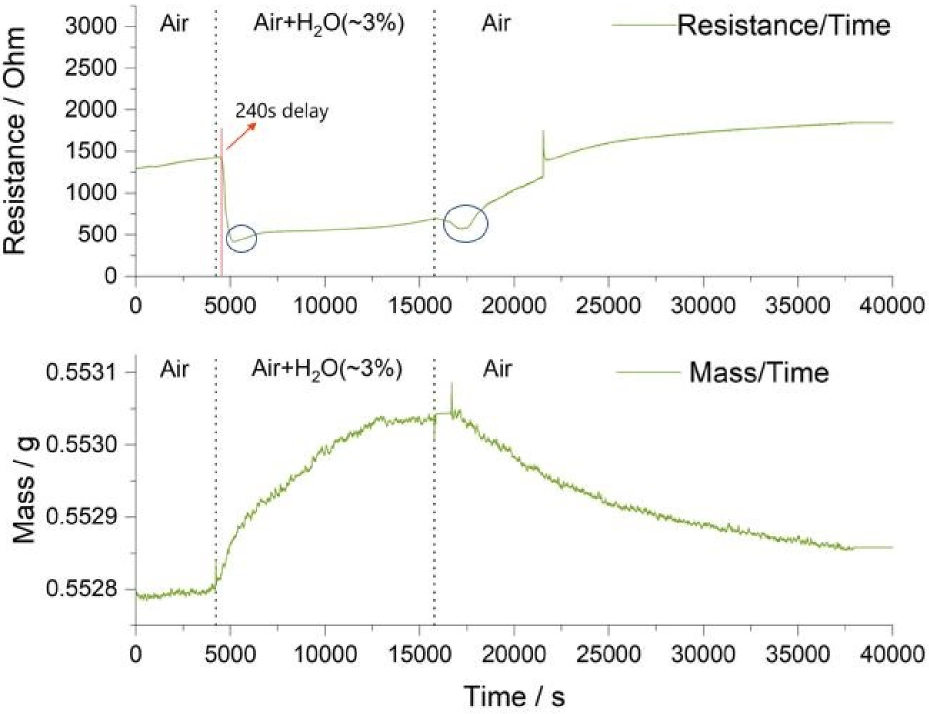

Figure 5.8 Mass (bottom) and resistance (top) versus time in the coupled TGA and conductivity measurements recorded at 500 °C. The dotted lines represent the time when the switch for water bubbler was turned on or turned off. The red solid line shows the '240 seconds delay' after which the resistance of the BNC20 sample started to decrease. The blue solid circles labelled the deflections in the resistance after changing the atmosphere.

The thermogravimetric analysis together with the DC conductivity measurement agreed well with the results obtained from the earlier EIS analysis, which again indicated that calcium substituted $BaNdInO_4$ exhibited protonic conduction under humid atmosphere. Besides, clear evidence of water uptake in the BNC20 sample when being annealed in wet atmosphere was recorded. The change in the conductivity of the sample according to the geometrical parameters can be viewed more clearly in Figure 5.9(a)&(b), where the resistivity and conductivity were plotted against annealing time.

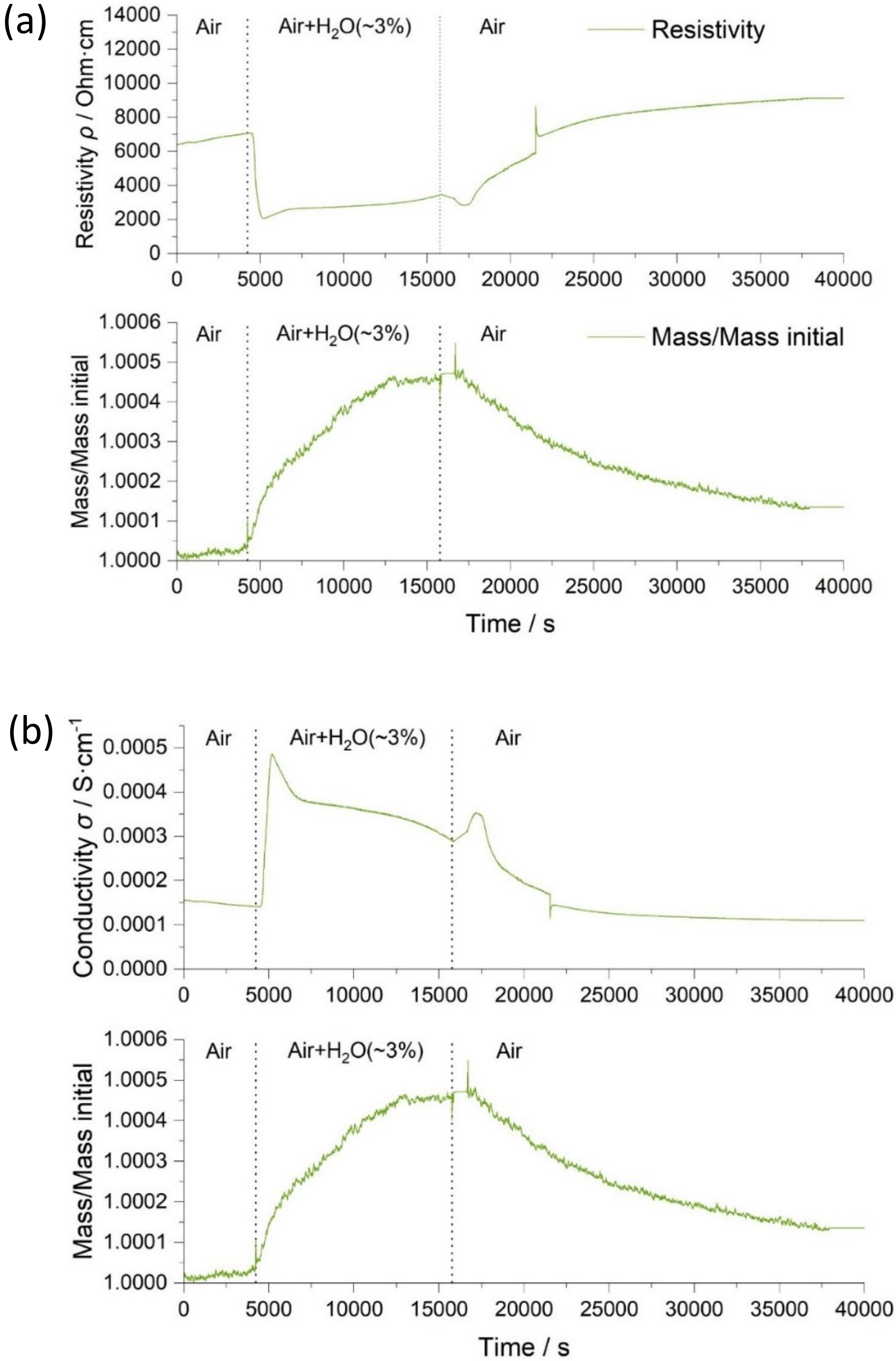

Figure 5.9 (a) Resistivity and (b) conductivity of BNC20 sample plotted against time measured at 500 ℃.

5.2.3 *In-situ* X-ray diffraction of hydrated BNC20 sample

After the TGA measurement described above, the BNC20 samples were hydrated again at 500 °C in humid air for 48 hours in preparation for the *in-situ* X-ray diffraction measurements. After wet annealing, the hydrated sample in the alumina crucible was taken out and mounted on the Z-stage in the *in-situ* XRD equipment. The pellet was heated at a rate of 5 °C/min from 100 °C to 800 °C with 100 °C step interval after an initial XRD measurement at room temperature. After being heated to 800 °C for 1 hr, the dehydrated sample was examined again on cooling in order to make a comparison with the previous data. All HT-XRD patterns were refined using the FullProf software suite(166) through the Le Bail method. The selected region of XRD patterns from 20° to 60° 2θ, are illustrated in Figure 5.10, where the patterns shown in dark lines represent the XRD data obtained in the heating cycle, and those shown in red lines are the cooling cycle data as the pellet sample had been heated up to 800 ℃ for about 2 hours.

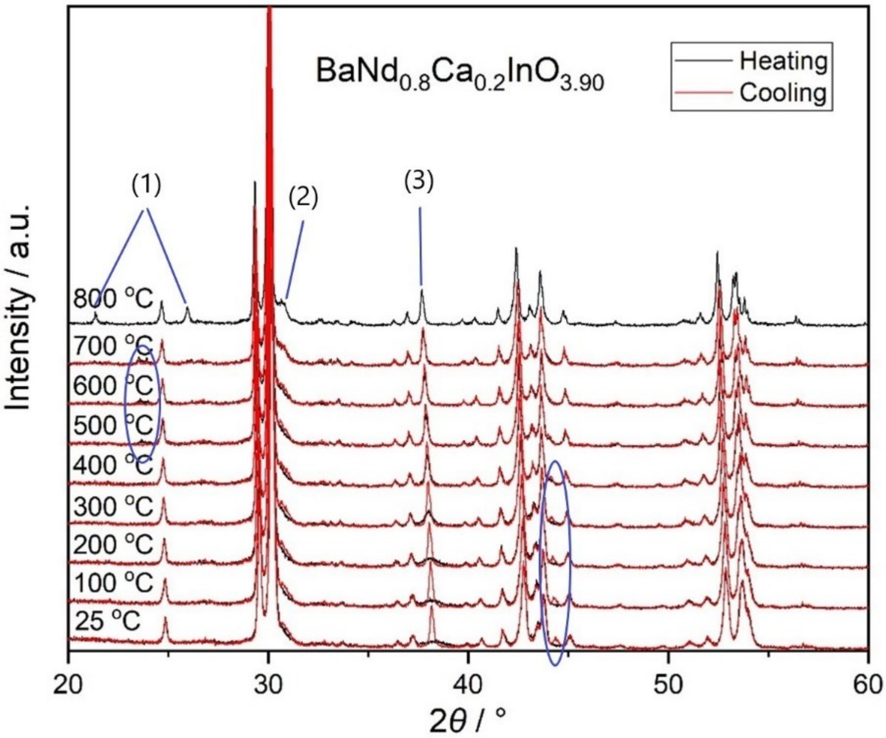

Figure 5.10 High temperature X-ray diffraction patterns of the hydrated BNC20 sample on heating (black) and cooling (red) cycles. (1),(2) & (3) with the labels represent the additional peaks which were not from the primitive monoclinic phase in the XRD patterns. The blue circles label some small additional peaks which could be due to the minor secondary phases.

There are several interesting findings with respect to the difference between XRD patterns derived in heating and cooling cycles. As labelled with blue solid lines and numbers, an additional peak (2) at 31.2°(2θ) appeared in the elevated temperature data and remained in the cooling cycle, which was also observed in the previous XRD measurements. This additional peak may arise from the secondary phase produced in the thermal treatment, which could be easily removed by polishing the sample surface with SiC grinding paper. A similar peak labelled as (3) could also be found at 38.2°(2θ) which emerged at elevated temperatures and remained in the cooling cycle. Peak (3) is not a regular peak observed in the previous room temperature XRD patterns, which cannot be indexed with the reflection belonging to the main primitive monoclinic phase. The comparison between the XRD patterns of the hydrated BNC20 sample and that of the as-sintered BNC20 sample is illustrated in Figure 5.11 below, where the blue line represents the XRD pattern of the as-sintered pellet sample measured at room temperature.

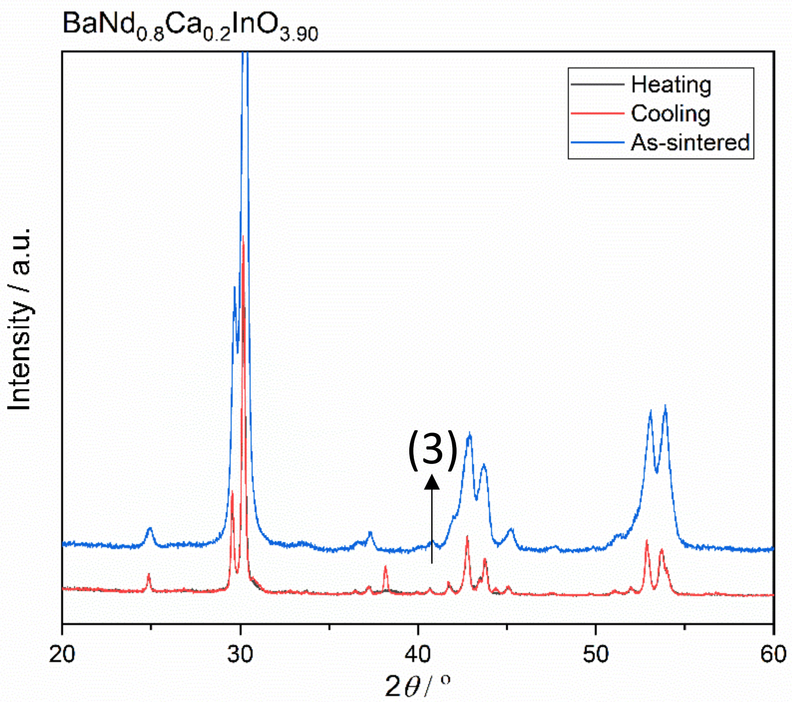

Figure 5.11 XRD patterns of the hydrated BNC20 sample measured on heating (dark) and cooling (red) cycles at 25 ℃ and the as-sintered BNC20 sample measured at room temperature.

According to the previous literature on the phase transition of $CaCO_3$(213), this particular peak appeared at 38.2°(2θ) can be indexed with the (104) reflection belonging to the calcite Ⅰ phase, as shown in Figure 5.12(b). The change of peak (3) from an amorphous shape into a sharp peak shape as the temperature increased implied that the correlated secondary phase of calcite crystalized on elevating temperature. Apart from that, it is interesting to note that there are two peaks, labelled as (1), that emerged at 800 ℃ at low angles (21.8° and 26.5°) which then disappeared in the cooling cycle. These two peaks could be ascribed to the phase transition of the $BaCO_3$ secondary phase which happened at 1073-1093 K from the orthorhombic $BaCO_3$ (α-$BaCO_3$) structure into the trigonal β phase (β-$BaCO_3$) as illustrated in Figure 5.12(a) from previous phase transition study on $BaCO_3$(214). The blue circles labelled some other minor changes in the *in-situ* XRD patterns of the hydrated BNC20 sample which could be ascribed to other secondary phases that emerged after the long period of annealing. The Le Bail refinements on the main phase of the *in-situ* XRD patterns gave reasonably good fit results with a primitive monoclinic lattice structure and a lattice symmetry of $P2_1/c$ as shown in Table 5.3 below. The goodness of fit, χ^2, are not ideal, especially in the data of the heating cycle.

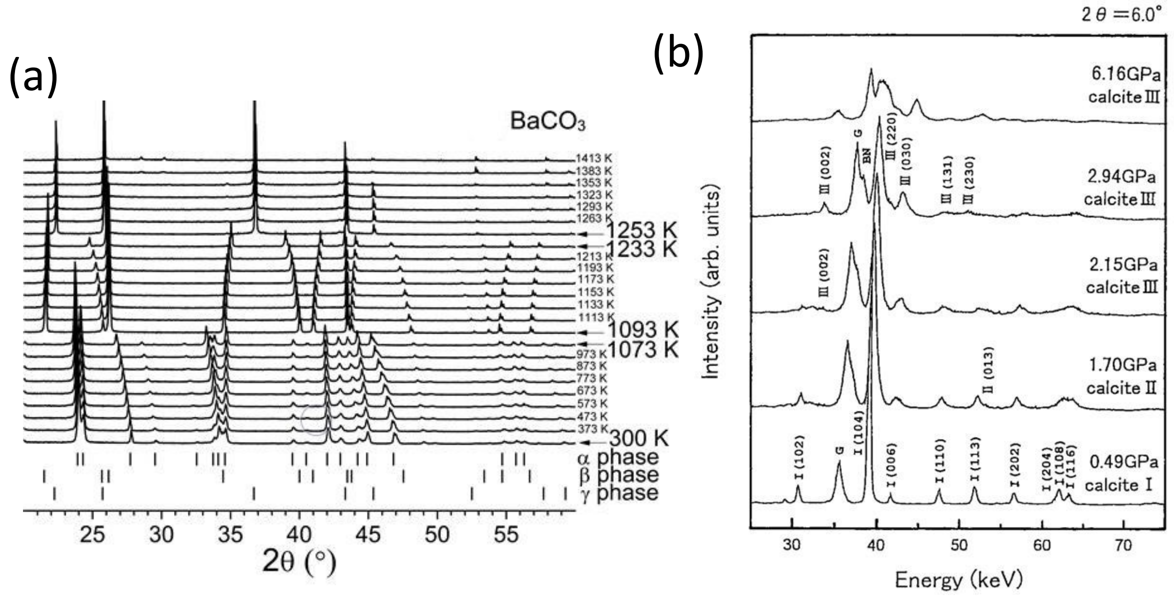

Figure 5.12 Comparison of XRD patterns at various temperatures for (a) $BaCO_3$ (300-1413 K)(214) and at various pressure for (b) $CaCO_3$(213).

Table 5.3 Refined lattice parameters of the hydrated BNC20 sample measured in heating (top) and cooling (bottom) cycles after being annealed in wet atmosphere for over a week.

Temperature(℃)	*a*(Å)	*b*(Å)	*c*(Å)	β(°)	*V*(Å^3)	χ^2
25	9.1122(2)	6.0373(1)	8.2631(2)	103.0883(25)	442.771(18)	5.93
100	9.1201(2)	6.0420(1)	8.2654(2)	103.1583(19)	443.496(16)	4.19
200	9.1284(2)	6.0470(1)	8.2720(2)	103.1195(20)	444.693(16)	4.39
300	9.1375(2)	6.0539(1)	8.2771(2)	103.1639(16)	445.832(15)	3.85
400	9.1455(2)	6.0602(1)	8.2825(2)	103.1829(15)	446.949(15)	3.83
500	9.1493(2)	6.0609(1)	8.2830(2)	103.1466(13)	447.280(14)	3.11
600	9.1589(2)	6.0604(2)	8.2826(2)	103.1627(16)	447.660(19)	3.73
700	9.1700(3)	6.0658(2)	8.2891(2)	103.1862(17)	448.914(21)	4.62
800	9.1788(3)	6.0747(2)	8.2999(3)	103.2128(21)	450.539(26)	5.38
800	9.1740(3)	6.0758(2)	8.2973(3)	103.2252(23)	450.220(23)	5.60
700	9.1692(3)	6.0678(2)	8.2896(2)	103.1900(17)	449.034(21)	4.36
600	9.1580(2)	6.0631(1)	8.2826(2)	103.1678(14)	447.809(15)	2.68
500	9.1484(2)	6.0613(1)	8.2822(2)	103.1663(14)	447.183(14)	2.51
400	9.1379(2)	6.0584(1)	8.2797(2)	103.2245(20)	446.210(15)	2.88
300	9.1326(2)	6.0509(1)	8.2746(1)	103.1990(14)	445.179(12)	2.36
200	9.1202(2)	6.0402(1)	8.2669(2)	103.2144(19)	443.341(13)	2.93
100	9.1141(3)	6.0384(2)	8.2652(3)	103.2443(32)	442.771(25)	4.69
25	9.1080(2)	6.0337(1)	8.2608(2)	103.2281(20)	441.929(16)	2.97
*CTE α (K^{-1})	9.67(3) x10^{-6}	9.04(7) x10^{-6}	5.11(4) x10^{-6}		2.42(1) x10^{-5}	

*Thermal expansion coefficient (CTE) here is the derivation derived from the linear fitting of the refined lattice parameters as a function of temperatures, assuming that there is no chemical expansion involved.

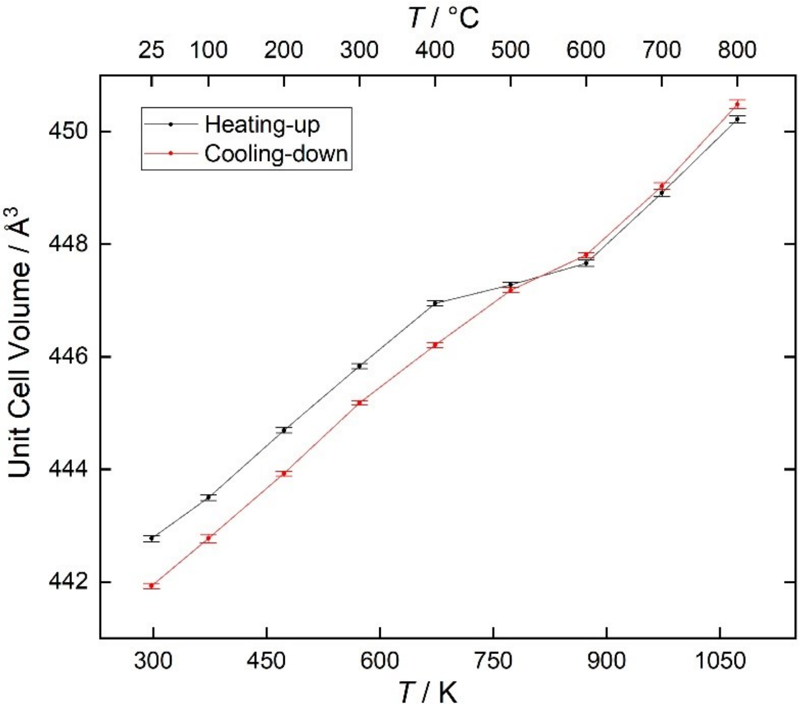

Fig 5.13 Fitted unit cell volume with error bars (3σ) of the hydrated BNC20 sample versus temperature.(202)

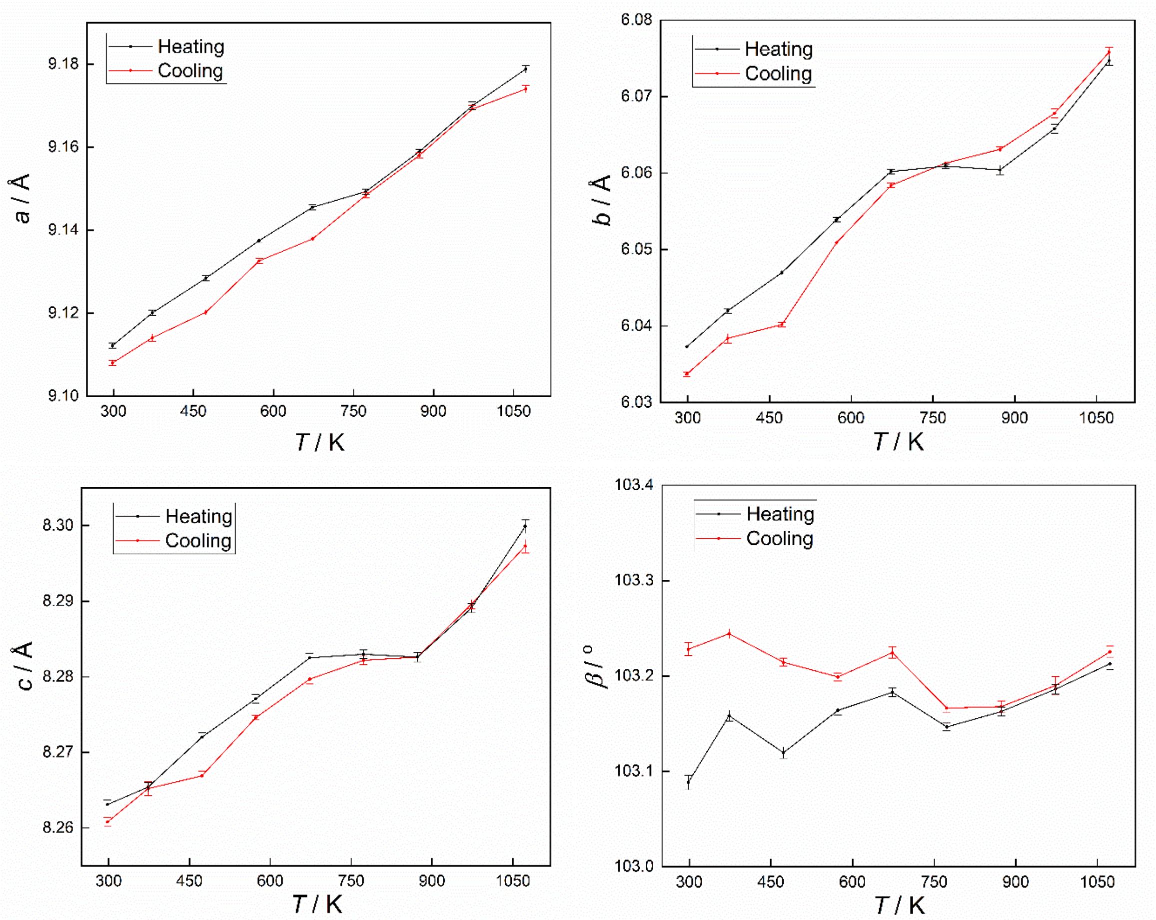

Fig 5.14 Fitted lattice parameters with error bars (3σ) of the hydrated BNC20 sample versus temperature.(202)

By plotting the fitted unit cell volume against temperature, a clear lattice expansion was observed in the fitted unit cell volume of the hydrated BNC20 sample on heating compared with the data obtained on cooling, as shown in Figure 5.13, which is a further evidence to suggest that $BaNd_{1-x}Ca_xInO_{4-x/2}$ is a proton conductor under humid atmosphere. The dimensional thermal expansion coefficients of the lattice, α_a=9.67(3) x10 $^{-6}$ K^{-1}, α_b=9.04(7) x10 $^{-6}$ K^{-1} and α_c=5.11(4) x10 $^{-6}$ K^{-1}, as listed in Table 5.3, were derived by linear fitting of the refined lattice parameters as a function of temperatures in the cooling cycle (red lines in Figure 5.14). The changes in the refined lattice parameters in heating and cooling cycles are consistent with the observation in the symmetrical TGA analysis, which implied that BNC20 exhibited protonic conduction under wet atmospheres.

In addition, the difference between the unit cell volume of the dehydrated sample obtained here at room temperature (441.93(2) Å^3) and the one obtained in the previous sample (438.21(1) Å^3) could be ascribed to the z-shift in different sample holders. The degree of hydration of the sample and the chemical change of the material after being annealed in wet atmosphere for a long period of time may also lead to a change in the lattice parameters obtained in the XRD measurements.

5.3 Chemical stability

The *in-situ* XRD measurements on the BNC20 sample which had been annealed in wet air at 500 ℃ for one week showed clear evidence for the formation of secondary phases of $CaCO_3$ and $BaCO_3$ on the sample surface. The crystallization of the $CaCO_3$ phase on the sample surface was observed in the in-situ XRD patterns as shown in Figure 5.10. To probe the topographic information of the sample surface, the BNC20 sample before and after being annealed at 500 ℃ in the humid environment for one week was imaged using the Zeiss Crossbeam 340 SEM equipment.

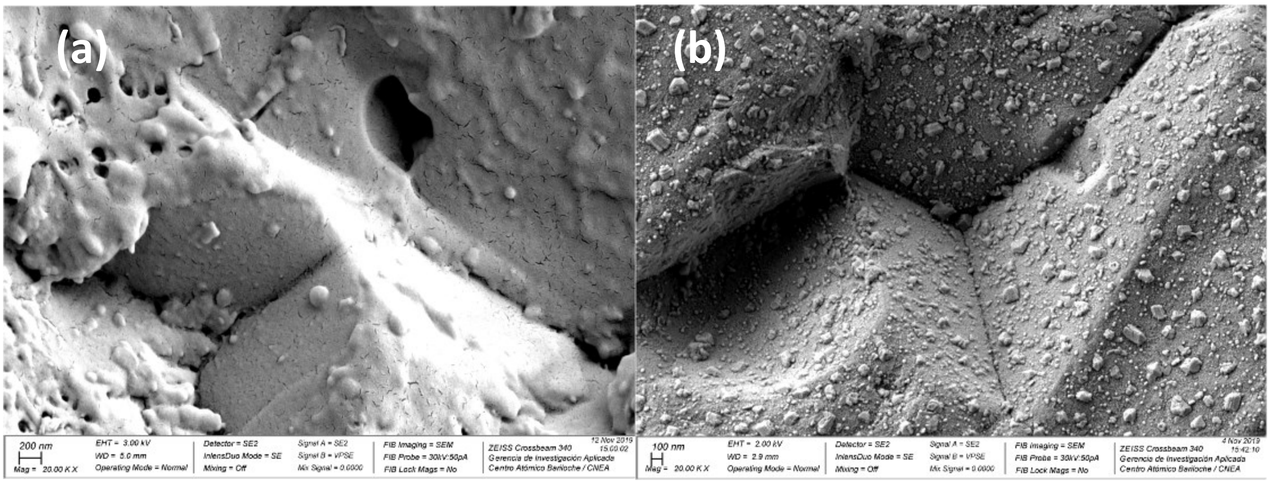

Figure 5.15 Secondary electron microscopy (SEM) images of the BNC20 sample (a) before and (b) after being annealed at 500 ℃ in humid environment for a week.

As can be seen in Fig 5.15, after wet annealing and the following heat treatment in the *in-situ* XRD measurement (where the hydrated BNC20 sample was heated up to 800 ℃ for 2 hours including the XRD data collecting time), a great number of faceted grains grew out from not only the grain boundaries but also from the surface of the original grains, as seen in Figure 5.15(b). The observation of these faceted grains with a grain size of 100~200 nm on the sample surface is consistent with the appearance of peak (3) in the cooling cycle, which could be ascribed to the crystallization of $BaCO_3$/$CaCO_3$ secondary phases. These SEM images along with the aforementioned *in-situ* XRD data suggested that BNC20 shows a poor chemical stability in the wet atmosphere, where an A-cation exsolution process will happen resulting in secondary phases of $BaCO_3$, $CaCO_3$ and so on. The A-site deficiency on the surface of perovskite materials has been investigated by many groups(183, 215-217). The surface termination and subsurface restructuring of the perovskite-based solid oxides was investigated by Druce *et al.*(217) using low energy ion scattering spectroscopy (LEIS), which confirmed that after high temperature treatment, segregated A-site (or substituent) cations dominated the outer surfaces and the subsurface showed B-site enrichment(217). The secondary phases formation in the $BaNd_{0.8}Ca_{0.2}InO_{3.9}$ sample after a long period of annealing in a wet atmosphere could be related to the segregation of A-site cations on the outer surfaces of the sample, which then react with the moisture forming $Ca(OH)_2$ and $Ba(OH)_2$ on the sample surface. The energy required for the exsolution of the calcium cations in the lattice can be compensated by the energy released from the subsequent reaction as depicted below:

$$\mathrm{Ca(OH)_2 + CO_2 = CaCO_3 + H_2O} \quad \Delta\mathrm{H}^{\circ}_{298\mathrm{K}} = -109\ kJ \cdot mol^{-1}(218)$$

The reaction above is thermodynamically favourable in the temperature range 20-750 ℃ according to the previous literature(219), and its kinetics are augmented with high relative humidity where the water vapor exhibited the catalytic effect(218, 220, 221). The exsolution of barium cations and the formation of $BaCO_3$ can also be ascribed to this mechanism. According to the in-situ XRD patterns, after calcium and barium segregation, the main phase in the bulk material was still monoclinic. Therefore, segregation of calcium and barium seemed to happen at the upmost surface where decomposition of the $BaNd_{0.8}Ca_{0.2}InO_{3.90}$ happened forming hydroxides and Indium/Neodymium oxide. If there is A-cation exsolution process happened in the material, an A-site deficient region could be found near the sample surface, which requires more experimental data (using surface analysis techniques, such as SIMS or LEIS) to verify. But majority of the grains in the bulk remained the same stoichiometry with a monoclinic crystal structure.

5.4 D/H Isotopic effect

The deuterium isotope effect on the electrical properties of the BNC20 solid solution was investigated by EIS measurement and the symmetrical DC conductivity measurement as described above. A water bubbler containing deuterium water (~ 99% D_2O) was introduced when measuring the conductivity of the BNC20 sample under wet atmosphere.

5.4.1 AC impedance spectroscopy under D_2O-related wet atmosphere

A symmetrical cell comprising a BNC20 sample coated on both sides with platinum electrodes was annealed in the D_2O vapor containing air at 500 ℃ for 8 hours. The D_2O vapor of ~ 2.5%(222) in air was introduced by adding a water bubbler containing 99% pure D_2O between the gas cylinder and the sealed impedance apparatus. To make a comparison with the impedance data obtained previously in a wet atmosphere (3% H_2O vapor in air), the experimental set-up was kept the same as before.

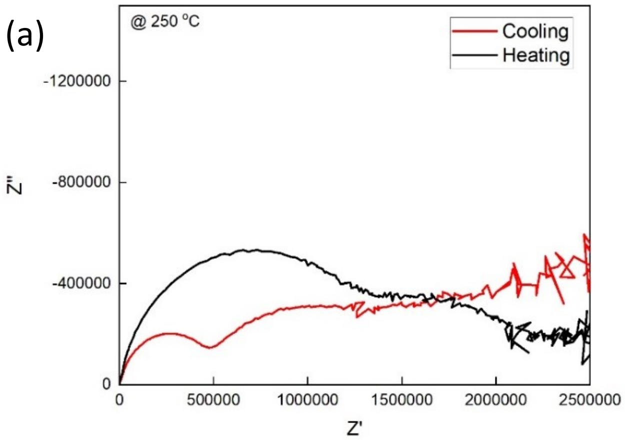

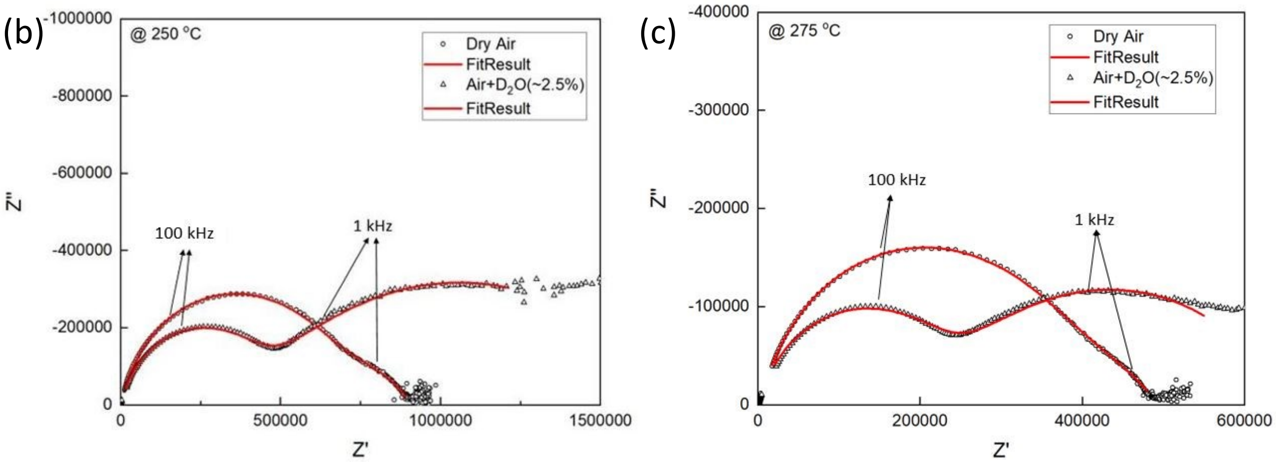

Figure 5.16 (a) Impedance spectra of BNC20 measured in D_2O humidified air at 250 ℃ in the heating and cooling cycles. (b) & (c) Nyquist plots of BNC20 measured in dry and D_2O humidified air at (b) 250 ℃ and (c) 275 ℃, where the hollow circles represent the dry impedance data, the hollow triangles are the wet data and the red line represent the fit result.

The Nyquist plots of the sample measured at 250 ℃ in the heating and cooling cycles were shown in Figure 5.16(a). A clear decrease in diameter of the first semi-circle appeared at high frequency was observed in the cooling cycle. The difference of the data obtained in heating and cooling cycles at the same temperature could be ascribed to the incomplete hydration of D_2O during the prior 8 hours annealing step. In order to keep consistency in the obtained data and focus on the fully hydrated sample, the data obtained in the cooling cycle was chosen for further analysis.

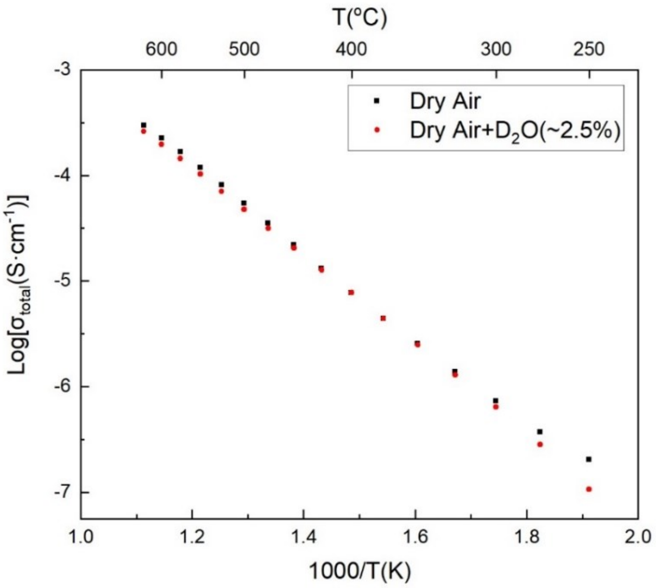

Figure 5.17 Arrhenius plots of the total conductivities of the BNC20 sample measured under dry and D2O wetted atmospheres.

As can be seen in Figure 5.16 (b) and (c), at low temperatures the incorporation of D_2O in the BNC20 sample resulted in a smaller semi-circle at the high frequency range, which belongs to the bulk response, and a much broader depressed semi-circle corresponding to the grain boundary response. The Nyquist plots indicated a higher bulk conductivity and a lower grain boundary conduction in BNC20 after D_2O incorporation, as the latter could be ascribed to the secondary phase that emerged from the grain boundaries. The reduced semi-circle at the high frequency range implied a fast conduction mechanism after D_2O humidification, though the reduction of which is less significant in the H_2O impedance data. On the other hand, the overall resistance of the sample excluding the electrode response at lower frequencies, was increased by D_2O incorporation. The Arrhenius plot of the total conductivities of BNC20 measured under dry and D_2O humidified atmospheres are illustrated in Figure 5.17.

Unlike the influence of the water incorporation in the BNC20 sample, which increased the total conductivity of the sample, the D_2O water incorporation appeared to decrease the total conductivity of BNC20 at both low and high temperature ranges. In the temperature range from 325℃ to 450 ℃, the total conductivity of the BNC 20 sample in dry and D_2O humidified atmospheres were almost the same. A more detailed analysis by separating the bulk and grain boundary responses in the impedance data could have provided more information about the D_2O incorporation. But due to the poor quality of the EIS equipment during the COVID-19 pandemic, it is difficult to extract reliable information when analysing these data sets. However, the Nyquist plot together with the Arrhenius plots for total conductivities showed some clear evidence of D_2O incorporation into the BNC20 sample. The further analysis in probing the influence of D_2O on the conductivity of the BNC20 sample could be carried out on the following symmetrical DC conductivity measurements, where a change of gaseous atmosphere from Air+D_2O (~ 2.5%) to Air+H_2O (~ 3%) was involved. The reduction in the conductivity was expected due to the H/D isotope effect, which will be further explored in Section 5.4.2.

5.4.2 Deuterium isotope effect measured by symmetrical DC conductivity measurement

Two BNC20 samples synthesized from the same batch as the samples used in Section 5.2 were prepared and mounted through the same process. One pellet coated with platinum electrodes was placed on the blocking quartz-tube and connected with the conductivity measuring circuit, while the other one was put in the alumina crucible for TGA measurement. Two samples were annealed in dry air first till both the mass and resistance reached a plateau. Then the gaseous atmosphere was changed from dry air to D_2O humidified air by switching on the water bubbler which contained 99% pure D_2O water. The D_2O wet annealing continued until the mass and resistance of the sample reached a new plateau indicating the completion of D_2O incorporation. The gaseous atmosphere was then switched into Air+H_2O (~ 3%) by replacing the D_2O water bubbler with a H_2O water bubbler.

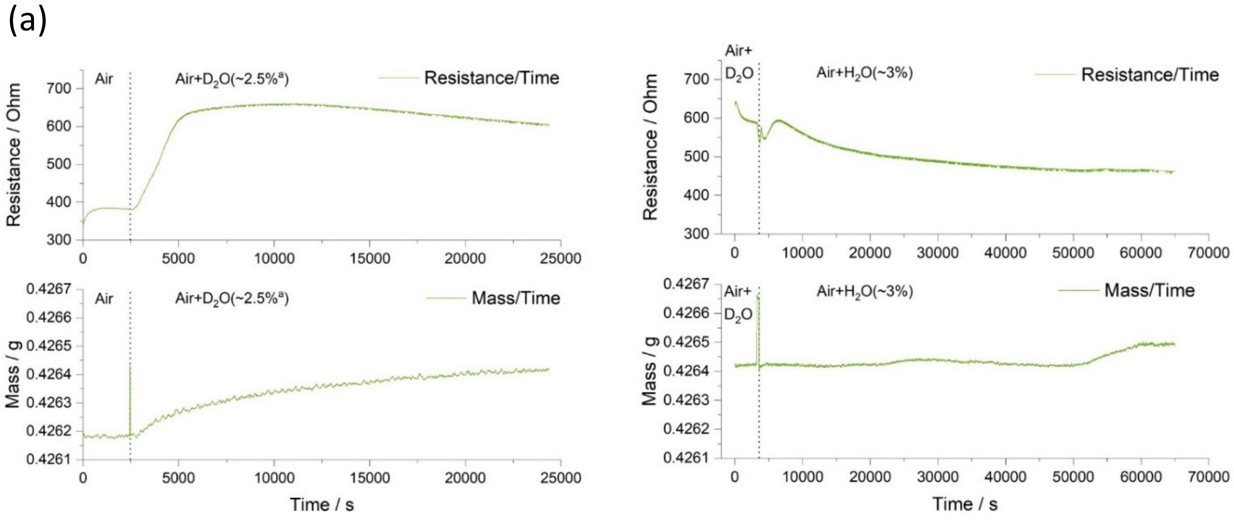

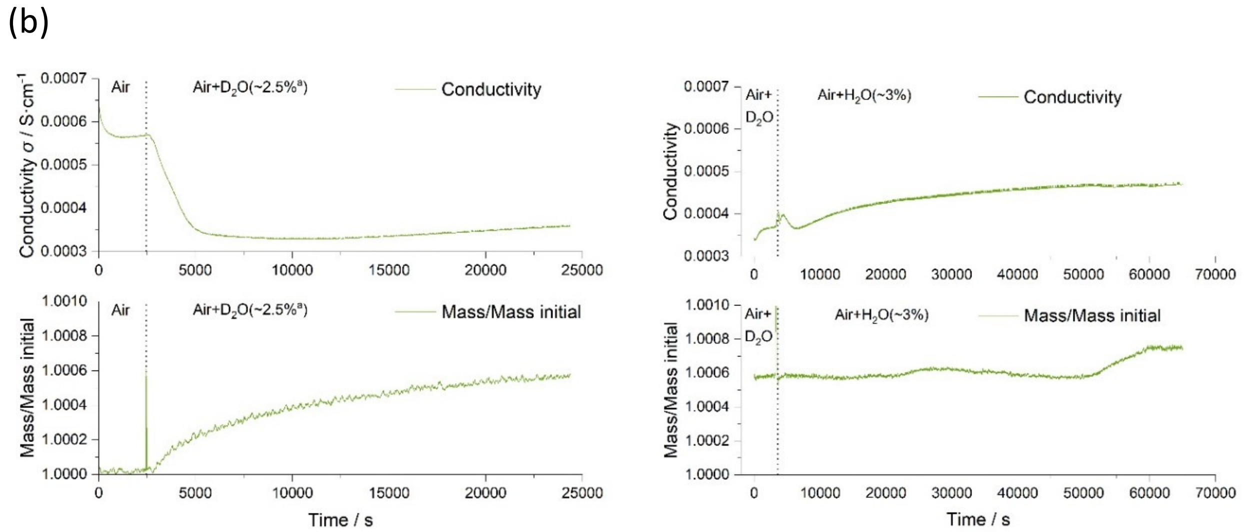

Figure 5.18 (a) Resistance and (b) conductivity of BNC20 sample plotted against time measured in varying atmospheres at 500 ℃. The dotted lines label the switch of atmospheres.

Compared with previous H_2O wet atmosphere test, four interesting findings could be concluded according to the measurement above. First of all, the resistance of BNC20 was increased after D_2O incorporation, which was consistent with the EIS results. The corresponding mass changes indicated a much slower D_2O absorption process which took more than 6 hours for the pellet sample to be completely hydrated by D_2O as the H_2O incorporation only took 3 hours to complete. Secondly, the atmospheric change from D_2O humidified air to H_2O humidified air resulted in a decrease in the sample resistance, and therefore, the total conductivity of the sample in H_2O wet atmosphere was higher than that in D_2O atmosphere. The deuterium isotope effect on the total conductivity of BNC20 can be calculated as the ratio of the resistance in D_2O humidified air, R_D, and the resistance in H_2O humidified air, R_H, to be 1.416(2). The value of isotope effect in this measurement was consistent with the value 1.414 as usually quoted in the previous literature(223, 224). Apart from that, it is interesting to note that the exchange of D for H in BNC20 after switching the atmosphere was a relatively slow process as the mass nearly change for quite a long period of time after switching the water bubbler. This can be attributed to the higher mass of D (2.01) than that of H (1.01). Last but not least, the solubility of H_2O in the BNC20 solid solution is higher than that of D_2O as the mass ratio of the pellet sample started to increase from t=52000s after changing the atmosphere from air+D_2O to air+H_2O.

5.5 Summary

In summary of this chapter, calcium substitution at the Nd site can significantly increase the total conductivity of $BaNdInO_4$ pristine material by 1-2 orders of magnitude in dry air. Under dry atmosphere, the highest total conductivity of 2.6 x 10^{-3} Scm^{-1} was obtained in the $BaNd_{0.8}Ca_{0.2}InO_{3.90}$ sample at 750 °C in air. The BNC20 sample exhibits p-type and oxide-ion mixed conduction under dry atmospheres within the O_2-N_2 $p(O_2)$ range as the total conductivity, σ_{Total} (Scm^{-1}), and the bulk conductivity, σ_{Bulk} (Scm^{-1}), of BNC20 were both lower in the N_2 atmosphere. Both the total conductivity and the bulk conductivity of BNC20 were enhanced in wet atmospheres over a large temperature range (250 °C-750 °C) compared with those measured in dry atmospheres which implies that this material may exhibit triple (oxygen-ions, protons and holes) conduction under wet atmospheres. Compared with the Sr and Ba substituted $BaNdInO_4$-based solid solutions in the previous literature, calcium substitution on the Nd site resulted in the highest oxide-ion conductivity and lowest activation energy for oxide-ion conduction, which could be ascribed to the defect associations in the system. The tendency of oxygen vacancies to be associated with the heavy doping cations would increase the activation energy of conduction by adding an association enthalpy ΔH_A. Further experimental results are required to support this hypothesis.

The thermogravimetric analysis (TGA) and the simultaneous DC conductivity measurement showed a consistent result with the previous EIS data as the mass increased and the resistance of BNC20 decreased when the water vapour was introduced. The protonic defects concentration of the saturated BNC20 sample was 2.2 mol% according to the TGA measurement. Apart from that, an expansion in the lattice parameters of the BNC20 sample after hydration was observed under *in-situ* XRD measurements according to the Le Bail refinements on the XRD patterns obtained in the heating cycle. Several experimental results have indicated that calcium substituted $BaNdInO_4$ oxides can be used as a proton conductor.

However, an A-cation exsolution process was observed in BNC20 being annealed at 500 °C in humid atmosphere over one week which suggested that this type of material shows a poor chemical stability when being exposed in humid environment for a long period of time. A large number of faceted grains of $CaCO_3$ were observed in the SEM images of the hydrated sample surface after heat treatment of the *in-situ* XRD measurement. In the *in-situ* XRD patterns, an additional peak appeared at 38.2° was observed, which changed from an amorphous shape into a sharp peak shape as the temperature increased. The appearance of this additional peak confirmed that the correlated secondary phase of calcite crystalized in elevating temperature on the sample surface(213). Apart from that, a secondary phase of $BaCO_3$ was also detected in the hydrated BNC20 sample from analysis of the XRD patterns. Two additional peaks emerged at 800 ℃ at low angles (21.8° and 26.5°) which then disappeared in the cooling cycle, and could be ascribed to the phase transition of $BaCO_3$ that occurs at 1073-1093 K from the orthorhombic $BaCO_3$ (α-$BaCO_3$) structure into the trigonal β phase (β-$BaCO_3$)(214).

The deuterium isotope effect on the electrical conductivity of BNC20 solid solution was investigated by EIS and symmetrical dc conductivity measurements. Both EIS and dc conductivity measurements showed a decrease in the total conductivity of the BNC20 sample after D_2O incorporation, and the process of D_2O uptake was confirmed to be relatively slower than the H_2O uptake. The deuterium isotope effect on the total conductivity of BNC20 measured by the dc conductivity measurement was calculated to be 1.416(2), the value of which was close to 1.414 as usually quoted in the previous literature(223, 224).

5.6 Suggested future work

One of the potential future works is the $P(O_2)$ dependence measurements of the total conductivity on the BNC20 sample using the symmetrical TGA and dc conductivity system. It would be a great idea to conduct the conductivity measurement whilst varying the gaseous atmospheres (O_2/N_2 ratio, N_2/H_2 ratio) to obtain the Brouwer diagram of the BNC20 solid solution. The oxide-ion conductivity of the sample at a specific temperature could then be derived from the pure oxide-ion conduction region where the constant conductivities are independent of $P(O_2)$. A more profound investigation regarding the charge carrier distribution and conduction mechanism in the system can therefore be discussed in detailed. Instead of a pellet-shaped sample, a bar-shaped sample could be used in the 4-probe dc conductivity measurement to avoid the electrode effect.

The deuterium isotope effect on the electrical properties of the BNC20 sample could be investigated more deeply by impedance spectroscopy. It is worth mentioning that, before the impedance measurement, a long period D_2O vapour annealing process is required to ensure D_2O fully incorporation.

A material recovering test on the hydrated BNC20 sample after a long period of wet annealing is worth attempting since all the secondary phases detected were precursors used for synthesis. A high temperature sintering process could be conducted on the hydrated sample to let the carbonate decompose and react with the bulk material to form a primitive monoclinic phase again.

Chapter 6

Oxygen diffusion in BNC20 solid solution

In the last chapter, the electrical properties of the BNC20 solid solution were investigated generally through the total conductivity measured by electrochemical impedance spectroscopy or dc conductivity measurement without separating different charge carriers and analysing their distributions. In this chapter, the oxygen diffusion kinetics in the BNC20 sample along with the surface exchange coefficient for oxygen will be measured by isotope exchange depth profiling method, which offers an opportunity for probing the oxygen diffusion mechanism alone in the bulk material. Both dry and wet ^{18}O isotopic exchange experiments were performed on the sectioned dense BNC20 samples with a polished surface. To obtain reliable data, a mirror finish should be achieved on the polished sample surface, and the density of the bulk materials needs to be greater than 95% of the theoretical value. The environmental influences on the oxygen diffusion kinetics will be discussed. The obtained oxygen diffusion coefficients will be compared with the previous EIS results according to the Einstein relation (Equation (1)). Deuterium diffusion measurements were also performed isothermally on the BNC20 sample using the D_2O vapour as the diffusion source。

The obtained depth profiles were analysed using the Matlab app TraceX(186), where the fitting process is based on the Crank solution expressed as Equation 67(184). The TraceX app is capable of estimating the errors occurred in the fitting of the experimental data with the Crank solution expression. A typical diffusion profile with a representative error analysis by TraceX is shown in Figure 6.1(a)&(b) as an example. For each specific value of the standard deviation for the overall fit residual, the deviation for diffusion coefficient, *D*, and for surface exchange coefficient, *k*, could be derived from the edge of the single-colored polygon.

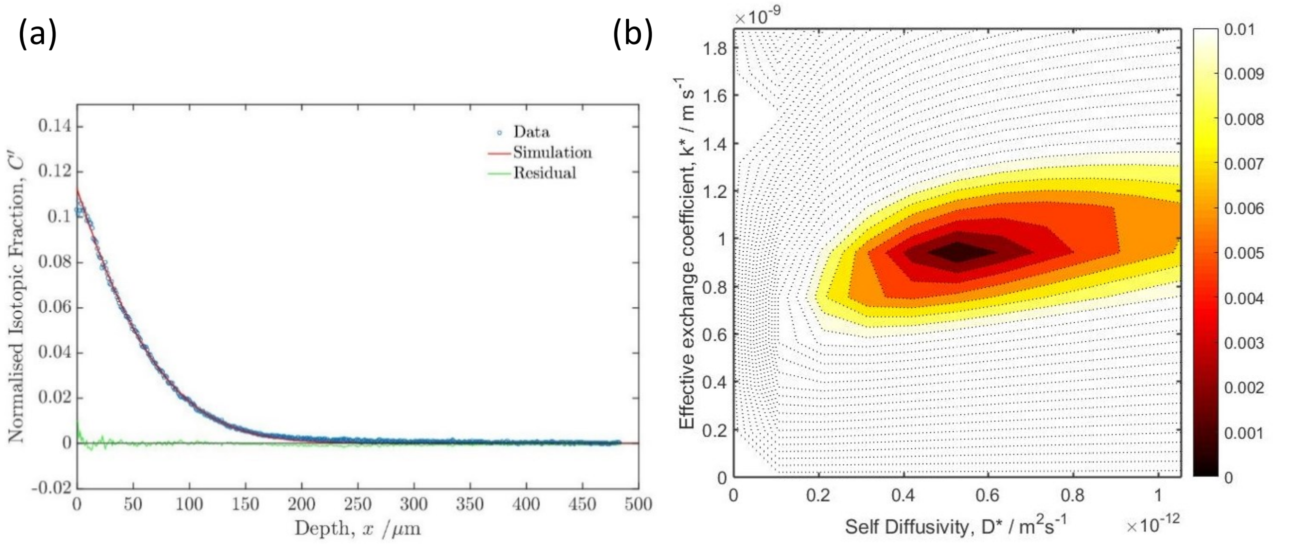

Figure 6.1 (a) A typical depth profile data fitting and (b) a representative error analysis of the $Ba_7Nb_4MoO_{20}$-Based oxides(Collaboration with Tokyo Tech, published on Nat. Com. (225)) exchanged in $^{18}O_2$ at 700 ℃ for 2 hours by the Matlab app TraceX(186). The deviation are given as D=5.4x$10^{-9}\left(\begin{matrix}-0.8\times10^{-9}\\+1.0\times10^{-9}\end{matrix}\right)$ cm^2s^{-1} and k=9.6x$10^{-8}\left(\begin{matrix}-0.5\times10^{-8}\\+0.4\times10^{-8}\end{matrix}\right)$ cm s^{-1}.

For the above depth profile, according to the error analysis by Matlab, a deviation of 15-20% for the diffusion coefficient and a deviation of 10% for the surface exchange coefficient are given during the mathematical data fitting process. However, the majority of errors introduced in the IEDP-SIMS analysis was from the experimental procedures, for instance, the exchange time regarding the heating and cooling rate of the experiment, the sample geometry after sectioning etc. A detailed discussion of the potential origins of the errors in the IEDP-SIMS technique can be found in the previous literature(226), in which a deviation of 10-30% was estimated for the diffusion coefficient. In this Chapter, the mathematical standard deviations introduced during the TraceX data processing will not be added in the plots due to the larger uncertainty arising from the former experimental procedures, but an estimation of the errors in the obtained kinetics can be assumed as around 15-30%.

6.1 Experimentation for the IEDP measurement

6.1.1 Sample preparation and experimental procedures for an isotope exchange experiment

Sample preparation: The BNC20 samples for the isotopic exchange measurements were synthesized by the modified solid reaction solution method, the relative density of which was confirmed to be more than 98% by the Archimedes method. To reduce the error caused by surface roughness in practice, the sintered pellet samples were ground initially using SiC grinding papers (Struer® Co.) with grits of 600, 1200 and 2000 successively. The pellet shaped sample was then sectioned into several bar-shaped samples using the diamond blade. After being ultra-sonically cleaned for 3 minutes in acetone to remove the cutting residue on the sample surface, the sectioned parts were then mounted on the polishing block fixed with wax and glass slides for the automatic polishing process. With the polished surface facing up on the polishing block, the sectioned samples were then automatically polished using a Struer-automated polishing machine (Struer® Co.) in the water-based diamond suspensions of 6 μm, 3μm, 1μm and a quarter μm successively. The corresponding polishing time and force exerted on the sample for each step was 10 min/20 N, 10 mins/20 N, 20 mins/15 N and 20 mins/10 N respectively until a mirror-finish on the sample surface was achieved. The resulting bar samples were ultra-sonically cleaned in acetone to remove the polishing residue and the wax. The surface finish of the sectioned samples was checked by optical microscopy before being placed in the sample boat for the following isotopic exchange experiment.

Experimental procedures for a dry $^{18}O_2$ exchange: A typical dry $^{18}O_2$ exchange measurement consists of two main steps, namely the $^{16}O_2$ pre-annealing and the $^{18}O_2$ exchange annealing. One of the purposes of a $^{16}O_2$ pre-annealing process before the exchange is to mitigate the mechanical damage induced by the previous grinding and polishing steps. Besides, it is also an equilibration step to give a flat background of oxygen for isotopic diffusion. The time for $^{16}O_2$ pre-annealing is usually 10 times longer than the isotopic exchange time, while the determination of the latter one is based on material properties and the required permeation depth of the tracer atoms into the bulk material.

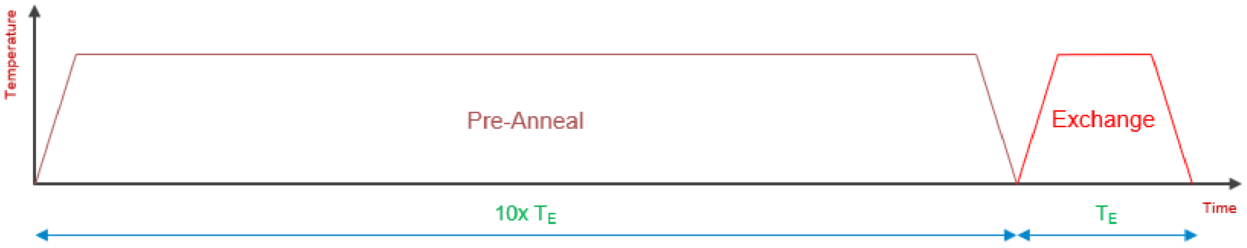

Figure 6.2 Schematic diagram of the timeline for a typical isotopic exchange experiment.

After placing the polished sample in the sample boat next to the thermocouple, the exchange tube should be sealed and evacuated to a base pressure lower than 4×10^{-7} mbar. To freeze the oxygen exchange process at the set temperatures, a roll-on and roll-off furnace is applied. Special cares should be taken when operating a short time exchange process where the actual exchange time needs to be calibrated to exclude the heating and cooling tail of the temperature profile. In this research, an exchange time of 1 hour or 2 hours were chosen in order to avoid introducing extra errors with respect to the actual exchange time. After evacuating the apparatus, 200 mbar of $^{16}O_2$(99.9995%) was let in and the furnace was rolled on to start the pre-anneal. When the pre-annealing step was complete, the furnace was rolled off and the main chamber was evacuated again. After evacuating the main chamber, 200 mbar $^{18}O_2$ with the ^{18}O concentration of 91% was introduced and the furnace was rolled on again to start the exchange annealing. After 1 or 2 hours exchange time, the furnace was rolled off, the sample was allowed to cool to room temperature and the residual ^{18}O in the chamber was recovered. The exchanged sample was then taken out and stored in a small sample box for the following SIMS analysis.

Experimental procedures for a wet $H_2{}^{18}O$ exchange are similar to that for a dry exchange experiment, while the introduction of water vapor was done by opening the valve between the water tank and the main chamber. The temperature of the water source stored in the water tank was controlled by a water bath, so that the amount of water vapour in the apparatus after equilibrium was determined based on the water bath temperature. After equilibrium of the valve was switched off, and 200 mbar O_2 was let in to mimic the atmospheric condition. A heating strip and aluminium foil was used to wrap the exchange tube and main chamber during the experiment in order to avoid the condensation point in the system.

Line scan sample preparation: The permeation depths of the exchange experiments in this research were controlled in the line scan sample preparation range of 50-300 μm on purpose to have a better data consistency. Therefore, the exchange samples need to be polished again on the lateral surface perpendicular to the original flat exchanged surface for further SIMS analysis to achieve the depth profile. In practice, to avoid edge effects in the SIMS analysis, two exchanged samples were stuck together with the flat exchanged surfaces facing each other using the super glue. The exchanged samples was then mounted on the polishing block fixed with wax again for the polishing process. It is worth noting that the sample should be mounted on the polishing block properly so that the top surface for polishing is perpendicular to the original flat exchanged surface to avoid introducing errors caused by sample geometry. The aforementioned grinding and polishing steps were repeated here to achieve a flat surface for the later SIMS analysis.

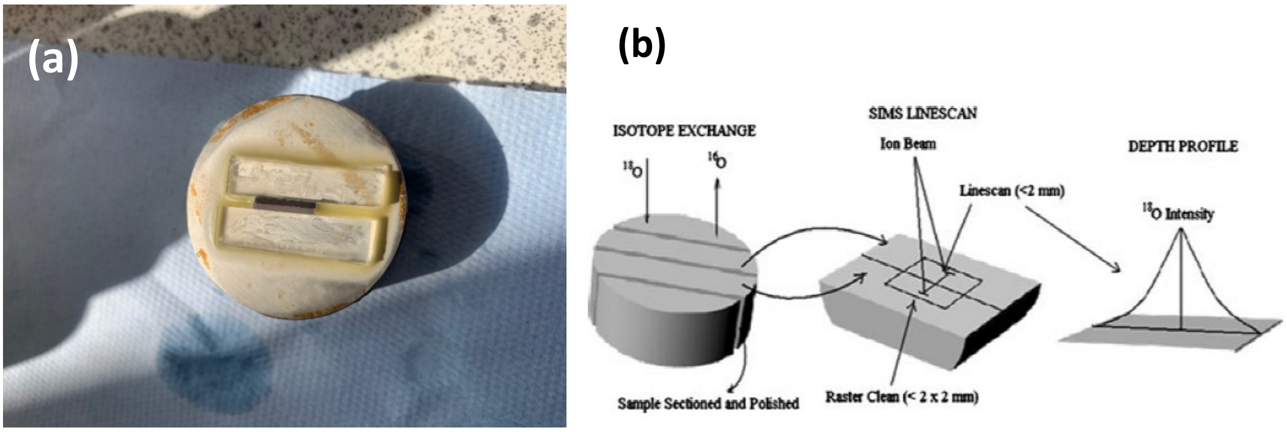

Figure 6.3 (a) Picture of two exchanged samples stuck together being mounted on the polishing block fixed with wax and glass slides. (b) Schematic diagrams of a SIMS-linescan analysis mode(60).

6.1.2 SIMS-LINESCAN analysis mode to obtain diffusion profiles

In this research, the ToF-SIMS (ION-TOF GmbH, Münster, Germany) working at ultra-high vacuum equipped with a dual ion-beam machine using a bismuth liquid metal ion gun and a low-energy sputtering ion gun was used to obtain the diffusion profiles. For the line scan samples, the elemental mapping mode of SIMS is capable of observing the isotope fraction across the sample surface, in which the sputtering gun was used for large area sputtering purpose. Depending on different samples and analysis purpose, different sputtering beams were used. In this chapter, the oxygen isotope exchanged sample surfaces were analyzed using the Cs^+ beam which is beneficial for the negative secondary ions yields. An electron flood gun was used during the sputtering process to avoid the charge build-up on the sample surface since the BNC20 samples were electrically insulating at room temperature. Before extracting the elemental mapping of the selected area, a cleaning process was done by sputtering of the top surface of the sample with a larger area including the area of interest until the intensities of the surface contamination species, i.e. chlorine, hydrocarbon species, decreased to a plateau. During the cleaning step, all the signals of interest were defined and calibrated based on the light ions using the installed software. The obtained profiles were then analyzed using the TraceX Matlab app to extract the diffusion coefficients, *D*, and the surface exchange coefficients, *k*.

6.2 Oxygen diffusion in BNC20

6.2.1 Oxygen diffusion in BNC20 under dry atmosphere

As described above in the experimentation part, the dry $^{18}O_2$ isotope exchange experiments were performed on the dense BNC20 samples, and the depth profiles starting from the original polished surfaces obtained by SIMS-linescan analysis mode were analysed using TraceX app in Matlab. The data fitting of the depth profiles and the obtained diffusion kinetics are shown in the following figures and listed in Table 6.1.

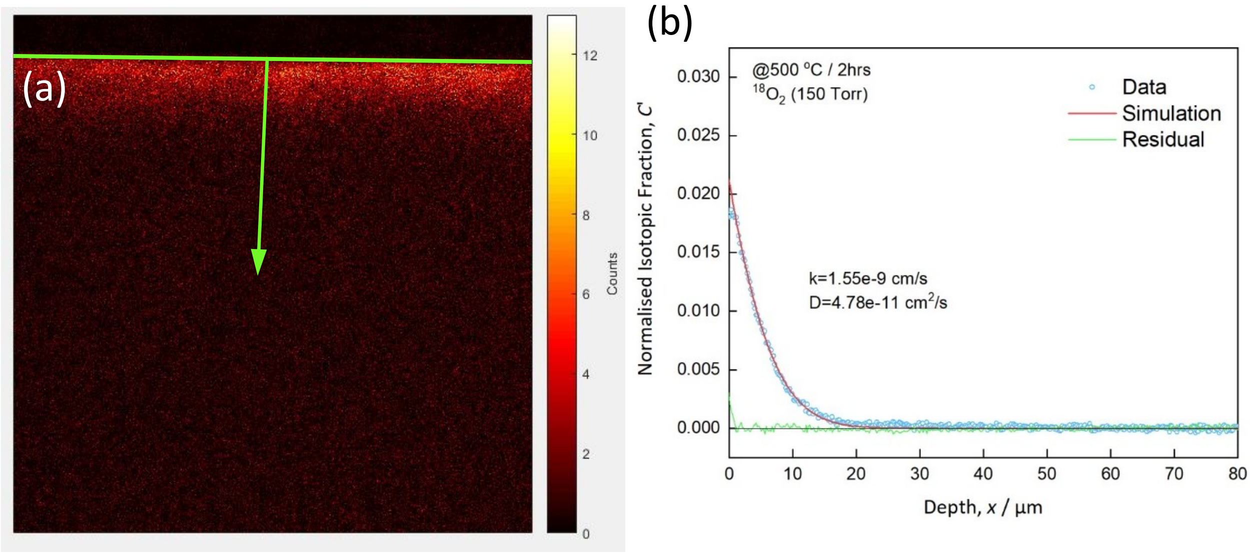

Figure 6.4 (a) ^{18}O map of the selected area of the BNC20 sample exchanged in $^{18}O_2$ at 500 ℃ for 2 hours. The green lines present the starting line of the diffusion profile and the diffusion direction. (b) The corresponding fitted depth profile of the selected region, where the blue circles represent data points, the red line shows the simulation results and the green line is the fitted residual.

Figure 6.4 (a) showed a representative ^{18}O map of the selected area of the BNC20 sample which had been exchanged in $^{18}O_2$ at 500 ℃ for 2 hours, where the green lines illustrate the starting line of the diffusion profile and the diffusion direction. As can be depicted from Figure 6.4(a), the starting edge of the diffusion profile was well defined, so that a whole region analysis using TraceX can be applied. Figure 6.4(b) showed the corresponding fitted depth profile of the selected region which included the experimental conditions in the top left corner and the obtained diffusion kinetics.

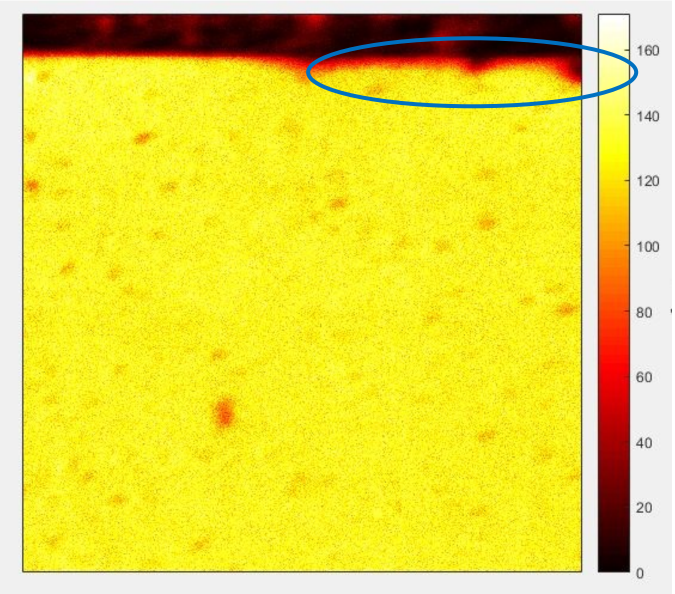

Figure 6.5 ^{16}O+^{18}O map of the selected area of the BNC20 sample exchanged in $^{18}O_2$ at 550 ℃ for 2 hours

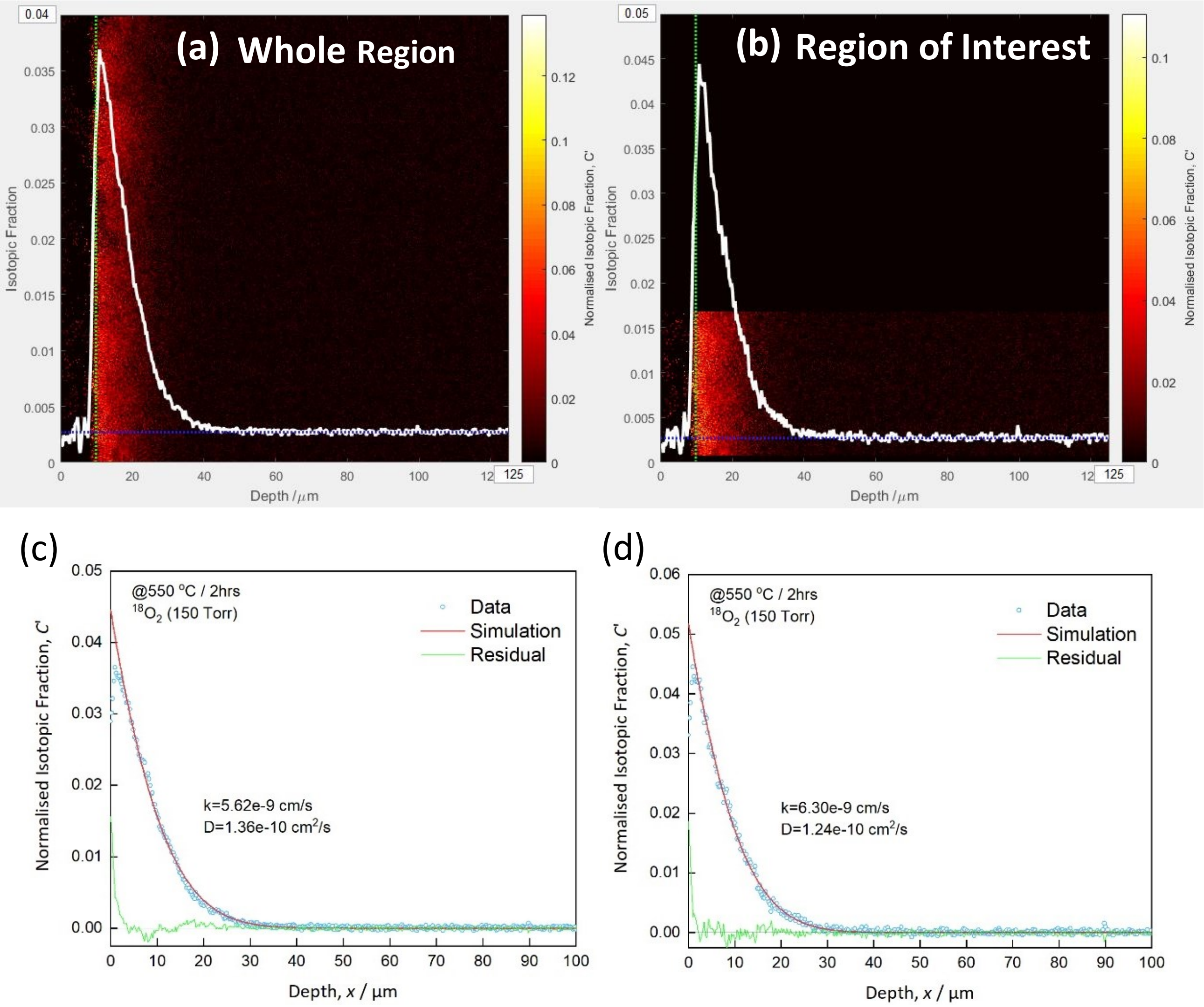

Figure 6.6 ^{18}O map of the selected area of the BNC20 sample exchanged in $^{18}O_2$ at 550 ℃ for 2 hours and two analysing solutions, namely the (a) whole region and the (b) region of interest (ROI) analysis. The green dotted lines point out the starting line for diffusion and the blue dotted lines show the background fraction of ^{18}O. Corresponding fitted depth profiles of the selected regions, respectively for the (c) whole region analysis and the (d) ROI analysis.

In some derived $^{16}O/^{18}O$ maps, the uniformity of the sample edge was not ideal as shown in Figure 6.5. In the ^{16}O map of the 550 ℃ exchanged sample, the edge of the diffusion profile was not a straight line where many geometric defects could be seen on the right hand side, as emphasized with the blue circle. To avoid inducing extra errors, the region of high uniformity was selected in the Region of Interest (ROI) analysis mode of TraceX to produce the depth profile. However, a drawback of the ROI analysis mode was that more noise was introduced in the derived depth profile due to the small amount of data included as seen in Figure 6.6(b). The poor uniformity of the starting edge could be ascribed to many factors, for instance, grinding and polishing damage, original porosities in the sample and the quenching thermal history during the exchange experiment.

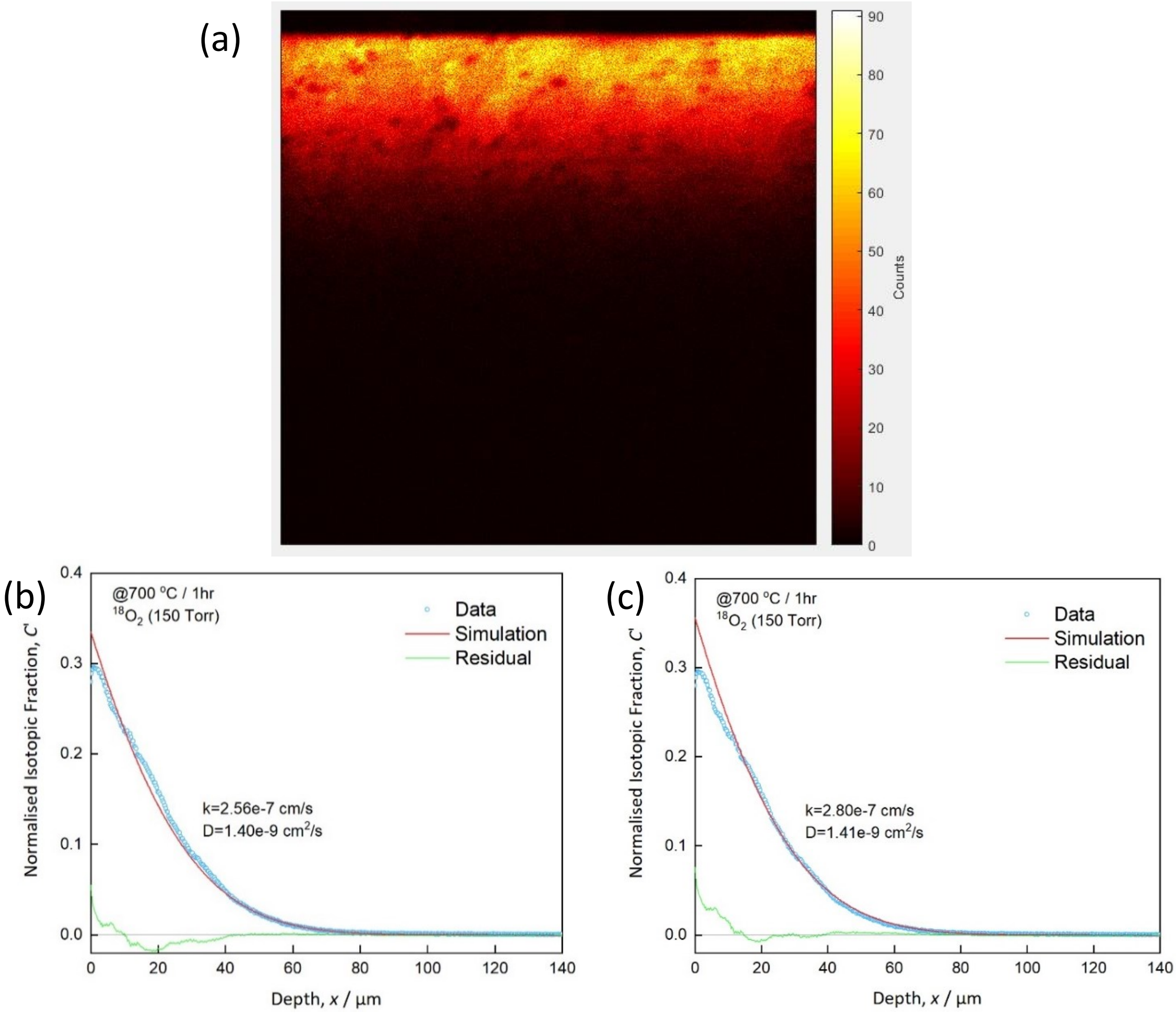

Figure 6.7 (a) ^{18}O map of the selected area of the BNC20 sample exchanged in $^{18}O_2$ at 700 ℃ for 1 hour. The green line presents the starting line of the diffusion profile. (b) The corresponding fitted depth profile of the whole region. (c) Manual fit of the depth profile excluding the inhomogeneous area and fitting from 18 μm to 120 μm in diffusion depth.

Overall, the obtained depth profiles were fitted quite well with the Crank solution according to the residuals shown with the green lines except for the 700 ℃ depth profile as shown in Figure 6.7 above. The relatively large mismatch between the obtained data and the simulation results around the sample edge can be attributed to the edge effect of the SIMS technique. The 'dead time' and saturation effects of a ToF-SIMS detector may also contribute to the underestimation of the surface exchange coefficient obtained in the SIMS-linescan method. In the 700 ℃ depth profile, the mismatch could be referred to the inhomogeneity as noticed in Figure 6.7(a). These surface features appeared near the diffusion frontier showed low ^{18}O concentration as these region were darker in the ^{18}O map. Therefore, a manual fit of the 700 ℃ depth profile excluding the inhomogeneous area and fitting from 18 μm to 120 μm in diffusion depth was performed in comparison with the automatic fit of the whole region. The new restriction zone of the fit didn't affect the diffusion coefficient, *D*, significantly, however, the obtained surface exchange coefficient, *k*, was increased by approximately 10%. Therefore, additional attention should be paid upon the obtained surface exchange coefficients in the extensive analysis.

To investigate the data validity and reliability of the derived diffusion kinetics, the *h*-plot was employed, in which the normalised ^{18}O isotopic fraction at the sample surface, $C'(0)$, is plotted against the dimensionless variable $h'=h\sqrt{Dt}$. In the plot, the solid dark line represents the theoretical or calculated values, while the solid triangles are the empirical data obtained in the SIMS-linescan measurements above. The diffusion kinetics obtained in the dry isotope exchange experiments are listed in Table 6.1 below.

Table 6.1 Dry oxygen diffusion kinetics of BNC20 sample obtained by SIMS-linescan analysis.

Exchange atmosphere	T (℃)	t (s)	$C'(0)$	D (cm^2/s)	k (cm/s)	$h=k/D$ (cm^{-1})	$h'=h\sqrt{Dt}$
$^{18}O_2$ (150 Torr)	500	7200	0.018	4.78×10^{-11}	1.55×10^{-9}	32.43	0.019
$^{18}O_2$ (150 Torr)	550	7200	0.036	1.36×10^{-10}	5.62×10^{-9}	41.32	0.041
(ROI) (▲)			0.045	1.24×10^{-10}	6.30×10^{-9}	50.81	0.048
$^{18}O_2$ (150 Torr)	600	3600	0.152	2.27×10^{-10}	4.42×10^{-8}	194.7	0.176
$^{18}O_2$ (150 Torr)	700	3600	0.300	1.40×10^{-9}	2.56×10^{-7}	182.9	0.410
(Manual) (▲)			0.300	1.41×10^{-9}	2.80×10^{-7}	198.6	0.447

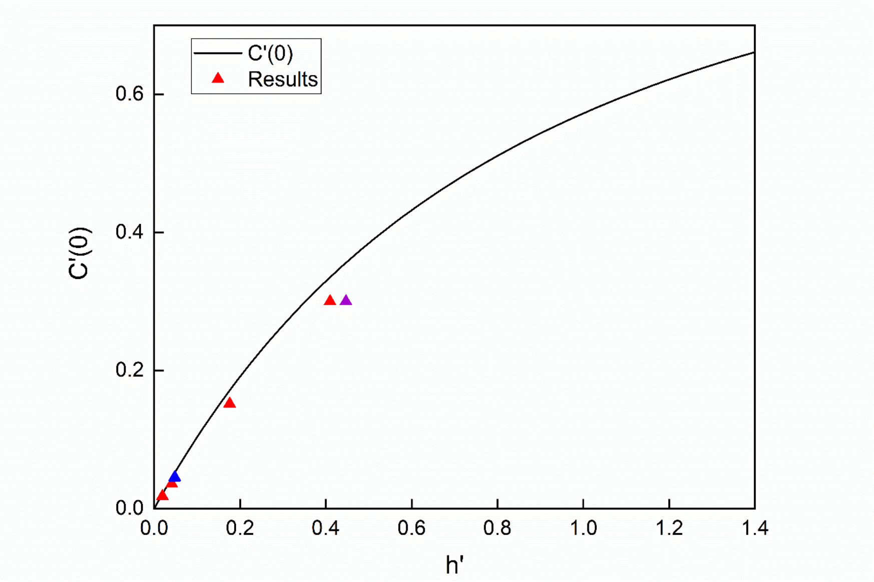

Figure 6.8 Normalised surface isotope fraction as a function of the reduced variable *h*′, where the curve represents the calculated surface isotope fractions based on Eq. (47) and the solid triangles are the experimental data obtained in the dry ^{18}O isotopic exchange experiments. The blue sign is the 550 ℃ region of interest data and the purple one is the 700 ℃ manually fitted data, respectively.

Except for the data point belonging to the manual fit of the 700 ℃ depth profile, all the data points derived from the SIMS-linescan analysis agree reasonably well with the calculated profile. The relatively significant discrepancy between the experimental values and the theoretical values in the 700 ℃ depth profile can be referred to the lower quality of the SIMS mapping results where significant surface inhomogeneity can be observed. The data consistency of the set of experiment needs to be confirmed either by repeating the exchange experiment or by reanalysing the previous sample and finding another flat region on the sample surface. Another solution proposed in the previous literature(60) to achieve reliable surface exchange coefficients was to determine the surface tracer fraction additionally by depth profiling on the original exchanged surface of the correlated sample. By doing so, the fitting of the derived depth profile can be refined by a certain surface isotopic fraction value at x=0, which will result in a significant discrepancy between the simulation results and the derived depth profile near the sample surface(183). However, as can be seen in Table 6.1, the diffusion coefficients obtained within the bulk material were quite consistent when changing the analysis methods.

The temperature dependence of the diffusion kinetics will be discussed in detail in the following sections with the ones obtained in various wet atmospheres. Here instead, comparisons of the depth profiles measured under different temperatures were illustrated in the figures below. A clear increase in both *D* and *k* can be noted in the elevated temperatures according to the increasing normalised surface ^{18}O fractions and the longer permeation depth.

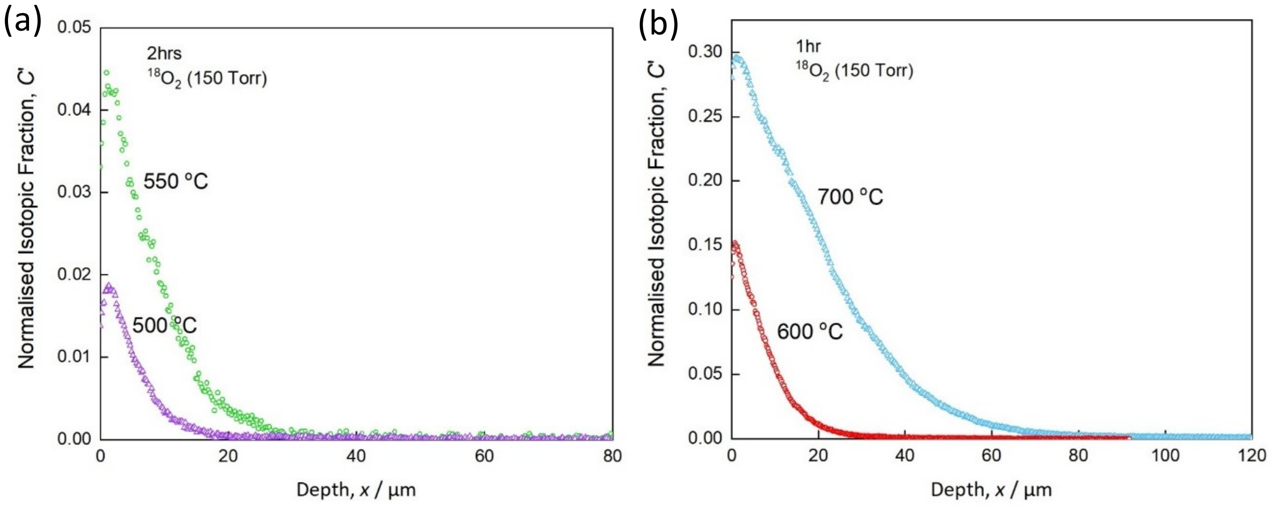

Figure 6.9 Line scan profiles of ^{18}O penetration into BNC20 samples exchanged at (a) 500 and 550 ℃ for two hours and at (b) 600 and 700 ℃ for 1 hour.

6.2.2 Oxygen diffusion in BNC20 under wet atmosphere

Unlike the dry $^{18}O_2$ isotope exchange experiments where the ^{18}O tracer came from the simple-substance gaseous atmosphere of $^{18}O_2$, in the wet ^{18}O exchange, a mixed gaseous atmosphere of 150 Torr $^{16}O_2$ with ~ 30 Torr $H_2{}^{18}O$ was introduced and the tracer originated from the water vapor in the environment. As a result, the surface exchange process of the sample with the mixed gas in wet exchange is more complicated, and therefore, the residual gas composition after the exchange experiment was monitored using the coupled Residual Gas Analyzer (RGA) system with mass spectrometry. A typical mass spectrum after a wet exchange is shown in Figure 6.10, which was obtained by RGA measurement of the residual gas after 2 hours wet exchange at 700 ℃. The isotopic fraction of the original $H_2{}^{18}O$ source was confirmed to be 87% by RGA measurement before the exchange experiments. In the wet exchange experiments the residual gas is not recovered, and thus, the ^{18}O concentration of 0.87 can be used in the simulations of the wet exchange depth profiles. The RGA results of the residual gas after the exchange experiment performed at 500 ℃ and 700 ℃ for 2 hours and 1 hour, respectively are shown in Table 6.2 below. Owing to the severe molecular scrambling at high temperatures (700 ℃), one of the assumed boundary conditions: $-D\left(\frac{\partial\varphi}{\partial x}\right)_{x=0} = k[C_{gas} - \varphi(x=0,t)]$, is no longer valid because the C_{gas} variable can not be treated as a constant now. During the high temperature exchange experiment, the isotopic fraction in the environmental gas kept decreasing as a result of the molecular scrambling, which then lead to significant errors in the determination of the diffusion kinetics, especially in the obtained *k* values.

Table 6.2 ^{18}O isotopic fraction before and after wet exchange experiment measured by RGA.

Experiment	Temperature (℃)	Exchange Time (s)	$C_{gas}(^{18}O)$ before	$C_{gas}(^{18}O)$ after
$H_2{}^{18}O+O_2$	500	7200	0.87	0.84
$H_2{}^{18}O+O_2$	700	7200	0.87	0.49
$H_2{}^{18}O$	500	7200	0.87	0.86

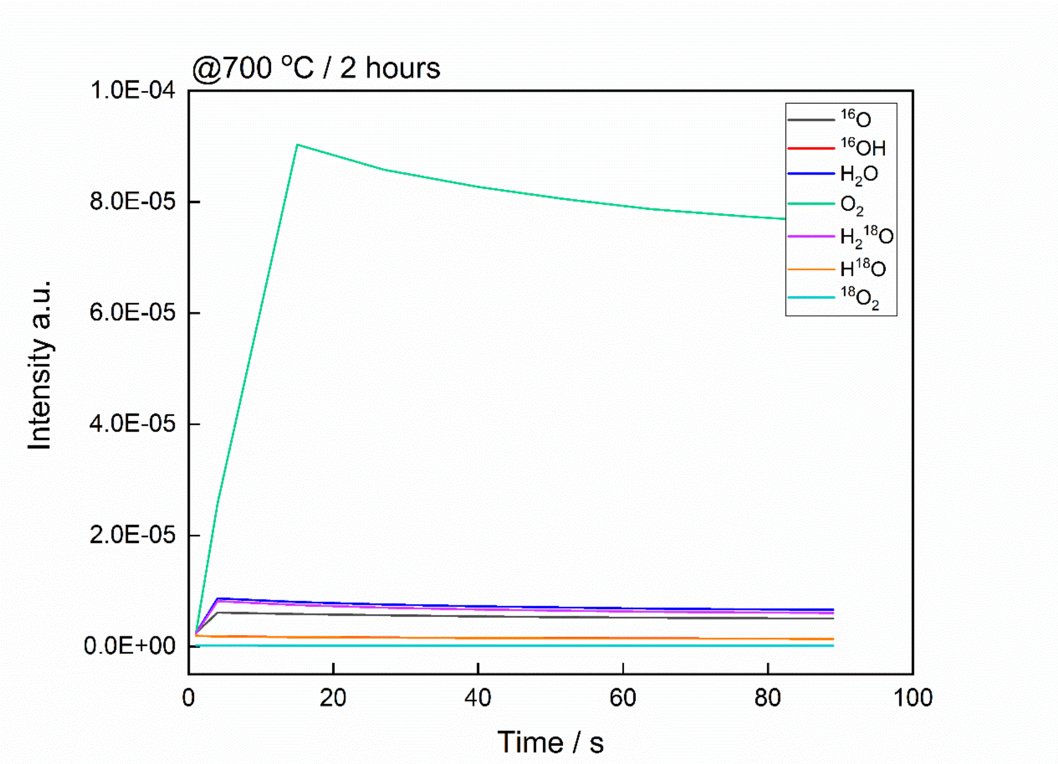

Figure 6.10 RGA measurement results of the residual gas after the 2 hours' exchange experiment at 700 ℃.

Therefore, the wet ^{18}O exchange experiments were selectively performed on the dense BNC20 samples at 500, 550 and 600 ℃ in the $H_2{}^{18}O+O_2$ environment and at 500 ℃ particularly in the pure $H_2{}^{18}O$ atmosphere. The ^{18}O map obtained by SIMS along with the simulation results are shown in the figures below. It needs to be mentioned that the detected intensities of the $^{18}O^-$ and $^{18}OH^-$ ions under SIMS are similar. Figure 6.11-6.14 below are the ^{18}O maps because it gave slightly higher counts, while the total oxygen counts were included in the Appendices as A.6-A.9. Both of the depth profiles achieved from the $^{18}O/^{16}O$ maps and from the $^{18}OH/OH$ maps respectively were analysed using TraceX, while the resulting diffusion coefficients were almost the same. The statistics of the fitted results are listed in the Table 6.3.

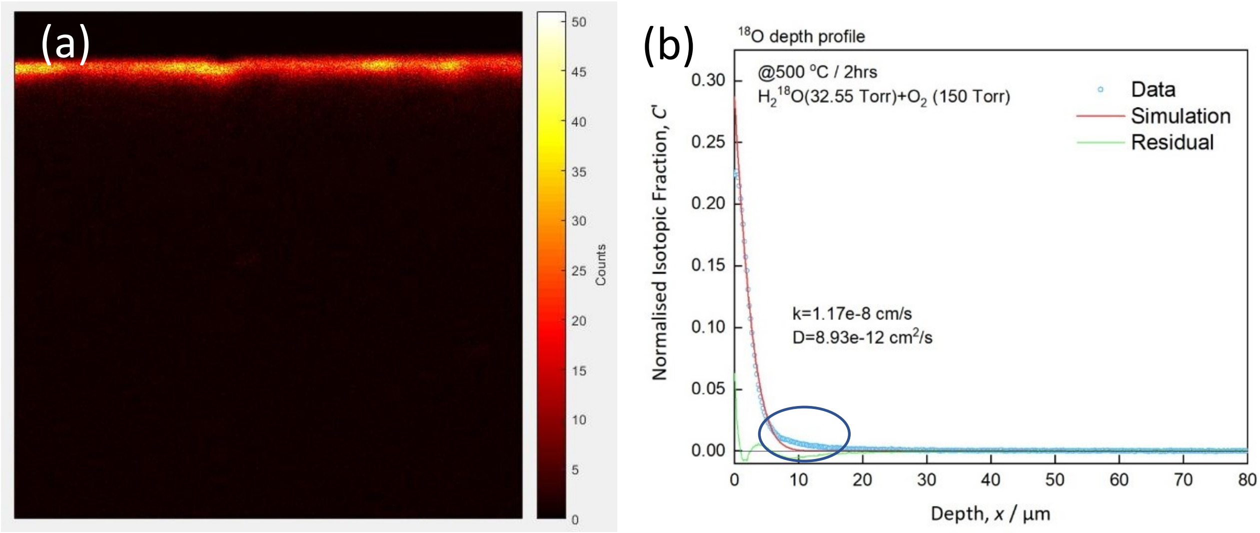

Figure 6.11 (a) ^{18}O map of the selected area of the BNC20 sample exchanged in O_2 (150 Torr)+ $H_2{}^{18}O$ (32.55 Torr) at 500 ℃ for 2 hours. (b) The corresponding fitted depth profile of the whole region. The blue circle labels the major mismatch of the data.

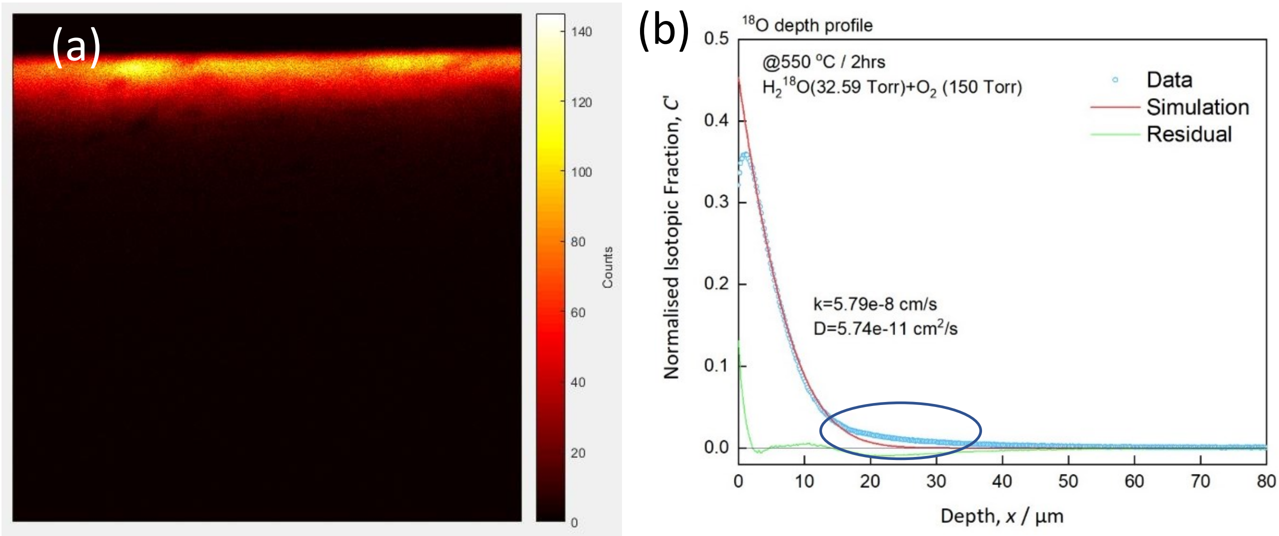

Figure 6.12 (a) ^{18}O map of the selected area of the BNC20 sample exchanged in O_2 (150 Torr)+ $H_2{}^{18}O$ (32.59 Torr) at 550 ℃ for 2 hours. (b) The corresponding fitted depth profile of the whole region. The blue circle labels the major mismatch of the data.

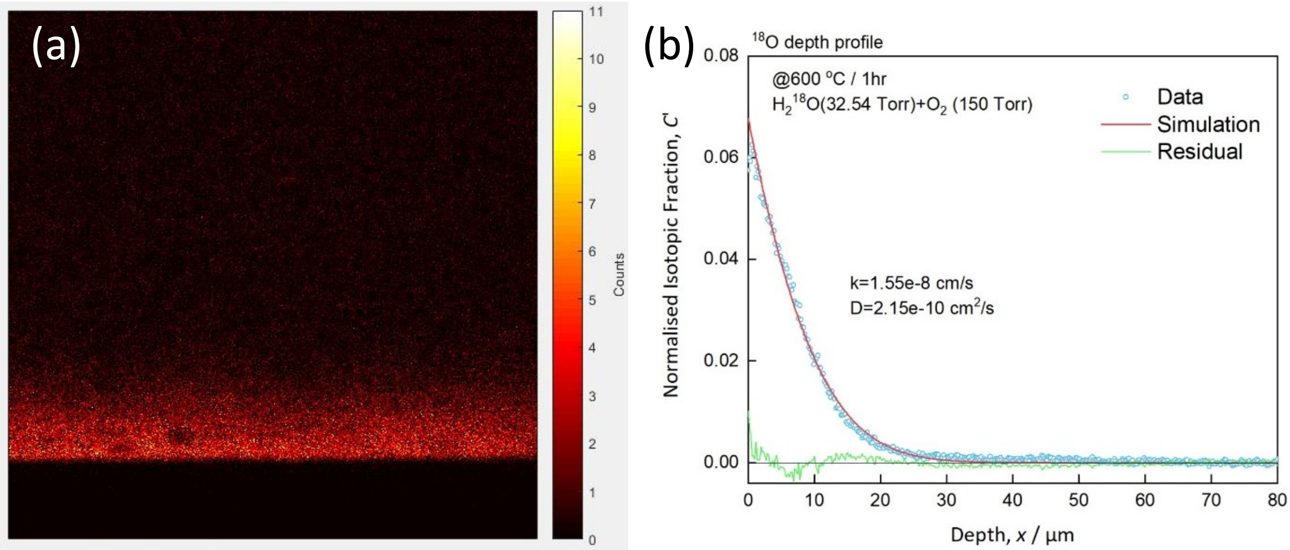

Figure 6.13 (a) ^{18}O map of the selected area of the BNC20 sample exchanged in O_2 (150 Torr)+ $H_2{}^{18}O$ (32.54 Torr) at 600 ℃ for 1 hour. (b) The corresponding fitted depth profile of the whole region.

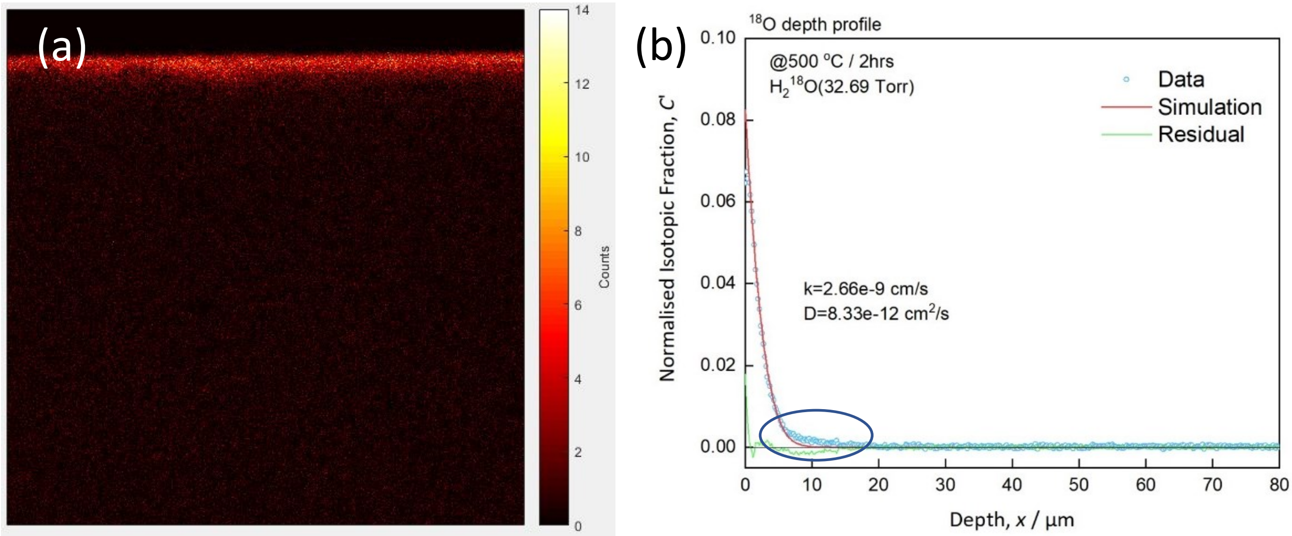

Figure 6.14 (a) ^{18}O map of the selected area of the BNC20 sample exchanged in pure $H_2{}^{18}O$ (32.69 Torr) at 500 ℃ for 2 hours. (b) The corresponding fitted depth profile of the whole region.

As labelled by blue circles in the corresponding depth profiles obtained from the wet exchange experiments, the major mismatch between the simulated result and the empirical result appeared as a shoulder in the depth profile, which indicated, potentially, a fast grain boundary diffusion mechanism for oxygen migration under wet atmospheres. Other sources of error may also account for the discrepancy in the data fitting, such as surface roughness and features caused by polishing process. A larger depth profile achieved through an exchange experiment with a longer period of time can effectively minimized the error caused by small features on the sample surface. Considering fast grain boundary diffusion of oxide-ions in the system, since the diffusivity of oxygen ions through grain boundary is faster than in grains, grain boundaries can function as shortcuts for oxide-ion migration which resulted in large discrepancy in the depth profile fitting using Crank's solution. Similar observations for the fast grain boundary diffusion in the oxygen diffusion depth profiles in solid oxides could be found in the previous literature(183, 227-229). All the wet exchange depth profiles except for the 600 ℃ one showed an unfitted shoulder indicating fast grain boundary diffusion. According to Kilner(229), the critical value for material diffusivity to observe the fast grain boundary diffusion behavior in an oxygen depth profile is 10^{-12} cm^2/s. In the 600 ℃ wet exchange profile, the obtained diffusion coefficient was 2.15 x 10^{-10} cm^2/s which was much larger than this critical value, and therefore, the fast grain boundary tail is no longer visible. Table 6.3 concludes all the obtained diffusion kinetics of the wet exchange experiments.

Table 6.3 Wet oxygen diffusion kinetics of BNC20 sample obtained by SIMS-linescan analysis.

Exchange atmosphere	T (℃)	t (s)	$C'(0)$	D (cm^2/s)	k (cm/s)	$h=k/D$ (cm^{-1})	$h'=h\sqrt{Dt}$
$O_2+H_2{}^{18}O$	500	7200	0.225	8.93 x 10^{-12}	1.17 x 10^{-8}	1310	0.332
($^{18}OH/OH$)				8.80 x 10^{-12}	1.11 x 10^{-8}		
$O_2+H_2{}^{18}O$	550	7200	0.355	5.74 x 10^{-11}	5.79 x 10^{-8}	1009	0.648
($^{18}OH/OH$)				5.10 x 10^{-11}	4.28 x 10^{-8}		
$O_2+H_2{}^{18}O$	600	3600	0.633	2.15 x 10^{-10}	1.55 x 10^{-8}	72.09	0.634
($^{18}OH/OH$)				2.05 x 10^{-10}	1.38 x 10^{-8}		
$H_2{}^{18}O$	500	7200	0.068	8.33 x 10^{-12}	2.66 x 10^{-9}	319.3	0.078
($^{18}OH/OH$)				8.25 x 10^{-12}	2.48 x 10^{-9}		

*Second row of each data represents the *D* and *k* values obtained from the $^{18}OH/OH$ maps.

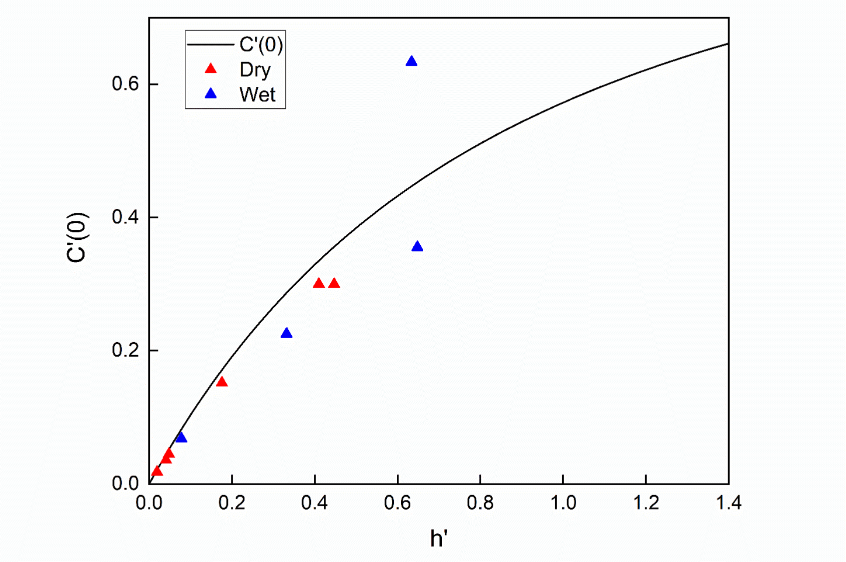

Figure 6.15 Normalised surface isotope fraction as a function of the reduced variable *h'*, where the curve represents the calculated surface isotope fractions based on Eq. (47) and the solid red triangles represent the experimental data obtained in the dry ^{18}O isotopic exchange experiments, while the blue ones are data points obtained in the wet exchange experiments.

According to the *h'*-plot, the normalised surface isotope fractions of the wet exchange depth profiles are quite different from the calculated values compared with data points from the dry exchange experiments. The dramatic difference in the *h'*-plot with the calculated value may result in poor reliability of the obtained wet surface exchange coefficients, especially for the 600 ℃ wet exchanged sample. This could be referred to the discrepancy of the fitting in the 600 ℃ depth profile.

6.2.3 Grain boundary diffusion product

To investigate the potential fast grain boundary diffusion of the oxygen ions within the system, a grain boundary model was induced (Figure 6.16), where the grain boundary is treated as a uniform and isotropic slab of material of width δ with a coefficient D_{gb} much greater than the coefficient D_{b} for diffusion in the grains on either side. Subject to the normal continuity conditions at the grain boundary edges, $c=c'$ and $D_{\mathrm{gb}}\,{}^{\partial c'}\!/_{\partial x} = D_{\mathrm{b}}\,{}^{\partial c}\!/_{\partial x}$ where c and c' donate concentrations outside and inside the slab respectively, two additional boundary conditions were chosen to solve the equation of Fick's 2nd law for the region inside and outside the slab as expressed below.

$$\frac{2D_{\mathrm{b}}}{\delta}\frac{\partial c}{\partial x} + D_{\mathrm{gb}}\frac{\partial^2 c}{\partial y^2} = \frac{\partial c}{t} \tag{74}$$

$$C(x, y, t) = C_0; t \geq 0; y = 0 \tag{75}$$

while Equation (75) assuming the surface concentrations maintained everywhere at some constant value from t=0 onwards was chosen by Whipple(230) to solve the two-dimensional Fick equation: $D_{\mathrm{b}}\left(\frac{\partial^2 c}{\partial y^2} + \frac{\partial^2 c}{\partial x^2}\right) = \frac{\partial c}{\partial t}$. Two reduced and dimensionless variables and one parameter were also introduced:

$$\eta = \frac{y}{\sqrt{D_{\mathrm{b}} t}}, \xi = \frac{x - {}^{\delta}\!/_{2}}{\sqrt{D_{\mathrm{b}} t}} \tag{76}$$

$$\beta = \frac{D_{\mathrm{gb}}}{D_{\mathrm{b}}}\frac{{}^{\delta}\!/_{2}}{\sqrt{D_{\mathrm{b}} t}} \tag{77}$$

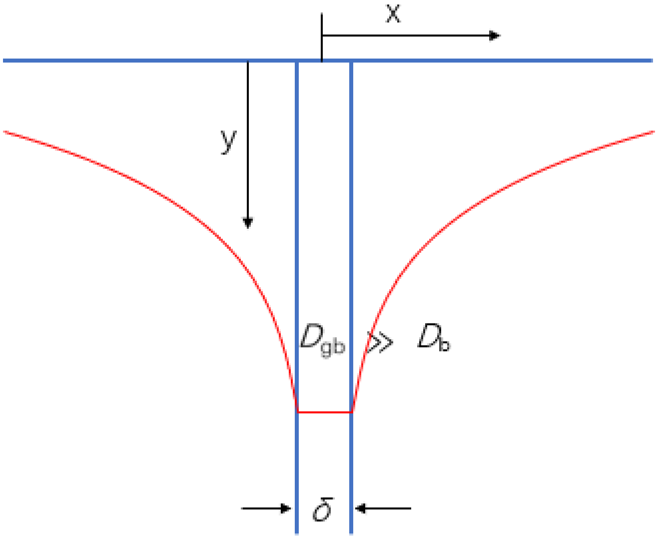

Figure 6.16 Schematic of the two dimensional fast grain boundary diffusion model for mathematic calculations

The solution of the two-dimensional Fick equation in detail will not be discussed here, but the reader is directed to the comprehensive discussion of the solution by reference (230, 231). According to De Souza(232), a modified expression of Whipple's exact solution can be expressed as:

$$C'(y, t) = \frac{C(y, t) - C_{\mathrm{bg}}}{C_{\mathrm{gas}} - C_{\mathrm{bg}}}$$

$$= \mathrm{erfc}\left(\frac{y}{2\sqrt{Dt}}\right) - \left[\exp\left(\frac{ky}{D_\mathrm{b}} + \frac{k^2t}{D_\mathrm{b}}\right) \times \mathrm{erfc}\left(\frac{y}{2\sqrt{D_\mathrm{b}t}} + k\sqrt{\frac{t}{D_\mathrm{b}}}\right)\right] + A_\mathrm{gb} exp\left(-Zy^{6/5}\right) \tag{78}$$

where A_gb and Z are the reduced parameters for grain boundary fast diffusion. The whole solution can be seen as an extension from the Crank solution by adding a grain boundary diffusion term in the end. In this research, the approximation expression proposed by Chung and Wuensch (231) for the determination of a grain boundary diffusion product, $D_\mathrm{gb} \cdot \delta$, was used for further calculations, which can be expressed as:

$$D_\mathrm{gb}\delta = 2D_\mathrm{b}^{3/2}t^{1/2}\left[10^A\left(-\frac{\partial \ln C}{\partial \eta^{\frac{6}{5}}}\right)^B\right] \tag{79}$$

where *A* and *B* are constants which can be determined according to the value of β as listed in Table 6.4.

Table 6.4 Ranges of values for β; the resulting ranges of average slope, $\partial \ln C / \partial \eta^{\frac{6}{5}}$; and the parameters *A, B,* and *R* obtained by computations(231).

Ranges of β selected for computation	Resulting ranges of computed average values for $\partial \ln C / \partial \eta^{\frac{6}{5}}$	Parameters resulting from regression analysis		
		A	B	R
1-10	-0.702627– -0.195588	-0.274313	-1.797654	0.99999
10-100	-0.195588– -0.056815	-0.326028	-1.865051	0.99997
100-1000	-0.056815– -0.0173545	-0.422809	-1.943238	0.99999
1000-10000	-0.0173545– -0.0054179	-0.484307	-1.978574	0.99999
10000-100000	-0.0054179– -0.0016949	-0.498762	-1.985363	0.99999

The use of these results to obtain grain boundary diffusion products, $D_\mathrm{gb}\delta$, or grain boundary diffusion coefficient, D_gb, essentially reverses the computational procedures as described in the previous reference(231). The average slope of $\partial \ln C / \partial \eta^{5/6}$ can be determined by linear fitting of the $\ln C$-$\eta^{5/6}$ in the selected area of $6 \le \eta \le 10$. The specific range of η were selected to ensure no significant contrition from bulk diffusion while the fractional contribution to *C* at this limit range are 2.2 x 10^{-5} to 1.5 x 10^{-12}, respectively. Larger values of η were not included in the linear fitting due to the consideration of distinguishing SIMS data near the end of the profiles from the background natural abundance. Then the obtained average slope values were fit in the appropriate ranges in the Table above to achieve the corresponding *A* and *B* values, which could be substitute into Equation (79) with the $\partial \ln C / \partial \eta^{5/6}$ value to yield the grain boundary diffusion products, $D_\mathrm{gb}\delta$. The grain boundary diffusion coefficient could therefore be estimated according to the dimension of the grain boundaries in the material.

By plotting the $\ln C$ against $\eta^{5/6}$, the wet exchange profiles were linear fitted in the selected region of $6 \le \eta \le 10$ as shown in Figure 6.17 & Figure 6.18. The 500 ℃ and 550 ℃ wet exchange profiles showed obvious linear region in the specific area indicated a fast grain boundary diffusion mechanism, while in the 500 ℃ pure $H_2{}^{18}O$ wet exchanged profile, and in the 600 ℃ wet exchange profile, the fast grain boundary diffusion was not that obvious, and the experimental data points of that region in the $\ln C$-$\eta^{5/6}$ plot were not linearly distributed. The grain boundary diffusion products obtained by the aforementioned solution for the 500 ℃ and 550 ℃ wet exchange profiles are listed in the chart below. Assuming that the grain boundary dimension, δ, is around 2 ~ 8 nm(68), then the oxygen diffusion coefficient in grain boundary can be estimated to be ~

10^{-7} cm^2/s which is orders-of-magnitude higher than the bulk oxygen diffusion coefficient. Therefore, fast grain boundary oxygen diffusion in the BNC20 sample under $H_2{}^{18}O+O_2$ gaseous atmosphere was confirmed. However, in the 500 ℃ pure $H_2{}^{18}O$ wet exchanged profile, and in the 600 ℃ wet exchange profile, the grain boundary tail was not well defined, while the latter one could be ascribed to the relatively large bulk diffusion coefficient which exceeds the critical value for visible fast grain boundary diffusion(229).

Table 6.5 The grain boundary diffusion products obtained according to Chung and Wuensch approximation(231).

T (℃)	D_b (cm^2/s)	t (s)	$\partial \ln C / \partial \eta^{5/6}$	$D_{gb} \cdot \delta$ (cm^3/s)	β
500	8.93×10^{-12}	7200	-0.15848	6.64×10^{-14}	14.7
550	5.74×10^{-11}	7200	-0.23466	5.31×10^{-13}	7.20

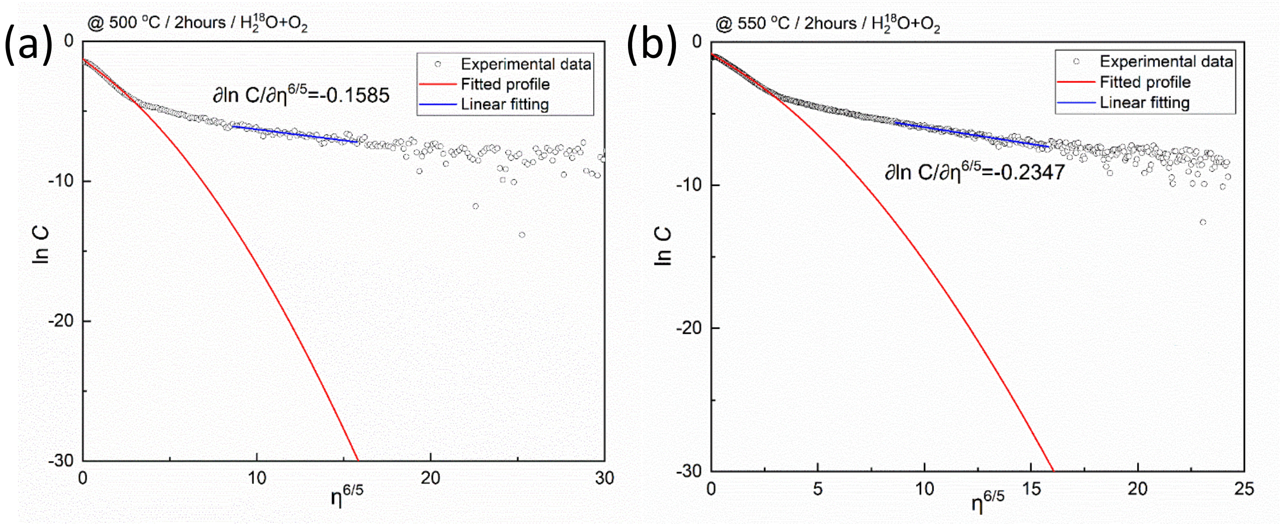

Figure 6.17 $\ln C$-$\eta^{\frac{6}{5}}$ plots with the fast grain boundary diffusion profile fitting of BNC20 samples wet exchanged at (a) 500 ℃ and (b) 550 ℃for 2 hours, where the red solid lines represent the fitted profile discussed in the last section.

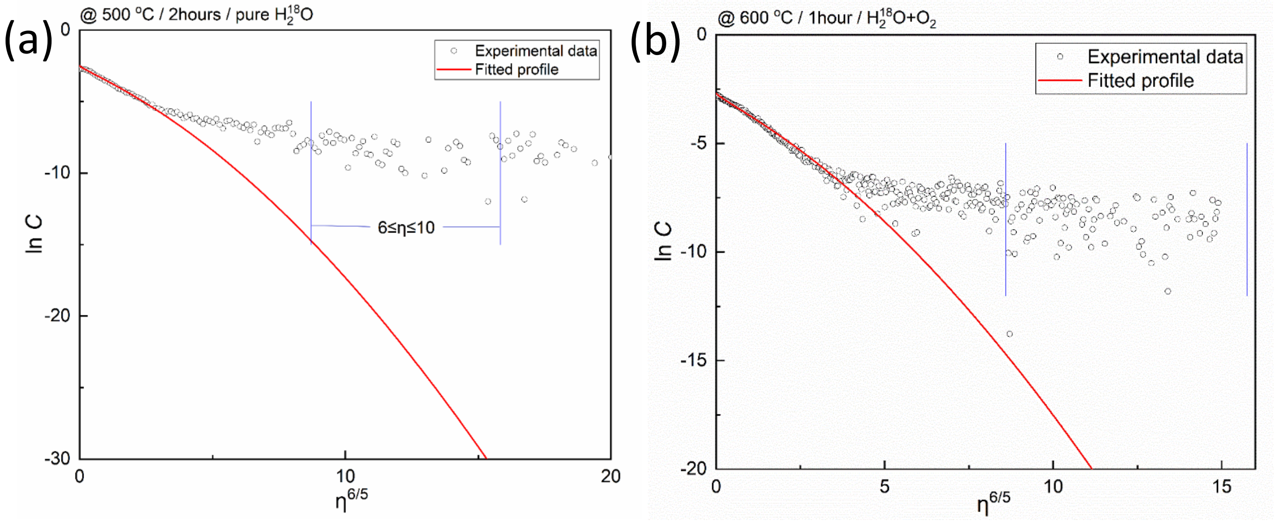

Figure 6.18 (a) $\ln C$-$\eta^{\frac{6}{5}}$ plot of BNC20 sample wet exchanged in pure $H_2{}^{18}O$ at 500 ℃ for 2 hours, where the data from the selected region $6 \leq \eta \leq 10$ was labelled by blue vertical lines. (b) $\ln C$-$\eta^{\frac{6}{5}}$ plot of BNC20 sample wet exchanged at 600 ℃ for 1 hour.

6.2.4 Oxygen diffusion kinetics of BNC20

The comparison between oxygen diffusion depth profiles obtained in dry $^{18}O_2$ exchange experiments and the ones obtained in wet $H_2{}^{18}O+O_2$ exchange experiments is illustrated in the Figure 6.19, where the red marks represent the wet profiles and the blue ones represent the dry profiles. At 500 and 550 ℃ the existence of water vapor in the gas significantly improved the surface exchange process as the surface isotope fraction in these two profiles were greatly increased. A reverse trend was seen in the 600 ℃ exchange profile, the corresponding sample was analysed in particular under STEM-EDS for further elemental analysis. On the other hand, the oxygen diffusion coefficients, *D*, were slightly decreased in the wet condition in all three plots of depth profiles, which could be referred to as further evidence for the formation of protonic defects. And the formed protonic defects seemed to add an extra barrier for the oxygen diffusion in the bulk materials. The resulting diffusion kinetics were plotted in the Arrhenius plots as shown in Figure 6.20 (a)&(b).

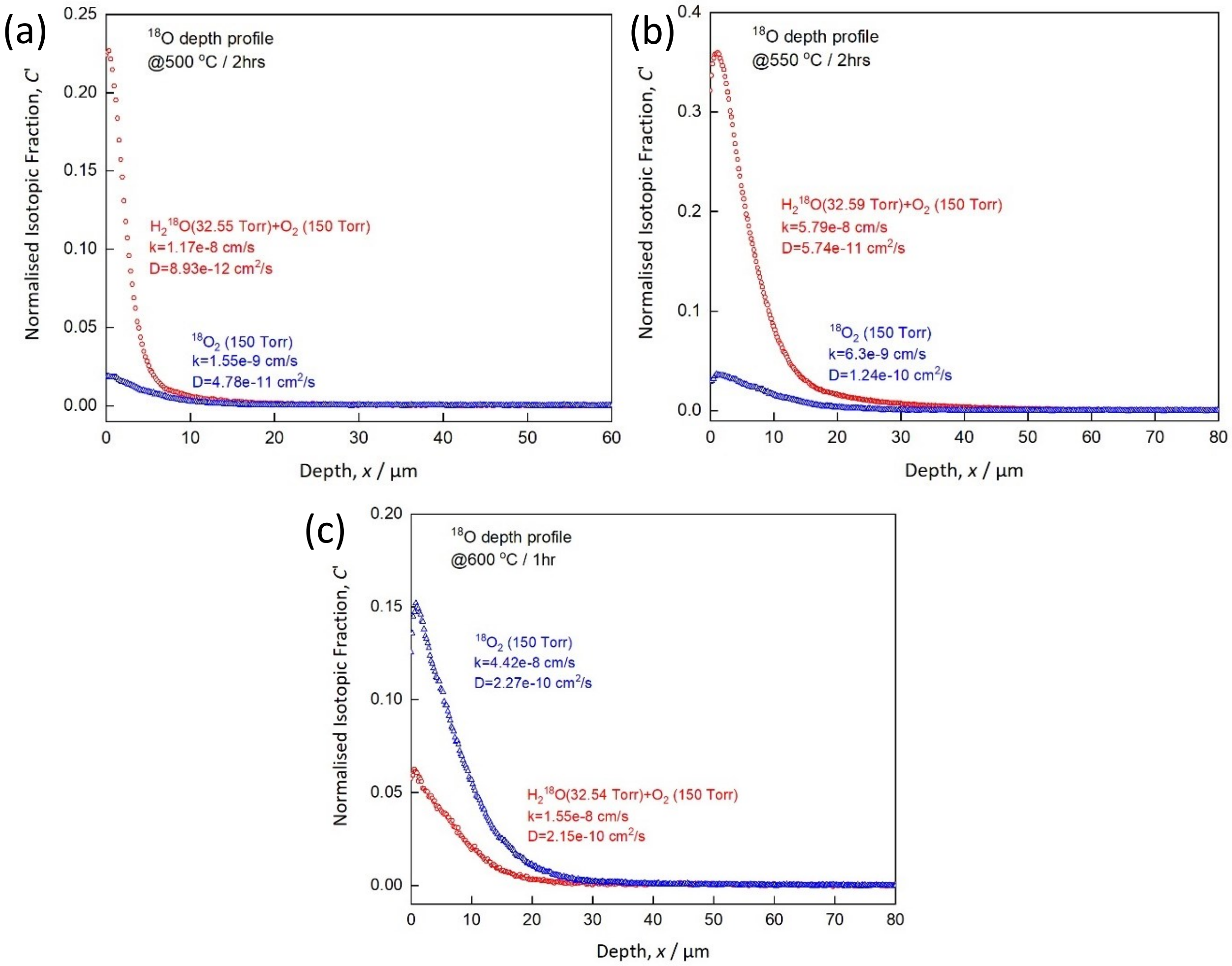

Figure 6.19 ^{18}O depth profiles of BNC20 sample obtained in dry and wet exchange experiments at (a) 500 ℃ (b) 550 ℃ and (c) 600 ℃.

Figure 6.20(a) shows the Arrhenius plot for oxygen diffusion coefficients, where the dark circles are the diffusion coefficients obtained in dry exchange experiments, the red triangles represent the values obtained in wet $H_2{}^{18}O+O_2$ exchange experiments and the blue rectangle is the on achieved in the 500 ℃ pure $H_2{}^{18}O$ wet exchange experiment. The water incorporation resulted in lower oxygen diffusion coefficients and a higher activation energy for oxygen diffusion coefficient. The activation energy was increased from 1.08(8) eV in dry condition to 1.86(11) eV after water incorporation, which implied a hindering effect of protonic defects on the oxygen diffusion process in the bulk material. As for the surface exchange process, a clear improvement can be seen in the surface exchange coefficients of the 500 and 550 ℃ wet exchange data, while at a higher temperature of 600 ℃ the surface exchange process seemed to be hindered, which could be ascribed to the dehydration of water on the sample surface or because of the secondary phases that emerged from the grain boundaries that block the oxygen permeation. Further experimental results are required to explain this unusual observation.

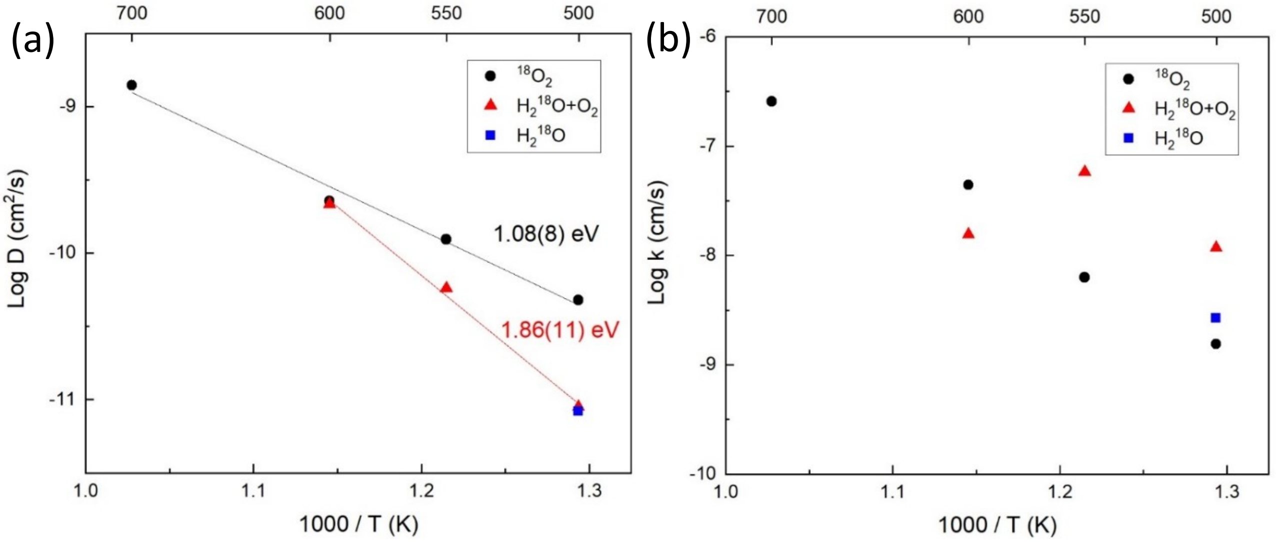

Figure 6.20 Arrhenius plots of the obtained (a) oxygen diffusion coefficients, *D*, and (b) surface exchange coefficients, *k*.

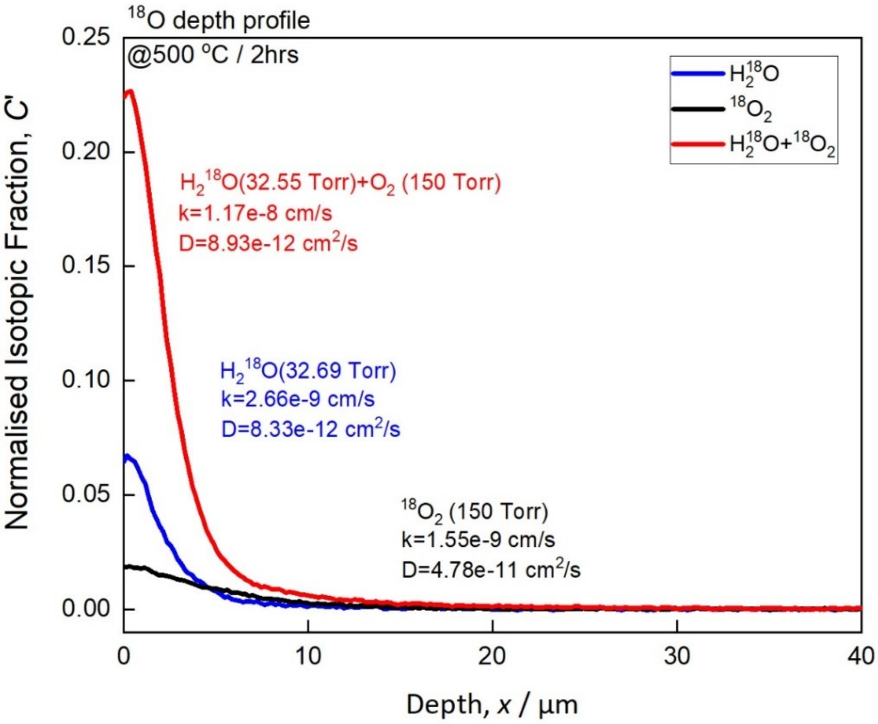

Figure 6.21 ^{18}O depth profiles of BNC20 sample obtained in different atmospheres.

Particularly, a sectioned sample of BNC20 was exchanged in pure $H_2{}^{18}O$ water vapor to make a comparison with the dry and wet exchange profiles. In the more reducing pure $H_2{}^{18}O$ environment, the surface exchange process was severely prohibited compared with that in $H_2{}^{18}O+O_2$ atmosphere, while the oxygen diffusion coefficients were almost the same in the wet conditions. This interesting observation in the surface exchange coefficients allows a probe on the surface exchange mechanism happened during the wet exchange experiments that oxygen molecules are involved in the surface exchange process. To obtain a more comprehensive understanding of the oxygen surface exchange mechanism on the surface of this material, more experimental data are required.

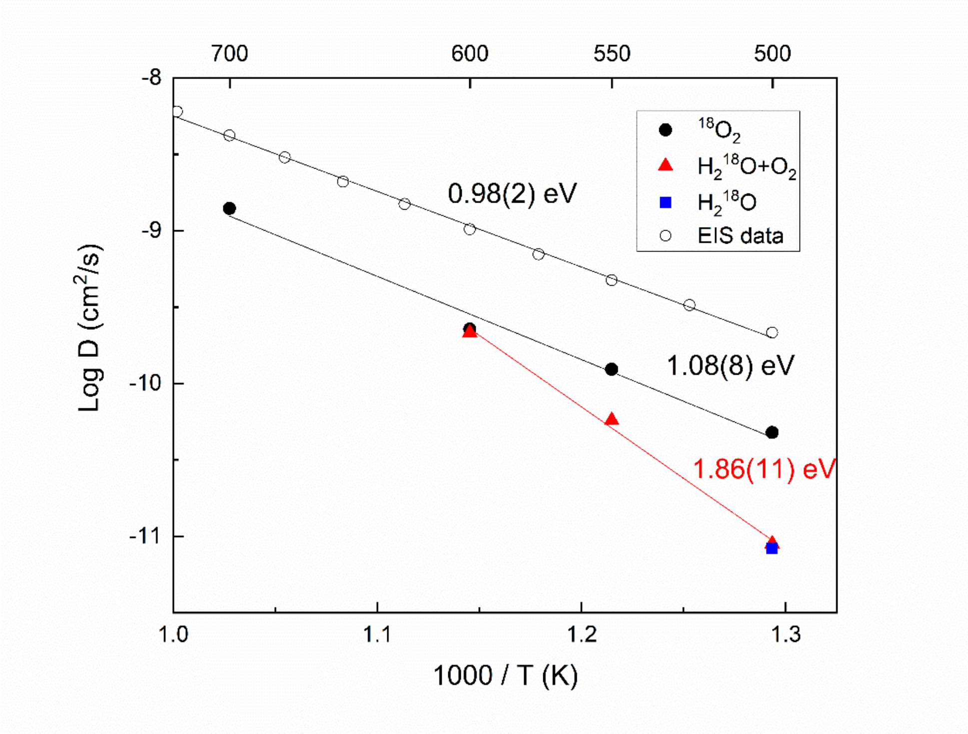

Figure 6.22 Arrhenius plots of the oxygen diffusion coefficients for BNC20 samples obtained through different methods.

According to the Nernst-Einstein relation $\mu = \frac{qD}{kT}$ (Equ. 1), the diffusion constants can also be calculated from the oxide-ion conductivity obtained in the EIS measurements. The electrical conductivity data of the BNC20 sample measured under N_2 atmosphere by EIS were substituted into the Einstein equation to achieve the calculated *D* values for oxygen diffusion. It needs to be mentioned that, the electrical conductivity data used for the calculation here were obtained in the dry N_2 condition, the oxygen partial pressure of which was around 10^{-4} atm. According to the previous literature(121), the oxygen partial pressure range of the oxide-ion dominant region (where the measured total conductivity equals the oxide-ion conductivity) for $BaNd_{0.9}Sr_{0.1}InO_{3.95}$ is below 10^{-6} atm. Therefore, the contribution of electronic carriers cannot be neglected here. The exact expression of the D_{calc} is shown below:

$$D_{calc} = fD_{self} = f \cdot \frac{\mu_{\mathrm{O}} k_{\mathrm{B}} T}{q} = 0.69 \cdot \frac{\sigma_{\mathrm{O}} k_{\mathrm{B}} T}{q^2 n_{\mathrm{O}}} \tag{80}$$

where D_{self} is the self-diffusion coefficient and f is the correlation factor which is 0.69 for a perovskite-structured material. μ_O represents the oxide-ion mobility in the bulk material, k_{B} is the Boltzmann constant and q is the electrical charge of oxide-ions; σ_{O}, in S·cm^{-1}, donates the oxide-ion conductivities which were substituted with electrical conductivities measured in dry N_2 in EIS measurements; n_{O} , in cm^{-3}, is the charge carrier density which can be calculated by dividing the number of charge carriers in a unit cell (3.9) by the unit cell volume (438.21 Å^3).

The resulting oxide-ion diffusion coefficients, D_{calc}, were plotted against 1000/T as shown in Figure 6.22. The calculated values of diffusion coefficients are larger than those obtained in the dry exchange profiles which could be due to the residual hole conduction of the material in N_2 atmosphere. A small difference was observed between the activation energies obtained by different methods, 0.98(2) eV by EIS measurement and 1.08(8) by dry isotope diffusion profiling method, which confirmed that in N_2 the dominant charge carriers in the BNC20 sample are oxide-ions. Apart from that, it is interesting to note that the incorporation of water in the system reduced the oxygen diffusion coefficients according to the isotope exchange experiments in dry and wet conditions. That is to say, the enhancement in the electrical conductivities in wet atmospheres compared with those in dry atmospheres as observed in the previous EIS data was not due to the faster oxygen diffusion in the material. In fact, the oxygen diffusion was hindered under wet atmospheres. Therefore, the improved electrical conductivity in the BNC20 sample measured under wet conditions in EIS measurements must be due to an enhancement in the hole conduction or due to the protonic conductivities. The isotopic exchange experiments could be regarded as further evidence for the existence of protonic conduction in the acceptor-doped $BaNdInO_4$ materials under wet gaseous atmospheres. However, there is an non-negligible difference between the calculated *D* values and the ones obtained in the isotope exchange experiments, which could be attributed to many reasons. Firstly, as mentioned above, the attribution from electronic conduction in the BNC20 material under N_2 atmosphere can result in a higher D_{calc} values. Secondly, the specific correlation factor *f* for this unique crystal structure remains unknown. Last but not least, in the calculation of the *D* values, the charge carrier density was calculated by dividing the number of charge carriers in a unit cell (3.9) by the unit cell volume (438.21 Å^3). The exact number of charge carriers in a unit cell is difficult to define and the defect association may also play a role in determining the charge carrier density in the material.

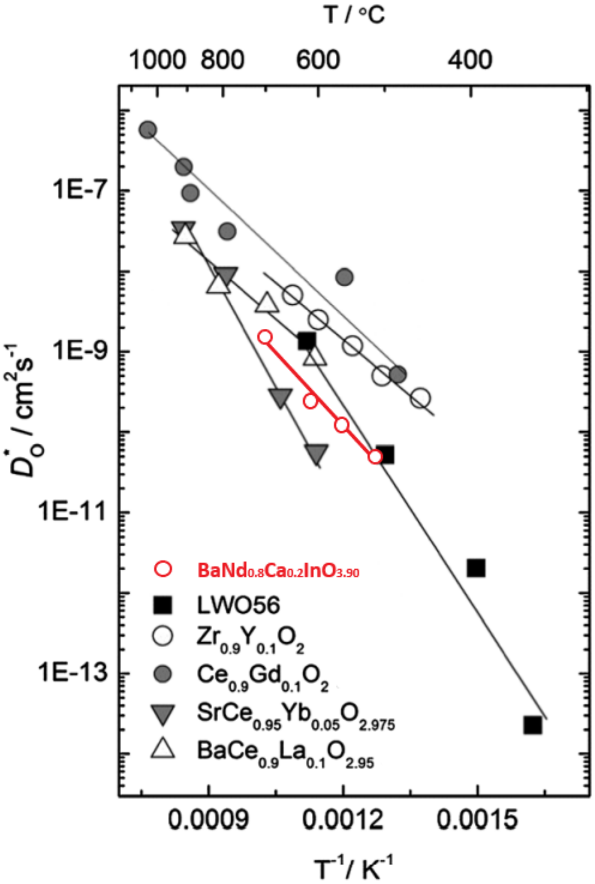

Figure 6.23 Temperature dependency of oxygen diffusion coefficient, *D*, for $BaNd_{0.8}Ca_{0.2}InO_{3.90}$ compared to state-of-the-art oxide-ion conductors. LWO56 represented the lanthanum tungstate with the general formula of $La_{27.15}W_{4.85}O_{55.275}$.(233) The diffusivity data of $Zr_{0.9}Y_{0.1}O_2$, $Ce_{0.9}Gd_{0.1}O_2$ and $SrCe_{0.95}Yb_{0.05}O_{2.975}$, $BaCe_{0.9}La_{0.1}O_{2.95}$ were included with permission from (234, 235). Reproduced with permission from (233).

Figure 6.23 illustrated the Arrhenius plot of oxygen diffusion coefficient for $BaNd_{0.8}Ca_{0.2}InO_{3.90}$ compared with those of the state-of-the-art oxide-ion conductors which were discussed in Chapter 1 and Chapter 2. As shown in the figure, the diffusivity of oxygen in the $BaNd_{0.8}Ca_{0.2}InO_{3.90}$ is about two orders of magnitude lower than that of CGO, and the activation energies for oxygen migration in these two materials are quite similar as the slopes of the Arrhenius plots are similar to each other. As a pure oxide-ion conductor, $BaNd_{0.8}Ca_{0.2}InO_{3.90}$ showed slightly lower oxygen diffusion coefficient than those state-of-art ionic conductors. However, as implied by previous characterizations, this layered perovskite material exhibits improved protonic conduction under wet atmospheres. In order to probe the protonic diffusivity, the deuterium D/H isotope exchange depth profiling were performed which will be discussed in the next section.

6.3 D/H isotope diffusion

The deuterium D/H isotope exchange depth profiling measurements were performed using the same set-up with the wet oxygen diffusion experiment, where the D_2O vapor was created using a D_2O water tank. Dense sectioned BNC20 samples were exchanged under D_2O+O_2 (150 Torr) at 500 and 550 ℃ for 2 hours. All the procedures for sample preparation and exchange experiments were similar to those of the wet oxygen diffusion experiments as described in the last section. However, to avoid the influence of water in the polishing process when preparing the line scan sample, the anhydrous ethanol based polishing medium (Struer®) was used in the polishing steps. In SIMS analysis, Cs^+ sputtering beam was used to extract the OD^- and D^- species. In the corresponding mass spectra of the two exchanged samples as shown in Figure 6.24, the mass 2.015 (D^-) peak and the mass 18.012 (OD^-) were well defined, the intensities of which are greater than the deuterium natural abundance. The corresponding OD^- maps were used for further analysis to obtain the diffusion kinetics for deuterium diffusion because the intensity of OD^- species detected were much higher than that of D^-. The resulting OH/OD depth profiles are illustrated as Figure 6.25 (a) & (b).

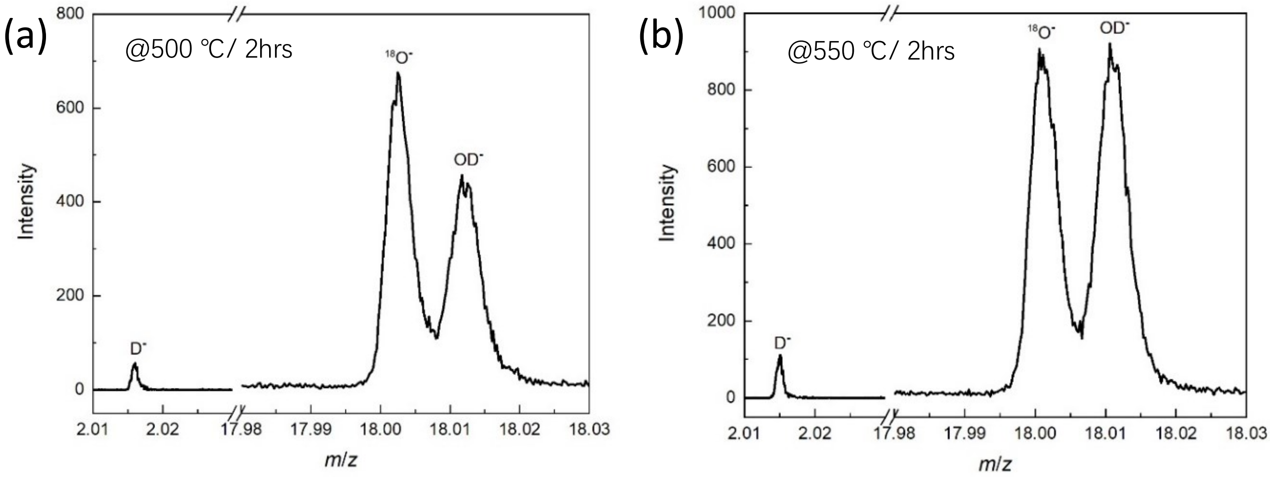

Figure 6.24 Mass spectra of the (a) 500 ℃ and (b) 550℃ D_2O exchanged sample by SIMS.

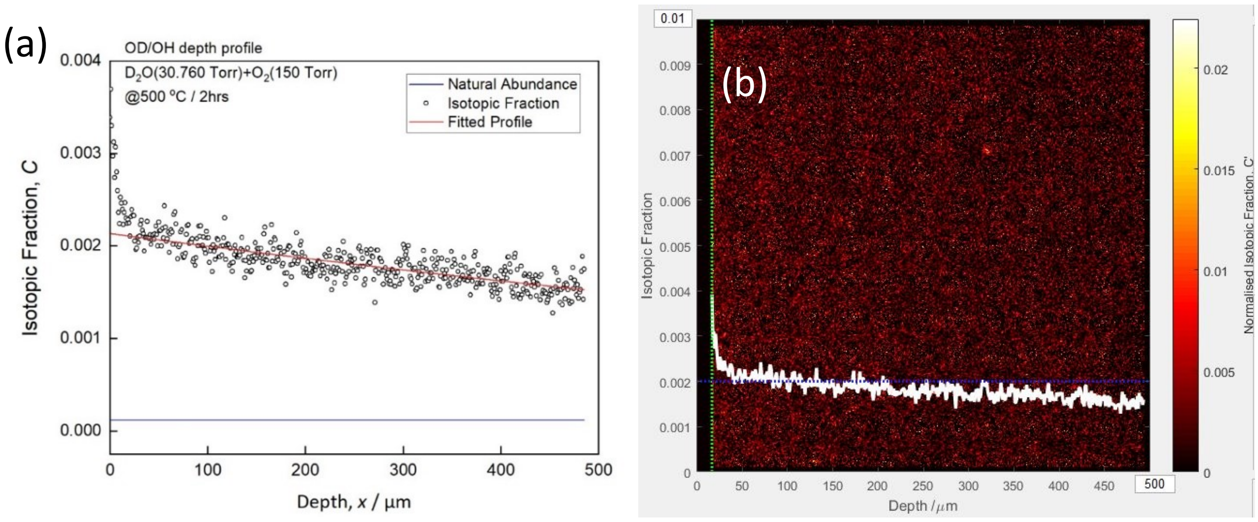

Figure 6.25 (a) OD/OH depth profile of BNC20 sample exchanged in D_2O(30.7 Torr)+O_2 (150 Torr) atmosphere at 500 ℃ for 2 hours, where the horizontal blue line represents the theoretical natural abundance of deuterium. (b) The OD map aligned by TraceX where the green dotted line represent the sample edge.

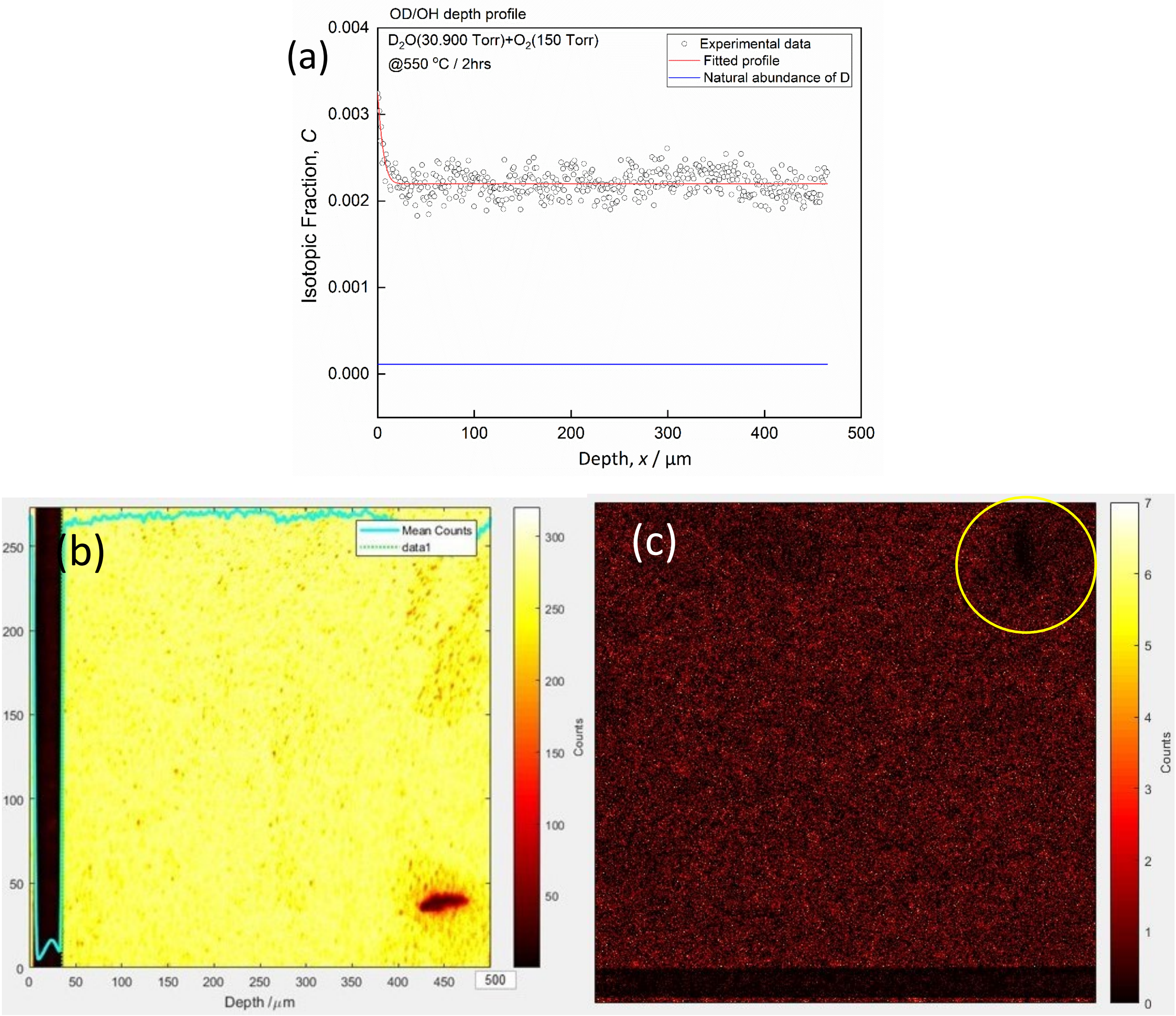

Figure 6.26 (a) OD/OH depth profile of BNC20 sample exchanged in D_2O(30.9 Torr)+O_2 (150 Torr) atmosphere at 550 ℃ for 2 hours, where the horizontal blue line represents the theoretical natural abundance of deuterium. (b) The total counts map of 550 D_2O exchanged sample measured under SIMS. (c) The OD map of 550 D_2O exchanged sample measured under SIMS, where the yellow circle labels the porosity area.

As shown in the obtained OD/OH depth profiles above (Figure 6.25(a) & Figure 6.26(a)), a severe data fluctuation could be noticed in both depth profiles, which is due to the relatively slow surface exchange process compared with the considerably fast diffusion in the bulk materials for deuterium ions. The extremely low surface isotopic fractions in the depth profiles also implied a small surface exchange coefficient of deuterium. The relatively slow surface exchange process between the D_2O molecules and the BNC20 sample surface observed in this measurement was in agreement with the previous EIS results and the symmetrical TGA/dc conductivity measurement results in Section 5.4. All these experimental results indicated that, compared with H_2O incorporation, D_2O incorporation happened on the BNC20 sample surface was a significantly slow process.

On the other hand, according to the obtained OD/OH depth profiles, a deuterium enriched region was confirmed at the sample surface with permeation depth of around 20-40 μm in both samples which seems like the beginning section of the depth profiles, followed by an extremely long diffusion 'tail' of over 500 μm. The end of the profile or the background was not recorded as the isotopic fraction values of the whole depth profiles were much higher than the natural abundance of deuterium, which was due to the surprisingly large diffusion coefficient of deuterium in the bulk material. According to the obtained depth profiles, the thickness of the samples used in the D_2O exchange experiments were not thick enough to meet the criterion of the semi-infinite boundary conditions for deuterium diffusion (the dimension of the sample thickness, $L < 4\sqrt{D_{\mathrm{deuterium}}t}$). Therefore, the Crank solution for simulation of the diffusion depth profile in a semi-infinite sample is no longer appropriate. However, based on the obtained mass spectra the incorporation of deuterium in the BNC20 sample was confirmed. Additionally, a fast deuterium diffusion in the bulk material with a relatively slow surface exchange process for D ions on the sample surface can be assumed according to the OD depth profiles. All these observations are consistent with the previous conductivity and TGA characterisation results on the BNC20 composition proving that the deuterium incorporation is a relatively slow process compared with the H_2O incorporation in the BNC20 sample, and the protonic defects are the dominant charge carriers in the BNC20 sample at around 500 ℃ in wet atmospheres.

However, to achieve valid diffusion kinetics of the deuterium diffusion in the BNC samples, the D_2O exchange experiments above need to be modified regarding the exchange time and temperatures. The permeation depths of the deuterium species into the sample needs to be tuned in the semi-infinite boundary condition range with regard to the sample thickness. The major problem though is the slow surface exchange process, which would lead to severe fluctuation in the depth profile data points. A possible solution to the slow deuterium surface exchange process on the sample surface is deposition of a thin activating layer, such as platinum, on one surface of the sample. But, by platinum deposition, the surface coefficients *k* would be no longer achievable.

6.4 Calcium exsolution and phase stability

Figure 6.27 shows the colour difference between the BNC20 samples exchanged in pure $H_2{}^{18}O$ at 500 ℃ for 2 hours (lighter colour, bottom) and in $H_2{}^{18}O+O_2$ at 600 ℃ for 1 hour (darker colour, top), which was noticed during the line scan sample preparation after the exchange annealing. These two samples were analysed using STEM-EDS characterisation after obtaining the depth profiles by SIMS measurements. A focused ion beam scanning electron microscope (FIB-SEM, Helios Nanolab 600, FEI) was used to prepare electron transmitting lamellae.

Figure 6.27 A photo of two exchanged sample stuck together fixed on the polishing block with wax during line scan sample preparation.

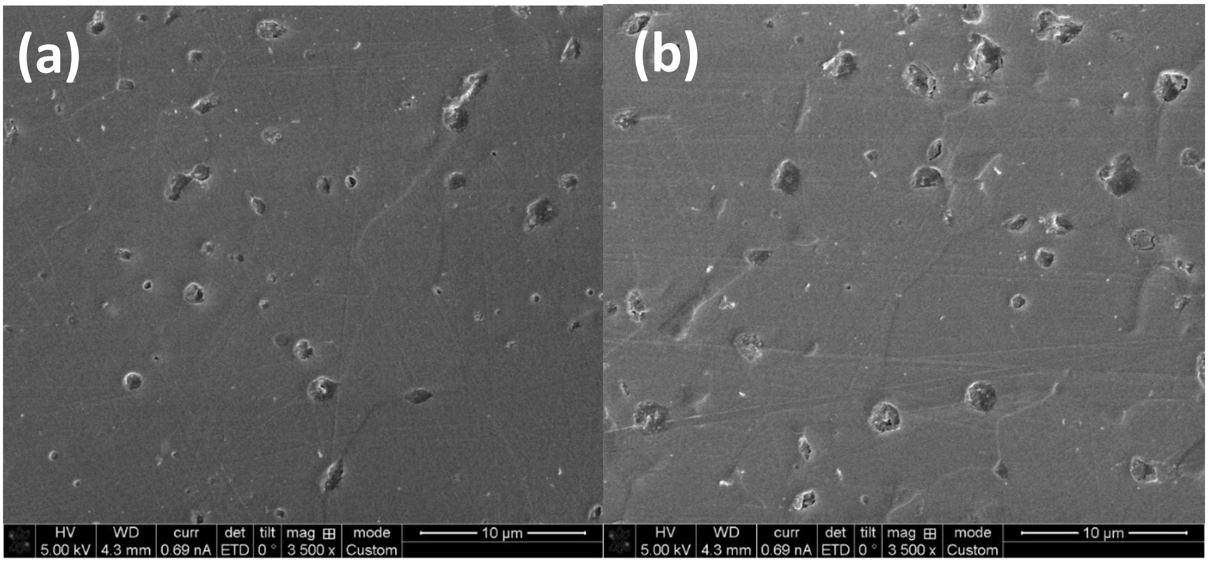

Figure 6.28 SEM images of (a) the $H_2{}^{18}O+O_2$ exchanged darker sample and (b) the pure $H_2{}^{18}O$ exchanged lighter sample under Helios FIB-SEM.

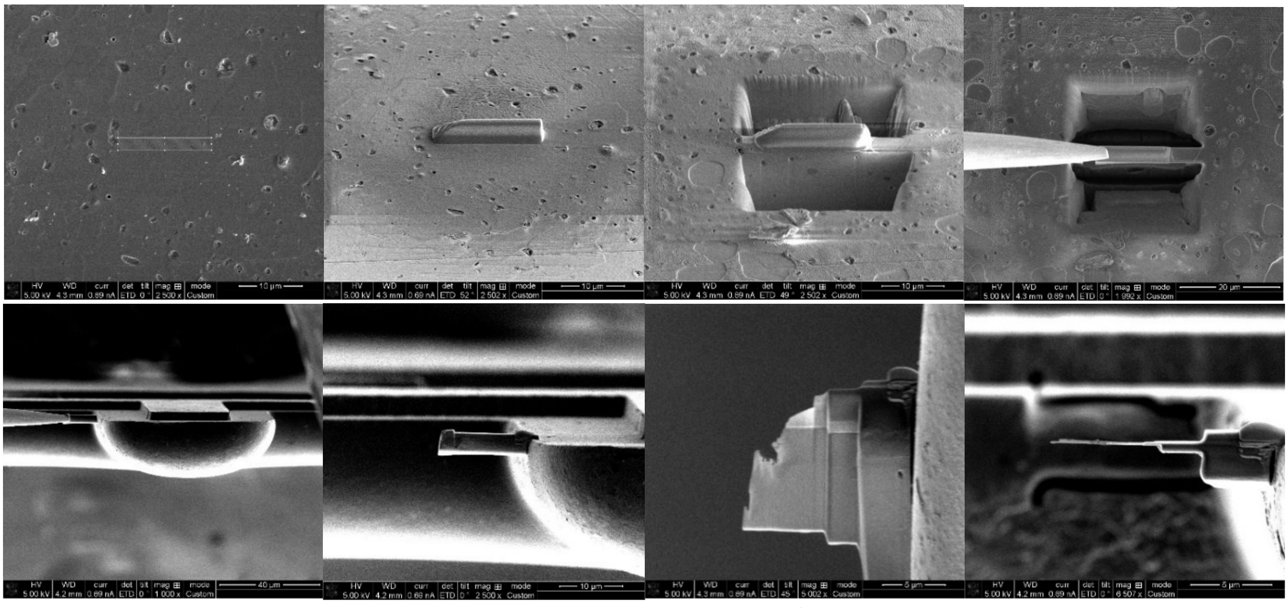

Figure 6.29 Preparation of the electron transparent lamellae from the $H_2{}^{18}O+O_2$ exchanged BNC20 sample with Ga^+ ion beam milling using Helios.

The STEM instrument used to analyse the exchanged samples was a high resolution TEM 2100F working at 200 keV equipped with an EDX detector (Inca X-act EDS) and an Aztec data analyzer to give the elemental information. The resulting elemental mapping and spectra for two samples are shown below.

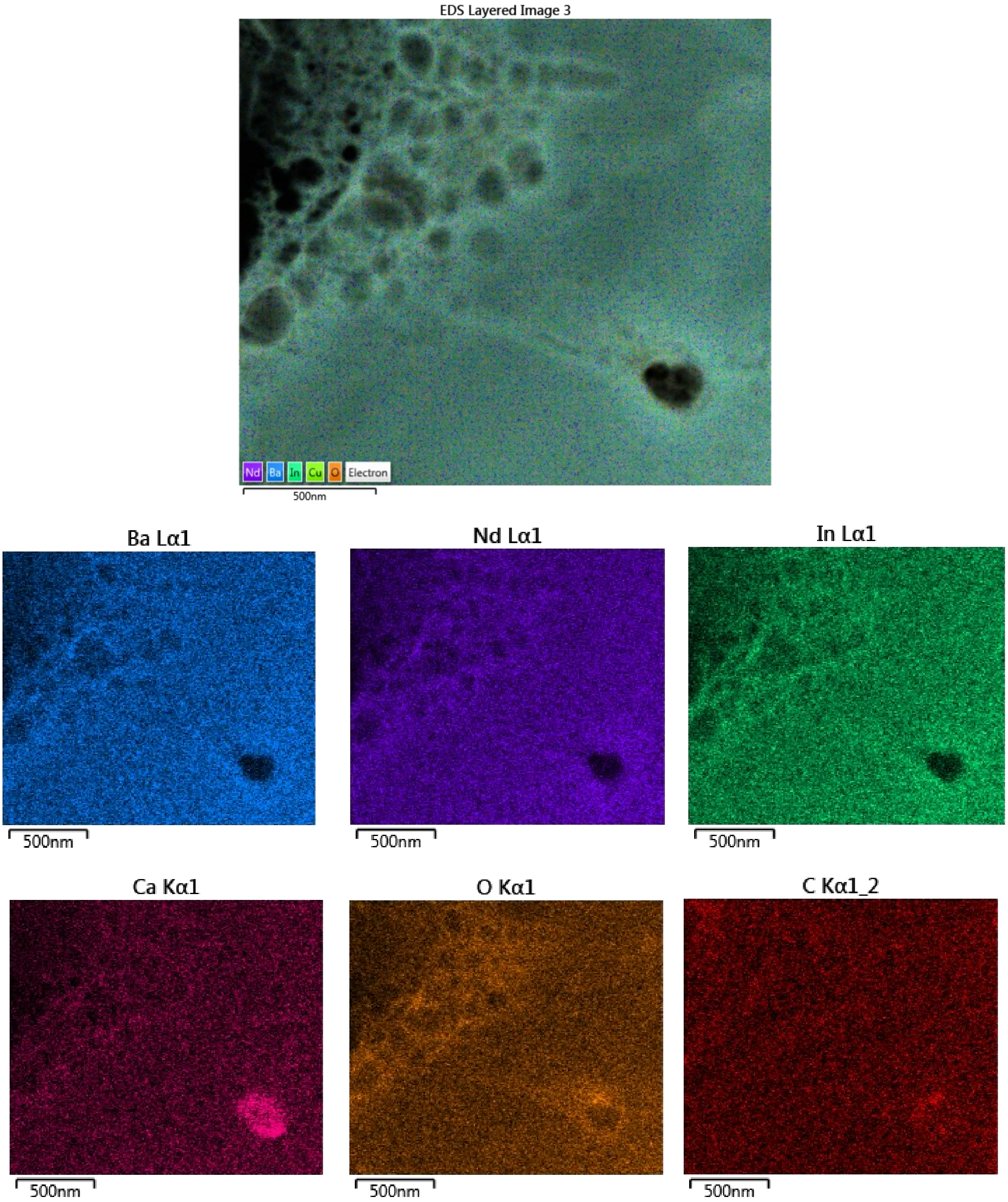

Figure 6.30 Elemental mappings of the selected area of the lighter sample (pure $H_2{}^{18}O$ exchanged at 500 ℃ for 2 hours) under STEM-EDS.

As shown in the elemental mappings, a clear calcium segregation in the porosity area within the selected region was observed, which lead to the formation of $CaCO_3$ secondary phases as the Ca, O and C counts were all higher near the porosity. In the selected area, the chemical composition on average was measured as

Ca:Nd:Ba:In =0.11:0.85:1:1.15 (atomic ratio, Ba was set as 1), where a loss in the atomic ratio of calcium and barium cations was observed compared with the original stoichiometry of BNC20. This result was in agreement with the *in-situ* XRD results after the long period of time wet annealing, showing that the BNC20 sample experienced calcium exsolution forming $CaCO_3$ on the sample surface during wet annealing processes. The full EDS elemental spectra were included in the Appendices as figure A.4 and A.5.

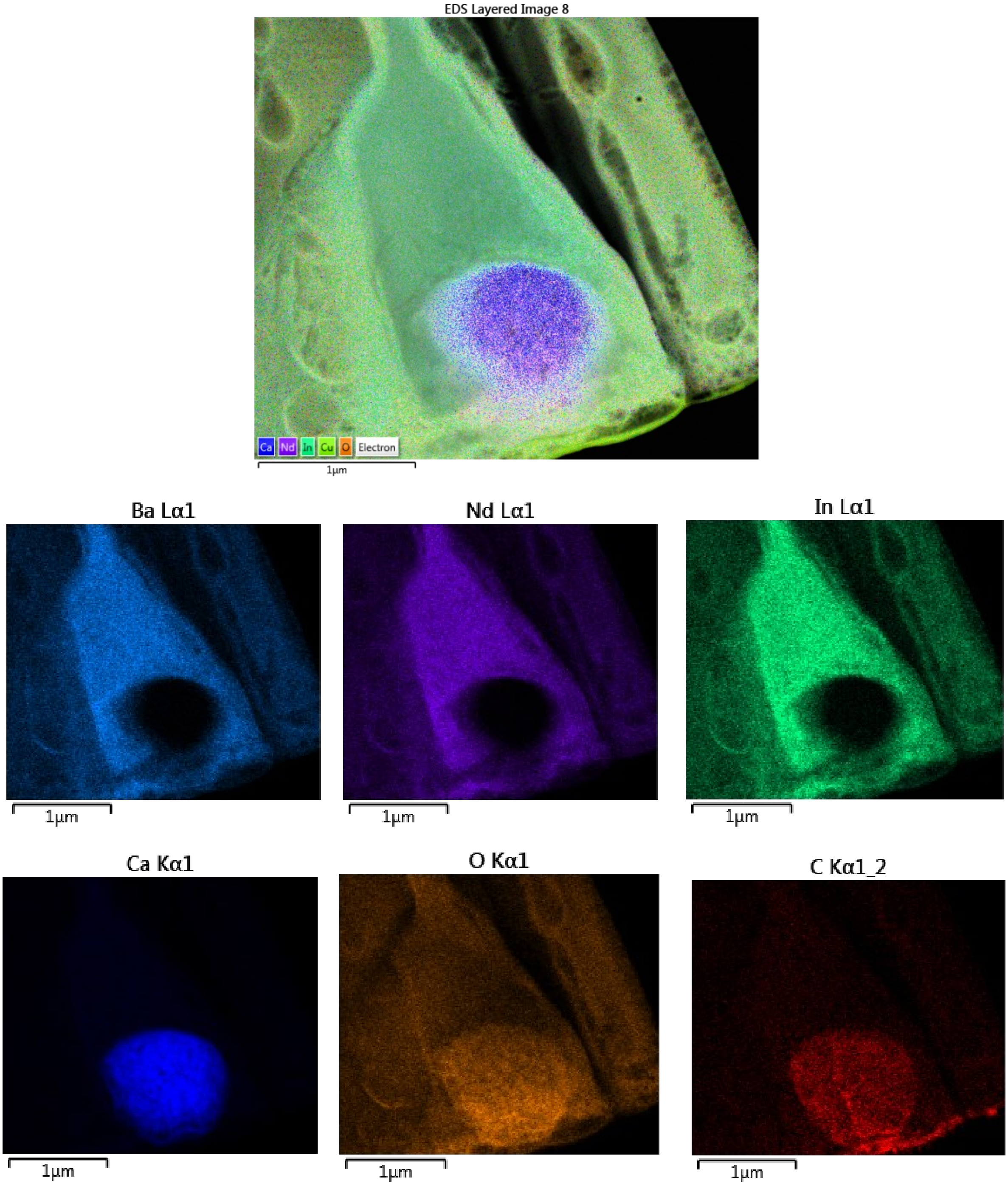

Figure 6.31 Elemental mappings of the selected area of the darker sample ($H_2{}^{18}O+O_2$ exchanged at 600 ℃ for 1 hour) under STEM-EDS.

The darker sample which has been exchanged in $H_2{}^{18}O+O_2$ at 600 ℃ for 1 hour, showed a more significant calcium exsolution in the defect region as shown in the elemental mappings under STEM-EDS. Besides, it is interesting to note that calcium signals were almost invisible in other area of the milled sample implying a non-calcium chemical composition in the rest of the area except for the defect area. The severe segregation of calcium forming $CaCO_3$ on the sample surface may explain the off-trend observation in the surface exchange coefficients(Figure 6.20(b)). The formation of $CaCO_3$ secondary phase during the wet annealing on the sample surface may hinder the ^{18}O surface exchange process resulting in a low surface exchange coefficient at 600 ℃. Therefore, further attention should be paid upon the choice of exchange temperature and exchange time for the wet isotope exchange experiment since the BNC20 solution is quite sensitive to humidity at high temperatures.

6.5 Summary

To conclude this chapter, the oxygen and deuterium diffusion mechanism in the BNC20 sample was analysed by the isotope exchange depth profiling (IEDP) method coupled with SIMS analysis. In the dry $^{18}O_2$ exchange experiments, sectioned BNC20 samples were exchanged in 150 Torr $^{18}O_2$ at different temperatures for appropriate exchange times to achieve $^{18}O/(^{16}O+^{18}O)$ depth profiles, which could then be analysed by TraceX solving Crank's solution to Fick's second law of diffusion for a semi-infinite medium. The wet oxygen diffusion experiments were performed using $H_2{}^{18}O$ labelled water to create a gaseous atmosphere of $H_2{}^{18}O$ (~ 30 torr)+O_2 (150 Torr) to achieve $^{18}O/(^{16}O+^{18}O)$ depth profiles. On the other hand, deuterium diffusion in the BNC20 sample was measured using D_2O to produce the depth profile of the tracer OD at 500 ℃ and 550 ℃ in particular. All the isotope exchange experiments were performed using the SIMS-linescan analysis mode, the data validity of which was confirmed with the normalised surface isotope fraction plotted as a function of the reduced variable *h'*.

The oxygen diffusion coefficients measured in the dry isotope exchange experiments at 500, 550, 600 and 700 ℃ were 4.78×10^{-11} , 1.24×10^{-10}, 2.27×10^{-10} and 1.40×10^{-9} cm^2/s respectively, which decreased with water incorporation as measured in the wet isotope exchange experiments (8.93×10^{-12} at 500 ℃, 5.74×10^{-11} at 550 ℃ and 2.14×10^{-10} at 600 ℃). The activation energy for oxygen diffusion increased from 1.08(8) eV to 1.86(11) eV after water incorporation, which implied a hindering effect of protonic defects on the oxygen diffusion process in the bulk material. As for the surface exchange process, a clear improvement can be seen in the surface exchange coefficients of the 500 and 550 ℃ wet exchange data, while at a higher temperature of 600 ℃ the surface exchange process seemed to be hindered, which could be ascribed to the dehydration of water at higher temperatures or because of the secondary phases of $CaCO_3$ that emerged on the sample surface that blocked the oxygen permeation. The exsolution of calcium and the formation of $CaCO_3$ secondary phase was confirmed in the following STEM-EDS measurements.

Besides, in the 500 ℃ and 550 ℃ ($H_2{}^{18}O+O_2$) wet exchange depth profiles, a clear unfitted tail was observed which implied a fast grain boundary diffusion mechanism. The grain boundary diffusion products, $D_{\mathrm{gb}} \cdot \delta$, were calculated through a modified expression of the Whipple's exact solution(232) with the Chung and Wuensch approximation(231) as 6.64×10^{-14} and 5.31×10^{-13} cm^3/s at 500 ℃ and 550 ℃ respectively, which were orders-of-magnitude higher than the corresponding bulk diffusion coefficients assuming the grain boundary dimension, δ, was around 2 ~ 8 nm(68). In particular, a BNC20 sample was exchanged in pure $H_2{}^{18}O$ environment at 500 ℃ for 2 hours, and a significant decrease in the surface exchange coefficient from 1.17×10^{-8} cm/s to 2.66×10^{-9} cm/s was obtained compared with the oxygen-enriched atmosphere wet exchange result. This observation provides a probe of the surface exchange mechanism that happened during the wet exchange experiments, showing that oxygen molecules are involved in the surface exchange process.

Based on the obtained mass spectra by SIMS of the D_2O exchanged samples, the incorporation of deuterium in the BNC20 sample was confirmed. A fast deuterium diffusion in the bulk material with a relatively slow surface exchange process for D ions on the sample surface can be assumed according to the OD depth profiles, where the OD isotope fraction values of the whole depth profile are much higher than the natural abundance value of deuterium. All these observations are consistent with the previous conductivity and TGA characterisation results of the BNC20 composition proving that the deuterium incorporation is a relatively slow process compared with the H_2O incorporation in the BNC20 sample, and the protonic defects are the dominant charge carriers with a much faster diffusion coefficient than oxide-ions in the BNC20 sample at around 500 ℃ in wet atmospheres.

6.6 Suggested future work

More dry and wet oxygen isotope diffusion experiments should be conducted on the BNC20 composition to obtain more reliable activation energy values for the oxygen diffusion in the bulk materials. Special cares should be taken on the determination of the exchange temperatures and exchange time for the wet isotope exchange measurements because BNC20 is quite sensitive to humidity. To avoid severe segregation and calcium exsolution on the sample surface, which may introduce extra errors in deciding the diffusion kinetics, a lower temperature with a short exchange time is recommended. And the pure $H_2{}^{18}O$ exchange experiment should be repeated at different temperatures, so that the oxygen surface exchange process that happened on the BNC sample surface could be explored in detailed. Long exchange time (4 hours or longer) for the IEDP measurements are suggested to obtain depth profiles with larger profile which can effectively mitigate the statistic errors caused by surface roughness or features of the sample. These empirical studies can also be coupled with computational simulation results for a more detailed surface exchange mechanism study on the BNC20 sample or the related solid solutions.

The oxygen isotope exchange depth profiling measurements on the strontium and barium substituted $BaNdInO_4$ solid solutions and the pristine $BaNdInO_4$ samples are worth performing as well, the values of which could be used to derive the corresponding activation energies for oxygen diffusion providing more information on the oxygen diffusion mechanism within the lattice. These experimental results could be compared with the oxide-ion conductivity data obtained in the previous research(121, 124) to give a more comprehensive understanding of the relationship between the acceptor-doping cations and the oxygen diffusion process in the materials. As a by-product, high quality data of the oxygen diffusion coefficients obtained from the oxygen isotope exchange measurements on the acceptor-doped $BaNdInO_4$-related solid solutions can be used to estimate the charge carrier density, n_O, in the bulk material during the calculation process using the Nernst-Einstein equation. The value of charge carrier density, n_O, can then be substituted to obtain the number of oxygen vacancies in a unit cell volume, which could be extremely useful to investigate the defect association in the structures. However, the validity of the D values from the isotope exchange measurements may not good enough for such analysis.

The fast grain boundary diffusion observed in the wet oxygen exchange data could be discussed in detailed by conducting more wet exchange experiments at around 500 ℃. The critical value of bulk diffusion around 10^{-12} cm^2/s for a visible fast grain boundary diffusion tail in the profiles should be paid more attention when deciding the experimental parameters. The grain boundary diffusion products could then be used to yield the activation energy for oxygen diffusion through grain boundaries, the discussion of which could be rather interesting.

Last but not least, the deuterium diffusion experiment should be redesigned based on the two D_2O exchanged experiments above. A lower exchange temperature with a short exchange time should be adapted to obtain valid deuterium diffusion kinetics, which could be useful in comparison with the wet EIS data in investigating the charge carrier distribution in the BNC20 composition under wet atmospheres.

Chapter 7

Conclusion and Future work

7.1 Conclusions

Consistent research interest in the development of high efficiency fuel cell devices based on solid ionic conducting electrolytes has led to various studies on finding novel crystal structure families of oxide-ion conductors for further developments with regard to lowering the operating temperatures of the existing high temperature solid oxide fuel cells and improving their performance. Among all the known oxide-ion conductors, fluorite-type and the perovskite-type structure families are the mostly investigated ceramics, the electrical performance and the oxygen transport mechanism of which have been widely explored both empirically by experiments and theoretically through simulations and computations in the previous literatures. However, further development and commercialization of SOFC devices based on electrolytes of these two crystal structures seemed to hit a plateau when extending their application into the intermediate temperature range due to the complicated fabrication process or the chemical stability problem of the corresponding materials. The discovery of a new structure family based on the $BaNdInO_4$ layered perovskite-related structure by Fujii *et al*.(115) proposed a new potential candidate for the further development in the choice of the electrolyte material in the application of SOFCs. However, the electrical conductivity of the pristine $BaNdInO_4$ solid solution needs to be improved to meet the requirements for fabrication of a thin film of the electrolyte material using in a SOFC device. On the other hand, though several acceptor-doping cations have been tried to improve the electrochemical performance of the pristine material, no approach has been taken on probing the possible proton conduction in these solid solutions and few empirical study has been performed investigating the oxygen transport in this unique structure. The development of this structure family was selected as the main topic of this research, with the aim of investigating the fundamentals of its properties through material characterization and improving the electrochemical performance of this material.

The synthesis and preliminary material characterization of the $BaNd_{1-x}Ca_xInO_{4-x/2}$ (x = 0, 0.05, 0.10, 0.15, 0.20, 0.25, 0.30) solid solution series was discussed in Chapter 4, where the modification of the traditional solid reaction solution to achieve dense pellet samples was explored in detail. The optimal synthesis process consists of two sintering process, each accompanied by a ball milling step to decrease the particle size before pressing, which resulted in single-phased dense pellet samples with relative densities around 98%. The crystal structure of the formed phase in the $BaNd_{1-x}Ca_xInO_{4-x/2}$ solid solutions was determined in static air by XRD, where a single phase of primitive monoclinic crystal structure with the $P2_1/c$ symmetry was confirmed in most of the samples except for the BNC30 sample. According to the refined lattice parameters obtained by Le Bail refinement of the XRD patterns, the substitution of calcium at the Nd sites in $BaNd_{1-x}Ca_xInO_{4-x/2}$ caused a contraction in the unit cell volume as the calcium content x increased from 0 to 0.2. This decrease in the lattice size can be ascribed to the small size mismatch of the calcium and neodymium cations. An additional peak corresponding to the emerged secondary phase of $Ba_2In_2O_5$ was identified in the XRD pattern of the BNC30 sample, which can be used in combination with the out-of-trend changes in the lattice parameters as the calcium content x exceeded 20% to estimate the solubility limit of calcium doping in the $BaNdInO_4$ system (~ 25%). On the other hand, the chemical compositions of the solid solutions were confirmed by EDS characterization method, where the atomic ratios of the heavy cations agreed considerably well with the designed stoichiometry and a lower atomic fraction of calcium and oxygen was observed due to the poor quantitative accuracy of the EDS technique in detecting light elements.

In Chapter 5, the electrical properties of the obtained dense pellet $BaNd_{1-x}Ca_xInO_{4-x/2}$ (x = 0, 0.10, 020) samples were investigated by electrochemical impedance spectroscopy (EIS) under various gaseous atmospheres, the results of which showed that calcium substitution at the Nd site can significantly increase the total conductivity of $BaNdInO_4$ pristine material by 1-2 orders of magnitude in dry air. Under dry atmosphere, the highest total conductivity of 2.6 x 10^{-3} Scm^{-1} was obtained in the BNC20 sample at 750 °C in air. The BNC20 sample exhibits p-type and oxide-ion mixed conduction under dry atmospheres within the O_2-N_2 $p(O_2)$ range as the total conductivity, σ_{Total} (Scm^{-1}), and the bulk conductivity, σ_{Bulk} (Scm^{-1}), of BNC20 were both lower in the N_2 atmosphere. Compared with the Sr and Ba substituted $BaNdInO_4$-based solid solutions in the previous literature, calcium substitution on the Nd site resulted in the highest oxide-ion conductivity (2.60 x 10^{-3} $S\cdot cm^{-1}$ in dry air at 750 ℃) and lowest activation energy (0.740(4) eV in N_2) for oxide-ion conduction, which could be ascribed to the defect associations happened in the system. Moreover, it is interesting to note that the total conductivity of the BNC10 and BNC20 samples were enhanced in wet atmospheres over a large temperature range (250 °C-750 °C) compared with those measured in dry atmospheres which implies that this material may exhibit triple (oxygen-ion, proton and hole) conduction under wet atmospheres.

To confirm the attribution of protonic conduction within the acceptor-doped $BaNdInO_4$ materials under wet atmosphere, the symmetrical TGA analysis coupled with the simultaneous DC conductivity measurement was performed in the lab of Centro Atomico Bariloche (CAB), the results of which showed a clear mass increase and resistance decrease of the BNC20 sample after introducing water vapor into the sealed system. The protonic defects concentration of the saturated BNC20 sample was 2.2 mol% according to the TGA measurement. The sample after wet annealing was taken out and measured under *in-situ* XRD in heating and then cooling cycles. An expansion in the lattice parameters of the BNC20 sample after hydration was observed according to the Le Bail refinements on the XRD patterns obtained in the heating cycle. These results can be referred to as further evidence showing that BNC20 oxides exhibits protonic conduction under wet atmospheres.

However, an A-cation exsolution process was observed in the BNC20 sample being annealed at 500 ℃ in humid atmosphere over a week as a large number of faceted grains of the $CaCO_3$ secondary phase was observed in the SEM image of the hydrated sample surface after long time annealing. In the *in-situ* XRD patterns, the change of an additional peak appeared at 38.2° from an amorphous shape into a sharp peak shape as the temperature increased confirmed that the correlated secondary phase of calcite crystalized in elevating temperatures on the sample surface(213). Apart from that, secondary phase of $BaCO_3$ was also detected in the hydrated BNC20 sample by XRD patterns, in which two additional peaks emerged at 800 ℃ at low angles (21.8° and 26.5°) and disappeared in the cooling cycle. These two extra peaks could be ascribed to the phase transition of $BaCO_3$ happened at 1073-1093 K from the orthorhombic $BaCO_3$ (α-$BaCO_3$) structure into the trigonal β phase (β-$BaCO_3$)(214).

The deuterium isotope effect on the electrical conductivity of BNC20 solid solution was investigated by EIS and symmetrical dc conductivity measurements. Both EIS and dc conductivity measurement showed a decrease in the total conductivity of the BNC20 sample after D_2O incorporation, and the process of D_2O uptake was confirmed to be relatively slow than the H_2O uptake. The deuterium isotope effect on the total conductivity of the BNC20 sample measured by dc conductivity measurement was calculated to be 1.416(2), the value of which was close to 1.414 as usually quoted in the previous literatures(223). This isotope effect confirms the protonic nature of the measurements.

To probe the oxygen and proton diffusion mechanism in the BNC20 solid solution, the dense BNC20 samples was analyzed using the isotope exchange depth profiling (IEDP) method with the SIMS-linescan analysis mode. In the dry $^{18}O_2$ exchange experiments, sectioned BNC20 samples were exchanged in 150 Torr $^{18}O_2$ at different temperatures for appropriate exchanging times to achieve $^{18}O/O$ depth profiles, while the wet oxygen diffusion experiments were performed using $H_2{}^{18}O$ labelled water to create a gaseous atmosphere of $H_2{}^{18}O$ (~ 30 torr)+O_2 (150 Torr) for achieving $^{18}O/O$ depth profiles. The obtained depth profiles were analyzed using a Matlab app TraceX. On the other hand, deuterium diffusion in the BNC20 sample was measured using D_2O to produce the depth profile of the tracer OD at 500 ℃ and 550 ℃ in particular. The data validity of the IEDP data was confirmed with the normalised surface isotope fraction plotted as a function of the reduced variable *h*′, and the errors introduced in the mathematical calculation of deriving the diffusion kinetics during the data analysis was given by the standard deviation map.

The oxygen diffusion coefficients measured in the dry isotope exchange experiments at 500, 550, 600 and 700 ℃ are 4.78×10^{-11} , 1.24×10^{-10}, 2.27×10^{-10} and 1.40×10^{-9} cm^2/s respectively, which were decreased by water incorporation as measured in the wet isotope exchange experiments (8.93×10^{-12} at 500 ℃, 5.74×10^{-11} at 550 ℃ and 2.14×10^{-10} at 600 ℃). The activation energy for oxygen diffusion was increased from 1.08(8) eV to 1.86(11) eV after water incorporation, which implied a hindering effect of protonic defects on the oxygen diffusion process in the bulk material. As for the surface exchange process, a clear improvement can be seen in the surface exchange coefficients of the 500 and 550 ℃ wet exchange data, while at a higher temperature of 600 ℃ the surface exchange process seemed to be hindered, which could be ascribed to the dehydration of water at higher temperatures or because of the secondary phases of $CaCO_3$ emerged on the sample surface that blocked the oxygen permeation. The exsolution of calcium and the formation of $CaCO_3$ secondary phase was confirmed in the elemental maps measured by STEM-EDS, which was consistent with the previous in-situ XRD results from Chapter 5.

Fast grain boundary diffusion mechanism for oxygen diffusion in the BNC20 solid solution was confirmed as a clear unfitted ‘shoulder’ in the 500 ℃ and 550 ℃ ($H_2{}^{18}O$+O_2) wet exchange depth profiles was observed. The grain boundary diffusion products, $D_{\mathrm{gb}} \cdot \delta$, were calculated through a modified expression of the Whipple’s exact solution(230) with the Chung and Wuensch approximation(231) as 6.64×10^{-14} and 5.31×10^{-13} cm^3/s at 500 ℃ and 550 ℃ respectively, which were 2-3 orders of magnitude higher than the corresponding bulk diffusion coefficients assuming the grain boundary dimension, δ, was around 1 µm. In particular, a BNC20 sample was exchanged in pure $H_2{}^{18}O$ water vaper at 500 ℃ for 2 hours, the achieved depth profile of which exhibited a significantly decreased surface exchange coefficient compared with that obtained in the oxygen-enriched atmosphere wet exchange experiment. This observation provides a probe on the surface exchange mechanism that happens during the wet exchange experiments that the involvement of oxygen molecules could promote the surface exchange process.

The proton diffusion in the BNC20 sample was investigated by deuterium isotope exchange measurement using D_2O to produce the depth profile of tracer OD at 500 ℃ and 550 ℃ in particular. The incorporation of deuterium water vapor was confirmed by the obtained mass spectra by SIMS showing much higher intensities of D^- and OD^- than the natural abundance of D isotope. A fast deuterium diffusion in the bulk material with a relatively slow surface exchange process for D ions on the sample surface can be assumed according to the OD depth profiles, where the OD isotope fraction values of the whole depth profile are much higher than the natural abundance value of deuterium. These results are consistent with the previous conductivity and symmetrical TGA results of the BNC20 sample that the deuterium incorporation is a relatively slow process compared with the absorption of H_2O, and protonic defects are the dominant charge carriers in the BNC20 sample having a much faster diffusion coefficient than oxide-ions in wet atmospheres.

Overall, high density calcium substituted $BaNdInO_4$ samples were successfully synthesized through a two-sintering-step solid reaction method, which showing improving electrical properties than the pristine material and other acceptor-doped $BaNdInO_4$-related solid solutions. Various material characterization methods were performed on the synthesized BNC20 pellet samples indicating that this material exhibits triple (oxygen-ions, protons and holes) conduction under wet atmospheres.

7.2 Suggested further work

Based on the findings of the research, a lot of questions remained unknown which requires further material characterizations through other methods. For instance, the detailed crystal structure of the calcium substituted $BaNdInO_4$ could be examined by neutron powder diffraction or synchrotron beam. The utilization of these methods will provide more detailed information on the crystallography of the formed phases regarding the lattice parameters and atomic positions within the unit cell. By performing a more precise Rietveld refinement on the neutron or synchrotron diffraction data, the calcium substitution on the Nd sites in the lattice could be confirmed, and more information could be achieved with regard to the d-spacings between the ions in the lattice, which could be useful to probe the oxygen migration path in the lattice.

Although, a series of $BaNd_{1-x}Ca_xInO_{4-x/2}$ (x = 0, 0.05, 0.10, 0.15, 0.20, 0.25, 0.30) solid solution series were prepared through the two-sintering-steps approach, the chemical composition of the sintered sample needs to be confirmed more precisely through characterization methods other than the EDS. Inductively coupled plasma atomic emission spectroscopy (ICP-AES) might be an appropriate option, which uses the inductively coupled plasma to produce excited atoms and ions that emit electromagnetic radiation at wavelengths characteristic of a particular element. With regard to the probe resolution, STEM-EDS measurements could be a powerful method in probing the elemental distributions near different topographic features in the bulk material to explore whether there is any segregation or elemental deficiency in the sample.

Due to the pandemic situation, further analysis investigating the deuterium isotope effect on the electrical conductivity of the BNC20 sample under EIS measurements was suspended. The D_2O humidified atmosphere EIS measurements are worth repeating on the BNC20 sample, while special attentions should be paid on the sample preparation process before the impedance measurement. A long period of time (over 24 hours is suggested) wet annealing should be performed to let the D_2O uptake complete, because several experimental results have shown that the incorporation of D_2O into the BNC20 sample is a relatively slow process. In this research, various atmospheres regarding the oxygen partial pressure have been tried when conducting impedance measurements on BNC20 sample, however, the $P(O_2)$ dependence of the conductivity and the Brouwer diagram of the BNC20 solid solution have not been obtained. Based on the experience obtained in the two previous failed experiments, a bar-shaped sample instead of a pellet sample should be used in the 4-probe dc conductivity measurements under different atmospheres with regard to various oxygen partial pressures. The $P(O_2)$ dependence of conductivity under wet atmospheres would also be of great interest, the results of which could be used to analyse the charge carrier distributions in the BNC20 material. The obtained oxide-ion conductivities within the pure oxide-ion conduction region under extremely low oxygen partial pressures could be used to compare with the oxygen diffusion coefficients achieved in the IEDP measurements.

A more profound chemical stability study on the $BaNd_{1-x}Ca_xInO_{4-x/2}$ solid solutions is suggested, especially in humid atmospheres. According to the SEM image and the STEM-EDS maps on the BNC20 sample after being annealed in humidity for a long time, severe segregation regarding the exsolution of calcium and barium from the bulk forming corresponding carbonates on the surface was confirmed. The poor chemical stability of the solid solutions under wet atmosphere may significantly influence its further development and applications. A material recovery test is worth conducting on the wet annealed samples through the crushing/ball-milling/calcination/pressing/sintering process since the secondary phased detected so far were all precursors used in the synthesis process. One the other hand, co-doping of calcium cations with other impurities in the $BaNdInO_4$ system might be a solution to tackle the problem of poor chemical stability.

IEDP measurements coupled with SIMS analysis is a powerful technique on probing the oxygen diffusion kinetics in the BNC20 solid solutions. More dry and wet oxygen isotope exchange experiments should be performed on the dense BNC20 samples to ensure the data validity and obtained more accurate values for the activation energies for oxygen diffusion in the material. The fast grain boundary diffusion mechanism could be probed in detail through more depths profiles obtained under wet annealing. In order to obtain reliable grain boundary diffusion products through wet exchange measurements, exchange temperatures should not be higher than 550 ℃ as the correlated high bulk diffusion coefficient will exclude the fast grain boundary diffusion 'tails' in the depth profiles. In addition, a longer diffusion time is suggested to achieve more obvious fast grain boundary 'tails'.

It would be also interesting to obtain the oxygen diffusion kinetics of other chemical compositions with different acceptor dopants, i.e. Sr and Ba, which would be useful to discuss the oxygen diffusion mechanism in the lattice. The activation energies for the oxygen diffusion obtained in the IEDP measurements could be used to compare with those obtained in the conductivity measurements in the previous literatures(121, 124) giving a profound understanding on the effect of surrounding cations on the oxygen diffusion in the crystal structure.

Finally, to obtain reliable diffusion kinetics for deuterium in the BNC20 bulk material, the D_2O exchange experiments should be redesigned, where a lower exchange temperature with a short exchange time should be adapted to decrease the permeation depth of the tracer and obtain complete depth profiles. However, the significantly low surface exchange coefficient might still be a big problem which would cause severe fluctuation in the data points of the derived depth profiles. In order to avoid these errors caused by low surface exchange coefficients, a thin film of platinum can be deposited on one of the sample surfaces to function as an activation layer enhancing the surface exchange process. As a drawback of the platinum coating, information about the deuterium surface exchange coefficient will no longer available. More information could be given if one can combine the diffusion kinetics data obtained by IEDP method with corresponding simulation results by DFT methods, Molecular Dynamics etc.

Finding an appropriate electrolyte material for SOFC applications is critical for realisation of a brand new power generation system with high efficiency and zero emission. According to the previous studies(115, 116, 121, 122, 124) and this work, the $BaNdInO_4$ structure type oxide is one of the potential candidates for this application in SOFC devices but needs further optimization regarding the chemical stability and electrochemical properties. It is always worth trying to design and synthesize a new structure family for this specific application, for instance the newly discovered $Ba_7Nb_4MoO_{20}$-based hexagonal perovskite related oxides(225, 236). Only through continuous optimization and discussion on these 'new' structure families, the most appropriate material could be found for a particular application in the future.

References

1. Forschungszentrum J. Solid Oxide Fuel Cells (SOFCs) [Available from: https://www.fz-juelich.de/portal/EN/Research/EnergyEnvironment/Fuelcells/SOFC/_node.html.
2. Singhal SC. Advances in solid oxide fuel cell technology. Solid State Ionics. 2000;135:305-13.
3. Yamamoto O. Solid oxide fuel cells: fundamental aspects and prospects. Electrochimica Acta. 2000;45:2423-35.
4. Pachauri RK, Reisinger A. IPCC fifth assessment report. IPCC, Geneva. 2014;2014.
5. Agency USEP. Greenhouse Gas Emissions 2019 [Available from: https://www.epa.gov/ghgemissions/sources-greenhouse-gas-emissions.
6. Olivier JG, Schure K, Peters J. Trends in global CO2 and total greenhouse gas emissions. PBL Netherlands Environmental Assessment Agency. 2017;5.
7. Sharaf OZ, Orhan MF. An overview of fuel cell technology: Fundamentals and applications. Renew Sust Energ Rev. 2014;32:810-53.
8. Grove WR. On voltaic series and the combination of gases by platinum. The London, Edinburgh, and Dublin Philosophical Magazine and Journal of Science. 1839;14:127-30.
9. Grove WR. On a gaseous voltaic battery. The London, Edinburgh, and Dublin Philosophical Magazine and Journal of Science. 1842;21:417-20.
10. Rayleigh L. XX. On the equilibrium of liquid conducting masses charged with electricity. The London, Edinburgh, and Dublin Philosophical Magazine and Journal of Science. 1882;14:184-6.
11. Mond L, Langer C. V. A new form of gas battery. Proceedings of the Royal Society of London. 1890;46:296-304.
12. Srinivasan S, Ticianelli EA, Derouin CR, Redondo A. Advances in Solid Polymer Electrolyte Fuel-Cell Technology with Low Platinum Loading Electrodes. J Power Sources. 1988;22:359-75.
13. Tomantschger K, McClusky F, Oporto L, Reid A, Kordesch K. Development of low cost alkaline fuel cells. J Power Sources. 1986;18:317-35.
14. Warshay M, Prokopius PR. *The fuel cell in space: yesterday, today and tomorrow.* 1989.NAS 1.15:102366
15. de Bruijn F. The current status of fuel cell technology for mobile and stationary applications. Green Chemistry. 2005;7:132-50.
16. Wilberforce T, Alaswad A, Palumbo A, Dassisti M, Olabi A-G. Advances in stationary and portable fuel cell applications. Int J Hydrogen Energ. 2016;41:16509-22.
17. Hamelin J, Agbossou K, Laperriere A, Laurencelle F, Bose T. Dynamic behavior of a PEM fuel cell stack for stationary applications. Int J Hydrogen Energ. 2001;26:625-9.
18. Barbera O, Stassi A, Sebastian D, Bonde J, Giacoppo G, D'Urso C, et al. Simple and functional direct methanol fuel cell stack designs for application in portable and auxiliary power units. Int J Hydrogen Energ. 2016;41:12320-9.
19. Goor M, Menkin S, Peled E. High power direct methanol fuel cell for mobility and portable applications. Int J Hydrogen Energ. 2019;44:3138-43.
20. Sammes N, Bove R, Stahl K. Phosphoric acid fuel cells: Fundamentals and applications. Curr Opin Solid St M. 2004;8:372-8.
21. von Helmolt R, Eberle U. Fuel cell vehicles: Status 2007. J Power Sources. 2007;165:833-43.
22. Lee S, Mukerjee S, McBreen J, Rho Y, Kho Y, Lee T. Effects of Nafion impregnation on performances of PEMFC electrodes. Electrochim Acta. 1998;43:3693-701.
23. Mahato N, Banerjee A, Gupta A, Omar S, Balani K. Progress in material selection for solid oxide fuel cell technology: A review. Progress in Materials Science. 2015;72:141-337.
24. Livermore SJ, Cotton JW, Ormerod RM. Fuel reforming and electrical performance studies in intermediate temperature ceria–gadolinia-based SOFCs. J Power Sources. 2000;86:411-6.

25. Ni M, Leung MK, Leung DY. A modeling study on concentration overpotentials of a reversible solid oxide fuel cell. J Power Sources. 2006;163:460-6.

26. Singhal SC, Kendall K. *High-temperature solid oxide fuel cells: fundamentals, design and applications*: 1st edition. Elsevier; 2003.

27. Gür TM. Comprehensive review of methane conversion in solid oxide fuel cells: prospects for efficient electricity generation from natural gas. Progress in Energy and Combustion Science. 2016;54:1-64.

28. Buonomano A, Calise F, d'Accadia MD, Palombo A, Vicidomini M. Hybrid solid oxide fuel cells–gas turbine systems for combined heat and power: a review. Applied Energy. 2015;156:32-85.

29. Baur E, Preis H. Über Brennstoff‐Ketten mit Festleitern. Zeitschrift für Elektrochemie und angewandte physikalische Chemie. 1937;43:727-32.

30. Koide H, Someya Y, Yoshida T, Maruyama T. Properties of Ni/YSZ cermet as anode for SOFC. Solid State Ionics. 2000;132:253-60.

31. Prakash BS, Kumar SS, Aruna S. Properties and development of Ni/YSZ as an anode material in solid oxide fuel cell: a review. Renewable and Sustainable Energy Reviews. 2014;36:149-79.

32. Lee J-H, Moon H, Lee H-W, Kim J, Kim J-D, Yoon K-H. Quantitative analysis of microstructure and its related electrical property of SOFC anode, Ni–YSZ cermet. Solid State Ionics. 2002;148:15-26.

33. Simwonis D, Tietz F, Stöver D. Nickel coarsening in annealed Ni/8YSZ anode substrates for solid oxide fuel cells. Solid State Ionics. 2000;132:241-51.

34. Huang Y-H, Dass RI, Xing Z-L, Goodenough JB. Double perovskites as anode materials for solid-oxide fuel cells. Science. 2006;312:254-7.

35. Wang Z, Tian Y, Li Y. Direct CH4 fuel cell using Sr2FeMoO6 as an anode material. J Power Sources. 2011;196:6104-9.

36. Huang Y-H, Liang G, Croft M, Lehtimaki M, Karppinen M, Goodenough JB. Double-perovskite anode materials Sr2MMoO6 (M= Co, Ni) for solid oxide fuel cells. Chem Mater. 2009;21:2319-26.

37. Wei T, Ji Y, Meng X, Zhang Y. Sr2NiMoO6− δ as anode material for LaGaO3-based solid oxide fuel cell. Electrochemistry communications. 2008;10:1369-72.

38. Gödickemeier M, Sasaki K, Gauckler L, Riess I. Perovskite cathodes for solid oxide fuel cells based on ceria electrolytes. Solid State Ionics. 1996;86:691-701.

39. Tu H, Takeda Y, Imanishi N, Yamamoto O. Ln1− xSrxCoO3 (Ln= Sm, Dy) for the electrode of solid oxide fuel cells. ECS Proceedings Volumes. 1997;1997:394-403.

40. Kawada T, Masuda K, Suzuki J, Kaimai A, Kawamura K, Nigara Y, et al. Oxygen isotope exchange with a dense La0. 6Sr0. 4CoO3− δ electrode on a Ce0. 9Ca0. 1O1. 9 electrolyte. Solid State Ionics. 1999;121:271-9.

41. Aguadero A, Calle Cdl, Alonso J, Escudero M, Fernández-Díaz M, Daza L. Structural and electrical characterization of the novel SrCo0. 9Sb0. 1O3–δ perovskite: evaluation as a solid oxide fuel cell cathode material. Chem Mater. 2007;19:6437-44.

42. Aguadero A, Pérez-Coll D, De la Calle C, Alonso J, Escudero M, Daza L. SrCo1− xSbxO3− δ perovskite oxides as cathode materials in solid oxide fuel cells. J Power Sources. 2009;192:132-7.

43. Takeda Y, Sakaki Y, Ichikawa T, Imanishi N, Yamamoto O, Mori M, et al. Stability of La1− xAxMnO3− z (A= Ca, Sr) as cathode materials for solid oxide fuel cells. Solid State Ionics. 1994;72:257-64.

44. Mitterdorfer A, Gauckler L. La2Zr2O7 formation and oxygen reduction kinetics of the La0. 85Sr0. 15MnyO3, O2 (g)| YSZ system. Solid State Ionics. 1998;111:185-218.

45. Skinner SJ. Recent advances in Perovskite-type materials for solid oxide fuel cell cathodes. International Journal of Inorganic Materials. 2001;3:113-21.

46. De Souza RA, Islam MS, Ivers-Tiffée E. Formation and migration of cation defects in the perovskite oxide LaMnO 3. Journal of Materials Chemistry. 1999;9:1621-7.

47. Brugnoni C, Ducati U, Scagliotti M. SOFC cathode/electrolyte interface. Part I: Reactivity between La0. 85Sr0. 15MnO3 and ZrO2-Y2O3. Solid State Ionics. 1995;76:177-82.

48. Aruna S, Muthuraman M, Patil K. Studies on strontium substituted rare earth manganites. Solid State Ionics. 1999;120:275-80.

49. Zhou W, Shao Z, Ran R, Cai R. Novel SrSc0. 2Co0. 8O3− δ as a cathode material for low temperature solid-oxide fuel cell. Electrochemistry communications. 2008;10:1647-51.

50. Shaigan N, Qu W, Ivey DG, Chen W. A review of recent progress in coatings, surface modifications and alloy developments for solid oxide fuel cell ferritic stainless steel interconnects. J Power Sources. 2010;195:1529-42.

51. Badwal S, Deller R, Foger K, Ramprakash Y, Zhang J. Interaction between chromia forming alloy interconnects and air. Solid State Ionics. 1997;99:297-310.

52. Zhu WZ, Deevi S. Development of interconnect materials for solid oxide fuel cells. Materials Science and Engineering: A. 2003;348:227-43.

53. Zhu J, Zhang Y, Basu A, Lu Z, Paranthaman M, Lee D, et al. LaCrO3-based coatings on ferritic stainless steel for solid oxide fuel cell interconnect applications. Surface and Coatings Technology. 2004;177:65-72.

54. Shaigan N, Ivey DG, Chen W. Co/LaCrO3 composite coatings for AISI 430 stainless steel solid oxide fuel cell interconnects. J Power Sources. 2008;185:331-7.

55. Kilner JA, Burriel M. Materials for Intermediate-Temperature Solid-Oxide Fuel Cells. Annual Review of Materials Research, Vol 44. 2014;44:365-93.

56. Kilner JA, Burriel M. Materials for intermediate-temperature solid-oxide fuel cells. Annual Review of Materials Research. 2014;44:365-93.

57. Punn R, Feteira AM, Sinclair DC, Greaves C. Enhanced oxide ion conductivity in stabilized δ-Bi2O3. J Am Chem Soc. 2006;128:15386-7.

58. Inaba H, Tagawa H. Ceria-based solid electrolytes. Solid State Ionics. 1996;83:1-16.

59. Kilner JA. Fast oxygen transport in acceptor doped oxides. Solid State Ionics. 2000;129:13-23.

60. Kilner JA, Skinner SJ, Brongersma HH. The isotope exchange depth profiling (IEDP) technique using SIMS and LEIS. Journal of Solid State Electrochemistry. 2011;15:861-76.

61. Brouwer G. A general asymptotic solution of reaction equations common in solid-state chemistry. Philips Res Rep. 1954;9:366-76.

62. Kröger F, Vink H. Relations between the concentrations of imperfections in solids. J Phys Chem Solids. 1958;5:208-23.

63. Nowick A, Park D. Fluorite-type oxygen conductors.Superionic Conductors: Springer; 1976. p. 395-412.

64. Abraham M, Weeks R, Clark G, Finch C. Electron Spin Resonance of Rare-Earth Ions in Ce O 2: Yb 3+ and Er 3+. Physical Review. 1966;148:350.

65. Kilner JA, Drennan J, et al. A Study of Anion Transport in Bismuth Based Oxide Systems by Electrical-Conductivity and Secondary Ion Mass-Spectroscopy (Sims). Solid State Ionics. 1981;5(Oct):527-30.

66. Dufour L-C, Monty C. *Surfaces and interfaces of ceramic materials*, 1st edition. Springer Science & Business Media; 2012.

67. Maier J. Ionic conduction in space charge regions. Progress in solid state chemistry. 1995;23:171-263.

68. Mistler R, Coble R. Grain‐boundary diffusion and boundary widths in metals and ceramics. Journal of Applied Physics. 1974;45:1507-9.

69. Aoki M, Chiang YM, Kosacki I, Lee LJR, Tuller H, Liu Y. Solute segregation and grain‐boundary impedance in high‐purity stabilized zirconia. J Am Ceram Soc. 1996;79:1169-80.

70. Tuller HL. Ionic conduction in nanocrystalline materials. Solid State Ionics. 2000;131:143-57.

71. Guo X. Size dependent grain-boundary conductivity in doped zirconia. Computational Materials Science. 2001;20:168-76.

72. De Souza RA, Pietrowski MJ, Anselmi-Tamburini U, Kim S, Munir ZA, Martin M. Oxygen diffusion in nanocrystalline yttria-stabilized zirconia: the effect of grain boundaries. Phys Chem Chem Phys. 2008;10:2067-72.

73. Kosacki I, Rouleau CM, Becher PF, Bentley J, Lowndes DH. Nanoscale effects on the ionic conductivity in highly textured YSZ thin films. Solid State Ionics. 2005;176:1319-26.

74. Schichtel N, Korte C, Hesse D, Janek J. Elastic strain at interfaces and its influence on ionic conductivity in nanoscaled solid electrolyte thin films—theoretical considerations and experimental studies. Phys Chem Chem Phys. 2009;11:3043-8.

75. Korte C, Peters A, Janek J, Hesse D, Zakharov N. Ionic conductivity and activation energy for oxygen ion transport in superlattices—the semicoherent multilayer system YSZ (ZrO 2+ 9.5 mol% Y 2 O 3)/Y 2 O 3. Phys Chem Chem Phys. 2008;10:4623-35.

76. Peters A, Korte C, Hesse D, Zakharov N, Janek J. Ionic conductivity and activation energy for oxygen ion transport in superlattices—The multilayer system CSZ (ZrO2+ CaO)/Al2O3. Solid State Ionics. 2007;178:67-76.

77. Korte C, Schichtel N, Hesse D, Janek J. Influence of interface structure on mass transport in phase boundaries between different ionic materials. Monatshefte für Chemie-Chemical Monthly. 2009;140:1069-80.

78. Garcia-Barriocanal J, Rivera-Calzada A, Varela M, Sefrioui Z, Iborra E, Leon C, et al. Colossal ionic conductivity at interfaces of epitaxial ZrO2: Y2O3/SrTiO3 heterostructures. Science. 2008;321:676-80.

79. Guo X. Physical origin of the intrinsic grain-boundary resistivity of stabilized-zirconia: role of the space-charge layers. Solid State Ionics. 1995;81:235-42.

80. Goodenough JB. Oxide-ion conductors by design. Nature. 2000;404:821-3.

81. Faber J, Geoffroy C, Roux A, Sylvestre A, Abelard P. A systematic investigation of the dc electrical conductivity of rare-earth doped ceria. Applied Physics A. 1989;49:225-32.

82. Kilner J, Waters C. The effects of dopant cation-oxygen vacancy complexes on the anion transport properties of non-stoichiometric fluorite oxides. Solid State Ionics. 1982;6:253-9.

83. Kilner J, Steele B. Mass transport in anion-deficient fluorite oxides. Nonstoichiometric oxides. 1981;5:233-69.

84. Burbano M, Norberg ST, Hull S, Eriksson SG, Marrocchelli D, Madden PA, et al. Oxygen vacancy ordering and the conductivity maximum in Y2O3-doped CeO2. Chem Mater. 2012;24:222-9.

85. Minervini L, Zacate MO, Grimes RW. Defect cluster formation in M2O3-doped CeO2. Solid State Ionics. 1999;116:339-49.

86. Andersson DA, Simak SI, Skorodumova NV, Abrikosov IA, Johansson B. Optimization of ionic conductivity in doped ceria. Proceedings of the National Academy of Sciences. 2006;103:3518-21.

87. Navrotsky A, Simoncic P, Yokokawa H, Chen W, Lee T. Calorimetric measurements of energetics of defect interactions in fluorite oxides. Faraday discussions. 2007;134:171-80.

88. Yamazaki S, Matsui T, Ohashi T, Arita Y. Defect structures in doped CeO2 studied by using XAFS spectrometry. Solid State Ionics. 2000;136:913-20.

89. Deguchi H, Yoshida H, Inagaki T, Horiuchi M. EXAFS study of doped ceria using multiple data set fit. Solid State Ionics. 2005;176:1817-25.

90. Kosacki I, Gorman B, Anderson H, Ramanarayanan T, Worrell W, Tuller H, et al. *Ionic and Mixed Conductors*. Vol III (Eds: TA Ramanayanaran, WL Worrel, HL Tuller, AC Kandkar, M Mogensen, W Gopel), Electrochemical Society, Pennington. 1998:631.

91. Mondal P, Hahn H. Investigation of the complex conductivity of nanocrystalline Y2O3‐stabilized zirconia. Berichte der Bunsengesellschaft für physikalische Chemie. 1997;101:1765-8.

92. Jiang S, Schulze WA, Amarakoon VR, Stangle GC. Electrical properties of ultrafine-grained yttria-stabilized zirconia ceramics. J Mater Res. 1997;12:2374-80.

93. Wan J-H, Yan J-Q, Goodenough JB. LSGM-based solid oxide fuel cell with 1.4 W/cm2 power density and 30 day long-term stability. Journal of the Electrochemical Society. 2005;152:A1511.

94. Huang K, Wan J-H, Goodenough JB. Increasing power density of LSGM-based solid oxide fuel cells using new anode materials. Journal of the Electrochemical Society. 2001;148:A788.

95. Huang K, Tichy R, Goodenough JB, Milliken C. Superior Perovskite Oxide‐Ion Conductor; Strontium‐and Magnesium‐Doped LaGaO3: III, Performance Tests of Single Ceramic Fuel Cells. Journal of the American ceramic society. 1998;81:2581-5.

96. Huang K, Wan J, Goodenough JB. Oxide-ion conducting ceramics for solid oxide fuel cells. Journal of materials science. 2001;36:1093-8.

97. Teraoka Y, Zhang H, Okamoto K, Yamazoe N. Mixed ionic-electronic conductivity of La1− xSrxCo1− yFeyO3− δ perovskite-type oxides. Materials research bulletin. 1988;23:51-8.

98. Takahashi T. Solid-state ionics: protonic conduction in perovskite type oxide solid solutions. 1980.

99. Kreuer KD. Aspects of the formation and mobility of protonic charge carriers and the stability of perovskite-type oxides. Solid State Ionics. 1999;125:285-302.

100. Taniguchi N, Hatoh K, Niikura J, Gamo T, Iwahara H. Proton conductive properties of gadolinium-doped barium cerates at high temperatures. Solid State Ionics. 1992;53:998-1003.

101. Yajima T, Iwahara H, Uchida H. Protonic and oxide ionic conduction in BaCeO3-based ceramics—effect of partial substitution for Ba in BaCe0. 9O3− α with Ca. Solid State Ionics. 1991;47:117-24.

102. Bonanos N, Ellis B, Knight K, Mahmood M. Ionic conductivity of gadolinium-doped barium cerate perovskites. Solid State Ionics. 1989;35:179-88.

103. Iwahara H, Yajima T, Hibino T, Ushida H. Performance of Solid Oxide Fuel Cell Using Proton and Oxide Ion Mixed Conductors Based on BaCe1− x Sm x O 3− α. J Electrochem Soc. 1993;140:1687.

104. Bonanos N, Knight K, Ellis B. Perovskite solid electrolytes: structure, transport properties and fuel cell applications. Solid State Ionics. 1995;79:161-70.

105. Knight KS, Bonanos N. Space group and lattice constants for barium cerate and minor corrections to the crystal structures of BaCe0. 9Y0. 1O2. 95 and BaCe0. 9Gd0. 1O2. 95. Journal of Materials Chemistry. 1994;4:899-901.

106. Knight K. Structural phase transitions in BaCeO3. Solid State Ionics. 1994;74:109-17.

107. Knight K. Structural phase transitions, oxygen vacancy ordering and protonation in doped BaCeO3: results from time-of-flight neutron powder diffraction investigations. Solid State Ionics. 2001;145:275-94.

108. Knight K, Bonanos N. A high-resolution neutron powder diffraction study of neodymium doping in barium cerate. Solid State Ionics. 1995;77:189-94.

109. Bonanos N, Knight KS, Ellis B. Perovskite Solid Electrolytes - Structure, Transport-Properties and Fuel-Cell Applications. Solid State Ionics. 1995;79:161-70.

110. Goutenoire F, Isnard O, Retoux R, Lacorre P. Crystal structure of La2Mo2O9, a new fast oxide− ion conductor. Chemistry of materials. 2000;12:2575-80.

111. Goodenough J, Ruiz-Diaz J, Zhen Y. Oxide-ion conduction in Ba2In2O5 and Ba3In2MO8 (M= Ce, Hf, or Zr). Solid State Ionics. 1990;44:21-31.

112. Kramer S, Tuller H. A novel titanate-based oxygen ion conductor: Gd2Ti2O7. Solid State Ionics. 1995;82:15-23.

113. Porat O, Heremans C, Tuller H. Stability and mixed ionic electronic conduction in Gd2 (Ti1− xMox) 2O7 under anodic conditions. Solid State Ionics. 1997;94:75-83.

114. Zhang G, Smyth D. Protonic conduction in Ba2In2O5. Solid State Ionics. 1995;82:153-60.

115. Fujii K, Esaki Y, Omoto K, Yashima M, Hoshikawa A, Ishigaki T, et al. New perovskite-related structure family of oxide-ion conducting materials NdBaInO4. Chemistry of Materials. 2014;26:2488-91.

116. Fujii K, Yashima M. Discovery and development of BaNdInO4—A brief review—. Journal of the Ceramic Society of Japan. 2018;126:852-9.

117. Ruddlesden S, Popper P. New compounds of the K2NiF4 type. Acta Crystallographica. 1957;10:538-9.

118. Ruddlesden S, Popper P. The compound Sr3Ti2O7 and its structure. Acta Crystallographica. 1958;11:54-5.

119. Dion M, Ganne M, Tournoux M. Nouvelles familles de phases MIMII2Nb3O10 a feuillets "perovskites". Materials Research Bulletin. 1981;16:1429-35.

120. Aurivillius B. Mixed Bismuth Oxides with Layer Lattices I. The Structure Type of CaNb_2Bi_2O_9. Arkiv kemi. 1949;1:463-80.

121. Fujii K, Shiraiwa M, Esaki Y, Yashima M, Kim SJ, Lee S. Improved oxide-ion conductivity of NdBaInO 4 by Sr doping. Journal of Materials Chemistry A. 2015;3:11985-90.

122. Yang X, Liu S, Lu F, Xu J, Kuang X. Acceptor doping and oxygen vacancy migration in layered perovskite NdBaInO4-based mixed conductors. The Journal of Physical Chemistry C. 2016;120:6416-26.

123. Ishihara T, Yan Y, Sakai T, Ida S. Oxide ion conductivity in doped NdBaInO4. Solid State Ionics. 2016;288:262-5.

124. Shiraiwa M, Fujii K, Esaki Y, Kim SJ, Lee S, Yashima M. Crystal structure and oxide-ion conductivity of Ba1+ xNd1− xInO4− x/2. Journal of The Electrochemical Society. 2017;164:F1392.

125. Adams S. Modelling ion conduction pathways by bond valence pseudopotential maps. Solid State Ionics. 2000;136:1351-61.

126. Sale M, Avdeev M. 3DBVSMAPPER: a program for automatically generating bond-valence sum landscapes. Journal of Applied Crystallography. 2012;45:1054-6.

127. Todorov IT, Smith W, Trachenko K, Dove MT. DL_POLY_3: new dimensions in molecular dynamics simulations via massive parallelism. Journal of Materials Chemistry. 2006;16:1911-8.

128. Lee D, Lee HN. Controlling oxygen mobility in Ruddlesden–Popper oxides. Materials. 2017;10:368.

129. Xu S, Jacobs R, Morgan D. Factors Controlling Oxygen Interstitial Diffusion in the Ruddlesden–Popper Oxide La2–x Sr x NiO4+ δ. Chemistry of Materials. 2018;30:7166-77.

130. Liu J, Nowick A. The incorporation and migration of protons in Nd-doped BaCeO3. Solid State Ionics. 1992;50:131-8.

131. Slade RC, Singh N. Generation of charge carriers and an H/D isotope effect in proton-conducting doped barium cerate ceramics. Journal of Materials Chemistry. 1991;1:441-5.

132. Nowick A, Du Y. High-temperature protonic conductors with perovskite-related structures. Solid State Ionics. 1995;77:137-46.

133. Kreuer K. Aspects of the formation and mobility of protonic charge carriers and the stability of perovskite-type oxides. Solid State Ionics. 1999;125:285-302.

134. Münch W, Kreuer K, Adams S, Seifert G, Maier J. The relation between crystal structure and the formation and mobility of protonic charge carriers in perovskite-type oxides: A case study of Y-doped BaCeO3 and SrCeO3. Phase Transitions. 1999;68:567-86.

135. Irvine J, West A, Amano E, Huanosta A, Valenzuela R. Characterisation of magnetic materials by impedance spectroscopy. Solid State Ionics. 1990;40:220-3.

136. Kreuer KD, Adams S, Munch W, Fuchs A, Klock U, Maier J. Proton conducting alkaline earth zirconates and titanates for high drain electrochemical applications. Solid State Ionics. 2001;145:295-306.

137. Kreuer KD. Proton-conducting oxides. Annu Rev Mater Res. 2003;33:333-59.

138. Norby T, Larring Y. Concentration and transport of protons in oxides. Current Opinion in Solid State and Materials Science. 1997;2:593-9.

139. Bohn HG, Schober T. Electrical conductivity of the high‐temperature proton conductor BaZr0. 9Y0. 1O2. 95. J Am Ceram Soc. 2000;83:768-72.

140. Ricote S, Bonanos N, Caboche G. Water vapour solubility and conductivity study of the proton conductor BaCe (0.9− x) ZrxY0. 1O (3− δ). Solid State Ionics. 2009;180:990-7.

141. Oishi M, Akoshima S, Yashiro K, Sato K, Mizusaki J, Kawada T. Defect structure analysis of B-site doped perovskite-type proton conducting oxide BaCeO3: Part 2: The electrical conductivity and diffusion coefficient of BaCe0. 9Y0. 1O3− δ. Solid State Ionics. 2008;179:2240-7.

142. Pionke M, Mono T, Schweika W, Springer T, Schober H. Investigation of the hydrogen mobility in a mixed perovskite: Ba [Ca (1+ x)/3Nb (2− x)/3] O3− x/2 by quasielastic neutron scattering. Solid State Ionics. 1997;97:497-504.

143. Matzke T, Stimming U, Karmonik C, Soetratmo M, Hempelmann R, Güthoff F. Quasielastic thermal neutron scattering experiment on the proton conductor SrCe0. 95Yb0. 05H0. 02O2. 985. Solid State Ionics. 1996;86:621-8.

144. Münch W, Seifert G, Kreuer K, Maier J. A quantum molecular dynamics study of the cubic phase of BaTiO3 and BaZrO3. Solid State Ionics. 1997;97:39-44.

145. Münch W, Seifert G, Kreuer K, Maier J. A quantum molecular dynamics study of proton conduction phenomena in BaCeO3. Solid State Ionics. 1996;86:647-52.

146. Kreuer K. On the development of proton conducting materials for technological applications. Solid state ionics. 1997;97:1-15.

147. Kreuer K. On the complexity of proton conduction phenomena. Solid state ionics. 2000;136:149-60.

148. Münch W, Kreuer K-D, Seifert G, Maier J. Proton diffusion in perovskites: comparison between BaCeO3, BaZrO3, SrTiO3, and CaTiO3 using quantum molecular dynamics. Solid State Ionics. 2000;136:183-9.

149. Kreuer K, Münch W, Traub U, Maier J. On proton transport in perovskite‐type oxides and plastic hydroxides. Berichte der Bunsengesellschaft für physikalische Chemie. 1998;102:552-9.

150. Kreuer K-D, Münch W, Fuchs A, Klock U, Maier J. Proton conducting alkaline earth zirconates and titanates for high drain electrochemical applications. Solid State Ionics. 2001;145:295-306.

151. Kreuer K, Münch W, Ise M, He T, Fuchs A. Defect interactions in proton conducting perovskite-type oxides. Berichte der Bunsen-Gesellschaft. 1997;101:1344-50.

152. Nowick AS, Du Y, Liang K. Some factors that determine proton conductivity in nonstoichiometric complex perovskites. Solid State Ionics. 1999;125:303-11.
153. Kreuer K, Dippel T, Baikov YM, Maier J. Water solubility, proton and oxygen diffusion in acceptor doped BaCeO3: A single crystal analysis. Solid State Ionics. 1996;86:613-20.
154. Scholten M, Schoonman J, Van Miltenburg J, Oonk H. Synthesis of strontium and barium cerate and their reaction with carbon dioxide. Solid State Ionics. 1993;61:83-91.
155. Barin I. Thermochemical data of pure substances. VCH. 1989.
156. Kreuer K, Schönherr E, Maier J. Proton and oxygen diffusion in BaCeO3 based compounds: A combined thermal gravimetric analysis and conductivity study. Solid State Ionics. 1994;70:278-84.
157. Szot K, Pawelczyk M, Herion J, Freiburg C, Albers J, Waser R, et al. Nature of the surface layer in ABO 3-type perovskites at elevated temperatures. Applied Physics A. 1996;62:335-43.
158. Iwahara H. Oxide-ionic and protonic conductors based on perovskite-type oxides and their possible applications. Solid State Ionics. 1992;52:99-104.
159. Norby T. Solid-state protonic conductors: principles, properties, progress and prospects. Solid State Ionics. 1999;125:1-11.
160. NETZSCH. [Available from: https://www.netzsch-thermal-analysis.com/en/products-solutions/dilatometer/?tx_solr%5Bfilter%5D=&tx_solr%5Bpage%5D=2.
161. Weast RC. *Handbook of Chemistry and Physics.* 53rd Edition. 1972-1973. F4 p.
162. Rodríguez-Carvajal J. Recent advances in magnetic structure determination by neutron powder diffraction. Physica B: Condensed Matter. 1993;192:55-69.
163. Bragg WL. The diffraction of short electromagnetic waves by a crystal. 1929.
164. Skinner SJ. MSE302 course slides: X-ray Diffraction.
165. Anton Parr Corporation Website [Available from: https://wiki.anton-paar.com/en/x-ray-diffraction-xrd/#temperature-validation.
166. Rodríguez-Carvajal J. FullProf. CEA/Saclay, France. 2001.
167. Rayleigh L. Investigations in optics, with special reference to the spectroscope. The London, Edinburgh, and Dublin Philosophical Magazine and Journal of Science. 1879;8:261-74.
168. Group S. SEM EDX [Available from: https://www.surfgroup.be/semedx.
169. McNaught AD, Wilkinson A. Compendium of chemical terminology: Blackwell Science Oxford; 1997.
170. Transmission electron microscopy [Available from: https://en.wikipedia.org/wiki/Transmission_electron_microscopy.
171. Goodhew PJ, Humphreys J. *Electron microscopy and analysis*, 1st Edition. CRC Press; 2000.
172. De Graef M. *Introduction to conventional transmission electron microscopy,* 1st Edition. Cambridge university press; 2003.
173. Li J, Malis T, Dionne S. Recent advances in FIB–TEM specimen preparation techniques. Materials characterization. 2006;57:64-70.
174. Moram S. Transmission electron microscopy [Master of Science Course Slide of MSE302].
175. Orazem ME, Tribollet B. Electrochemical impedance spectroscopy. New Jersey. 2008:383-9.
176. Brug G, van den Eeden AL, Sluyters-Rehbach M, Sluyters JH. The analysis of electrode impedances complicated by the presence of a constant phase element. Journal of electroanalytical chemistry and interfacial electrochemistry. 1984;176:275-95.
177. Rammelt U, Reinhard G. On the applicability of a constant phase element (CPE) to the estimation of roughness of solid metal electrodes. Electrochimica Acta. 1990;35:1045-9.
178. Hsu C, Mansfeld F. Concerning the conversion of the constant phase element parameter Y 0 into a capacitance. Corrosion. 2001;57:747.
179. Irvine JT, Sinclair DC, West AR. Electroceramics: characterization by impedance spectroscopy. Advanced materials. 1990;2:132-8.
180. Johnson D. ZView: a software program for IES analysis, version 2.8. Scribner Associates, Inc, Southern Pines, NC. 2002.
181. Tsai C-Y. Phase evolution and reactivity of $Pr_2NiO_{4+}d$ and $Ce_{0.9}Gd_{0.1}O_{2-d}$ solid oxide cell electrodes: Imperial College London; 2020.

182. Caneiro A, Bavdaz P, Fouletier J, Abriata J. Adaptation of an electrochemical system for measurement and regulation of oxygen partial pressure to a symmetrical thermogravimetric analysis system developed using a Cahn 1000 electrobalance. Review of Scientific Instruments. 1982;53:1072-5.

183. Shen Z, Kilner JA, Skinner SJ. Electrical conductivity and oxygen diffusion behaviour of the (La 0.8 Sr 0.2) 0.95 Cr x Fe 1− x O 3− δ (x= 0.3, 0.5 and 0.7) A-site deficient perovskites. Physical Chemistry Chemical Physics. 2018;20:18279-90.

184. Crank J. *The mathematics of diffusion*, 2rd Edition. Oxford university press; 1979.

185. Berenov A, Atkinson A, Kilner J, Bucher E, Sitte W. Oxygen tracer diffusion and surface exchange kinetics in La0. 6Sr0. 4CoO3− δ. Solid State Ionics. 2010;181:819-26.

186. Cooper S. Quantifying the transport properties of solid oxide fuel cell electrodes. Ph. D Thesis, Imperial College London. 2015.

187. Shen Z. Mass Transport in Mixed-Conducting LSCrF-ScSZ Dual Phase Composites for Oxygen Transport Membrane Applications. Ph. D Thesis. Imperial College London; 2017.

188. Kingery WD, Bowen HK, Uhlmann DR. *Introduction to ceramics*, 2rd edition. John wiley & sons; 1976.

189. Fearn S. An introduction to time-of-flight secondary ion mass spectrometry (ToF-SIMS) and its application to materials science: Morgan & Claypool Publishers San Rafael, CA, USA; 2015.

190. Vickerman JC, Gilmore IS. *Surface analysis: the principal techniques*, 2rd edition. John Wiley & Sons; 2011.

191. Fearn S. MSE302 course slides: Materials Characterisation Ion beam Techniques: Imperial College London.

192. Stephan T, Zehnpfenning J, Benninghoven A. Correction of dead time effects in time‐of‐flight mass spectrometry. Journal of Vacuum Science & Technology A: Vacuum, Surfaces, and Films. 1994;12:405-10.

193. De Souza R, Zehnpfenning J, Martin M, Maier J. Determining oxygen isotope profiles in oxides with Time-of-Flight SIMS. Solid State Ionics. 2005;176:1465-71.

194. Hofmann JP, Rohnke M, Weckhuysen BM. Recent advances in secondary ion mass spectrometry of solid acid catalysts: large zeolite crystals under bombardment. Physical Chemistry Chemical Physics. 2014;16:5465-74.

195. German RM. *Sintering theory and practice*, 1st edition. John wiley & sons; 1996.

196. Rahaman MN. *Ceramic processing and sintering*, 2rd edition. CRC press; 2017.

197. Kang S-JL. *Sintering: densification, grain growth and microstructure*, 1st edition. Elsevier; 2004.

198. Fujii K, Shiraiwa M, Esaki Y, Yashima M, Kim SJ, Lee S. Improved oxide-ion conductivity of NdBaInO4 by Sr doping. J Mater Chem A. 2015;3:11985-90.

199. Speakman S, Richardson J, Mitchell B, Misture S. In-situ diffraction study of Ba2In2O5. Solid State Ionics. 2002;149:247-59.

200. Fujii K, Esaki Y, Omoto K, Yashima M, Hoshikawa A, Ishigaki T, et al. New Perovskite-Related Structure Family of Oxide-Ion Conducting Materials NdBaInO(4). Chem Mater. 2014;26:2488-91.

201. Database of Ionic Radii [Available from: http://abulafia.mt.ic.ac.uk/shannon/ptable.php.

202. Yu. Zhou MS, Masanori Nagao, Kotaro Fujii, Isao Tanaka, Masatomo Yashima, Laura Baque, Juan F. Basbus, Liliana Mogni and Stephen J. Skinner. Protonic conduction in BaNdInO4 Structure achieved by acceptor doping. Journal of Materials Chemistry2021.

203. Brandao AD, Nasani N, Yaremchenko AA, Kovalevsky AV, Fagg DP. Solid solution limits and electrical properties of scheelite SryLa1-yNb1-xVxO4-delta materials for x=0.25 and 0.30 as potential proton conducting ceramic electrolytes. Int J Hydrogen Energ. 2018;43:18682-90.

204. Irvine JTS, West AR, Amano E, Huanosta A, Valenzuela R. Characterization of Magnetic-Materials by Impedance Spectroscopy. Solid State Ionics. 1990;40-1:220-3.

205. Kreuer K-D. Proton-conducting oxides. Annu Rev Mater Res. 2003;33:333-59.

206. Azad A, Irvine J. Synthesis, chemical stability and proton conductivity of the perovksites Ba (Ce, Zr) 1− x Scx O3− δ. Solid State Ionics. 2007;178:635-40.

207. Haugsrud R, Kjølseth C. Effects of protons and acceptor substitution on the electrical conductivity of La6WO12. Journal of Physics and chemistry of Solids. 2008;69:1758-65.

208. Haugsrud R, Risberg T. Protons in acceptor-doped La3NbO7 and La3TaO7. Journal of The Electrochemical Society. 2009;156:B425.
209. Han D, Kato K, Uda T. La 2 (Nb 1− x Y x) 2 O 7− δ: discovery of a novel fluorite structure-based ionic conductor. Chemical Communications. 2017;53:12684-7.
210. Haugsrud R, Norby T. High-temperature proton conductivity in acceptor-doped LaNbO4. Solid State Ionics. 2006;177:1129-35.
211. Kitamura N, Amezawa K, Tomii Y, Yamamoto N. Protonic conduction in rare earth orthophosphates with the monazite structure. Solid State Ionics. 2003;162:161-5.
212. Chesnaud A, Braida M-D, Estradé S, Peiro F, Tarancón A, Morata A, et al. High-temperature anion and proton conduction in RE3NbO7 (RE= La, Gd, Y, Yb, Lu) compounds. Journal of the European Ceramic Society. 2015;35:3051-61.
213. Suito K, Namba J, Horikawa T, Taniguchi Y, Sakurai N, Kobayashi M, et al. Phase relations of CaCO3 at high pressure and high temperature. American Mineralogist. 2001;86:997-1002.
214. Nie S, Liu Y, Liu Q, Wang M, Wang H. Phase transitions and thermal expansion of BaCO3 and SrCO3 up to 1413 K. European Journal of Mineralogy. 2017;29:433-43.
215. Li M, Zhang H, Cook SN, Li L, Kilner JA, Reaney IM, et al. Dramatic influence of A-site nonstoichiometry on the electrical conductivity and conduction mechanisms in the perovskite oxide Na0. 5Bi0. 5TiO3. Chemistry of Materials. 2015;27:629-34.
216. Waller D, Lane J, Kilner J, Steele B. The structure of and reaction of A-site deficient La0. 6Sr0. 4− xCo0. 2Fe0. 8O3− δ perovskites. Materials Letters. 1996;27:225-8.
217. Druce J, Tellez H, Burriel M, Sharp M, Fawcett L, Cook S, et al. Surface termination and subsurface restructuring of perovskite-based solid oxide electrode materials. Energy & Environmental Science. 2014;7:3593-9.
218. Zedtwitz-Nikulshyna. *CO_2 capture from atmospheric air via solar driven carbonation-calcination cycles*, 1st edition. ETH Zurich; 2009.
219. Abanades JC, Alvarez D. Conversion limits in the reaction of CO2 with lime. Energy & Fuels. 2003;17:308-15.
220. Beruto DT, Botter R. Liquid-like H2O adsorption layers to catalyze the Ca (OH) 2/CO2 solid–gas reaction and to form a non-protective solid product layer at 20° C. Journal of the European Ceramic Society. 2000;20:497-503.
221. Kang SH, Lee SG, Jung WM, Kim MC, Kim W-S, Choi CK, et al. Effect of Taylor vortices on calcium carbonate crystallization by gas–liquid reaction. Journal of crystal growth. 2003;254:196-205.
222. Miles FT, Menzies AW. The vapor pressure of deuterium water from 20 to 230. Journal of the American Chemical Society. 1936;58:1067-9.
223. Bonanos N, Huijser A, Poulsen FW. H/D isotope effects in high temperature proton conductors. Solid state ionics. 2015;275:9-13.
224. Chen Y-F, Tsai Y-T, Hirsch L, Bassani DM. Kinetic isotope effects provide experimental evidence for proton tunneling in methylammonium lead Triiodide Perovskites. Journal of the American Chemical Society. 2017;139:16359-64.
225. Yashima M, Tsujiguchi T, Sakuda Y, Yasui Y, Zhou Y, Fujii K, et al. High oxide-ion conductivity through the interstitial oxygen site in Ba 7 Nb 4 MoO 20-based hexagonal perovskite related oxides. Nature communications. 2021;12:1-7.
226. Chater R. Oxygen Self-Diffusion and Surface Exchange Measurements of the Polycrystalline Oxide (La0. 8Sr0. 2)(Cr0. 2Fe0. 8) O3‑d Using Secondary Ion Mass Spectrometry: Ph. D. Thesis, Imperial College London; 2014.
227. Parras JP, De Souza RA. Grain-boundary diffusion of cations in fluorite-type oxides is faster but not always easier. Acta Materialia. 2020;195:383-91.
228. Herzig C, Willecke R, Vieregge K. Self-diffusion and fast cobalt impurity diffusion in the bulk and in grain boundaries of hexagonal titanium. Philosophical Magazine A. 1991;63:949-58.
229. Kilner J. Optimisation of oxygen ion transport in materials for ceramic membrane devices. Faraday discussions. 2007;134:9-15.

230. Whipple R. CXXXVIII. Concentration contours in grain boundary diffusion. The London, Edinburgh, and Dublin Philosophical Magazine and Journal of Science. 1954;45:1225-36.
231. Chung YC, Wuensch BJ. An improved method, based on Whipple's exact solution, for obtaining accurate grain‐boundary diffusion coefficients from shallow solute concentration gradients. Journal of applied physics. 1996;79:8323-9.
232. De Souza R, Kilner J, Walker J. A SIMS study of oxygen tracer diffusion and surface exchange in La0. 8Sr0. 2MnO3+ δ. Materials Letters. 2000;43:43-52.
233. Hancke R, Fearn S, Kilner JA, Haugsrud R. Determination of proton-and oxide ion tracer diffusion in lanthanum tungstate (La/W= 5.6) by means of ToF-SIMS. Physical Chemistry Chemical Physics. 2012;14:13971-8.
234. Manning P, Sirman J, Kilner J. Oxygen self-diffusion and surface exchange studies of oxide electrolytes having the fluorite structure. Solid State Ionics. 1996;93:125-32.
235. De Souza R, Kilner J, Jeynes C. The application of secondary ion mass spectrometry (SIMS) to the study of high temperature proton conductors (HTPC). Solid State Ionics. 1997;97:409-19.
236. Fop S, McCombie KS, Wildman EJ, Skakle JM, Irvine JT, Connor PA, et al. High oxide ion and proton conductivity in a disordered hexagonal perovskite. Nature materials. 2020:1-6.

Appendices

Table A.1 The representative AC impedance data fitting of the BNC20 sample measured in the cooling cycle in dry air. The Nyquist plots were fitted with two R-CPE components connected in series at low temperatures and with an additional inductor connected in series at high temperature.

	R1/CPE1				R2/CPE2				Goodness of fit
T (℃)	R1 (Ω)	CPE1-T (F·cm^{-1})	CPE1-P	Capacitance C1(F)	R2 (Ω)	CPE2-T	CPE2-P	Capacitance C2(F)	χ^2
250	157430	4.85 x10^{-11}	0.88989	1.13 x10^{-11}	275580	4.39 x10^{-8}	0.74445	9.64 x10^{-9}	5.23 x10^{-5}
275	75896	6.61 x10^{-11}	0.87325	1.12 x10^{-11}	151340	4.82 x10^{-8}	0.76159	1.03 x10^{-8}	1.16 x10^{-4}
300	38569	8.98 x10^{-11}	0.85692	1.10 x10^{-11}	87214	5.39 x10^{-8}	0.76954	1.08 x10^{-8}	7.85 x10^{-4}
325	20570	1.23 x10^{-11}	0.83983	1.05 x10^{-11}	52354	6.11 x10^{-8}	0.77186	1.12 x10^{-8}	5.22 x10^{-4}
350	11135	4.99 x10^{-11}	0.90463	1.09 x10^{-11}	33431	8.31 x10^{-8}	0.74846	1.15 x10^{-8}	6.16 x10^{-4}
375	6481	5.91 x10^{-11}	0.89737	1.09 x10^{-11}	21042	9.02 x10^{-8}	0.75375	1.16 x10^{-8}	4.38 x10^{-4}
400	3831	4.14 x10^{-11}	0.92200	1.10 x10^{-11}	13383	1.00 x10^{-7}	0.75464	1.16 x10^{-8}	4.77 x10^{-4}
425	2400	3.38 x10^{-11}	0.93849	1.16 x10^{-11}	8739	1.04 x10^{-7}	0.76048	1.15 x10^{-8}	5.38 x10^{-5}
450	1556	2.45 x10^{-11}	0.96424	1.30 x10^{-11}	5823	1.08 x10^{-7}	0.76532	1.12 x10^{-8}	6.09 x10^{-4}
475	1037	1.79 x10^{-11}	0.99248	1.56 x10^{-11}	3920	1.07 x10^{-7}	0.77292	1.09 x10^{-8}	6.92 x10^{-4}
500	711.5	2.33 x10^{-11}	0.98694	1.84 x10^{-11}	2722	1.09 x10^{-7}	0.77768	1.07 x10^{-8}	9.98 x10^{-5}
525	491.7	3.53 x10^{-11}	0.97078	2.06 x10^{-11}	1932	1.24 x10^{-7}	0.77206	1.06 x10^{-8}	9.49 x10^{-5}
550	349.4	2.76 x10^{-11}	1	2.76 x10^{-11}	1376	1.32 x10^{-7}	0.77201	1.04 x10^{-8}	9.59 x10^{-5}
575	255.3	3.40 x10^{-11}	1	3.40 x10^{-11}	971.5	1.39 x10^{-7}	0.77318	1.02 x10^{-8}	9.20 x10^{-5}
600	191.9	4.20 x10^{-11}	1	4.20 x10^{-11}	677.5	1.46 x10^{-7}	0.77395	9.91 x10^{-9}	9.73 x10^{-5}
625	146.6	5.22 x10^{-11}	1	5.22 x10^{-11}	482.2	1.55 x10^{-7}	0.77422	9.72 x10^{-9}	1.01 x10^{-4}
650	113.6	6.49 x10^{-11}	1	6.49 x10^{-11}	341.8	1.73 x10^{-7}	0.77095	9.59 x10^{-9}	9.79 x10^{-5}
675	89.69	8.09 x10^{-11}	1	8.09 x10^{-11}	243.9	1.97 x10^{-7}	0.76655	9.53 x10^{-9}	1.02 x10^{-4}
700	72.15	1.01 x10^{-10}	1	1.01 x10^{-10}	173.4	2.32 x10^{-7}	0.76029	9.53 x10^{-9}	1.17 x10^{-4}
725	59.24	1.28 x10^{-10}	1	1.28 x10^{-10}	122.1	2.63 x10^{-7}	0.75719	9.54 x10^{-9}	1.23 x10^{-4}
750	48.71	1.62 x10^{-10}	1	1.62 x10^{-10}	84.94	3.00 x10^{-7}	0.75451	9.62 x10^{-9}	5.85 x10^{-5}

Table A.2 The AC impedance data fitting of the BNC20 sample measured in the cooling cycle in **wet** air. The Nyquist plots were fitted with two R-CPE components connected in series at low temperatures and with an additional inductor connected in series at high temperatures.

	R1/CPE1				R2/CPE2				Goodness of fit
T (℃)	R1 (Ω)	CPE1-T	CPE1-P	Capacitance C1(F)	R2 (Ω)	CPE2-T	CPE2-P	Capacitance C2(F)	χ^2
250	72106	8.86 x10^{-11}	0.85827	1.23 x10^{-11}	216220	4.69 x10^{-8}	0.74839	1.00 x10^{-8}	8.52 x10^{-8}
275	37533	1.09 x10^{-10}	0.84940	1.20 x10^{-11}	113770	5.59 x10^{-8}	0.75040	1.04 x10^{-8}	4.34 x10^{-5}
300	19904	5.31 x10^{-11}	0.90173	1.19 x10^{-11}	65540	8.37 x10^{-8}	0.71926	1.10 x10^{-8}	9.57 x10^{-5}
325	11514	5.09 x10^{-11}	0.89865	1.01 x10^{-11}	36303	9.34 x10^{-8}	0.72562	1.09 x10^{-8}	1.21 x10^{-4}
350	6949	6.51 x10^{-11}	0.89608	1.20 x10^{-11}	20827	1.02 x10^{-7}	0.73141	1.07 x10^{-8}	1.06 x10^{-4}
375	4325	4.41 x10^{-11}	0.92165	1.18 x10^{-11}	12415	1.13 x10^{-7}	0.73320	1.04 x10^{-8}	2.96 x10^{-4}
400	2743	3.40 x10^{-11}	0.94086	1.23 x10^{-11}	7325	1.12 x10^{-7}	0.74489	9.81 x10^{-9}	1.67 x10^{-4}
425	1815	2.35 x10^{-11}	0.96727	1.33 x10^{-11}	4703	1.23 x10^{-7}	0.74523	9.66 x10^{-9}	1.18 x10^{-4}
450	1233	1.73 x10^{-11}	0.99166	1.49 x10^{-11}	3036	1.22 x10^{-7}	0.75407	9.29 x10^{-9}	1.28 x10^{-4}
475	860.2	1.72 x10^{-11}	1	1.72 x10^{-11}	2013	1.16 x10^{-7}	0.76574	8.99 x10^{-9}	1.13 x10^{-4}
500	605.7	2.11 x10^{-11}	1	1.94 x10^{-11}	1457	1.57 x10^{-7}	0.74627	9.08 x10^{-9}	1.53 x10^{-4}
525	438.3	2.32 x10^{-11}	1	2.32 x10^{-11}	1010	1.47 x10^{-7}	0.75702	8.69 x10^{-9}	1.91 x10^{-4}
550	324.6	2.80 x10^{-11}	1	2.80 x10^{-11}	716.8	1.41 x10^{-7}	0.76568	8.44 x10^{-9}	1.54 x10^{-4}
575	243.5	3.45 x10^{-11}	1	3.45 x10^{-11}	514.2	1.33 x10^{-7}	0.77499	8.19 x10^{-9}	1.68 x10^{-4}
600	186.7	4.27 x10^{-11}	1	4.27 x10^{-11}	376.3	1.28 x10^{-7}	0.78207	7.99 x10^{-9}	1.10 x10^{-4}
625	144.0	5.32 x10^{-11}	1	5.32 x10^{-11}	276.2	1.27 x10^{-7}	0.78625	7.85 x10^{-9}	9.58 x10^{-5}
650	112.6	6.63 x10^{-11}	1	6.63 x10^{-11}	203.5	1.30 x10^{-7}	0.78877	7.75 x10^{-9}	2.82 x10^{-5}
675	89.31	8.20 x10^{-11}	1	8.20 x10^{-11}	150.7	1.42 x10^{-7}	0.78686	7.71 x10^{-9}	3.56 x10^{-5}
700	71.87	1.01 x10^{-10}	1	1.01 x10^{-10}	111.3	1.59 x10^{-7}	0.78339	7.74 x10^{-9}	3.94 x10^{-5}
725	58.60	1.27 x10^{-10}	1	1.27 x10^{-10}	81.50	1.80 x10^{-7}	0.78014	7.82 x10^{-9}	3.41 x10^{-5}
750	47.06	1.58 x10^{-10}	1	1.58 x10^{-10}	59.06	2.15 x10^{-7}	0.77294	7.85 x10^{-9}	4.12 x10^{-5}

A.3 Rietveld refinement on the $BaNdInO_4$ stoichiometry was done using Fullprof according to the structural model from the crystallographic information file (CIF) provided in the previous literature(115). In the Rietveld refinement only the positions of heavy atoms (Nd, Ba, In) in the unit cell volume were refined while the light elements (oxygen ions) are not detectable under X-ray diffraction. The refined lattice parameters were a=9.0983(7) Å, b=6.0451(3) Å, c=8.2630(4) Å, β=103.417(6)°, and the unit cell volume=442.061(43) $Å^3$, with conventional Rietveld R-factors R_p=17.8, R_{wp}=17.4 and a goodness of fit, χ^2=5.99. The main discrepancy as can be seen from figure A.3 was resulted from the relative intensities of the observed peaks. That is because the structural model used in the Rietveld refinement was obtained based on synchrotron X-ray powder diffraction(115), while the XRD patterns analysed in this work are collected using pellet samples. The grains being scanned under X-ray diffraction on the upmost surface of the pellet samples exhibited a certain degree of preferential orientations which can result in relative difference in peak intensities. As can be seen from table A.3(2), there is a difference in the lattice parameters obtained by two refinement methods. According to the goodness of fit, the results from Le Bail refinement are more reliable.

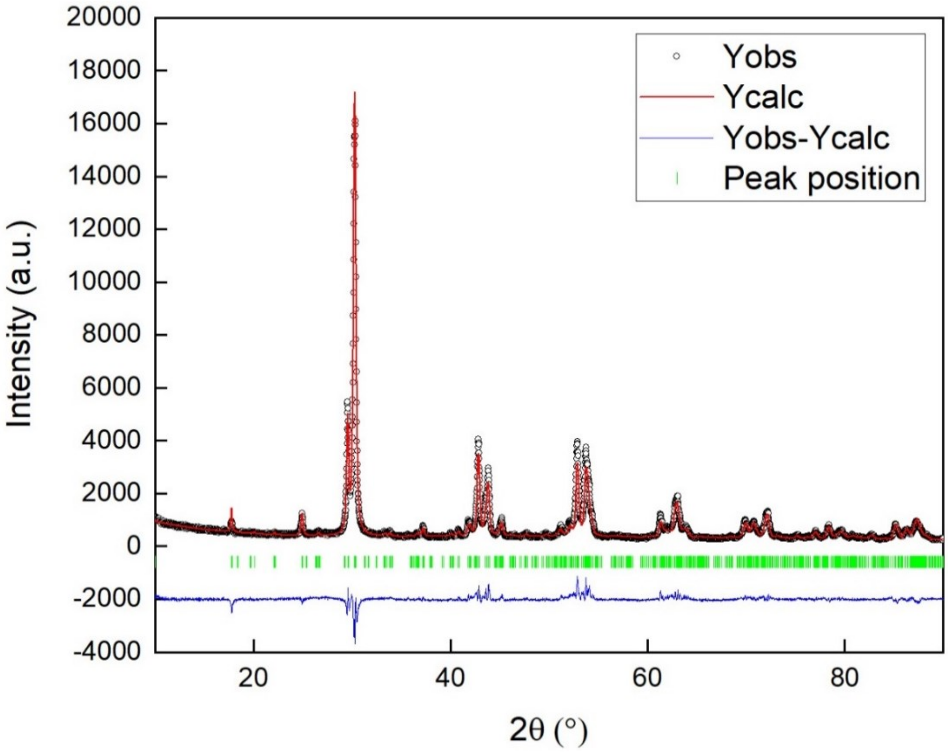

Figure A.3 The Rietveld refinement result for the $BaNdInO_4$ stoichiometry. The dark marks are the observed experimental data; red solid line represents the calculated intensities; green vertical bars label the positions of Bragg reflection; and the blue solid line is the difference between the observed intensities and the calculated ones

Table A.3(1) Refined heavy atoms' position in the unit cell by Rietveld refinement

Site label X	Atom Y	g*	x	y	z
Nd1	Nd	1	0.45734(11)	0.75487(87)	0.11020(33)
Ba1	Ba	1	0.14760(15)	0.25372(89)	0.03453(48)
In1	In	1	0.83303(15)	0.25400(108)	0.20960(44)

*g: occupancy factor of atom Y at the X site.

Table A.3(2) Comparison of refined lattice parameters obtained by Le Bail and Rietveld refinement.

$BaNdInO_4$	$a/Å$	$b/Å$	$c/Å$	$\beta/°$	$UCV/Å^3$	χ^2
Le Bail	9.0931(1)	6.0443(1)	8.2585(1)	103.401(1)	441.540(11)	2.61
Rietveld	9.0983(7)	6.0451(3)	8.2630(4)	103.417(6)	442.061(43)	5.99

Figure A.4

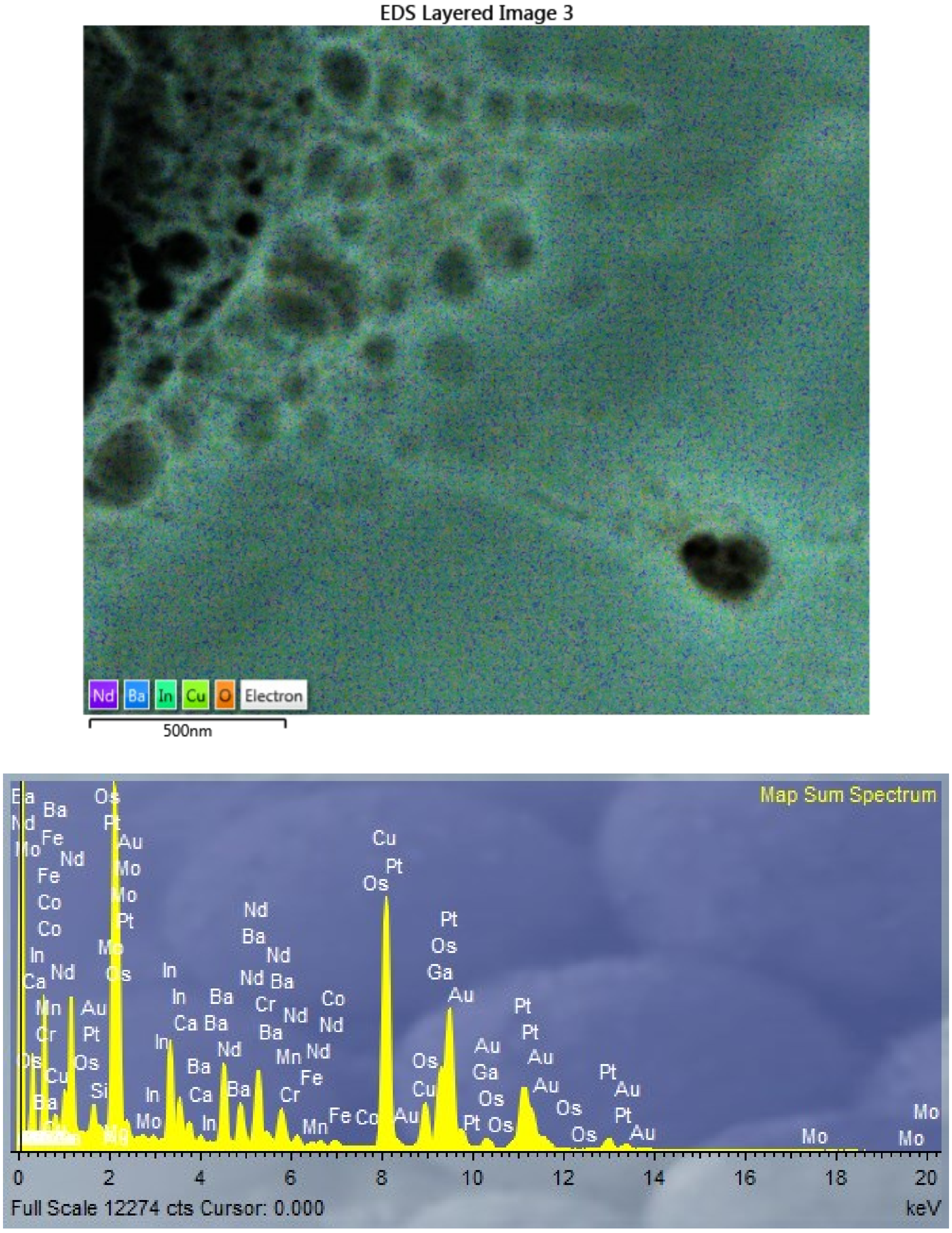

Figure A.4 (Top) Overall elemental mapping of the selected area of the lighter sample (pure $H_2{}^{18}O$ exchanged at 500 ℃ for 2 hours) under STEM-EDS. (Bottom) EDS spectrum of the whole selected area as shown in the elemental mappings

According to the EDS spectrum, small amounts of Mo, Fe and Mn were detected which could be due to the cross contamination of the previous annealed samples. Besides, certain amounts of Pt, Ga and Cr were also detected which was introduced in the lamellae sample preparation. In other parts of the selected area, the chemical composition on average was measured as Ca:Nd:Ba:In =0.11:0.85:1:1.15 (atomic ratio, Ba was set as 1), where a loss in the atomic ratio of calcium and barium cations was observed compared with the original stoichiometry of BNC20. This result was in agreement with the *in-situ* XRD results after the long period of time wet annealing, showing that the BNC20 sample experienced calcium exsolution forming $CaCO_3$ on the sample surface during wet annealing processes.

Figure A.5

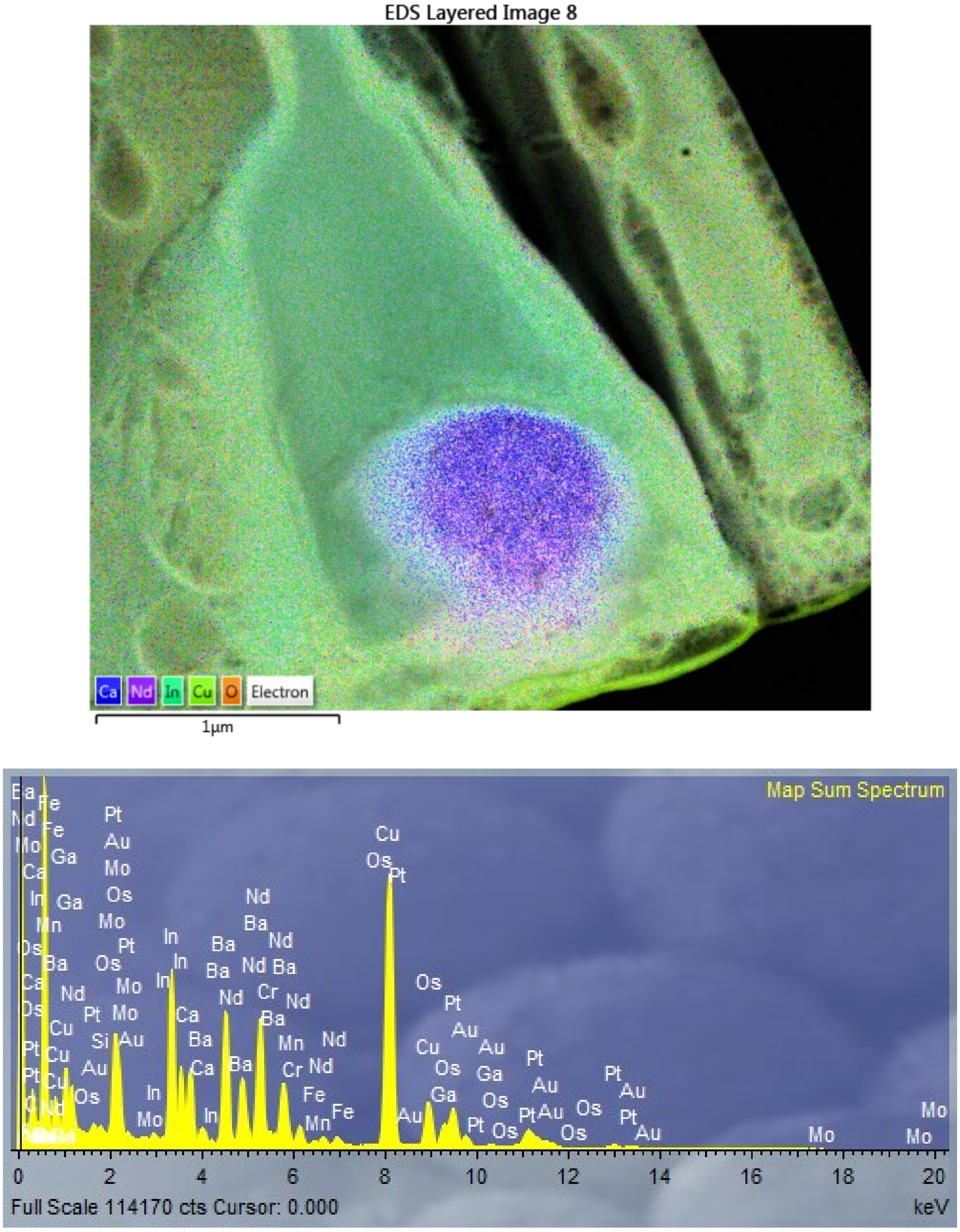

Figure A.5 (Top) Overall elemental mappings of the selected area of the darker sample ($H_2{}^{18}O$+O_2 exchanged at 600 ℃ for 1 hour) under STEM-EDS. (Bottom) EDS spectrum of the whole selected area as shown in the elemental mappings

Figure A.6

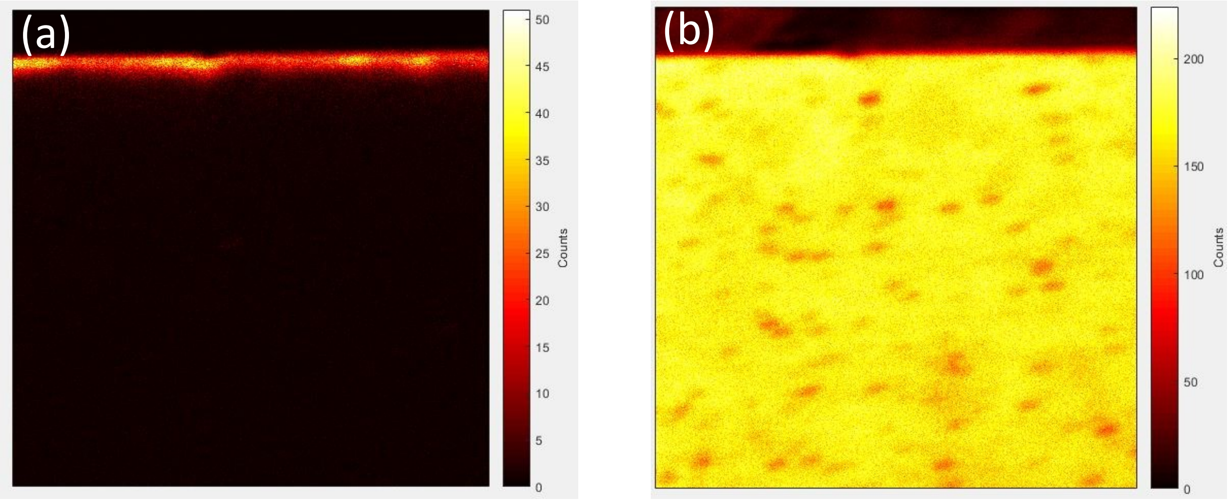

Figure A.6. (a) ^{18}O map and (b) ^{16}O+^{18}O map of the selected area of the BNC20 sample exchanged in O_2 (150 Torr)+ $H_2{}^{18}O$ (32.55 Torr) at 500 ℃ for 2 hours.

Figure A.7

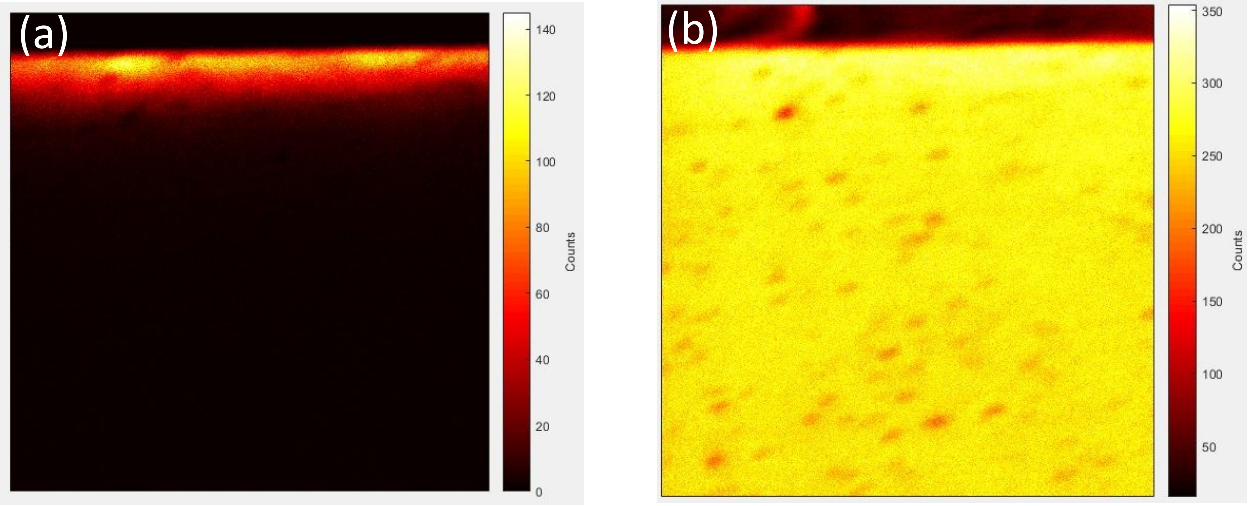

Figure A.7. (a) ^{18}O map and (b) ^{16}O+^{18}O map of the selected area of the BNC20 sample exchanged in O_2 (150 Torr)+ $H_2{}^{18}O$ (32.59 Torr) at 550 ℃ for 2 hours.

Figure A.8

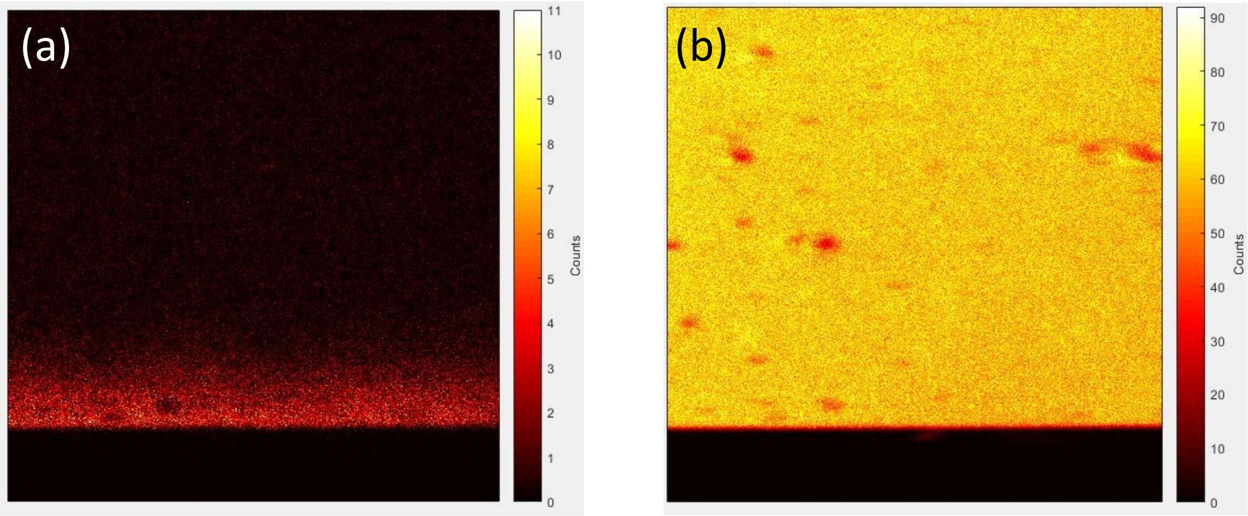

Figure A.8. (a) ^{18}O map and (b) ^{16}O+^{18}O map of the selected area of the BNC20 sample exchanged in O_2 (150 Torr)+ $H_2{}^{18}O$ (32.54 Torr) at 600 ℃ for 1 hour.

Figure A.9

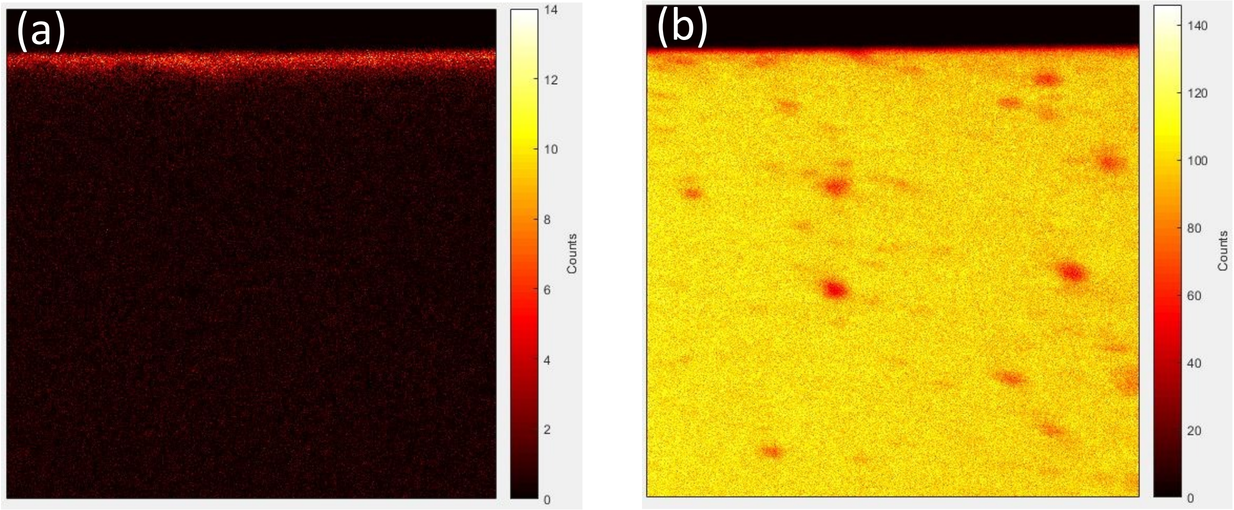

Figure A.9. (a) ^{18}O map and (b) $^{16}O+^{18}O$ map of the selected area of the BNC20 sample exchanged in $H_2{}^{18}O$ (32.69 Torr) at 500 ℃ for 2 hours.